Yaw control at high angles of attack by tangential forebody blowing

Crowther, William James

Award date:
1994

Awarding institution:
University of Bath

YAW CONTROL AT HIGH ANGLES OF ATTACK BY TANGENTIAL FOREBODY BLOWING

Submitted by William James Crowther
for the Degree of PhD
of the University of Bath
1994

COPYRIGHT

i

ProQuest LLC
789 East Eisenhower Parkway
P.O. Box 1346
Ann Arbor, MI 48106-1346

SUMMARY

Considerable tactical advantages are anticipated for combat aircraft able to manoeuvre freely at very high angles of attack. Currently, many aircraft are angle of attack limited through lack of control power, particularly in yaw. This experimental study investigates a novel technique known as Tangential Forebody Blowing which can provide control yawing moments at up to and beyond 90° angle of attack.

Tests were performed in the University of Bath 2.1 m x 1.5 m low speed wind tunnel using an approximately 6% scale generic combat aircraft model fitted with blowing slots in the nose cone. Six component force and moment data was measured for angles of attack up to 90° and for a number of different slot geometries and locations. Pressure data was measured at three stations on the forebody. The behaviour of the blowing jet under quiescent conditions was investigated through a series of flow visualisation experiments on a variable geometry slot rig.

Unblown tests on the generic combat aircraft model showed that above 35° angle of attack, destabilising yawing moments from asymmetries in the forebody flowfield were larger than the control moment available from the rudder. Also, between 20 and 45° angle of attack, the forebody and LEX flowfields were coupled. This coupling increases the complexity of the aircraft response to blowing.

With careful choice of slot location and geometry, low blowing rates (C_μ=0.008) could produce large control yawing moments (C_N=0.1) at angles of attack up to 90°. However, at very low blowing rates a control reversal developed. Also, slot stall occurred at very high angles of attack. Fluid mechanisms are proposed for these undesirable phenomena based on visualisation studies of forebody and wall jet flows.

The performance of massflow and momentum based scaling parameters is assessed and the feasibility of full scale application of the control device demonstrated.

ACKNOWLEDGEMENTS

I would like to express my thanks to all those who made this work possible, and to those who made it enjoyable.

Thanks is extended in the first instance to Norman Wood for setting up the project and for his guidance through the many stages of the work. My standards have been raised by our partnership. I hope his have not been lowered.

I would also particularly like to thank Adrian and Les in the workshop for all their efforts in making the models (and other things besides). Their 'can-do' attitude made a significant contribution to the success of the project.

Lastly, I would like to thank Dave P, Dave B, Doug, Uwe, Anna, Maggie, Jon, Paddy, Mark, Tony, and all the others who have passed through the office. Without their constant help and encouragement this thesis would have been completed in a lot less than three and a half years.

Financial support for this project was provided by a SERC CASE Award in conjunction with DRA Farnborough. Support for the writing-up stage was provided by the DSS.

CONTENTS

CHAPTER 3

EXPERIMENTAL FACILITIES AND TECHNIQUES

CHAPTER 4

PRESENTATION AND DISCUSSION OF RESULTS

CHAPTER 6

FUTURE WORK

LIST OF FIGURES

CHAPTER 3

NOMENCLATURE

A	area	m^2
A_{geom}	geometric slot area	m^2
A_j	effective aerodynamic slot area	m^2
A_{ref}	reference area	m^2
c	mean wing chord	0.3 m
C_D	slot discharge coefficient	
C_L	rolling moment coefficient	
C_M	pitching moment coefficient	
C_p	pressure coefficient	
$C_{p\,plen}$	plenum pressure coefficient	
C_Q	jet massflow coefficient	
C_Z	normal force coefficient	
C_μ	jet momentum coefficient	
D	base diameter of forebody	0.07 m
h	slot height	m
k	micromanometer calibration constant	Pa/V
k_a	jet augmentation ratio	
l	reference length	m
ℓ	slot length	m
L	length of forebody	0.28 m
m	jet massflow	kg/s
M	pitching moment	Nm
Ma_j	jet Mach number	
M_j	jet momentum flux	N
N	yawing moment	Nm
N_{RJ}	reaction jet yawing moment	Nm
p	static pressure	N/m^2
p_p	plenum pressure	N/m^2
p_∞	free stream static pressur	N/m^2
Δp	nozzle pressure difference	N/m^2
q	free stream dynamic pressure	N/m^2
r	wall radius	m
R	base radius of forebody	0.035 m

Re_j	jet Reynolds number	
s	distance downstream from jet exit plane	m
S	wing reference area	0.15 m^2
u,v	velocities in x-y coordinate system	m/s
w	crossflow velocity	m/s
v_m	maximum jet velocity	m/s
$v_{m/2}$	half maximum jet velocity	m/s
V	voltage	V
V_{man}	voltage output from micromanometer	V
V_j	jet velocity	m/s
V_∞	free stream velocity	m/s
V	volume flow	m^3/s
x	distance along forebody from nose tip	m
x_{cp}	location of longitudinal centre of pressure relative to balance neutral point	m
x_N	moment arm of aircraft nose about aircraft c.g.	m
X	axial force	N
y_m	location of v_m in a wall jet	m
$y_{m/2}$	location of $v_{m/2}$ in a wall jet	m
Y	side force	N
Z	normal force	N
α	angle of attack	degrees
α_{asym}	angle of attack for onset of vortex asymmetry	degrees
α_{pvs}	angle of attack for onset of periodic vortex shedding	degrees
δ	length scale of disturbance in jet sheet	m
ρ	density	kg/m^3
ρ_j	jet density	kg/m^3
ρ_∞	free stream density	kg/m^3
Θ	slot angular position	degrees

Subscripts

j	jet

p	port
s	starboard
∞	free stream

Abbreviations

c.g	Centre of Gravity
DRA	Defence Research Agency
HARV	High Angle of Attack Research Vehicle
HIRM	High Incidence Research Model
I/O	Input/Output
LEX	Leading Edge eXtension
PC	Personal Computer
PVC	Poly Vinyl Chloride
TFB	Tangential Forebody Blowing

Ideas and concepts come

out of the mind,

not out of

computers or wind tunnels.

Dietrich Küchemann

CHAPTER 1

INTRODUCTION

1.1 BACKGROUND

Good combat aircraft design involves finding a compromise between many conflicting requirements, figure 1.1. Between 1950 and 1970, the primary role of combat aircraft was perceived to be interception of incoming intruders[1]. This required a good climb rate and a high maximum speed, and could be achieved with a high thrust-to-weight ratio and good supersonic aerodynamics. Resulting aircraft, such as the Starfighter and F-4 Phantom, often had very high wing loadings and poor low speed/high angle of attack aerodynamic characteristics, meaning that they performed badly in close-in combat situations[2]. This was seen as an acceptable trade-off for the improved high speed performance since it was believed that future hostile encounters would take place at long range with sophisticated air-to-air missiles. Combat experience in Vietnam and Korea showed otherwise: high-speed, technologically superior aircraft were being lost to less sophisticated aircraft whose only advantage was better low speed manoeuvrability. In part response to this, the United States Air Force initiated the Light-Weight Fighter Programme, which resulted in the F-16 and F/A-18, both highly manoeuvrable fighters.

The next generation of fighter aircraft will need to be as, if not more, manoeuvrable than their predecessors, particularly in terms of sustained turn rate and the ability to point the fuselage independently of the aircraft trajectory[3,4,5]. To that end much research work is being directed at extending the flight envelope to high, post-stall angles of attack, where there are significant performance gains yet to be realised. A typical agile manoeuvre for an aircraft with high-alpha capability is the "J" turn, or Herbst Manoeuvre[6,7], figure 1.2. In this, the aircraft pitches up to a high angle of attack, rotates about its velocity vector, then pitches down and accelerates along a new

heading.

Provision of lateral control at very high angles of attack poses a number of challenges[8,9]. Above about 40° angle of attack, the yawing moment available from the rudder is severely limited as it becomes enveloped in the low energy wake of the wing and fuselage. Also, asymmetries in the forebody flowfield at high angles of attack can lead to the generation of large destabilising side forces on the forebody. This leads to a severe deficiency in yaw control power at angles of attack for post-stall manoeuvering.

The work described in this thesis focuses on improving combat aircraft agility through the development of a novel yaw control method, known as Tangential Forebody Blowing. This technique employs the unique attachment and entrainment properties of a curved wall jet to control the forebody flowfield and produce yawing moments where the rudder is no longer effective.

Previous work relevant to this study is split roughly into two areas:

1) Wall jet fluid dynamics, and
2) Slender Body Aerodynamics.

These are two fundamentally different fields of research and at present there is little overlap in the literature. In particular, fluidic devices are often being applied in an *ad hoc* manner through lack of understanding of the basic fluid dynamics involved. This has led to experiments where a multitude of configurations have been tested in an attempt to "optimize" a particular control.

A key theme in this thesis is the fusion of wall jet fluid dynamics with high angle of attack work. In this way, understanding of the flow physics can be used to provide sound principles from which an efficient and effective forebody flow control scheme can be designed.

At this stage, it is useful to define what is meant by angle of attack. In particular it is important to distinguish between aircraft angle of attack and aircraft pitch attitude.

The angle of attack of an aircraft[10] is a measure of the ratio of the component of the free stream flow aligned with the fuselage axis (u), to the component perpendicular to the fuselage axis (w), figure 1.3. At low angles of attack the flow is predominantly aligned with the fuselage axis whereas at high angles of attack, approaching 90°, the flow is predominantly perpendicular to the fuselage axis. Aircraft pitch attitude relates to the orientation of the aircraft relative to the gravity vector (or horizon) and has no direct bearing on the aircraft aerodynamics. To an observer on the ground, it is very difficult to distinguish between angle of attack and pitch attitude of a manoeuvering aircraft, and it is often incorrectly assumed that the angle of attack is the observed pitch angle.

The numerical value of what is considered to be a high angle of attack has steadily increased as aircraft technology has improved. During the F-4 Phantom era (1960-1970) the controllable angle of attack range was up to about 20° and aggressive manoeuvring at angles of attack above this was likely to lead to a departure from controlled flight. The F-16 and F/A-18 introduced in the 1970's were controllable up to about 40° angle of attack, though problems due to severe airframe buffeting at angles of attack below this have limited the operational usefulness of the extended alpha range. Today there are a number of research programmes involving the X-29, X-31 and F-18 HARV vehicles[11,12,13] which actively explore even higher angles of attack, up to 70°. Impressive displays at recent airshows by the Su-27 and MiG-29[14] have demonstrated a rapid pitch-up manoeuvre, known as the Cobra, actually going beyond 90°. Similarly, at the 1993 Dubai Aerospace and Defense Exhibition the Su-35 demonstrated a manoeuvre known as the Hook in which the angle of attack is rapidly increased to approximately 90° during a highly banked turn[15]. In a combat situation, this could greatly improve the aircraft's firing opportunities.

1.2 JET FLUID DYNAMICS

1.2.1 Overview

In this section the fluid dynamics of jets is examined, with the aim of providing a basis from which pneumatic devices used to control slender body flows may be understood. The simplest case of a free jet is considered first. This is then followed by a discussion of plane wall jets, i.e. a free jet with a solid boundary at its centreline. Finally, the relatively complex behaviour of curved wall jets is explored.

1.2.2 Two-Dimensional Free Jet

A sketch of a two-dimensional free jet issuing into quiescent (i.e. stationary) surroundings is shown in figure 1.4. As the jet develops in a streamwise direction, shear stresses at the edges of the jet induce mixing between the jet and the surroundings, leading to entrainment of fluid into the jet. This causes a reduction in the average velocity of the jet and an increase in the jet width.

Typical velocity profiles for a free jet are shown in figure 1.5. For a fully developed (i.e. fully turbulent) jet the profiles are self-similar, i.e.

$$\frac{u}{u_m} = F\left(\frac{y}{y_{m/2}}\right) \qquad 1.1$$

This result was first given by Prandtl[16]. Determination of the actual shape of the velocity profiles requires assumptions to be made about the variation of turbulent shearing stress through the flow. The first such solution was given by Tollmien using Prandtl's mixing length theory[17]. A simpler solution was developed by Görtler[16] who assumed that the eddy viscosity (i.e. the effective viscosity of the fluid under turbulent conditions) was constant across the flow at each longitudinal station.

The Reynolds number of a free jet is defined as

$$Re_j = \frac{x \rho_j V_j}{\mu} \qquad (1.2)$$

where x denotes a distance downstream of the jet exit. Transition to turbulence typically occurs at Reynolds numbers above 7×10^4.

1.2.3 Plane Wall Jet

By placing a solid surface along the centreline of a fully developed free jet, a turbulent plane wall jet is created[18], figure 1.6. This consists of an outer layer with a velocity profile similar to that of a free jet ($\partial u/\partial y$ negative) and a much thinner, inner layer with a velocity profile similar to that of a boundary layer ($\partial u/\partial y$ positive). The layer closest to the wall is largely governed by viscous forces, in contrast to the outer layer, which is driven by inertial forces. The ratio between the thickness of these two layers is determined by the jet Reynolds number, which in this case is defined as

$$Re_j = \frac{u_m (y_{m/2} - y_m) \rho}{\mu} \qquad (1.3)$$

This is similar to the definition of Reynolds number for a boundary layer, except in the boundary layer case, the boundary layer displacement thickness is used as the length scale.

A low Reynolds number for a wall jet signifies a thick inner layer.

The growth rate of a wall jet is reduced compared to that of the equivalent free jet. This is due to suppression of turbulent mixing processes in the vicinity of the wall.

1.2.4 Curved Wall jets

1.2.4.1 General Description

Plane wall jets are a special, simple case in the more general group of curved wall jets, figure 1.7. Curvature of the wall has two important effects:

1) A pressure gradient is created perpendicular to the streamlines in the jet (assuming they are curved by the presence of the wall), and

2) the turbulent intensity of the jet is modified.

For the case of a jet flowing over a convex wall, a strong surface suction is created and the turbulence is greatly increased. The surface suction enables the jet to remain attached to a highly divergent surface contour and the increase in turbulence increases the rate at which the surrounding fluid is entrained. These two effects are commonly known as the Coanda Effect, after Henry Coanda, who used the special properties of curved wall jet flows in a number of patented mixing devices in the 1930's[19]. The Coanda effect has been used to advantage in many aeronautical applications where control of flow separation is required. These include jet flap installations[20], circulation control aerofoils[21,22], control of wind tunnel boundary layers[23], drag reduction on bluff bodies such as road vehicles[24], and the control of vortical flow on delta wings by leading edge blowing[25,26].

The definition of jet Reynolds number for a curved wall jet is given by

$$Re_j = \frac{V_j \sqrt{hr}\,\rho}{\mu} \qquad (1.4)$$

from ref 16.

Note that in this case the length scale is defined as the root of the product of the slot height, h, and the wall radius r. This definition is only applicable to flows with

appreciable curvature, i.e. $r << \infty$. It is not clear how to resolve this difficulty. One solution might be to define the length scale relative to some growth/thickness parameter of the jet, which in turn is related to the wall radius.

A low jet Reynolds number is associated with a thin, low velocity jet developing over a highly curved surface.

From hereafter, all references to jet Reynolds number are based on the curved wall jet definition given in equation 1.4.

1.2.4.2 Jet Attachment

The behaviour by which a jet remains attached to a convex surface is essentially inviscid[27]. Equilibrium of a fluid element following a circular path is maintained by two equal and opposite forces: a centripetal force acting radially outwards and a pressure force acting radially inwards, figure 1.8. The equilibrium of the element may be expressed as the local pressure gradient equated to the inertial force on the element:

$$\frac{\partial p}{\partial y} = \frac{\rho u^2}{r} \tag{1.5}$$

The static pressure at a given radius r_1 in a potential flow is given by the integral of the pressure gradient from r_1 to infinity:

$$p_{r_1} = -\int_{r_1}^{\infty} \frac{\rho u^2}{r} dy + p_\infty \tag{1.6}$$

An experimental surface pressure distribution ($r_1=r_s$) for a two-dimensional jet developing round a circular cylinder is shown in figure 1.9, taken from ref 16. Note that pressure has been non-dimensionalised in a manner different from the normal definition of pressure coefficient. The suction under the jet is highest just after the jet

exit and reduces to zero 240° downstream of the jet exit, coincident with the separation of the jet. The surface pressure becomes less negative as the jet progresses for two reasons. Firstly, shear stresses at the wall reduce the total pressure of the flow and secondly (and more importantly), the streamlines of the jet diverge away from being true circular paths (r increases with s) due to the entrainment of the surrounding fluid. This means the relationship given in equation 1.5 no longer holds.

1.2.4.3 Entrainment

The process by which the turbulence in a curved wall jet, and hence entrainment rate, is modified by curvature effects is relatively complex. Extension of thin shear layer theory to account for an extra rate of strain ($\partial v/\partial x$) in the plane of the mean shear suggests that the turbulence is modified by an amount of the order of $y_{m/2}/r$. Experimental results suggest, however, that the effect is an order of magnitude larger than this[28] and that even small amounts of curvature can radically change the entrainment properties of a jet. Figure 1.10 (ref 29) illustrates the growth rate of a wall jet for different wall curvatures. Notice that for a value of $y_{m/2}/r$ of 0.25 the spreading rate for a convex wall jet is approximately four times greater than the spreading rate of the equivalent plane jet.

The stability of an ideal fluid in circulatory motion was first investigated by Lord Rayleigh. This work was extended by Taylor in 1923 to viscous fluid in laminar motion between two rotating cylinders[30]. Stability analysis is based on angular momentum considerations and the motion of a disturbed element of fluid.

Suppose that an element of fluid in a rotating flow is displaced by an externally-applied force in a radial direction, then released. If the fluid is frictionless then the displaced element conserves its angular momentum about the centre of curvature of the flow. Therefore if the angular momentum of the flow, ur per unit mass, decreases outwards, the displaced element will have a larger circumferential velocity than its surroundings. In consequence, the radial pressure gradient given by equation 1.5 that maintains the mean flow in its circular path is too small to keep the

displaced element in equilibrium and it will continue to move outwards. Conversely, if the angular momentum of the flow increases outwards, the pressure gradient will force the element inwards, returning it towards its original radius, about which it will oscillate.

Generally, for a boundary layer ($\partial u/\partial y$ positive) on a convex surface ($\partial v/\partial y$ negative) the angular momentum of the flow increases with radius. This means that displaced fluid elements tend to return to their original location and turbulence is suppressed. On the other hand, for the outer part of a wall jet ($\partial u/y\partial$ negative) flowing round a convex surface the angular momentum of the flow decreases with radius. Thus disturbances in the fluid are amplified and turbulence increased.

Note that the above argument is based on the radial pressure gradient due to inertial considerations of the streamline curvature, and that the pressure gradient contribution from fluid shear stresses is ignored. For the wall jet case, the shear stresses can be very high and the way in which they change through the part of the jet closest to the wall is highly non-linear. In this case, the fluid processes governing turbulence are considerably more complicated than those given above. The angular momentum/disturbed element explanation, however, does provide a useful, if simplified, starting point from which the complex nature of turbulence generation in curved jet flows may be understood.

1.2.4.4 Separation

A curved wall jet consisting of a real fluid will separate from the surface a given angular distance downstream of the jet exit. The range of jet velocities, for fixed slot geometry, over which a jet will attach to a curved surface is bounded by an upper jet Mach number limit and a lower jet Reynolds number limit.

At high jet Reynolds numbers and subsonic Jet Mach numbers, separation is caused by the adverse surface pressure gradient generated by the jet (Section 1.2.4.2).

Experiments with wall jets on circular cylinders suggest that the separation point is fixed at approximately 240° downstream from the slot exit. This result is also predicted by a theoretical analysis of curved wall jets by Roberts[31].

Below a certain critical jet Reynolds number of about 4 x 10^4 (ref 16) the shear stresses at the wall start to become large compared to the inertial forces in the outer part of the jet and separation tends to occur before 240°, figure 1.11. At very low jet Reynolds numbers the jet may separate from the surface only a few slot heights downstream and behave more like a free jet.

The jet Mach number above which the flow will no longer attach to a curved surface is an important design parameter since it effectively limits the maximum power (in terms of momentum flux) available from a given slot installation. Experimental studies[32] have shown that for practical slot installations, reasonable jet attachment is achieved up to pressure ratios of the order of 8, implying choked conditions at the jet exit. At higher pressure ratios it would appear that the expansion cells downstream of the nozzle exit prevent the surface suction necessary for jet attachment. Numerical studies of slot blowing on an F/A-18 Forebody[33] suggest that once the nozzle exit becomes choked, i.e. the jet is under expanded, a positive surface pressure is induced downstream of the slot. At a high enough blowing level, the positive pressure downstream of the slot forces the jet to separate from the surface. This phenomena has be described as overblowing.

1.2.4.5 Three-Dimensional Effects

The above discussion of curved wall jets has been confined to the ideal two-dimensional case. For practical application of wall jets for separation control applications, the slot from which the jet emanates will be of finite length and thus the jet may no longer be considered two-dimensional[34].

Launder and Rodi in their review paper on wall jet flows[35] cite spanwise variation in

the jet properties (i.e. three-dimensional effects) as a major cause of inaccuracy in two-dimensional wall jet studies. However, to achieve two dimensional conditions in laboratory experiments is not easy. A number of studies used endplates to simulate an infinite length slot. Even here, the boundary layer growth on the end plates was severe and led to a loss of two-dimensionality. Alternatively, slot end effects may be eliminated from experiments by using an annular wall jet, e.g. Rodman[36,37]. However in this case, an extra rate of fluid strain is introduced which cannot be ignored for high wall curvature on a finite radius annulus.

The McDonnell Douglas Notar concept, which uses slot blowing on the tail for torque reaction/yaw control, originally had endplates on the blowing slot. Although there is no published data on this design, it is apparent that the end plates were needed to increase the slot efficiency, i.e. the yawing moment produced for a given amount of jet momentum. In the latest Notar design, the MD Explorer[38], the end plates have been removed but there are now two slots at an angular spacing of approximately 40°. This is presumably to increase the amount of jet attachment on the tail boom.

Three-dimensional jet attachment effects also have an impact on the performance of slot blowing schemes for aircraft forebody flow control. Despite this, these effects are rarely mentioned in the literature.

1.3 SLENDER BODY AERODYNAMICS

1.3.1 Overview

Most combat aircraft have a relatively long, slender forebody to minimise drag at supersonic speeds. During cruise, the forebody is typically at zero angle of attack and the flow is fully attached. At high angles of attack, e.g. during a turning manoeuvre, the flow separates from either side of the forebody, leading to some form of lee-side vortex wake. The nature of this wake is dependent on the angle of attack, forebody shape and Reynolds number, and plays a key role in determining the aerodynamics

of the whole airframe.

Much of the early research in to slender body aerodynamics at high angles of attack was motivated by the requirements for highly agile missiles, e.g. Clark[39,40], Nielsen[41], Lamont[42,43], Wardlaw[44,45] and Ericsson[46]. These, and other researchers, found that above a certain incidence the flow separation on either side of the forebody can give rise to a pair of stable asymmetric vortices. The resulting asymmetric forebody pressure distribution produces a net out-of-plane side force. The orientation of the vortex asymmetry, and hence the sign of the side force, appeared to be sensitive to very small changes in experimental conditions and results from two nominally identical tests were often very different.

As the angle of attack of a slender body is increased from 0 to 90° three distinct types of vortex wake structure may be identified:

1) Low strength forebody vortices; symmetrically arranged

2) High strength forebody vortices; may form stable asymmetric arrangements

3) Periodic vortex shedding; coherent forebody vortices not formed

These are illustrated schematically in figure 1.12. The angle of attack at which stable vortex asymmetry occurs (α_{asym}) is approximately equal to the included angle of nose tip. The periodic vortex shedding angle of attack (α_{pvs}) depends to some extent on forebody cross-section and the slenderness of the body. For bodies of rounded cross-section and appreciable slenderness (length/diameter > 5) α_{pvs} is typically 60°.

1.3.2 Factors Affecting Vortex Asymmetry

The occurrence of large, unpredictable side forces on missile type bodies at high angles of attack is highly undesirable from a control systems point of view. This has

led to numerous attempts at "side force alleviation" on slender bodies. These studies include the effect of strakes[47], nose bluntness[48], nose cross-sectional shape[49,50] and forebody porosity[51]. In general, the angle of attack at which vortex asymmetry occurs is increased by blunting the nose and opting for a flattened forebody cross-section. Both these effects tend to laterally separate the forebody vortices at the nose tip which prevents amplification of the effects of physical asymmetries in this region. Careful positioning of strakes or chines can also eliminate vortex asymmetry over a given alpha range. However, at certain angles of attack/sideslip, vortex asymmetry may actually be amplified by the presence of strakes[52].

A number of studies have investigated the effect of nose roll angle on flow about symmetrical slender bodies[53,54]. Typically, the sign of the out-of-plane side force at a given angle of attack will reverse a number of times as the nose is rotated (at negligible speed) through 360°. This is due to asymmetries of the order of machining tolerances in the profile of the nominally symmetric nose cone shape. Nose cone roll orientation is not a reliable way of modifying flow asymmetry (apart from in the controlled conditions of a wind tunnel test) because normal service and handling of a missile or aircraft inevitably leads to alterations in the nose micro-asymmetries.

The most important message from the many studies of slender body flow at incidence is that vortex asymmetry is a fundamental feature of that type of flowfield. This means the problem is not going to be cured by small modifications to the body geometry. Rather, a new design approach must be used that is sympathetic to the nature of high angle of attack flowfields.

1.3.3 Numerical Studies of Slender Body Flow at Incidence

1.3.3.1 Overview

This section provides a brief introduction to numerical techniques for solving the flow around slender bodies. These techniques can be divided into analytical methods, which

can generally be solved with modest computing resources, and methods which attempt to a solve a simplified subset of the Navier-Stokes equations, which generally require mainframe computing facilities. The analytical methods have the advantage that solutions may be obtained relatively quickly and cheaply. However, the solutions are generally inviscid and the flow modelling relatively crude. On the other hand, Navier-Stokes methods offer the possibility of modelling viscous, turbulent flow around complex three-dimensional geometries, including shocks, three-dimensional separations and vortices, and the interactions between these flow structures. Computing costs, however, can be as high as performing the equivalent full-scale wind tunnel test.

1.3.3.2 Analytical Methods

At high Reynolds numbers, the effects of turbulence and fluid viscosity on a uniform stream past a body are confined to thin boundary layers on the surface of the body and to the wake, which arises when these layers separate from the body. Outside the boundary layers and wake the flow behaves as if the fluid were inviscid. In this case the effects of viscosity and turbulence can be modelled by the theory of thin shear layers[55]. As the Reynolds number of the flow tends to infinity, the thickness effect of the shear layers diminishes and the layers may be approximated by vortex sheets. This means that an inviscid model of the flow can be used. However this type of model can not accurately predict where the shear layers leave the body, i.e. the separation lines, and in general, information on separation line location must be supplied from outside the model. This information can come from experimental data or from a viscous boundary layer model used in conjunction with the inviscid model.

When modelling vortical flows it is useful to distinguish between the model of the vortex sheet and the framework of potential flow in which it is embedded[55]. Possible frameworks for the potential flow include the

1) the full nonlinear potential formulation
2) the nonlinear transonic small perturbation approximation

3) the linear small perturbation (Prandtl-Glauert) approximations for subsonic and supersonic flows, and
4) the slender-body approximation.

The simplest of these frameworks is the slender-body approximation and this has been used extensively for modelling three-dimensional separated flow on slender wings and missile-type bodies. A body is described as slender if its cross-sectional extent is small compared to its length. The slender-body approximation assumes that for such bodies at reasonably low angles of attack, the changes in velocity potential in the axial direction are small compared to changes in the crossflow direction. This means that the problem may be considered as two-dimensional in the crossflow plane. The main weakness of the slender-body approximation is that it does not allow for upstream and downstream influences between one crossflow plane and another, except via vorticity convected by the vortex sheets.

There are essentially three different models of the vortical flow arising from three-dimensional separation. These are the single line-vortex model, the multiple line-vortex model and the vortex sheet model, figure 1.13. The simplest model is the line-vortex model, first developed by Brown and Michael[56] in 1954 for flow over slender wings. In this model, the spiral vortex sheets on the upper surface of the wing are replaced with two concentrated line vortices. These vortices are connected to their respective wing leading edges by a cut, which is essentially a feeding sheet of vanishing strength.

The boundary conditions for this model are

1) zero normal velocity at solid surfaces
2) separation at the sharp leading edges
3) disturbances vanish at infinity, and
4) zero force acting on each line-vortex/feeding sheet pair.

Note that this last boundary condition does not require the pressure to be continuous

across the feeding sheet (which is always the case in the real flow). This is because forces acting the sheet due to a finite pressure difference across it can be balanced by pressure forces acting on the line-vortex.

Application of the line-vortex model to flows round cones at incidence is slightly more involved since the separation behaviour of the crossflow is not explicitly defined by a sharp edge. In this case it is usual to introduce a modified form of the Kutta condition at the separation lines. One of the earliest mathematical models of the separated flow around a cone at incidence was published by Bryson[57]. He introduces the condition that the separation points that feed the vortex sheet are stagnation points, i.e. that the fluid velocity relative to the cylinder is zero.

In Bryson's model the flow in the crossflow plane is made up of potentials due to the free-stream flow, a doublet at the origin to simulate the cylinder, the two vortices in the wake and the reflection of these two vortices inside the cylinder. The unknowns in this case are the strength and location of the vortices in the wake. These can be determined from the condition of no net force acting on the line-vortex/feeding sheet and the flow conditions implied by the modified form of the Kutta condition at the separation point.

The main advantage of the single line-vortex model is simplicity. When used in the slender-body framework, it is simple enough for exact analysis, i.e. the governing equations reduce to a (high order) polynomial equation. Thus all possible solutions of vortex location and strength for different separation positions may be determined. The simplicity of the single line-vortex model also makes a useful tool for quickly establishing basic properties of a given flowfield. This understanding can then be used to help set up more complicated models and to give guidance to the type of solution expected. For example, if lateral asymmetry is allowed for in Bryson's model of the separated flow about a cone, asymmetric vortex locations are predicted. These asymmetric vortex positions can then be used as a 'seed' to speed up the search for asymmetric solutions in more sophisticated models[58,59].

The single line-vortex model may be made to model the flow more accurately if part of the feeding sheet is modelled explicitly[60]. The feeding sheet may then be allowed to roll up for a number of turns forming the outer spiral of the vortex. Modelling of an infinite number of turns making up the whole of the vortex is impractical so after a given number of turns, the free edge of the feeding sheet is connected to a line-vortex at the vortex core by a cut. As in the single line-vortex model, this cut experiences a force which must be balanced out by an equal and opposite force on the line-vortex. This type of model is known as a vortex sheet model and was first used by Mangler and Smith[61] for solving the flow around delta wings with leading edge separation.

The boundary conditions for the vortex sheet model differ from those applied to the single line-vortex model in that the feeding sheet is now specified as a three-dimensional stream surface within the flow, and that the pressure is continuous across the feeding sheet. This latter condition means that there is no pressure difference across the sheet, and hence no net force acting on it.

The vortex sheet model has been applied to symmetrical separated flow around cones at incidence by Fiddes[58]. In this work, a vortex sheet model is used for the outer, inviscid separated flow, and a separate, viscous-inviscid 'triple-deck' model used for the interaction between the external flow predicted by the vortex sheet model and a laminar boundary layer on the cone.

The main advantage of the vortex sheet model is the realism with which it can describe separation from smooth surfaces, i.e. the sides of a cone. This is important since the local inviscid behaviour of the vortex sheet at separation can have a significant effect on the overall shape of the rolled-up shear layer[62]. Accurate inviscid modelling of smooth separation is also necessary if separation location is to be predicted. Note that although primary separation can be modelled using the vortex sheet method it is not generally practical to model secondary separation. Absence of secondary separation modelling tends to cause the primary vortex cores to be located slightly too close to their separation lines[58].

Another approach to modelling the rolled-up vortex sheet is offered by the multiple line-vortex model[63]. In this, the vortex sheet is approximated by series of line-vortices that spring from the separation line. Each of these vortices is constrained by the condition that it should be aligned with the local flow direction along the whole of its length. This results in a series of helically shaped line-vortices.

There are three main difficulties associated with the multiple line-vortex approach:

1) A large number of vortices are needed for accurate results.

2) Modelling of line-vortices which follow helical paths of small pitch, e.g. those springing the nose apex, requires a large number of elements for realistic modelling.

3) The paths of the line-vortices tend to become chaotic as the flow develops in a streamwise direction. This is due to the increased number and proximity of the vortices in the rolled up part of the sheet coupled with instabilities in the solution algorithm.

A major advantage of the multiple line-vortex method is its flexibility, which makes it possible to use one program to calculate very different vortex structures with minimal changes. A further advantage is that the model has the potential to predict vortex breakdown. This is manifest by a gross disorganisation of the line-vortices near the axis of the vortex. However, it is important to distinguish between numerical instabilities as described by point 3 above and the real instabilities in vorticity convection which cause vortex burst.

1.3.3.3 Navier-Stokes Solutions

The fundamental dynamical behaviour of a fluid particle is governed by the law of conservation of mass and by Newton's Second Law. These laws lead to the continuity

equation and the Navier-Stokes equations. For incompressible flow in cartesian coordinates these equations are, respectively:

$$\frac{\partial u}{\partial x} + \frac{\partial v}{\partial y} + \frac{\partial w}{\partial z} = 0 \qquad (1.7)$$

and

$$\rho\left[\frac{\partial u}{\partial t} + u\frac{\partial u}{\partial x} + v\frac{\partial u}{\partial y} + w\frac{\partial u}{\partial z}\right] = -\frac{\partial p}{\partial x} + \mu\left[\frac{\partial^2 u}{\partial x^2} + \frac{\partial^2 u}{\partial y^2} + \frac{\partial^2 u}{\partial z^2}\right] + F_x \qquad (1.8)$$

(similar equations for v and w)

In the Navier-Stokes equations the term F_x represents the body forces acting on a fluid particle, for example due to gravitational or magnetic fields. Most fluid flows of interest occur within the Earth's gravitational field. However the effect of this field is only of significance when there are large changes in density through the fluid, leading to the generation of buoyancy forces.

The continuity and Navier-Stokes equations constitute a pair of simultaneous partial differential equations for one scalar quantity (pressure) and one vector quantity (velocity). However these equations can not be solved easily because the Navier-Stokes equations are non-linear. This non-linearity arises because the velocity has a dual role in determining the acceleration of the flow; it changes as the fluid moves and determines how fast the change occurs. Historically, the mathematical difficulty of solving the Navier-Stokes equations has meant that much knowledge of the detailed behaviour of fluids in motion has come from experiments rather than theoretical prediction[64].

Although the Navier-Stokes equations have no known general solution, they may be solved using finite difference techniques. This has becomes an increasingly realistic option with the advent of high speed digital computers. However, some approximations have to be made to achieve solutions within sensible run times, i.e. hours rather than days, and within the limitations of computer memory, which, although very large, is finite.

An important simplification to the representation of turbulent flow may be made by using the time-averaged form of the Navier-Stokes equations. This requires the addition of Reynolds stress terms to the flow model. These terms describe the forces acting on a fluid element due to its time-dependent (turbulent) motion.

To represent Reynolds stresses in terms of the averaged motion and its history it is necessary to introduce turbulence models. These models describe the way in which turbulence of a fluid flow modifies the apparent viscosity of the fluid, giving rise to the concept of eddy viscosity (ε) for time-averaged turbulent flows. Thus the viscosity of a turbulent fluid becomes $\mu+\varepsilon$, i.e. the apparent viscosity of a fluid in turbulent motion is higher than that of the equivalent fluid in laminar motion. The most commonly used turbulence model used for high angle of attack flows is the Baldwin-Lomax model[65]. In this model, a fluid quantity containing the magnitude of the local vorticity is examined to determine the local length scale, and hence eddy viscosity. This model was improved by Degani and Schiff[66] to account for the difference between vorticity contained within the attached crossflow boundary layer and the vorticity in the free shear layer after separation.

Solution of the Navier-Stokes equations by finite difference methods is further simplified by the thin layer approximation[67]. In this method, it is assumed that the effects of fluid viscosity are only transmitted in a direction perpendicular to the body surface, i.e. across, not along, thin layers surrounding the body. This considerably reduces the computational effort required to solve the flow, in exchange for a small decrease in accuracy of modelling. Use of the thin-layer approximation does, however, require a body-fitted grid in the mathematical solution space.

One of the earliest demonstrations of asymmetric Navier-Stokes solutions to flow around slender bodies at incidence is provided by Siclari and Marconi[68]. This work is significant in that asymmetric vortical flows were predicted for exactly symmetric bodies. A similar study by Degani and Levy[69] also predicts large scale asymmetric flows around slender bodies at incidence, however, in this case, a small physical asymmetry at the nose tip was required to generate the flow asymmetry. When the

disturbance at the nose tip was removed, the solution returned to being symmetric.

An advantage of Navier-Stokes methods compared to simpler analytical techniques is that the former solves the whole flowfield. This means the data so produced can be used to provide detailed (though not necessarily accurate) pictures of the behaviour of a fluid as it passes round a body. A good example of this is the numerical investigation of the flow about a slender body at incidence by Vanden and Belk[70]. The imaginative use of computer graphics in this study provides a stimulating representation of complex vortical flows not possible with current flow visualisation techniques. If nothing else, these images provide inspiration for experimentalists.

At present, Navier-Stokes solutions of high angle of attack flows are still very much at the validation stage. This means that most work is being aimed at making the numerical solutions fit the experimental data. However, progress is being made rapidly and it is likely that Navier-Stokes solvers will become widespread design tools within the next ten years.

1.4 The Research Programme

1.4.1 Motivation

Current combat aircraft have limited high angle of attack manoeuvrability due to lateral control deficiency, particularly in yaw. In response to this, researchers have proposed a number of new techniques for improving the yaw control power at high angles of attack, including various types of mechanical and pneumatic forebody flow control devices and the use of vectored thrust. In recent years there have been numerous studies of various forebody flow control techniques and some technologies have reached the flight test stage. These schemes are discussed in detail in Chapter 2.

Preliminary research by Wood[71] in 1988 showed that the concept of Tangential Forebody Blowing offered many advantages over other schemes for providing yaw control at high angles of attack. The present study is motivated by the need to expand

on this work and explore the concept in greater depth.

1.4.2 Objectives

The two primary objectives of the research programme are to

1) demonstrate the viability of Tangential Forebody Blowing as a means of yaw control at high angles of attack, and

2) provide a sound understanding of the underlying fluid mechanisms.

Secondary objectives include

a) investigation of the interactions between the forebody flow and the flow over the LEX and wing,

b) determination of the sources of control forces and moments,

c) investigation of the effects of slot geometry and location, and

d) evaluation of mass flow and momentum-based aerodynamic scaling parameters.

1.5 GUIDE TO THE REST OF THE THESIS

In Chapter 2, other studies of forebody flow control techniques are described and compared. This highlights advantages of various different approaches to high angle of attack yaw control. Moreover, the particular benefits of yaw control by Tangential Forebody Blowing are emphasised.

Chapter 3 describes the experimental techniques used in the research programme. This includes a description of experimental facilities, wall jet rig and generic combat aircraft wind tunnel model. Data acquisition and reduction is discussed and an assessment is made of experimental accuracy.

Results from wall jet fluid dynamic experiments and generic combat aircraft wind tunnel tests are presented and discussed in Chapter 4. This chapter explores the concept of tangential forebody blowing and the underlying fluid mechanisms. The performance of Tangential Forebody Blowing over a range of conditions is established.

Chapter 5 summaries the important results from Chapter 4 and states a number of conclusions.

Finally, Chapter 6 offers some suggestions for further work.

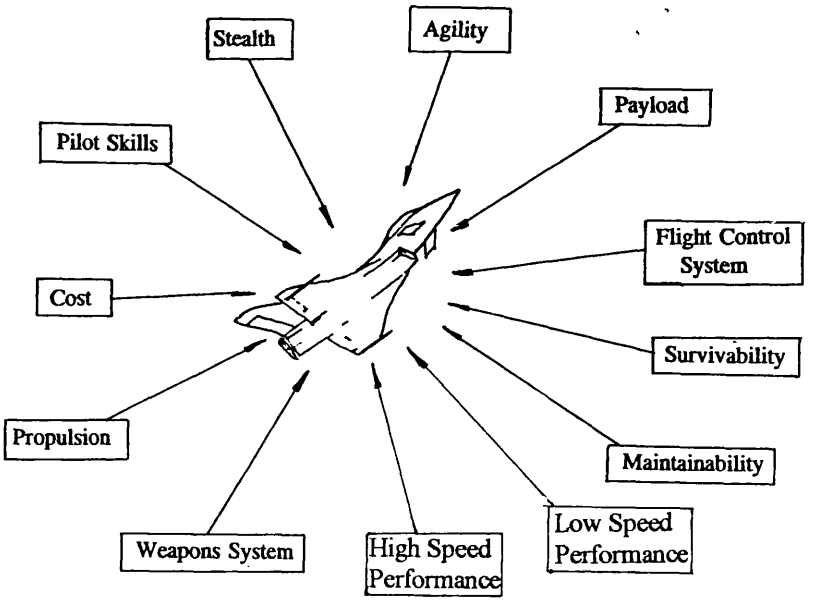

Figure 1.1 *Factors Affecting Combat Aircraft Design*

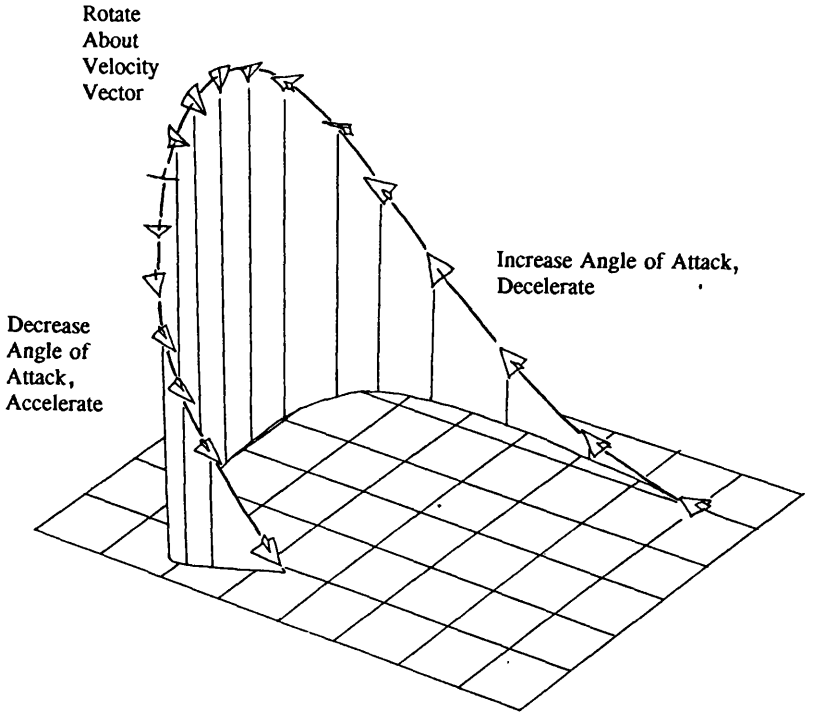

Figure 1.2 *The "J" Turn, or Herbst Manoeuvre*

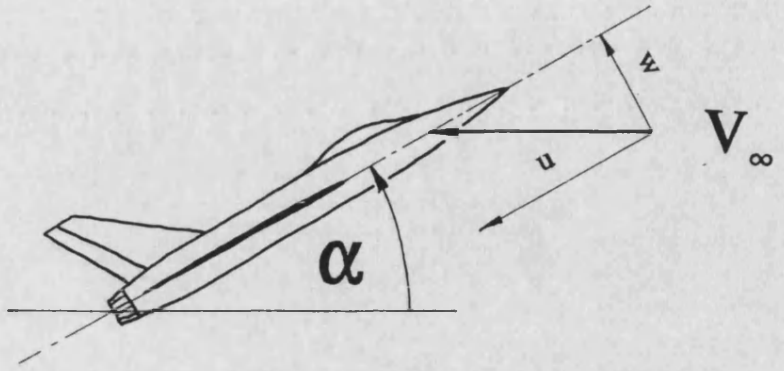

$$\text{Angle of Attack} = \alpha = \tan^{-1}\frac{w}{u}$$

Figure 1.3 *Definition of Angle of Attack*

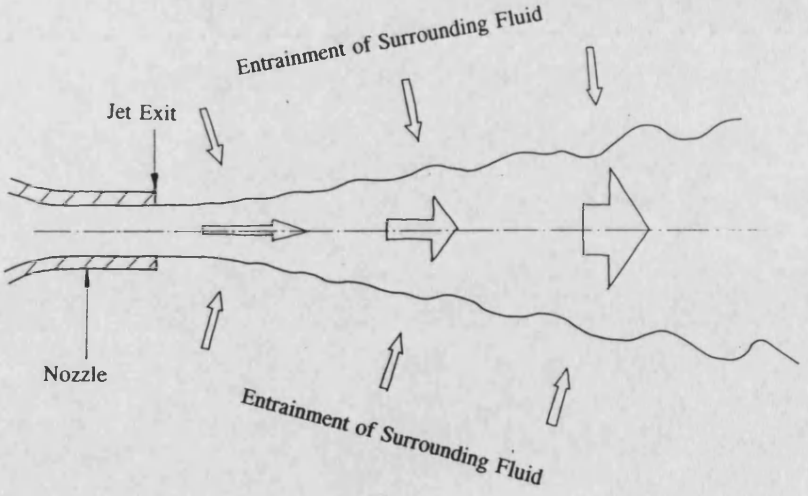

Figure 1.4 *Two-Dimensional Free jet Issuing into Quiescent Surroundings*

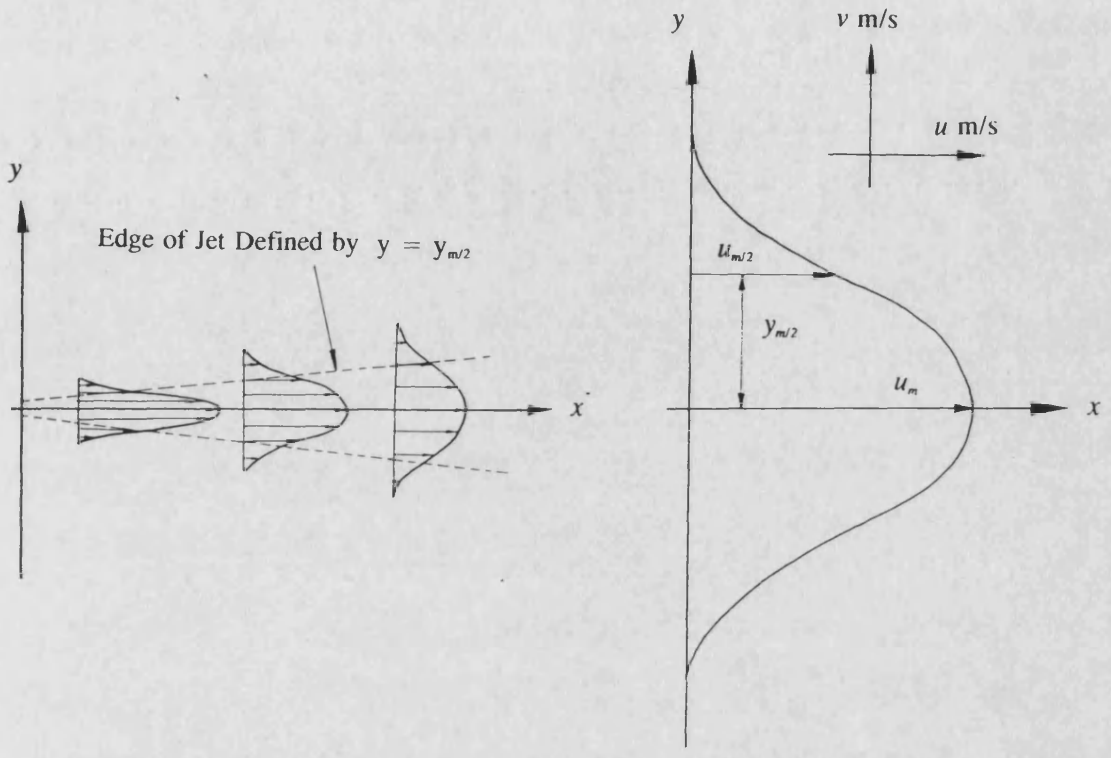

Figure 1.5 *Velocity Profiles for a Two-Dimensional Free Air Jet*

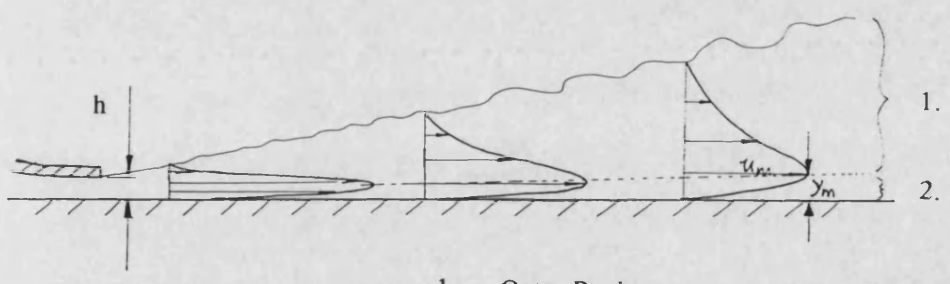

At $x = 0$, $u_m = V_j$

1.	Outer Region Dominated by Inertial Forces	$\frac{\delta u}{\delta y}$	Negative
2.	Inner Region Dominated by Viscous Forces	$\frac{\delta u}{\delta y}$	Positive

Figure 1.6 *Velocity Profiles in a Plane Wall Jet*

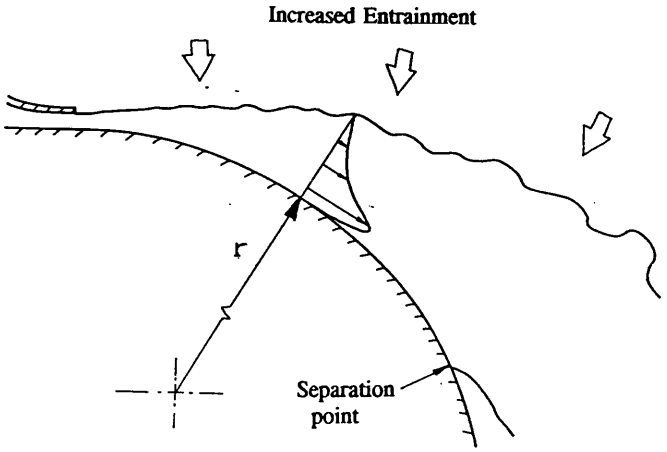

Figure 1.7 *The Curved Wall Jet*

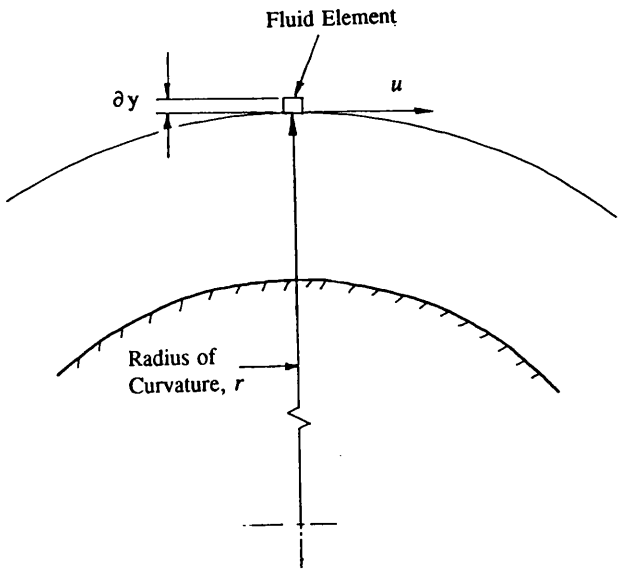

Pressure Force ≡ Inertial Force

$$\frac{\delta p}{\delta y} = - \frac{\rho u^2}{r}$$

(using local cartesian coordinates)

Figure 1.8 *Radial Pressure/Momentum Balance for Curved Flow*

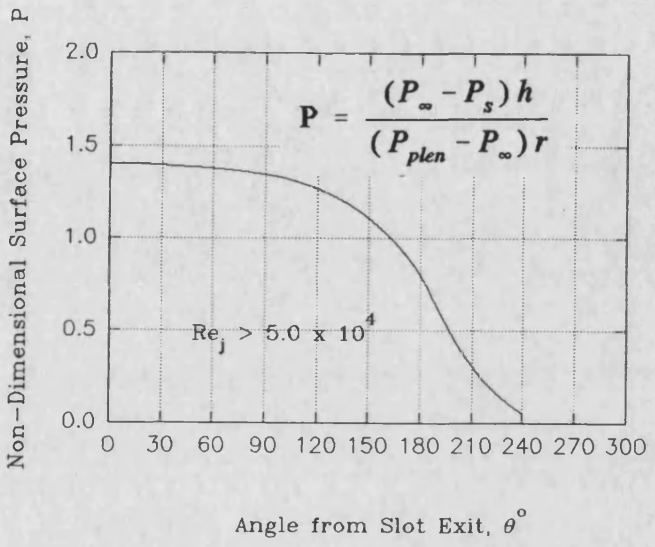

Figure 1.9 *Surface Pressure Distribution for a Wall Jet on a Circular Cylinder*

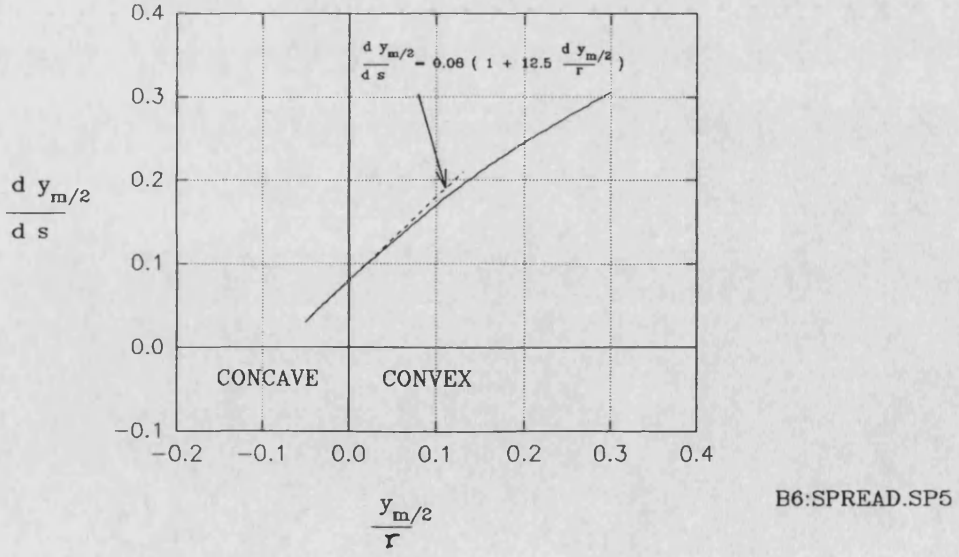

Figure 1.10 *Effect of Surface Curvature on Wall Jet Spreading Rate*

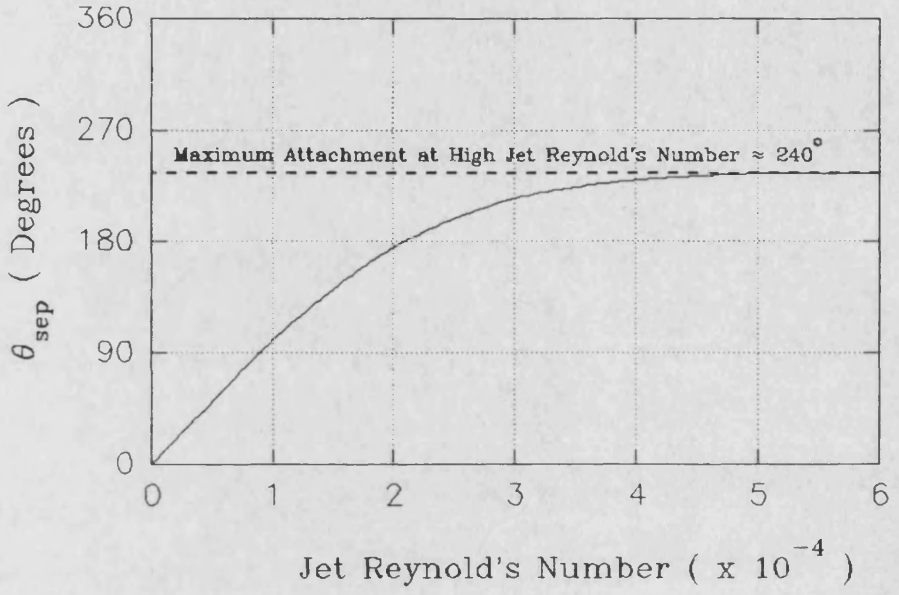

Figure 1.11 *Effect of Jet Reynolds Number on Wall Jet Attachment on a Circular Cylinder*

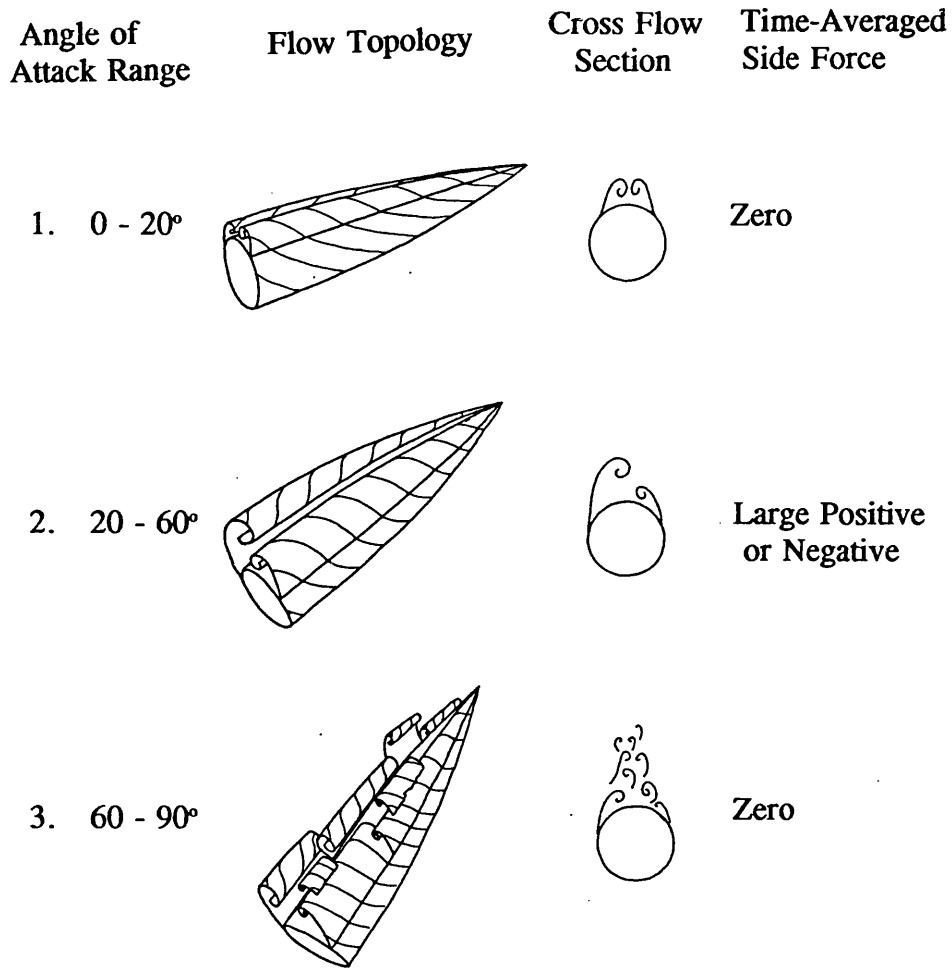

Figure 1.12 *Flow Regimes for a Slender Body at Incidence*

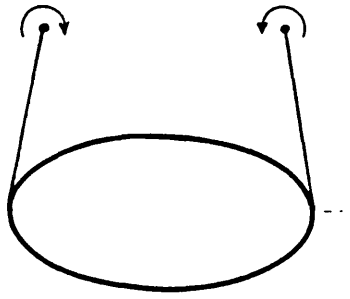

a) Single Line-Vortex Model

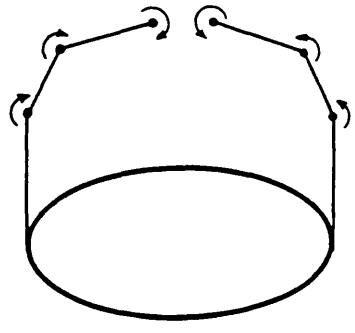

b) Multiple Line-Vortex Model

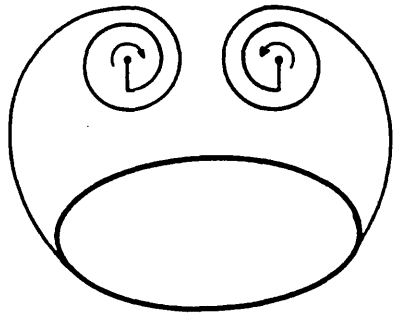

c) Vortex Sheet Model

Figure 1.13 *Analytical Methods for Modelling Vortical Flow*

CHAPTER 2

TECHNIQUES FOR YAW CONTROL AT HIGH ALPHA

2.1 OVERVIEW

At small angles of attack, the simplest way of providing aircraft yaw control is by the use of rear-mounted vertical surfaces. However, at high angles of attack, dorsal surfaces, i.e. conventional fins, become ineffective due to immersion in the wake from the forward fuselage and wing (Chapter 1). On the other hand, ventral surfaces remain effective, but they are generally of limited size due to ground clearance constraints (particularly during rotation). A solution to this problem is provided by a ventral fin that deploys once the aircraft is airborne (as on the MiG-23). This, however, adds undesirable weight and complexity to the airframe.

At very high angles of attack, i.e. $\alpha=90^{o}$, conventional dorsal or ventral surfaces are unable to produce yawing moments wherever they located since the local chord-wise velocity component reduces to zero. Special surfaces could be deployed that provided yaw control at this flight condition, but once again, weight and complexity considerations make this idea unattractive.

The two main alternatives to actuated surfaces for high angle of attack yaw control are thrust vectoring and forebody flow control. These are discussed in the following two sections.

2.2 THRUST VECTORING

Thrust vectoring provides control moments by varying the engine thrust line relative to the aircraft centre of gravity. This is achieved by deflecting the jet efflux with moveable paddles downstream of the nozzle exit or by providing a fully moving nozzle. In recent years thrust vectoring technology has been steadily improving and

the concept has been successfully flight tested on a number of aircraft, including the YF-22, F-15E[72], F/A-18, and F-16[73].

Three-dimensional thrust vectoring for a single engined aircraft provides control moments in pitch and yaw. With a twin-engined configuration, rolling moments can also be generated, though these are generally small compared to the pitch and yawing moments available. A major advantage of control moments generated by thrust vectoring is that they are essentially decoupled from the airframe aerodynamics (apart from intake distortion problems), i.e. independent of sideslip and angle of attack. This means that control moments due to thrust vectoring can be easily integrated into the flight control system.

From an installation point of view, the addition of thrust vectoring to an aircraft increases both the weight and complexity of the propulsion system. Also, in terms of aircraft performance, thrust vectoring is relatively inefficient. For example, a typical vectoring angle of 20° equates to a 5% loss in net thrust. This might be significant in a combat situation.

Application of thrust vectoring to highly stealthy aircraft is made difficult by the requirements of exhaust shielding for reduced infra-red signature. In the case of the F-117, the two-dimensional nature of the exhaust nozzles would make pitch vectoring much easier to implement than yaw vectoring. The relatively large lateral spacing of the nozzles would, however, make the aircraft an ideal candidate for roll vectoring.

2.3 FOREBODY FLOW CONTROL

2.3.1 Mechanical Approach

a) Conformal Actuated Strakes

After early experiments trying to force forebody vortex asymmetry with fixed strakes, it was natural for researchers to try moving the strakes to produce controlled vortex

asymmetry, and hence control yawing moments[74,75,76]. Experiments proved relatively successful, although it appears that this type of control is highly prone to reversal, i.e. the sign of the control response may change depending on Reynolds number, angle of attack and angle of sideslip. This is unsatisfactory from the point of view of control system implementation.

The cumulation of the many wind tunnel tests on actuated strakes will be the flight trial of the concept on NASA Dryden's F-18 HARV in October 1994[77]. For these tests, a new radome has been fitted to the aircraft which incorporates a pair of 1.2 m long by 0.15 m wide conformal strakes located approximately $\pm 120°$ from the windward generator[78]. The strakes are moved using a modified F-18 aileron actuator and hinge outwards from the lower edge, figure 2.1.

Moveable stakes can provide control yawing moments at angles of attack where there is coherent vortical flow in the lee of the forebody. The control power increases with increasing crossflow component ($V_\infty sin\alpha$) until α_{pvs} is reached whereupon the control power quickly reduces to zero. For a typical combat aircraft geometry, forebody strakes can provide useful control yawing moments over an angle of attack range from about 20 to 60° angle of attack. Below 20° the forebody vortices are too weak to generate significant side forces. Above 60° most forebody shapes exhibit unsteady vortex shedding leading to a zero time-averaged side force.

b) Rotatable Nose Tip Strakes

This type of control uses a pair of miniature strakes attached to the nose tip. The nose tip can rotate about the fuselage axis and thus the strakes can be orientated at a range of angles to the on-coming flow[79]. In principle, the control works in a similar manner to the actuated strake concept, i.e. a controlled physical asymmetry is introduced that modifies the forebody vortex equilibrium. This then gives rise to a control side force on the forebody. Since the nose tip strakes, by definition, are located on the furthest forward part of the forebody, they may be made small without losing effectiveness.

The useable angle of attack range for rotatable nose tip strakes is similar to that of conformal actuated strakes, i.e. $20° < \alpha < 60°$.

The use of strakes, and indeed any other methods that physically alter the crossflow shape of the forebody, to produce control forces is best described as vortex manipulation. The most important aspect of this type of device is that control power is proportional to the amount of organised vorticity contained with in the vortex, i.e. the vortex strength. This is not necessarily true for pneumatic forebody flow control schemes, in particular slot blowing (section 2.3.2. c)).

2.3.2 Pneumatic Approach

a) Nose Suction

Suction through a pair of small holes in the nose tip, figure 2.2, has been tested on HIRM (High Incidence Research Model) at DRA Farnborough as part of a high incidence departure prevention programme[80,81,82]. It is suggested that the local boundary layer is removed from around a hole to which suction is applied. This introduces a physical asymmetry at the nose tip which results in asymmetric forebody vortex formation. Varying the level of suction changes the magnitude of the physical asymmetry introduced and thus modulates the overall forebody vortex asymmetry. C_μ values required for this type of control are very small (of the order of 1×10^{-6}) making it a highly efficient control device (see Section 2.4.2).

b) Jet Blowing

Jet blowing is used as a general heading for types of forebody flow control that uses discrete, low aspect ratio air jets that may be normal[83,84] or tangential[85,86] to the surface. Normal jet blowing at the nose tip has a similar effect to nose tip suction, i.e. a controlled physical asymmetry is introduced. However the range of control available by normal jet blowing is relatively limited since once the jet has sufficient momentum to penetrate the local forebody boundary layer, further increases in jet momentum have little effect on the forebody flowfield.

By angling blowing ports tangential to the local surface, the resulting jet may be made to interact favourably with the forebody boundary layer, improving the control response and allowing it to function over a broader range of angle of attack and sideslip. Also by careful shaping of the nozzle, which will be typically operating at supersonic pressure ratios, the mixing of the jet may be enhanced, further increasing the efficiency of the control. This type of jet blowing scheme has recently been flight tested on the X-29[87]. In this case the nozzles were fed with high pressure nitrogen from bottles stowed in the aircraft forebody. At typical operating conditions the jet massflow required was of the order of 1 lb/sec, which equates to a C_μ of approximately 0.0005. This is one order of magnitude smaller than a typical C_μ required by a slot blowing scheme (see Chapter 4, Section 4.8).

c) Slot Blowing

Slot blowing is used to describe schemes incorporating relatively high aspect ratio slots that produce a jet tangential to the local surface curvature, e.g. Tangential Forebody Blowing. High slot aspect ratio is important if the beneficial effects of the Coanda effect are to be utilised (this will be clearly demonstrated by the results presented in Chapter 4).

Implementation of slot blowing for forebody flow control is shown in figure 2.3. Since the initiation of the present Tangential Forebody Blowing research programme in 1990, there has been increasing interest in slot blowing schemes, and a number of experimental studies have been reported[88,89,90]. There have also been a number of numerical studies of slot blowing schemes[91,92,93]. These studies complement the work presented in this thesis. However, at present, no other study has demonstrated yaw control up to 90° angle of attack.

2.4 COMPARISON OF FOREBODY FLOW CONTROL TECHNIQUES

2.4.1 Installation Considerations

The main problem concerning installation of a flow control device in an aircraft forebody is that of interference with the operation of the radar. Ideally, all materials in the radome should be non-metallic and there should be no moving parts. This essentially precludes the use of rotatable nose tip strakes and means that conformal actuated strakes must ideally start aft of the radome. Unfortunately, strakes are highly inefficient when located this far aft on the forebody and it is questionable how effective they would be.

The relatively simple physical requirements of the pneumatic flow control schemes make them amenable to installation within the radome. This means that slots or jets can be located right at the nose tip where maximum efficiency is achieved.

An important consideration with both mechanical and pneumatic nose tip devices is the resistance of the control to normal service life wear and tear. For example, any slight damage or build up of debris on a nose tip strake installation could radically alter the performance of the device. Similarly, any modification to the geometry of a nose tip suction installation or ingestion of ice or insect debris into the suction holes might render the control inoperable.

Devices that do not rely on modification of the nose tip flow, e.g. conformal strakes, slot blowing, will generally be more resilient to service wear and tear.

2.4.2 Power Requirements

For mechanical type forebody flow control, the power required to drive actuated strakes, etc., is modest and not a significant design issue. However, for pneumatic schemes, in which air is bled off from the propulsion system, careful evaluation of air massflow requirements is needed. To do this it is useful to define an augmentation

factor, k_a, given by

$$k_a = \frac{\text{Yawing Moment from Blowing Scheme}}{\text{Yawing Moment from Reaction Control Jet}} \tag{2.1}$$

Where the same jet momentum is used in the reaction control jet as in the blowing scheme.

For a reaction jet, the yawing moment produced is given by

$$N_{RJ} = x_N M_j \tag{2.2}$$

where x_N is the moment arm of the jet about the aircraft c.g. and M_j is the jet momentum. Converting to a yawing moment coefficient gives

$$C_{N_{RJ}} = \frac{x_N}{c} C_\mu \tag{2.3}$$

For a typical combat aircraft geometry and the reaction jet located at the nose tip, x_N is approximately equal to the wing chord, c, and thus the jet yawing moment is given simply by the jet momentum coefficient, C_μ. This means k_a is given by

$$k_a = \frac{\Delta C_N}{\Delta C_\mu} \tag{2.4}$$

The most efficient type of pneumatic control is nose suction. From the work at DRA Farnborough, typical values of k_a are of the order of 20×10^3. Normal jet blowing at the nose tip shows similar k_a values, however the maximum control moments attainable tend to be less than those achieved with suction through the same pair of holes. To achieve these remarkable levels of efficiency the forebody flow must be manipulated as far forward as possible. In the case of the DRA suction tests, the holes were in fact located at less than 1% of the forebody length back from the nose apex.

Moving the jet to a location further aft on the forebody makes installation easier and makes the control less sensitive to changes in nose tip geometry. However, the augmentation factor of the control drops by a number of orders of magnitude. For the

jet blowing on the X-29, k_a was typically 50.

Slot blowing is typically less efficient than jet blowing, with typical k_a values of around 20. The exact value is, of course, dependent on both slot geometry and location.

In Chapter 4, air massflow requirements for slot blowing is evaluated. It is seen that for a well designed installation the requirements are within engine bleed limits.

2.4.3 Angle of Attack Range

For forebody flow control devices that work on the basis of vortex manipulation, i.e. conformal strakes, rotatable nose tip strakes, nose tip suction/blowing, jet blowing, control yawing moments can only be generated when there are coherent forebody vortices. This effectively limits the applicability of this type of control to angles of attack less than α_{pvs} i.e. less than about 60°. Slot blowing, as will be described in detail in Chapter 4, produces side forces primarily by the interaction of a wall jet with the forebody crossflow component, and consequently the presence of forebody vortices is not a prerequisite. This means that slot blowing can produce control yawing moments up to 90° angle of attack and beyond.

Figure 2.4 illustrates different approaches to yaw control for 0 to 120° angle of attack range. Considering that the major advantages of post-stall manoeuvering are achieved at angles of attack approaching 90°, it is clear that slot blowing offers significant benefits over forebody flow control schemes that depend on vortex manipulation.

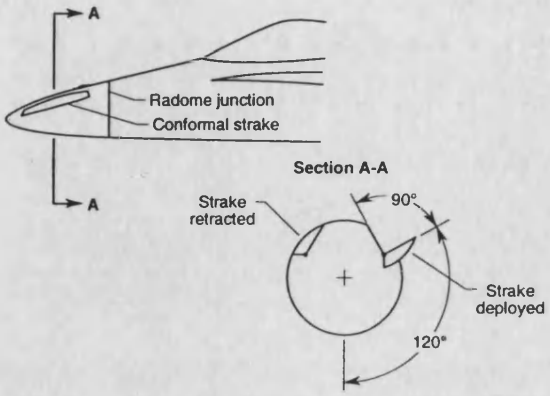

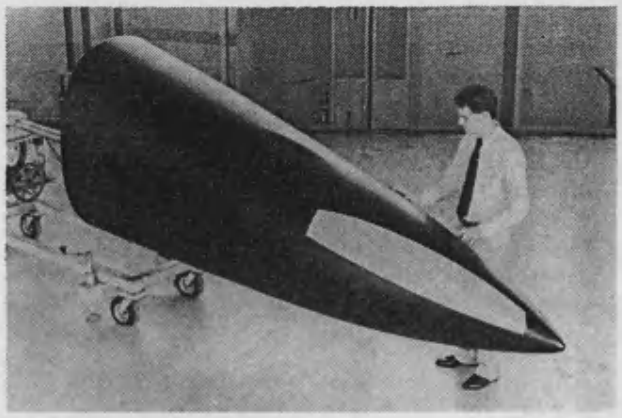

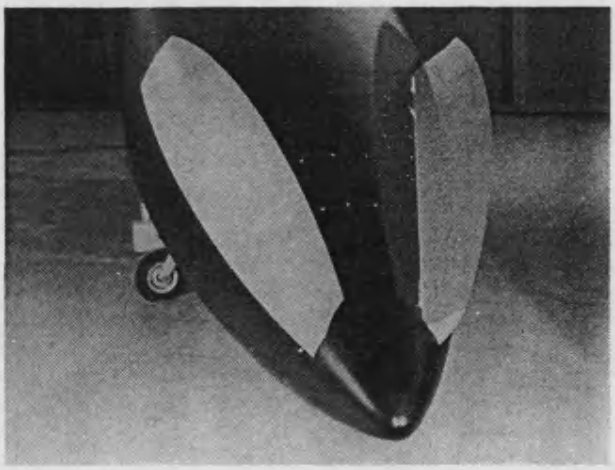

Figure 2.1 *Conformal Actuated Strakes on the F-18 HARV*

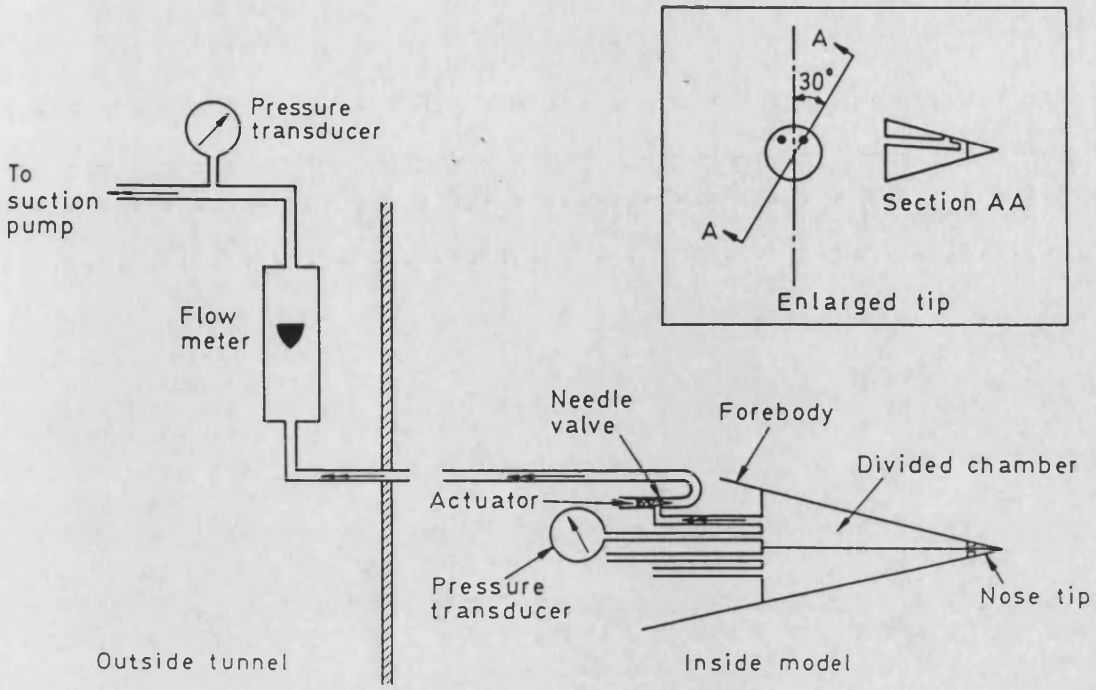

Figure 2.2 *Nose Tip Suction on the DRA HIRM*

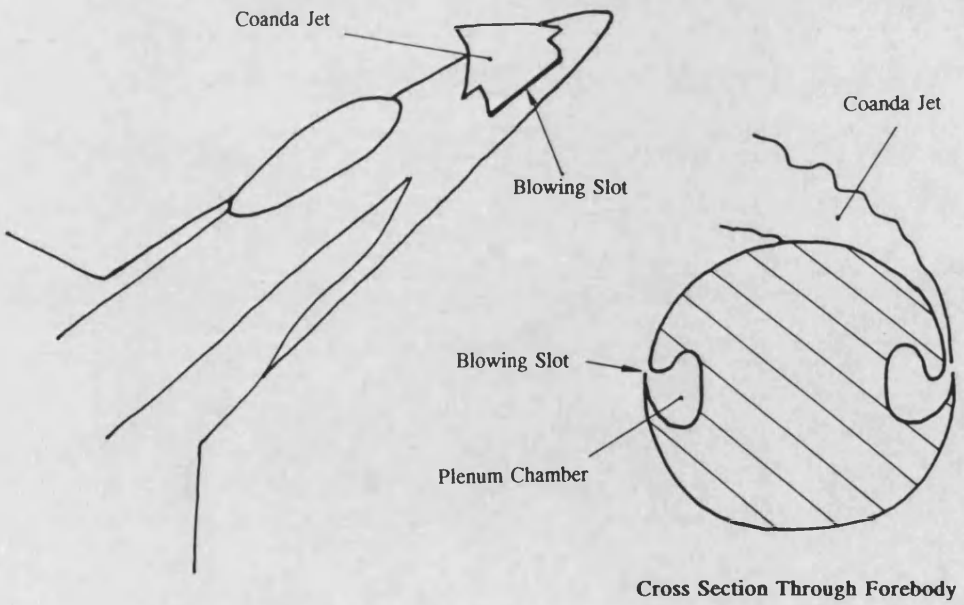

Figure 2.3 *Slot Blowing for Forebody Flow Control*

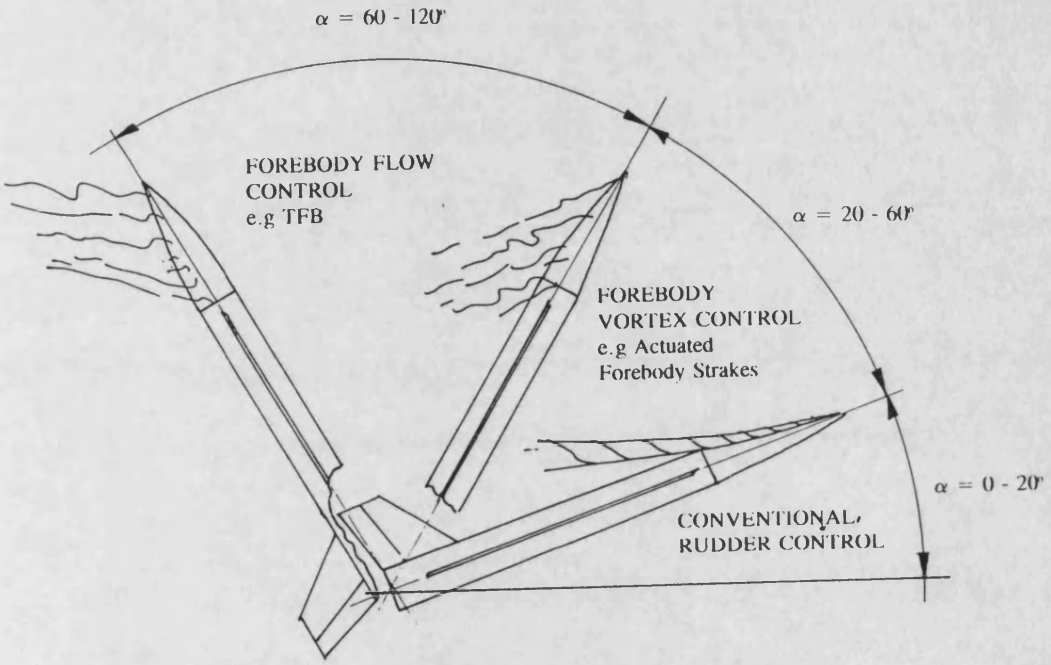

Figure 2.4 *Aerodynamic Control Strategies for Different Angle of Attack Regimes*

CHAPTER 3

EXPERIMENTAL FACILITIES AND TECHNIQUES

3.1 WIND TUNNEL

The University of Bath dual purpose wind tunnel is shown in figure 3.1. The tunnel is a closed-return dual-purpose facility, with a 2.1 m by 1.5 m 'high-speed' (45 m/s) aeronautical working section and a 'low-speed' (12 m/s) industrial working section. The experiments described in this thesis were performed in the 2.1m by 1.5m working section at a typical test speed of 22 m/s. The static pressure in the working section was maintained at atmospheric by means of small vent doors at the upstream end of the section. The flow in the high speed working section was surveyed in 1989[94] and the total pressure variation across the cross section was no more than $\pm$ 2%. Hot wire measurements at typical test conditions indicated centreline turbulence of the order of 0.5%.

3.2 BLOWING AIR SUPPLY

From a previous study on the effects of tangential leading edge blowing on delta wing aerodynamics at high angles of attack[26] a blowing supply had been established in the wind tunnel. This system had been sized for a 20 kPa plenum pressure and a mass flow of 0.05 kg/s. The maximum requirements for the present forebody blowing investigation are approximately 20% of these values.

Air was obtained from a 500 kPa shop main via a filter and regulator, then ducted to the rear of the model via the 'A' frames of the high angle of attack pitch rig through 1" bore PVC tubing. A 0.5" bore tube was then used to take the air through the model fuselage to the plenum chamber in the nose cone. Plenum pressure was monitored via a static pressure tapping connected to a pressure transducer outside the

tunnel. Air volume flow rate was measured using an in-line rotameter located outside of the working section, downstream of the pressure regulator.

3.3 HIGH ANGLE OF ATTACK PITCH RIG

In 1990 a computer controlled high angle of attack pitch had been installed in the wind tunnel[95]. The rig was of a pantograph design and enabled the model to be pitched about the centre of the working section, figure 3.2. The model was pitched about a vertical axis to keep its weight vector constant with respect to the balance centre. This means that balance zeroes due to model weight do not change with pitch angle.

The rig was controlled via the data acquisition system and during tests any angle of attack could be demanded directly from a numerical entry in to the acquisition system computer.

3.4 MEASUREMENT OF AERODYNAMIC FORCES AND MOMENTS

The sign convention used for the aerodynamic forces and moments acting on the wind tunnel model is defined in figure 3.3. The axes used are the aircraft body axes, i.e. a set of orthogonal axes defined relative to a datum on the aircraft that move with the aircraft.

Forces and moments were measured using a six component sting balance kindly loaned by DRA Farnborough, tables 3.1-3.3, figure 3.4. The balance was located inside the model fuselage such that the centre of the balance approximately coincided with the longitudinal centre of pressure of the model. This meant that the moment arm of the normal force about the balance centre was minimised and excessive pitching moments-due-to-normal force avoided.

The balance was designed to be used in the horizontal sense, i.e. with the weight component of the model acting in the direction of the normal force. In the present investigation the model was mounted on its side and thus the model weight component acts in the side force sense. This meant that the model had to be made as light as possible to avoid over-stressing the balance.

The balance consisted of six strain gauge wheatstone bridge circuits, each containing four active gauges, figure 3.5. Figure 3.6 shows the arrangement of gauges to measure pitching moments. For a positive moment, gauges R_1 and R_2 are in compression and gauges R_3 and R_4 are in tension, thus the resistance of R_1 and R_2 decreases and the resistance of R_3 and R_4 increases. Referring back to figure 3.5, this causes an imbalance between the two sides of the bridge and V_A becomes larger than V_B and the bridge output voltage V_o becomes positive. Similarly for a negative pitching moment the resistance of R_1 and R_2 increases and the resistance of R_3 and R_4 decreases and V_o is negative.

The voltage output from each bridge circuit is given by

$$
\begin{aligned}
V_X &= \frac{\partial V_X}{\partial X} X + \frac{\partial V_X}{\partial Y} Y + \frac{\partial V_X}{\partial Z} Z + \frac{\partial V_X}{\partial L} L + \frac{\partial V_X}{\partial M} M + \frac{\partial V_X}{\partial N} N \\
V_Y &= \frac{\partial V_Y}{\partial X} X + \frac{\partial V_Y}{\partial Y} Y + \frac{\partial V_Y}{\partial Z} Z + \ldots \\
V_Z &= \frac{\partial V_Z}{\partial X} X + \ldots \\
&\textit{etc.}
\end{aligned}
\qquad (3.1)
$$

Writing this in matrix form gives

$$\begin{bmatrix} V_X \\ V_Y \\ V_Z \\ V_L \\ V_M \\ V_N \end{bmatrix} = \begin{bmatrix} c_{11} & c_{12} & c_{13} & c_{14} & c_{15} & c_{16} \\ c_{21} & c_{22} & c_{23} & c_{24} & c_{25} & c_{26} \\ c_{31} & c_{32} & c_{33} & c_{34} & c_{35} & c_{36} \\ c_{41} & c_{42} & c_{43} & c_{44} & c_{45} & c_{45} \\ c_{51} & c_{52} & c_{53} & c_{54} & c_{55} & c_{56} \\ c_{61} & c_{62} & c_{63} & c_{64} & c_{65} & c_{66} \end{bmatrix} \begin{bmatrix} X \\ Y \\ Z \\ L \\ M \\ N \end{bmatrix} \qquad (3.2)$$

or

$$[V] = [C][F] \qquad (3.3)$$

where [V] is a voltage matrix, [C] is a calibration matrix and [F] is a force matrix. However the situation during a wind tunnel test is that the voltage output from each of the bridge circuits is known and the forces are unknown. Rearranging equation 3.3 to find the forces gives

$$[F] = [C]^{-1}[V] \qquad (3.4)$$

where $[C]^{-1}$ is the inverse of the calibration matrix.

The coefficients c_{11},c_{12} etc. in the calibration matrix were found by applying loads to the balance and measuring the voltage output from each of the bridge circuits. The loads were applied by hanging weights off a specially designed calibration arm fitted to the end of the balance, figure 3.7. By appropriate orientation of the calibration arm and balance, relative to the gravity vector, all the force and moment components could be generated apart from the axial force, X, which had to be applied with the balance mounted vertically.

Figure 3.8 shows balance calibration curves for positive normal force, side force,

yawing moment and rolling moment. The maximum value of the x-axis scale in each case is indicative of the maximum loading expected from the wind tunnel model for a test speed of 20 m/s. The y-axis represents the voltage output from the respective strain gauge bridge circuits after it has been amplified by a factor of 500. Voltage error bars represent 50 Hz electrical noise in the instrumentation circuitry.

Note that it was necessary to calibrate the balance from scratch since the only calibration data available from the DRA was from ten years ago and the balance had been modified since.

For the work described in this thesis the lateral force/moment components are most important, i.e. side force, yawing moment and rolling moment. These components are typically an order of magnitude smaller than the longitudinal components, i.e. normal force and pitching moment, and thus care must taken to minimise cross coupling.

Cross coupling between force/moment components arises from two separate sources:

1) Inaccuracies in the balance manufacture or gauge alignment that leads to a given bridge circuit being sensitive to force/moment components other than that for which it is intended, and

2) Inaccuracies in the alignment of the balance relative to the body axes of the wind tunnel model.

Cross coupling from balance imperfections is allowed for by the terms off the leading diagonal in the calibration matrix. In general the level of cross coupling was very small. Figure 3.9 shows balance calibration results for normal force cross coupling on the side force and yawing moment channels. At maximum normal force, the yawing moment due to cross coupling is less than 1% of the maximum expected yawing moment value.

The second source of cross coupling was much more of a problem. This arose due to

difficulties in achieving accurate angular alignment of the balance relative to the model. For instance, a 1° rotation of the balance relative to the XY plane of the model could lead to 100% errors in the side force and yawing moment due to cross coupling from the normal force. The alignment problem was eventually solved by changing the original keyway on the end of the balance for a hole in which a pin could be accurately located.

3.5 WALL JET EXPERIMENTAL RIG

To fulfil the need for basic research on the attachment characteristics of finite aspect ratio wall jets on curved surfaces a rig was designed with which wall radius and slot aspect ratio could be varied as independent parameters. The rig consisted of common base and rear plates upon which different nozzle blocks and side rails could be attached, figure 3.10. A 1 mm thick plastic sheet was sandwiched between the base plate and the nozzle block and then curved round the side rails to form a cylindrical surface over which the jet developed. A range of different side rails were made to provide a range of wall radii, figure 3.11. The rails could be mounted either way up to form positive or negative curvature.

The wall jet was produced by accelerating high pressure air from the shop supply through a simple two dimensional nozzle and ejecting it parallel to the surface of the curved plastic sheet, figure 3.12. Four different nozzle blocks were made allowing a range of jet aspect ratios between 6 and 360, figure 3.13. The area of the jet was, however, the same for all four nozzle blocks so that the jet massflow was uniquely related to the nozzle pressure ratio.

A basic design requirement for the nozzle blocks is that the flow at the jet exit should be uniform. This was achieved by the use of a plenum chamber with a diffuser screen (figure 3.10) and a minimum nozzle contraction ratio of 10. This minimum contraction ratio occurred for the aspect ratio 5.625 nozzle block. The aspect ratio 360 nozzle block, for which flow uniformity across the length of the slot was more

important, had a contraction ratio of 100.

A further question arises as to whether the jet is laminar or turbulent at the nozzle exit. This depends on both the geometry of the nozzle and the Reynolds number of the flow. For example, with a large contraction ratio nozzle, it may be possible to achieve a laminar jet at high Reynolds number. For all the surface flow visualisation experiments reported in Chapter 4, the nozzle pressure ratio was large enough such that the jet was either turbulent at the nozzle exit or transitioned to turbulence within a few slot heights downstream of the exit.

3.6 WIND TUNNEL MODEL

3.6.1 Model Design

The following specification was drawn up to define a wind tunnel model that was able to fulfil the requirements of the research programme at the same time as being relatively straight-forward to fabricate:

- Simple geometry representative of current combat aircraft
- Modular construction, i.e. interchangeable wings,tail plane, fin, nose cone
- Large enough to contain the 6 component balance, pressure tubing and plenum supply pipes within the fuselage
- Small enough to prevent excessive tunnel wall interference
- Nose cone removable without having to disassemble rest of model
- Access to balance whilst model is mounted in tunnel

- Light weight

The final model design is shown in figures 3.14 and 3.15. The shape of the model was determined by conducting a parametric study of current combat aircraft to determine characteristic geometric ratios, Table 3.4. By taking a rough average of these ratios a generic type combat aircraft was defined, Table 3.4 bottom row. Of the aircraft listed, the model is most similar to the F/A-18 (aside from the fact that the F/A-18 has twin fins). This turned out to be fortuitous since recently there have been a number of full and sub scale trials of forebody blowing on an F/A-18 and a useful comparison of data may be made.

The nose cone fineness ratio (ratio of length to diameter) of 4 is slightly higher than that of most of the comparison aircraft. This higher value was chosen to increase the magnitude of the out-of-plane side forces due to forebody vortex asymmetry, thus making them easier to measure accurately.

The tangent ogive shape of the nose cone was chosen as suitable representation of a typical fighter forebody shape. The profile is given by:

$$\frac{r}{R} = \left\{ F^2 + (2F+1)\left[1 - (1 - \frac{x}{L})^2 \right] \right\}^{0.5} - F \qquad (3.5)$$

where L is the length of the nose cone, R is the base radius, x is distance from the apex, r is the local radius and F is given by:

$$F = \frac{1}{2}\left[4 \left(\frac{L}{D}\right)^2 - 1 \right] \qquad (3.6)$$

The model is constructed from 3.65 mm sheet aluminium flying surfaces and a 70 mm diameter extruded aluminium tube fuselage with a wall thickness of 3 mm. The wing is mounted just below the centre line of the fuselage, with the balance passing over the top of it and the pressure tubing and plenum supply pipes passing under it,

figure 3.16. The top half of the fuselage is fixed to the wing by means of a pair of 'L' sections and can be removed to provide access to the balance, figure 3.17.

Figures 3.18 and 3.19 show the model mounted on the high angle of attack pitch rig in the 2.1 m by 1.5 m working section of the wind tunnel.

3.6.2 Nose Cone Fabrication

3.6.2.1 Perspex Nose Cone

The initial nose cone designed for the wind tunnel model was made up of three sections machined from perspex, figure 3.20. The centre section was divided into two plenum chambers, which supplied air to port and starboard slots formed from a thin plastic material called 'Plasticard'. The slot height was set by bonding 0.2 mm spacers between the slot lip and the side of the nose cone, figure 3.21.

This nose cone also had pressure tappings at three stations along its length, with each station containing 24 pressure taps spaced at 15° intervals. The pressure taps were made by bonding 2 mm outside diameter vinyl tubing directly into appropriately sized holes. The tubes were then trimmed flush with the surface using a razor blade.

3.6.2.2 Vacuum Formed Nose Cone

After the first series of wind tunnel tests, a need was identified for an experiment to systematically determine the effects of slot geometry and location. This would have been difficult with the original nose cone with the fixed slot so a new, simpler design was developed that enabled many different slot configurations to be set up on the same nose cone, figure 3.22.

The main body of this nose cone is made from a pair of 1 mm thick vacuum formed plastic shells, figure 3.23. The slot is created by cutting two slits at either end of the

upper most shell and forming the tab so produced to a tighter radius than the rest of the shell. the slot is then set up by drawing the tab in the upper shell towards the slot lip (formed by the lower shell) using a number of self-tapping, 1 mm diameter screws.

The core of the nose cone creates a large plenum chamber which is fed with high pressure air from a central tube perforated with numerous holes. This ensured that there was an even distribution of total pressure along the length of the slot. The vacuum formed shell assembly fits tightly over the end plug mounted in the fuselage and is secured in place by means of insulating tape.

During the development work for the new nose cone there was a high degree of trial and error involved since it was very hard to predict the behaviour of the thin plastic shells without actually making them. A particularly difficult problem was that of getting the right amount of stiffness in the tab cut-out: too little and the slot would be permanently closed, too much and the slot lip became distorted. In the end a fine balance was achieved between the lengths of the slits at either end of the tab and the radius to which it was formed and very satisfactory results were obtained.

Another problem concerned the location of the adjusting screws. From surface oil flow experiments, it had been found that inappropriate positioning of the screws could cause massive disturbances in the jet sheet downstream of the exit plane and in the worst case the jet would break up in to a number of segments marked out by the positions of the adjusting screws. This was clearly unacceptable and experiments were performed to try and find a way of minimising the disturbance caused by the screws. Eventually it was discovered that by placing the screws approximately 5 slot heights from the slot lip, and ensuring that the slot contraction continued after the screws, that the effect of their presence was minimal and could not be detected in the downstream surface oil flow patterns. Whilst doing these experiments it was observed that the flow disturbances originating from small burrs around the screw holes and on the slot lip became massively amplified as the jet developed, and could have global effects on the properties of the jet as a whole. For this reason great care had to taken to ensure that

the screw holes were made as tidily as possible and that the slot lip was cut very accurately.

Three separate nose cones were made for the second series of wind tunnel tests: a single port slot model, a single starboard slot model and a model with a port and starboard slot. The single slot models were used to investigate the effect of slot angular position and once the optimum had been found the two slot model was made. This model had a single plenum chamber like the single slot models and the unused slot had to be blocked off. The variables describing slot geometry and location are shown in figure 3.24. Variables x and ℓ were varied by partitioning the slot in to a number of sections and blocking off the parts not required. The slot angular position was varied by rotating the nose cone assembly relative to the fuselage.

A cylindrical version of the vacuum formed nose cone was built for the purposes of exploratory water tank flow visualisation studies, figure 3.25. Since the kinematic viscosity of water is approximately 15 times smaller than that of air, high jet Reynolds numbers can be achieved in water tank tests at jet velocities appreciably smaller than those in the equivalent test in air. This makes visualisation of the flow structures within the jet much easier.

3.7 DATA ACQUISITION SYSTEM

A block diagram of the data acquisition system used during the wind tunnel test programme is shown in figure 3.26. The system was based around a Data Translation DT2821 board in a Dell 310 PC. The DT2821 is a programmable analogue and digital I/O board with up to 16 analogue to digital input channels, 16 digital I/O lines and 2 digital to analogue output channels. Signals from the balance and pressure transducers were amplified before going to the I/O board using a rack of in-house designed amplifier cards, which also had on board passive low-pass filtering facilities.

The data acquisition process was controlled by a user-friendly wind tunnel test

program called Rigtest 4.1[96] which combined rig control and data acquisition functions. The experimental set up and runtime graphics options for the program were input by means of configuration files read from disk. These configuration files could be edited with any ASCII text editor and provided a very flexible means of tailoring the acquisition system to the needs of a particular experiment.

A typical test run during the wind tunnel test programme would be as follows:

1) Boot up computer, run Rigtest
2) Load configuration and display files relevant to particular test
3) Take wind off zeroes
4) Run wind tunnel up to speed
5) Initiate 'take data' routine on Rigtest
6) Input required angle of attack
7) Set blowing levels
8) Sample data
9) Observe data point on graph display
   If good, carry on; else go back to 6) or 7)
10) Save data point to file
11) Go back to 6) until test is finished
12) Quit Rigtest

After testing, data files were directly imported in to a graph plotting and basic data manipulation package called SigmaPlot where the data was further reduced and could be output as a hard copy on an inkjet printer.

3.8 DATA REDUCTION

3.8.1 Reference Pressure

Pressure, force/moment and jet blowing level data was normalised by the tunnel

centreline dynamic pressure, q. This was determined from the static pressure difference between a tapping in the roof of the working section and the start of the contraction:

$$q = k V_{man} \tag{3.7}$$

where k is a calibration constant (= 0.83 Pa/V), and V_{man} is the analogue voltage output from a micromanometer measuring the tunnel reference pressure difference.

3.8.2 Aerodynamic Coefficients

Force, moment and pressure coefficients are defined in the conventional form:

$$C_Z = \frac{Z}{qS}$$

$$C_Y = \frac{Y}{qS}$$

$$C_L = \frac{L}{qS\bar{c}} \tag{3.8}$$

$$C_N = \frac{N}{qS\bar{c}}$$

$$C_p = \frac{p - p_\infty}{q}$$

Note that because of the sting balance arrangement data is presented in body axes rather than wind axes.

3.8.3 Blowing Coefficients

Blowing level can be quantified in terms of a mass flow coefficient, C_Q, or a momentum coefficient, C_μ. For boundary layer suction work[81] it would appear that C_Q is the most appropriate parameter. For blown flaps and circulation control aerofoils

the most appropriate parameter is C_μ[21]. At present there is some controversy over which parameter is most appropriate to Tangential Forebody Blowing[97]. This will be discussed further in Chapter 4.

3.8.3.1 Mass Flow Coefficient

C_Q is defined as

$$C_Q = \frac{\text{Jet Mass Flow}}{\text{Free Stream Mass Flow}} = \frac{\rho_j A_j V_j}{\rho_\infty A_{ref} V_\infty} \tag{3.9}$$

With no leakage, the mass flow in the jet is equal to the mass flow at any point in the air supply, thus

$$C_Q = \frac{\rho_x A_x V_x}{\rho_\infty A_{ref} V_\infty} \tag{3.10}$$

where x indicates a particular measurement station.

For the present work the supply volume flow

$$\dot{V} = A_x V_x \tag{3.11}$$

was measured using the in-line rotameter. The flow velocity was sufficiently low in the rotameter that compressibility effects can be ignored and $\rho_x = \rho_\infty$. Equation 3.10 then simplifies to

$$C_Q = \frac{\dot{V}}{A_{ref} V_\infty} \tag{3.12}$$

3.8.3.2 Momentum Coefficient

The jet momentum coefficient is defined as

$$C_\mu = \frac{\text{Jet Momentum}}{\text{Free Stream Momentum}} = \frac{\rho_j A_j V_j^2}{q A_{ref}} \tag{3.13}$$

By suitable approximations, this may be determined from the plenum static pressure.

Writing Bernoulli's equation for incompressible flow in the jet nozzle gives

$$p_p + \frac{1}{2}\rho V_p^2 = p_\infty + \frac{1}{2}\rho V_j^2 + \text{Nozzle Losses} \tag{3.14}$$

With a well designed nozzle and plenum chamber, the nozzle losses should be small and $V_p \approx 0$. Thus equation 3.14 may be rewritten to give

$$p_p - p_\infty = \frac{\rho V_j^2}{2} \tag{3.15}$$

hence

$$V_j^2 = \frac{2\Delta p}{\rho} \tag{3.16}$$

Substituting equation 3.16 into equation 3.13 gives

$$C_\mu = \frac{2 A_j C_{p\,plen}}{A_{ref}} \tag{3.17}$$

where

$$C_{p\,plen} = \frac{\Delta p}{q} \tag{3.18}$$

Assuming a uniform velocity distribution at the slot exit, i.e. zero wall boundary layer thickness, A_j is equal to the geometric area of the slot exit:

$$A_j = A_{geom} = \ell . h \tag{3.19}$$

Normally, however, the velocity profile at the slot exit is not uniform, which means that

$$A_j = C_D A_{geom} \tag{3.20}$$

where C_D is a discharge coefficient. For a well designed nozzle and slot, and a turbulent jet, C_D is typically of the order of 0.8.

Slot discharge coefficients may be determined from the jet volume flow and jet velocity:

$$C_D = \frac{\dot{V}}{A_{geom} V_j} \tag{3.21}$$

A problem arises if the blowing slot distorts when pressurised. It was found that the slots on the vacuum formed nose cone opened up by approximately 0.05 mm at high blowing levels. For a slot height of 0.5 mm this gives a 10% increase in slot area. For smaller slot heights the problem is more severe. For this reason it was convenient to eliminate A_j from the derivation of C_μ. This can be done by using a combination of the plenum pressure and volume flow rate for the derivation:

Substituting

$$A_j = \frac{\dot{V}}{V_j} \tag{3.22}$$

into equation 3.13 yields

$$C_\mu = \frac{\rho_j \dot{V} V_j}{q A_{ref}} \tag{3.23}$$

Now substituting

$$V_j = \sqrt{\frac{2\,\Delta p}{\rho_j}} \tag{3.24}$$

leads to

$$C_\mu = \frac{\dot{V}}{qA_{ref}} \sqrt{2\rho_j \Delta p} \qquad (3.25)$$

At a typical test condition of $V_\infty = 22$ m/s and $C_\mu = 0.01$, $V_j = 70$ m/s and $M_j = 0.28$, the assumption of incompressibility used in the derivation of equation 3.25 means that the measured value of C_μ will be approximately 2% higher than the actual.

At a typical full scale flight Mach number of 0.3 and with relatively small, high pressure slots, it is likely that M_j will be sonic. In that case accurate values of C_μ will have to be obtained from a compressible analysis of the flow in the nozzle.

3.9 WIND TUNNEL CORRECTIONS

Aerodynamic forces and moments acting on a wind tunnel model are to some extent influenced by the fact that the model and its support structure are being tested in a finite volume of moving fluid bounded by solid walls. Wind tunnel corrections are applied to measured force and moment data to try and compensate for these non-ideal test conditions and to obtain results that are closer to the true free flight values. Tunnel corrections can be made for the following effects:

1) Blockage
2) Wall Interference
3) Support Interference
4) Support Deflection, and
5) Buoyancy

These are described in detail by Rae and Pope[98].

Model blockage may be divided into solid blockage and wake blockage. Solid blockage is essentially due to the physical volume of the model and is independent of angle of attack. Wake blockage, on the other hand, is primarily due to the drag on the

model and is dependent on angle of attack. At high angles of attack, wake blockage makes by far the largest contribution to the overall blockage. An additional complexity arises for vortical flows at high angles of attack since blockage tends to modify vortex burst positions[99,100]. This can have a large effect on the measured force moment characteristics of a model. A review of wind tunnel data on delta wings at high angles of attack has been made by Greenwell[101]. This study concludes that although no systematic guidelines to determine maximum model size have been developed, a model planform area to wind tunnel cross sectional area ratio of around 5% seems to be generally accepted as offering a reasonable compromise. In the present investigation, the model planform area to wind tunnel cross sectional area ratio is 4.8% and it was thus assumed that blockage effects would not affect trends observed in the model force and moment data.

Minimum clearance between the tunnel walls and model is reached at 90° angle of attack. In this case the tip of the nose cone is 0.5 m (two nose cone lengths) from the side of the tunnel. Comparison with other model arrangements for wind tunnel studies of forebody flows suggest this is sufficient clearance to make wall interference corrections unnecessary.

Flow distortion at the rear of the model was caused by the support frames of the high angle of attack pitch rig. This was most significant at low angles of attack. However, since over 90% of the control yawing moment from tangential forebody blowing arises from changes in the forebody flowfield, flow distortion at the rear of the model was not a significant issue.

Some pitch deflection of the model was expected due to flexibility of the high angle of attack pitch rig and balance. It was estimated that at the maximum normal force condition (90° angle of attack) the pitch deflection was approximately 1°.

Buoyancy effects are caused by pressure gradients in the tunnel working section. These are typically relevant when there is a longitudinal pressure gradient in the working section and very accurate drag forces are required. This is not the case in the

present investigation.

On balance, it was felt that there would be no significant improvement in quality of the test data through use of wind tunnel corrections. Thus the force and moment data presented in this thesis are in an uncorrected form.

3.10 ASSESSMENT OF EXPERIMENTAL ACCURACY

Throughout the experiments described in this thesis the emphasis has been on experimental consistency rather than experimental accuracy. This is because the focus of the work is on identifying and understanding trends in the aerodynamics, rather than quantifying them.

For a typical measurement of a blown yawing moment at a given angle of attack, the associated systematic errors are estimated to be:

Angle of attack	$\pm 1^{\circ}$
Blowing Coefficient	$\pm 5\%$
Yawing Moment Coefficient	$\pm 5\%$

Random errors due to electrical noise in the instrumentation system are small for the angle of attack and blowing coefficients measurements (rms error $< 1\%$ of full scale readings). Electrical noise from the balance instrumentation, however, was more significant. Typically the rms error in the yawing moment signal was 10% of the full scale reading.

The most serious source of random errors was yaw oscillation of the model due to unsteady vortex shedding from the forebody. Figure 3.27 shows a typical unblown yawing moment response for the model over an angle of attack range from 0 to 90°. At low angles of attack the model is steady and the error bars on the data points are due to electrical noise. At around 40° angle of attack the model suffers from quite

severe yaw oscillations (typically $\pm 2^{\circ}$ at 5 Hz) and the rms error in the yawing moment signal is large (50% of full scale reading). The yaw oscillations tended to be fairly regular and by sampling the yawing moment for half a second at 1 kHz, highly repeatable results were obtained. Tests done at speeds where the vibration levels were much lower showed similar yawing moment responses. This suggested that the model oscillation was not having a dominant effect on the forebody aerodynamics.

X	Y	Z	L	M	N
+/-90	+/-130	+ 1330 - 450	+/-6.78	+/-34.0	+/-5.65

Forces in N, moments in Nm

Table 3.1 *Jaguar Balance Maximum Forces and Moments*

Bridge	Resistance (Ohms)
X	706
Y	354
Z	354
L	355
M	354
N	785
Power Supply	79.8

Table 3.2 *Jaguar Balance, Resistance of Bridge Circuits (2 June 1981)*

Polarity	Colour	Pin	Channel
+	white	2	X
-	blue	15	
+	orange	3	Y
-	white	16	
+	brown	4	Z
-	white	17	
+	white	5	L
-	green	18	
+	red	6	M
-	white	19	
+	yellow	7	N
-	white	20	
+	white	1	Power Supply
-	black	14	

Table 3.3 *Jaguar Balance Wiring Colour Coding*

Aircraft	Wing Span/ Fuselage Length	Fuselage Fineness Ratio	Forebody Fineness Ratio	Tailplane Span/ Wing Span	Fin Height/ Fuselage Length	Wing Sweep (Degrees)	LEX Sweep (Degrees)
F-15	0.71	14.1	3.1	0.63	0.24	43	--
F-16	0.68	11.8	3.7	0.57	0.27	40	80
F-18	0.71	13.0	3.3	0.54	0.21	25	80
YF-22	0.63	10.5	3.5	0.71	0.23	50	--
YF-23	0.64	10.5	3.6	0.69	0.12	40	--
EAP	0.80	12.7	2.8	----	0.29	55	--
Wind Tunnel Model	0.71	14.8	4.0	0.48	0.25	40	75

Table 3.4 *Comparison of Various Current Combat Aircraft Geometries*

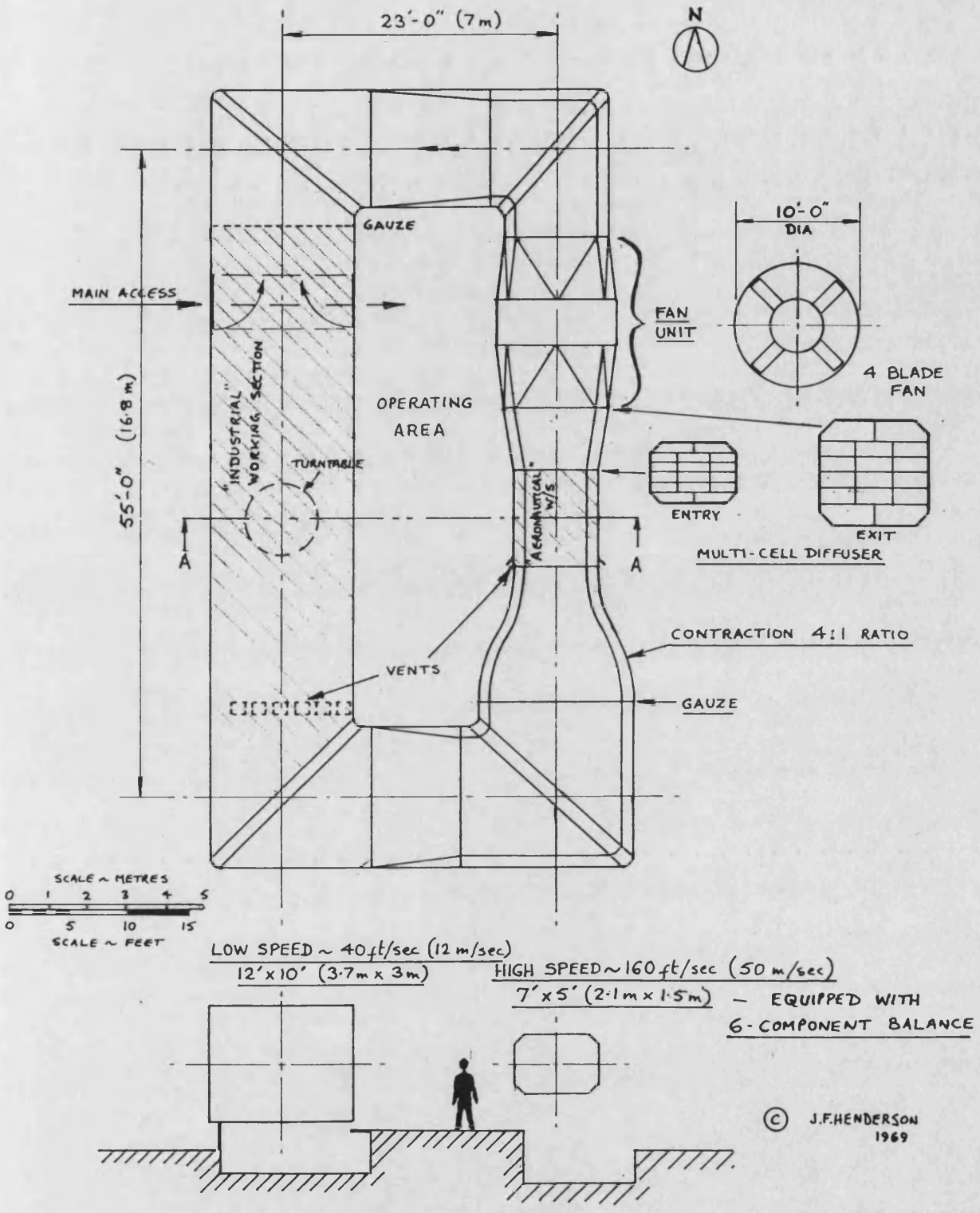

SECTION A-A SHOWING THE TWO WORKING SECTIONS, EITHER OF WHICH MAY BE OPERATED AT AMBIENT PRESSURE, AS REQUIRED

Figure 3.1 *University of Bath Dual Purpose Wind Tunnel*

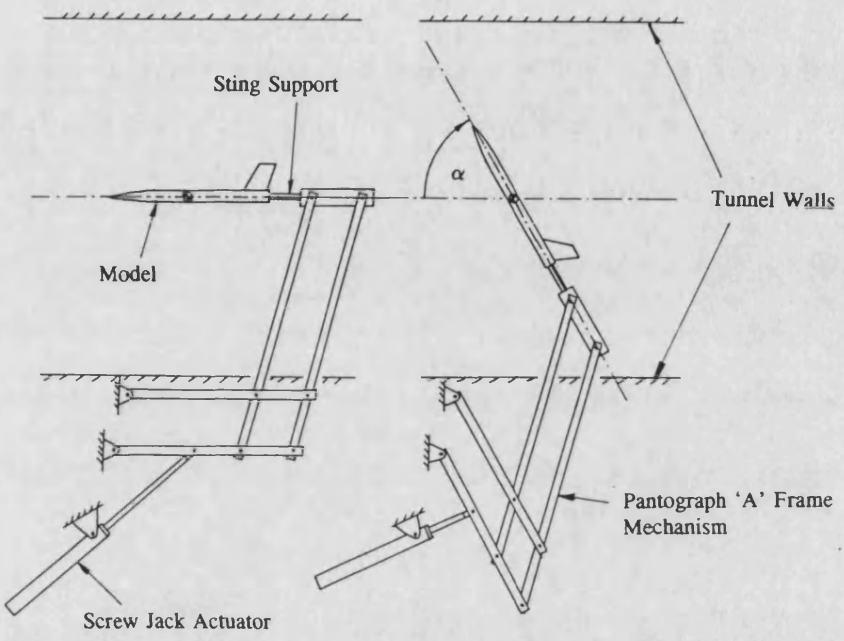

Figure 3.2 *High angle of Attack Pitch Rig*

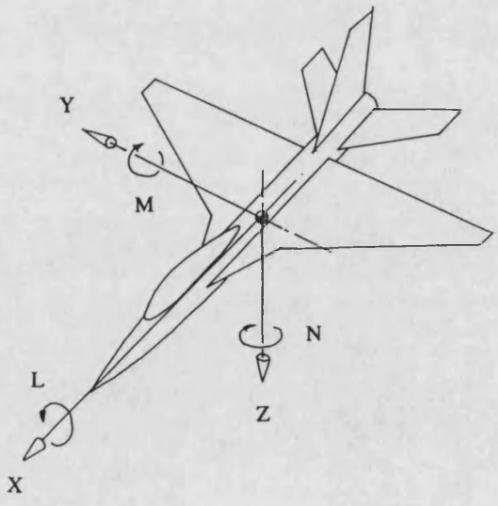

Figure 3.3 *Sign Convention for Aerodynamic Forces and Moments*

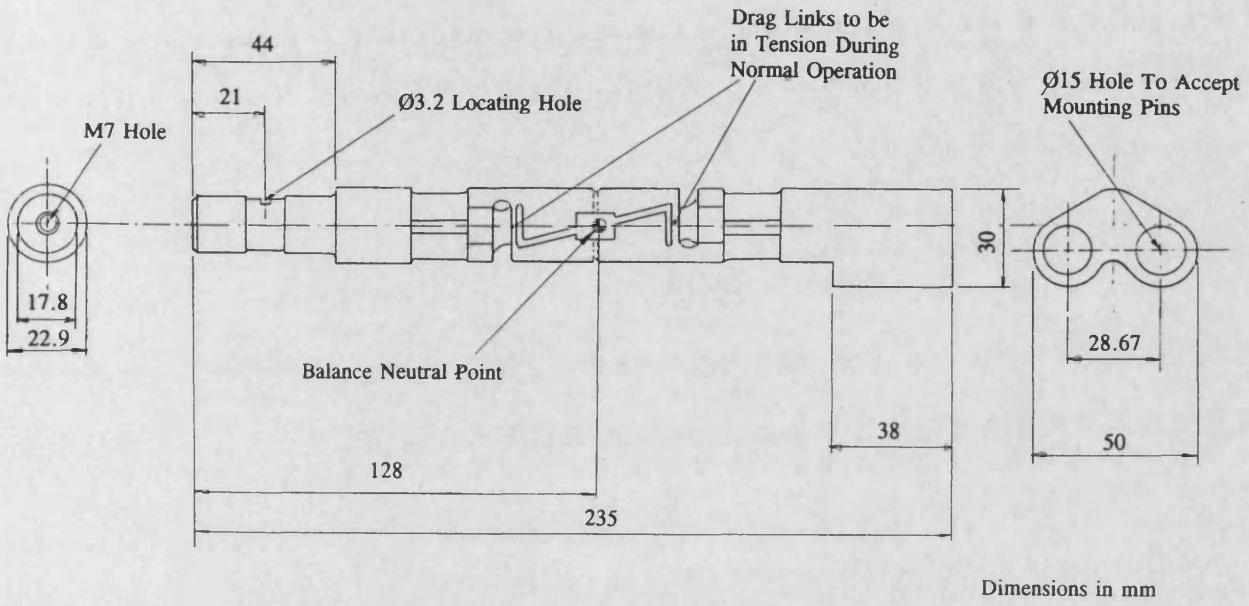

Figure 3.4 *DRA Six Component Jaguar Balance*

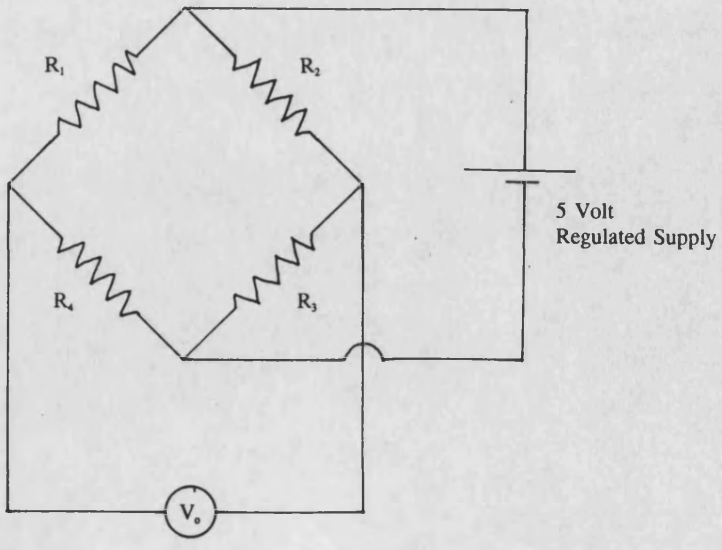

Figure 3.5 *Single Wheatstone Bridge Circuit from Jaguar Balance*

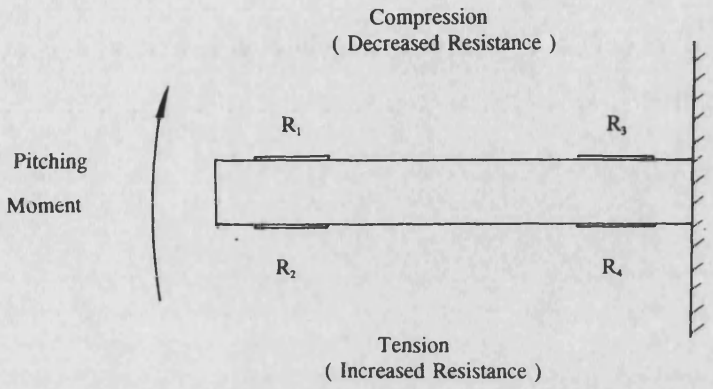

Figure 3.6 *Example Arrangement of Strain Gauges to Sense Pitching Moments*

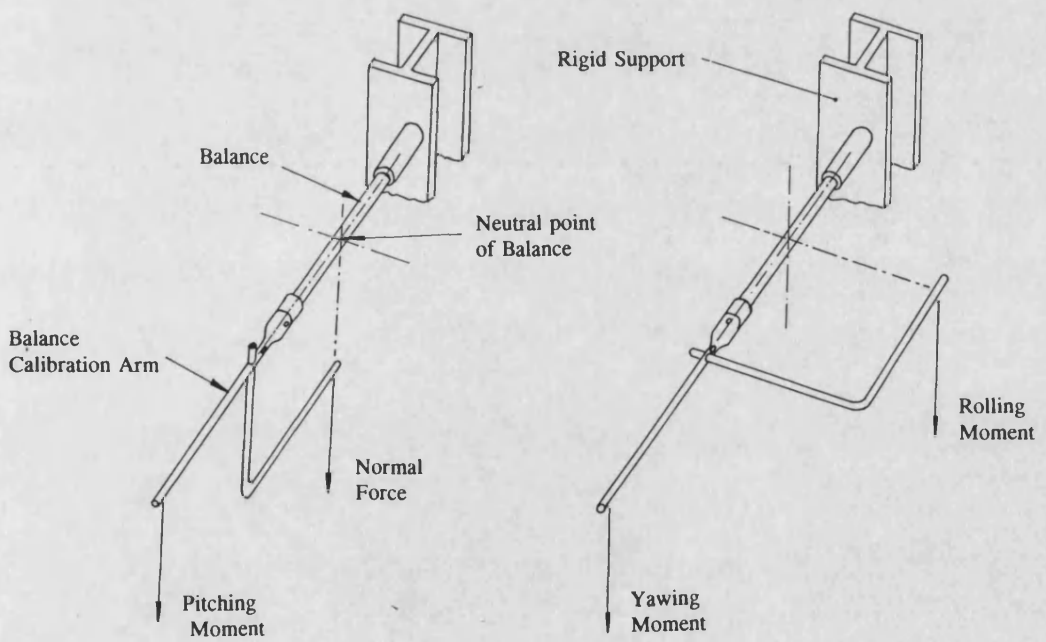

a) Balance Aligned with Z axis Vertical

b) Balance Aligned with Y axis Vertical

Figure 3.7 *Calibration Arm For Jaguar Balance*

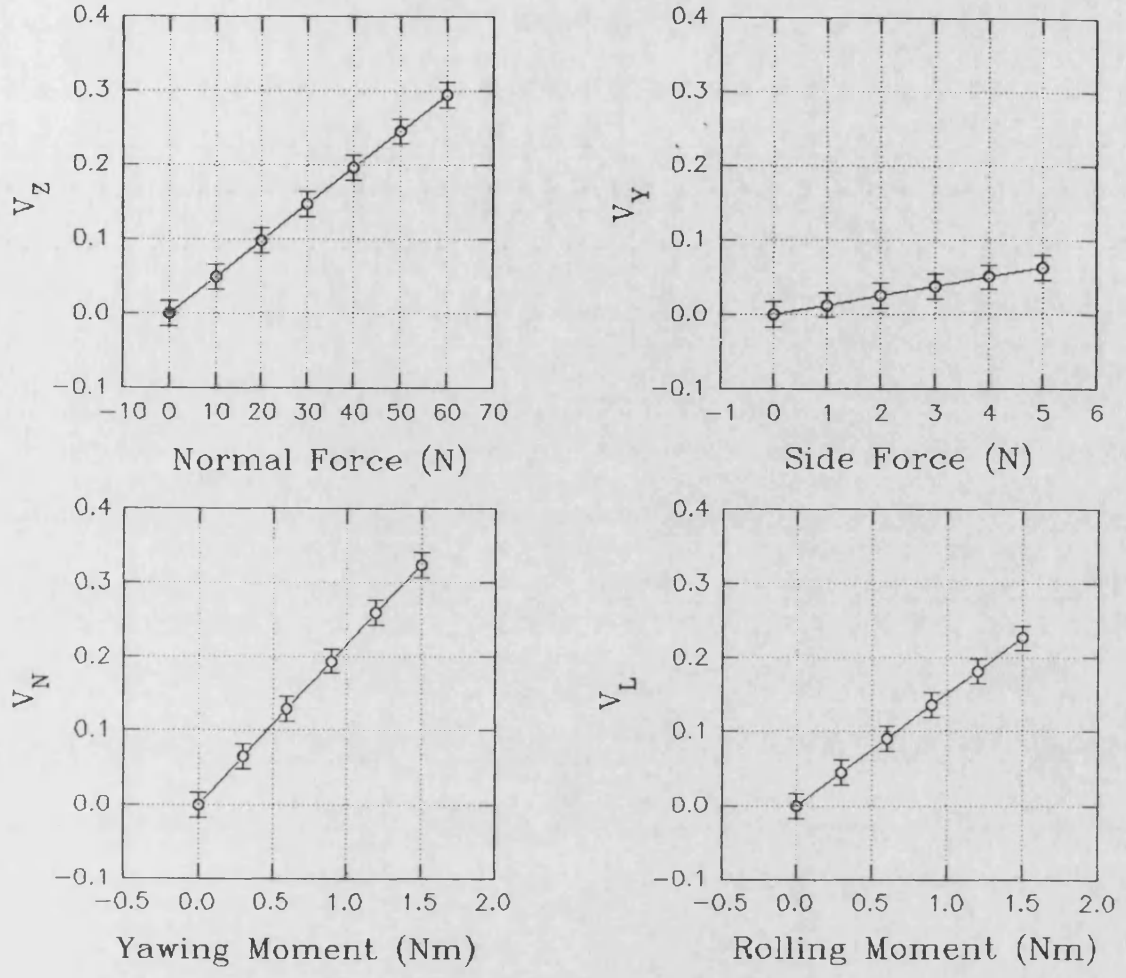

Figure 3.8 *Balance Calibration Curves Over Expected Loading Ranges*

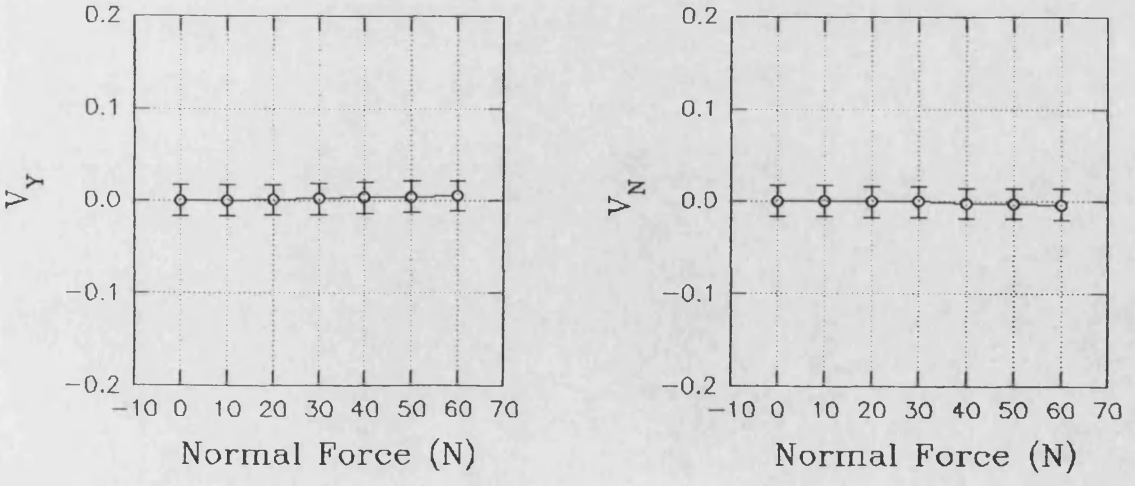

Figure 3.9 *Normal Force Cross Coupling into Side Force and Yawing Moment Components*

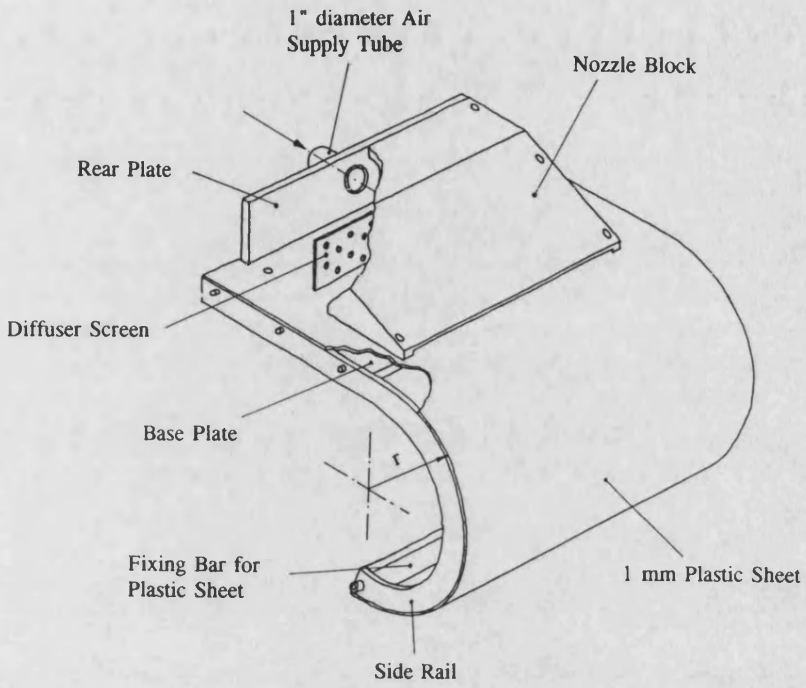

Figure 3.10 *Curved Wall Jet Experimental Rig*

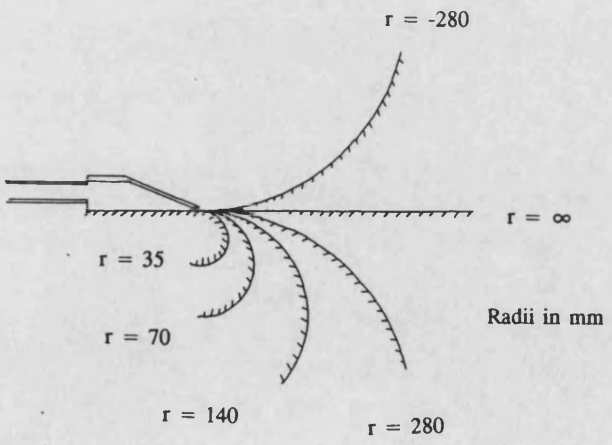

Figure 3.11 *Radii Used For Side Rails on Wall Jet Rig*

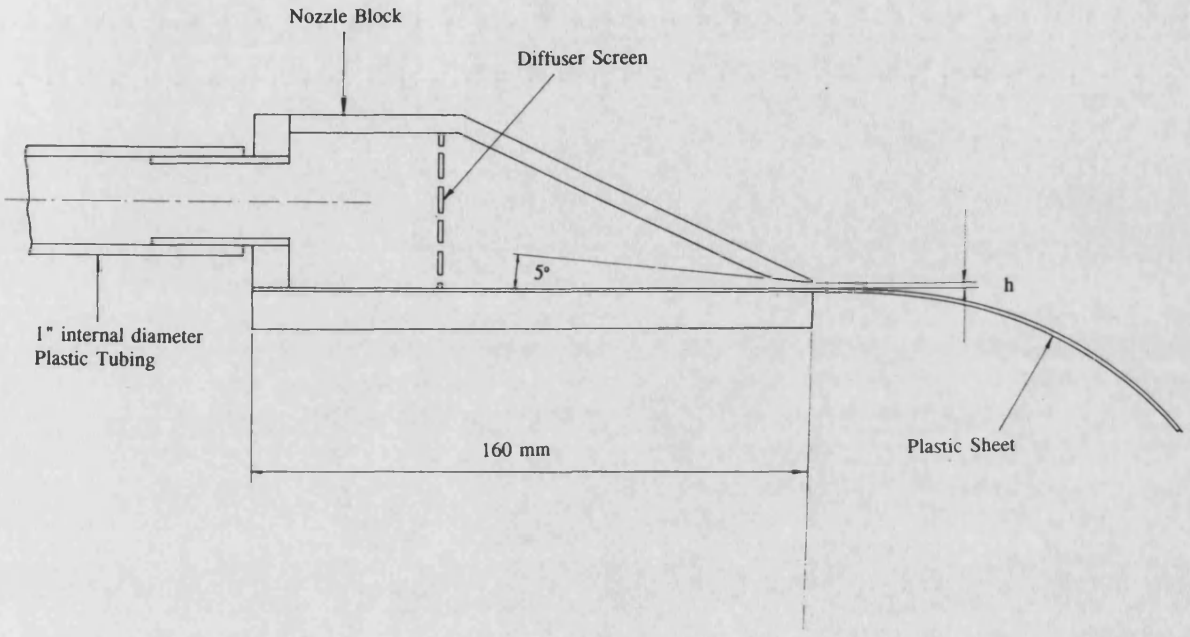

Figure 3.12 *Two-Dimensional Nozzle Geometry for Wall Jet Rig*

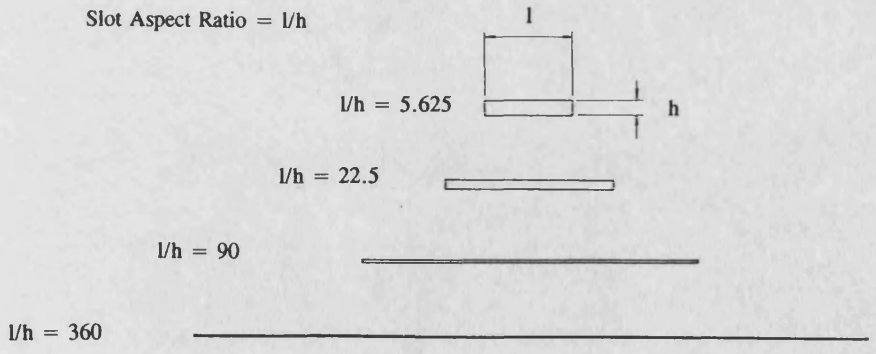

Figure 3.13 *Slot Aspect Ratios of Four Different Nozzle Blocks*

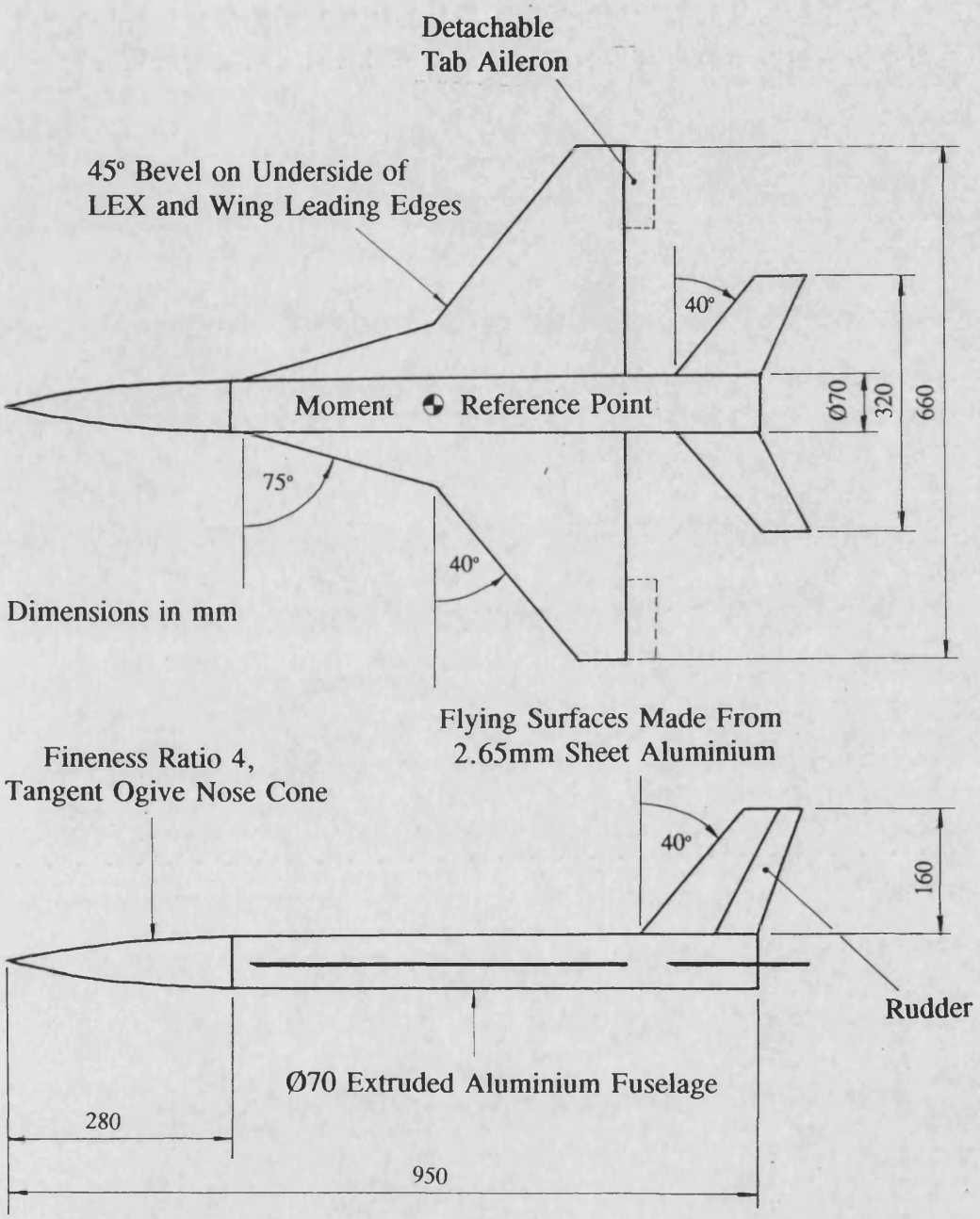

Figure 3.14 *General Arrangement of Wind Tunnel Model*

Figure 3.15 *View of Model with Perspex Nose Cone Attached*

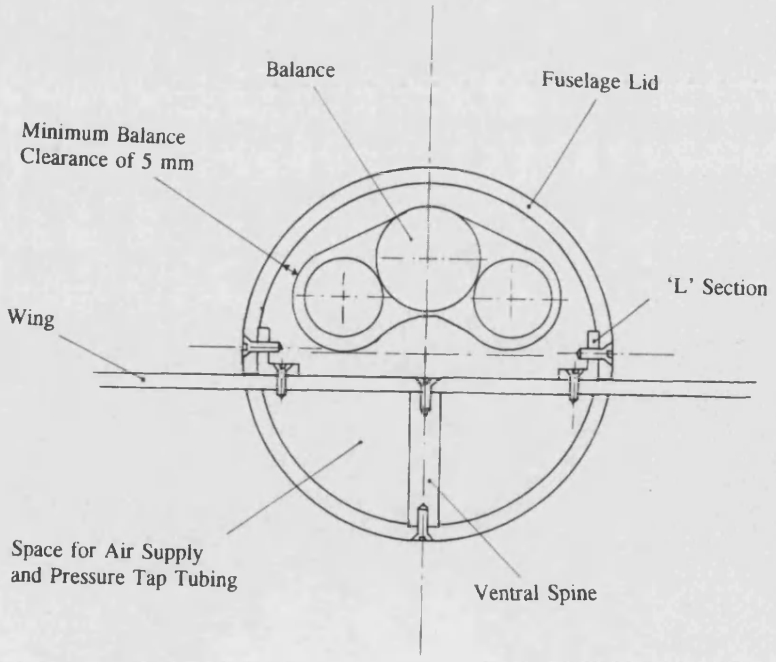

Figure 3.16 *Cross Section Through Model Fuselage at Point of Minimum Balance Clearance*

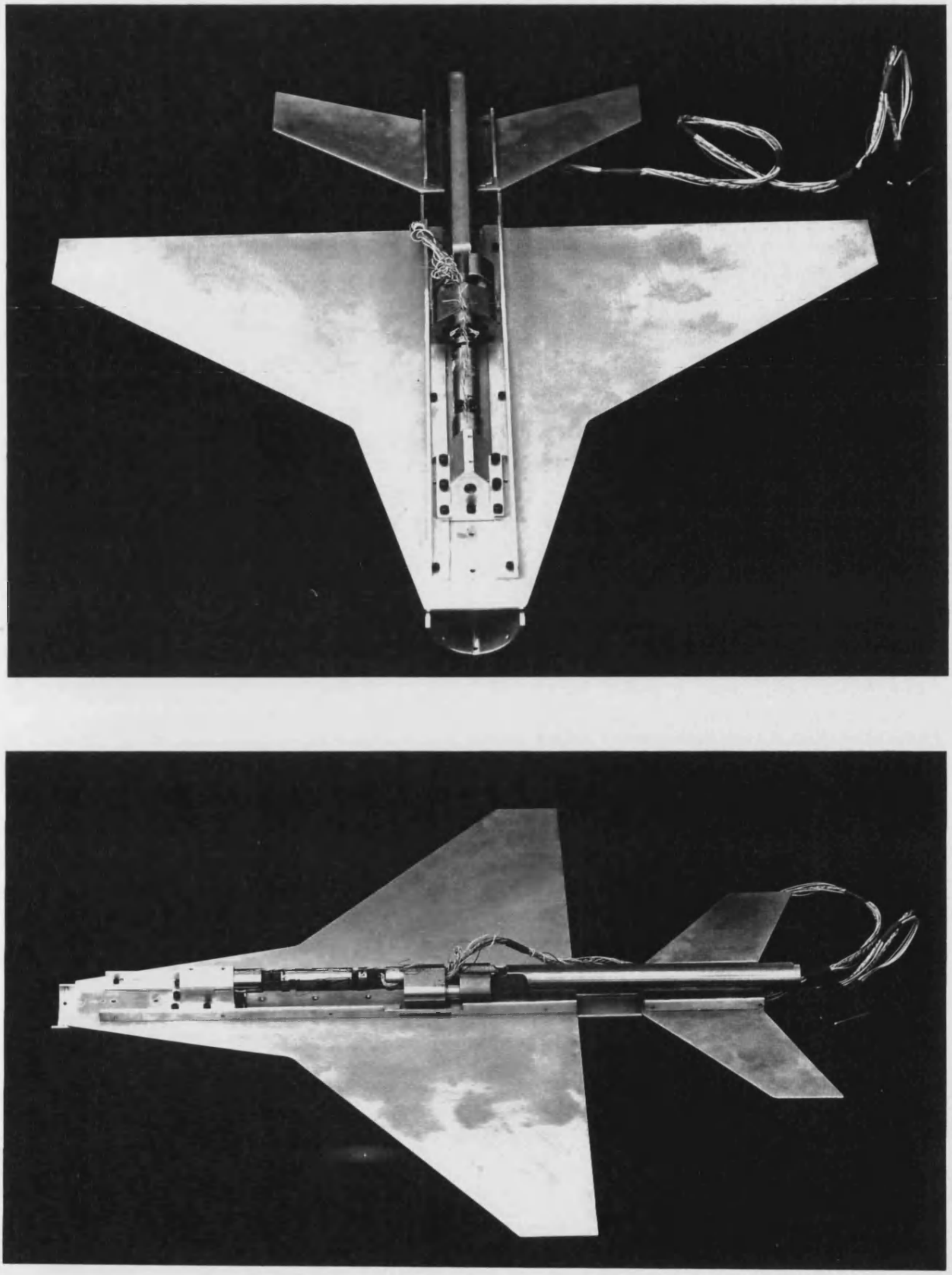

Figure 3.17 *View of Model with Fuselage Lid Removed*

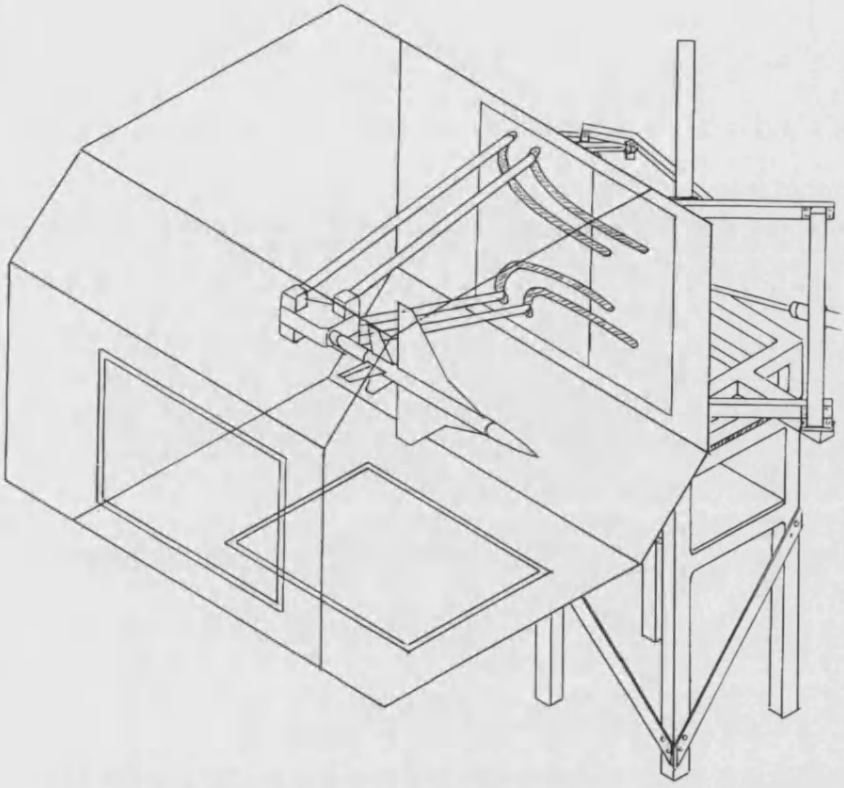

Figure 3.18 *Sketch of Model Mounted on High Angle of Attack Pitch Rig in the 2.1 x 1.5 m Tunnel Working Section*

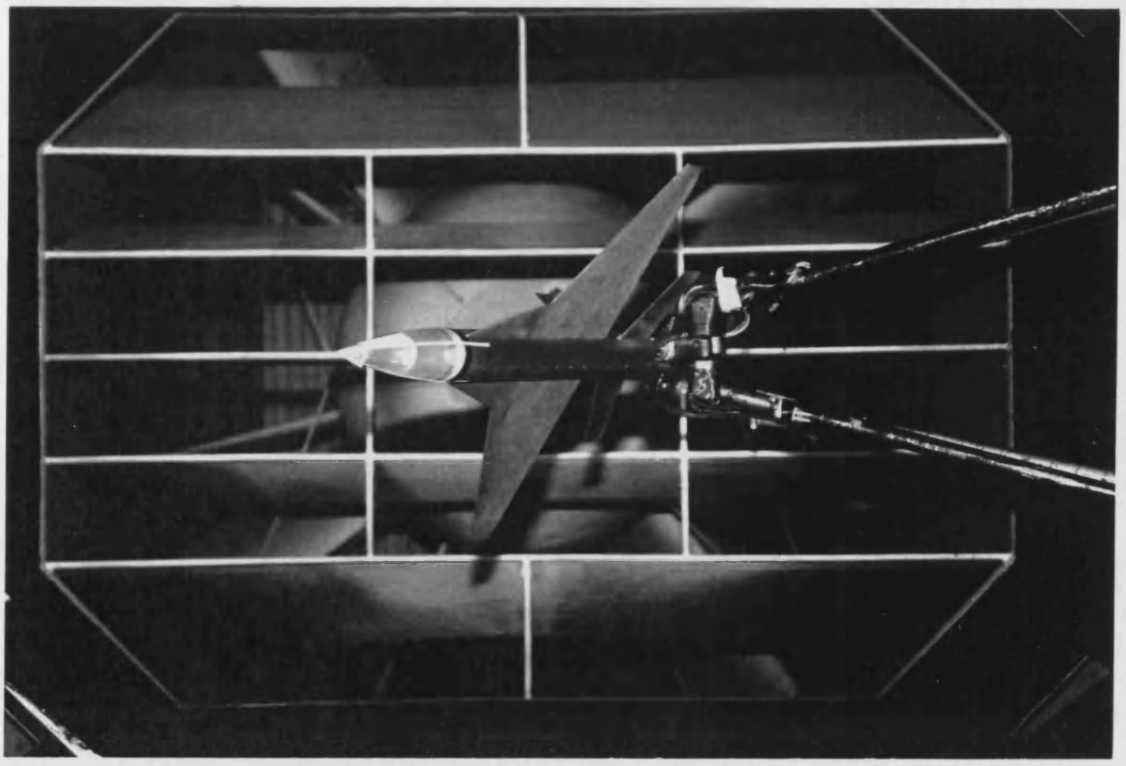

Figure 3.19 *Photo of Model in Tunnel Working Section*

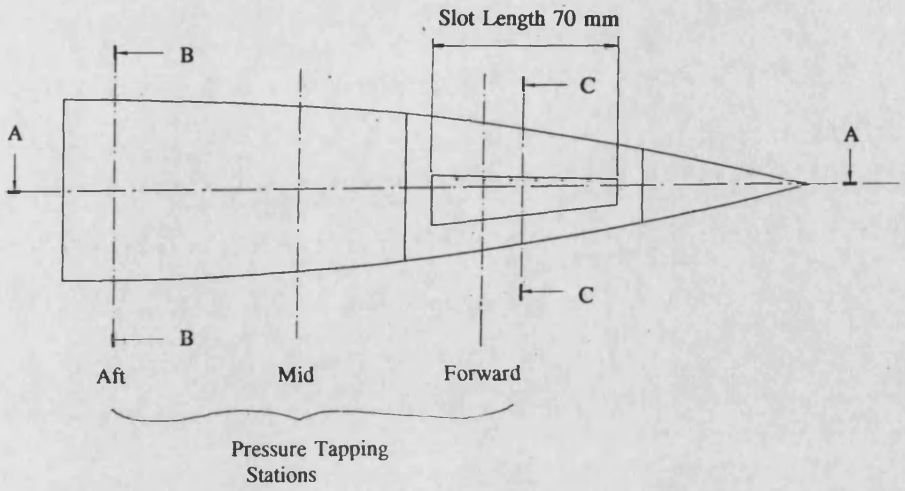

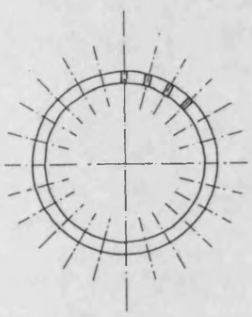

Section B-B

24 Pressure Tappings
Equispaced at 15° intervals

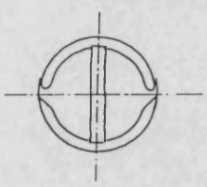

Section C-C

Port and Starboard Blowing Slots

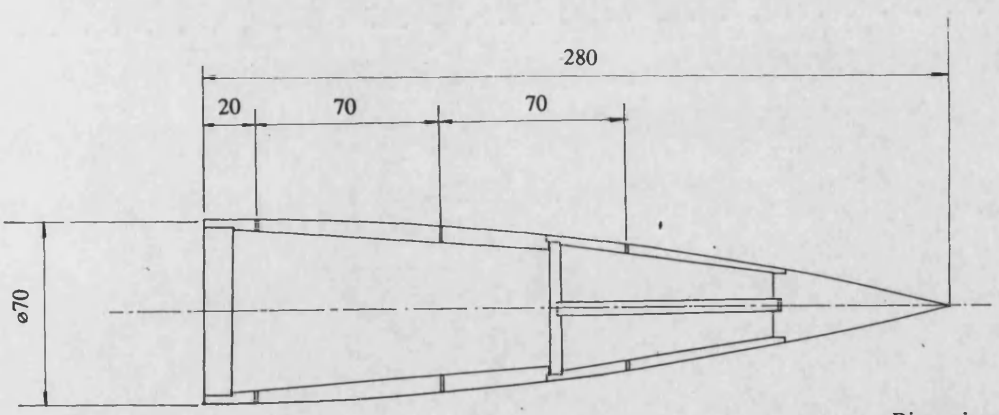

Dimensions in mm

Section A-A

Figure 3.20 *General Arrangement of Perspex Nose Cone*

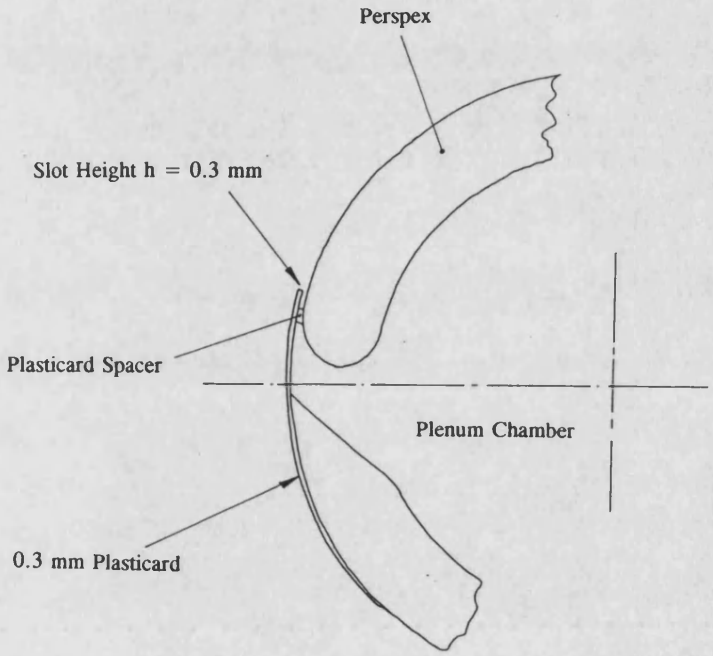

Figure 3.21 *Detail of Plasticard Slot Assembly on Perspex Nose Cone*

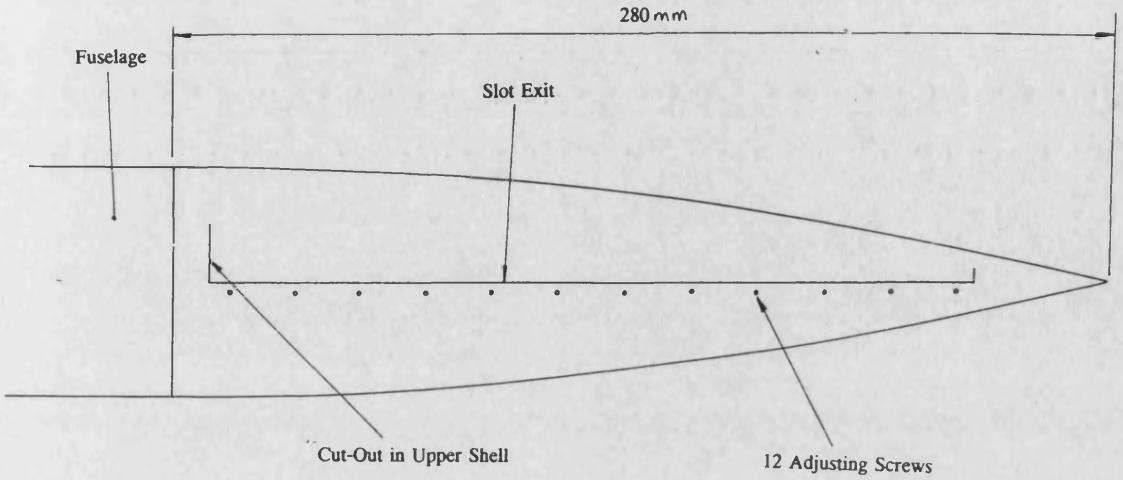

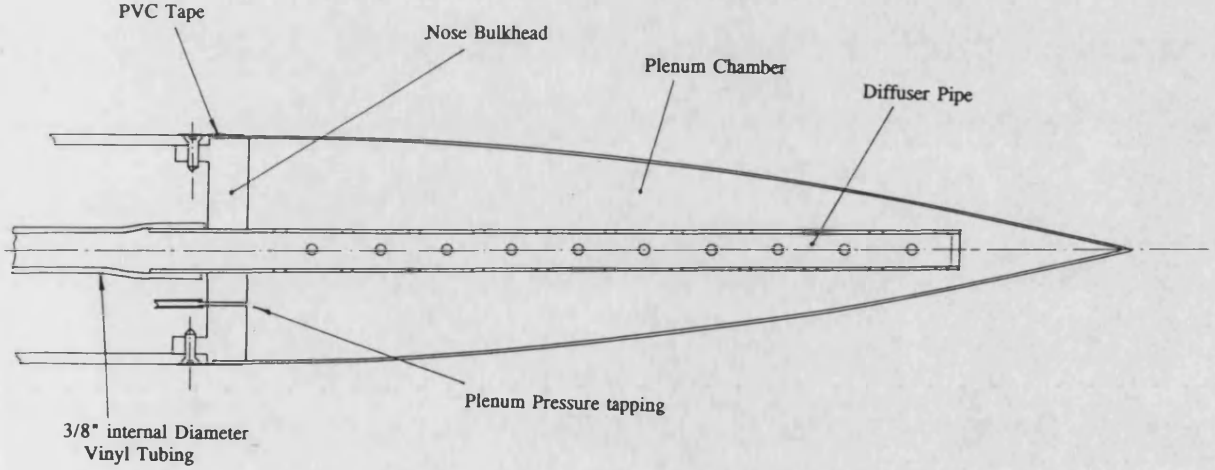

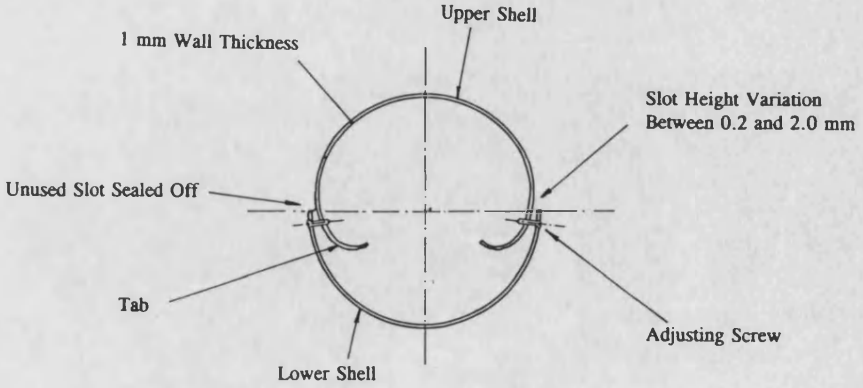

Typical Cross Section

Figure 3.22 *General Arrangement of Vacuum Formed Nose Cone Assembly*

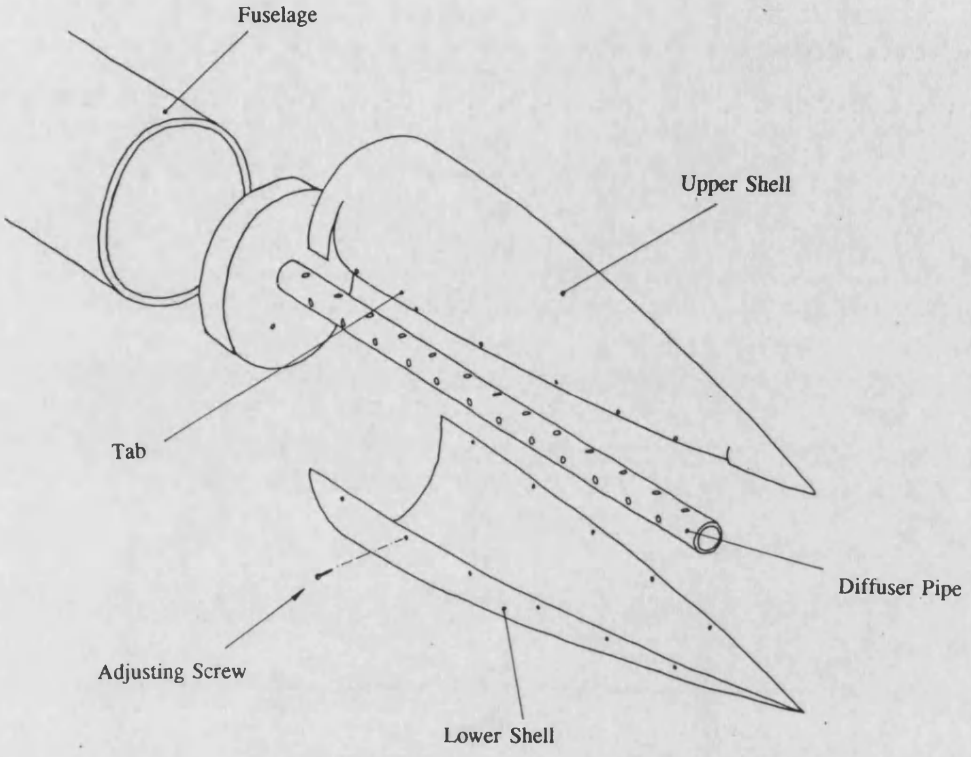

Figure 3.23 *Exploded View of Vacuum Formed Nose Cone*

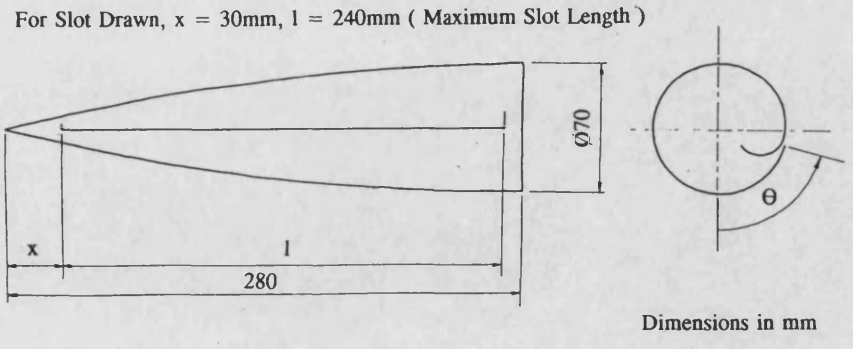

Figure 3.24 *Variables Describing Slot Geometry and Location*

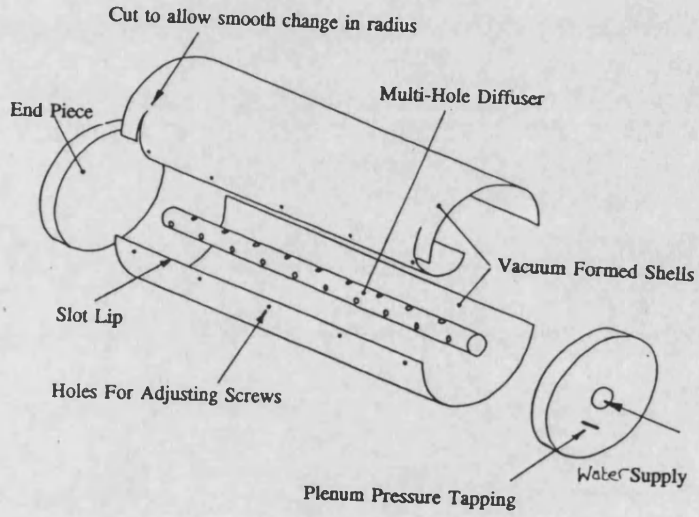

Figure 3.25 *Exploded View of Vacuum Formed Slot Rig*

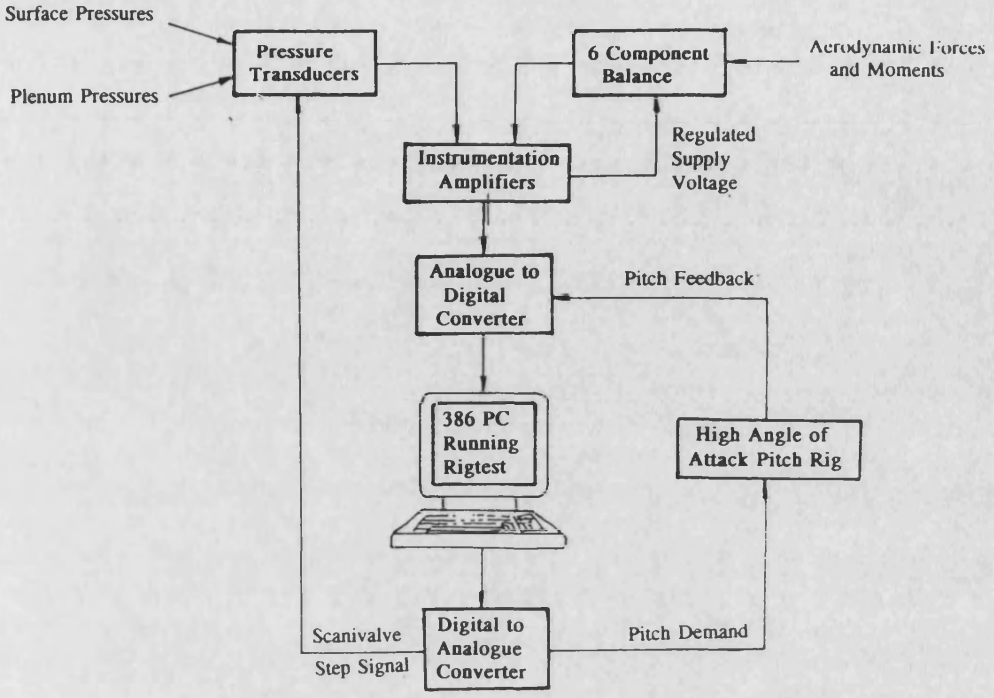

Figure 3.26 *Wind Tunnel Data Acquisition System*

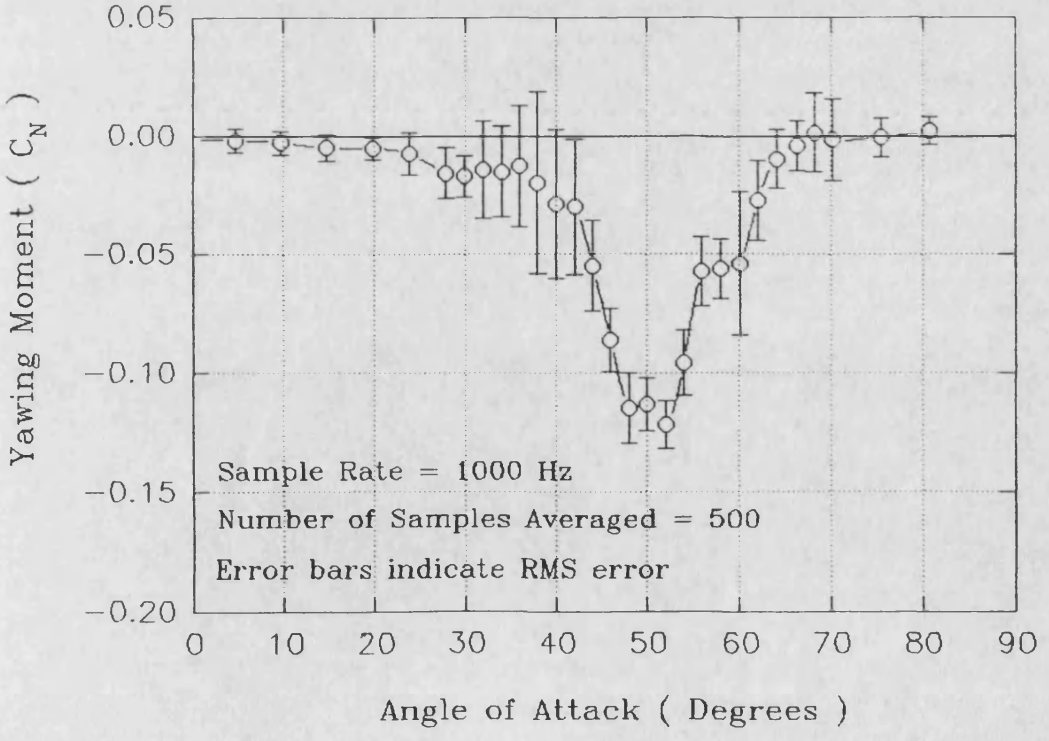

Figure 3.27 *Typical Unblown Yawing Moment Response Showing Unsteadiness in Data due Electrical Noise and Model Vibration*

CHAPTER 4

PRESENTATION AND DISCUSSION OF RESULTS

4.1 INTRODUCTION

In this chapter data is presented from tests on the curved wall jet rig and the generic combat aircraft wind tunnel model. The chapter begins by examining the three-dimensional fluid dynamics of curved wall jet flows. The basic flow topology is defined and the effects of slot aspect ratio, wall radius and jet Reynolds number are discussed. In Section 4.3 baseline, unblown force and moment data is presented for the wind tunnel model. This is followed by presentation of blown forces and moments in Section 4.4. Section 4.5 discusses the interaction between wall jet and forebody flowfields and suggests a mechanism for the control reversal which occurs at low blowing rates. The effects of slot geometry and location on blowing control performance are examined in Section 4.6. Finally, the chapter ends with a discussion of aerodynamic scaling and an example calculation of a typical air massflow required for application of slot blowing to a full-scale aircraft.

Unless otherwise stated, all wind tunnel force/moment data originate from the vacuum formed nose cone with both port and starboard full length slots located at 90° from the windward generator (x=30mm, ℓ=240mm, θ=90°). All pressure data was produced from the perspex nose cone. Since the force data and pressure data comes from two different models there is inevitably some discrepancy between the data sets. The general agreement is, however, good enough to illustrate the origin of forebody side forces.

4.2 WALL JET FLUID DYNAMICS

4.2.1 Three-Dimensional Characteristics

4.2.1.1 Fundamental Topology

As an initial example, consider results of experiments with an aspect ratio 360 jet (i.e. slot aspect ratio = 360) developing over a wall of radius 70 mm.

A section through the centre of the jet illuminated by a laser light sheet is shown in figure 4.1, accompanied by an explanatory sketch in figure 4.2. The jet is made visible by the entrainment of oil vapour smoke introduced near the slot exit, which, due to the very high turbulence levels, is rapidly distributed throughout the whole of the jet.

At the flow section considered, the jet separates from the surface approximately 120° from the slot exit. The separation is accompanied by an increase in spreading rate and unsteadiness of the jet. Note that to obtain quantitative measurements of the jet spreading rate, the rate of change of $y_{m/2}$ with distance from the jet exit is needed. This can only be determined from velocity profile measurements. It may be possible, however, to 'calibrate' smoke entrainment photographs against jets for which the velocity profiles are known, giving an empirical relationship between $y_{m/2}$ and the smoke-entrained width of the jet. This technique would probably be successful at higher jet speeds where the rate of mixing of the smoke due to natural diffusion is small compared to the turbulent mixing within the jet.

Looking at transverse sections through the jet, figure 4.3, it is evident that the flowfield is highly three-dimensional, and that the centreline case discussed above is a special case in which the flow is only quasi two-dimensional. The lack of two-dimensionality is caused by the edges of the jet sheet rolling up to form a pair of vortices which grow in strength and converge as the jet develops. The convergence of the vortices is associated with a narrowing of the region of jet flow attached to the surface. Maximum angular attachment of the jet is achieved at the jet centreline.

Referring back to figures 4.1 and 4.2, it is apparent that the observed increase in spreading rate and unsteadiness of the jet beyond the separation point is due to the

convergence of the jet edge shear layers with the jet centreline. This also accounts for the marked decrease in smoke intensity beyond the jet separation point since there is now a large increase in the lateral mixing of the jet due to the availability of spanwise fluid transport by the edge vortices.

Figure 4.4 shows water tank flow visualisation of the jet flow from the vacuum formed slot rig. In this experiment, dye (poster paint mixed with water) is introduced at the two ends of the slot and is subsequently rapidly entrained in to the edges of the jet. Although the jet flow is highly turbulent, a definite vortical structure is evident at jet edges. As the flow develops round the cylinder, the diameter of these jet edge vortices increases and they converge towards the centreline of the jet.

Combining the results from laser light sheet work on the variable geometry slot rig and water tank experiments with the vacuum formed slot rig, a highly three-dimensional picture of the wall jet flow emerges, figure 4.5. An additional feature shown in this figure is the presence of counter-rotating vortices embedded in the coherent jet sheet flow. These vortex pairs are usually associated with some form of disturbance upstream, such as a physical excrescence on the wall surface or, more often, a non-uniformity in the spanwise velocity distribution at the slot exit. This problem was mentioned in Chapter 3 in relation to the adjusting screws set in the vacuum formed slot, which if placed too close to the slot lip, cause a disturbance large enough to split the jet sheet. In this case the counter-rotating vortex pair downstream of the adjusting screw are essentially the roll-up vortices associated with the two free edges created by the splitting action of the disturbance.

The process of jet splitting results in a cellular type break-up of the jet sheet and may limit the amount of jet attachment possible for a given wall/slot geometry. For example, if the plenum conditions are poor and the slot exit badly designed, the resulting jet sheet is likely to rapidly break-up in to a number of cells. In this case the jet will probably separate from the surface a small distance downstream of the exit plane.

The problem of obtaining the maximum amount of jet attachment for a three-dimensional wall jet is fundamental to the design of an efficient slot installation on an aircraft forebody. This will be discussed further in Section 4.2.2 with relation to the effect of changing slot length and wall radius.

4.2.1.2 Surface Flow Patterns

Figure 4.6 shows a photograph of the surface oil flow pattern for the 360 aspect ratio jet developing over a 70 mm radius wall. An explanatory sketch is shown in figure 4.7. Note that the plastic sheet forming the wall of the slot rig has been released from the side rails and laid out flat for the photograph. This removes the distortion associated with perspective and makes analysis of the flow pattern easier.

The oil flow pattern is interpreted as follows: without any blowing, a mixture of titanium dioxide, oleic acid and paraffin provides a thin white covering over the wall surface, which has been sprayed black. When the blowing is turned on, oil is transported away from the regions where the surface shear stress is high, revealing the dark surface beneath. Lower levels of surface shear stress lead to partial transport of the oil and the surface becomes grey-coloured or streaked.

Two main regions may be identified in surface oil flow pattern made by the jet:

1) A main ogive-shaped central region produced by the strong shearing action of the attached jet flow, and

2) An outer region of streaklines produced by the secondary flow being entrained into the jet.

Considering the central attached jet flow region, a series of streaks perpendicular to the slot can seen, some of which start at the slot exit and end up at the ogive separation boundary. The orientation of the streaks perpendicular to the slot suggests that, to a first approximation, the velocity distribution along the slot exit is uniform.

However, the fact that streaks form, implies small-scale non-uniformities in the jet sheet, and it is believed that the streaks are in fact weak separation/attachment lines resulting from longitudinal vortices embedded in the flow, figure 4.8. It appears that vortices are formed where ever there is a discontinuity in the jet. The edges of the slot constitute a massive discontinuity and give rise to the well defined jet edge vortices. Smaller discontinuities, for example due non-uniformity in the total pressure distribution along the length of the slot, give rise to relatively weak embedded vortices.

Edge entrainment velocities for this slot/wall configuration are typically an order of magnitude less than the jet velocity and the surface oil flow pattern around the central attached flow region is quite hard to determine. The sketch in figure 4.7 illustrates the approximate orientation of the surface streak lines in the edge entrainment region. As the jet develops the attached flow region diminishes and the entrained flow region expands. Note that at the convergence of the ogive-shaped attached flow boundaries the surface streaklines in the entrained flow region are in a sense opposite to that of the main jet flow. This results in an abrupt separation of the jet from the wall.

4.2.2 Effect of Slot and Wall Geometry

4.2.2.1 Overview

When the wall jet rig was being designed, it was believed that the key parameters defining a three-dimensional wall jet flow were slot aspect ratio, ℓ/h, and wall radius r. Initial experiments, however, showed that the dominant parameter was ℓ/r. Unfortunately with the rig as it was designed, this parameter could not be varied independently, and thus its effect has to be deduced from tests where more than one parameter is varying at one time. None the less, the experiments reported below give some important insights in to the behaviour of wall jets under different geometric conditions and provide guidelines for designing efficient slot installations.

4.2.2.2 Effect of Slot Aspect Ratio

Figure 4.9 shows surface flow visualisation results for jets of differing aspect ratio developing over a wall of 70 mm radius. The scale at the bottom of the page corresponds to the distance round the surface from the slot exit, s, non-dimensionalised by the wall radius, giving an angular displacement. In each of the tests the slot area and the volume flow through the slot are the same, which leads to constant jet momentum.

From these photographs, a number of trends in flow pattern for decreasing slot aspect ratio emerge:

1) The ogive shape of the attached jet flow region is basically unchanged,
2) The area of the attached flow region decreases,
3) The maximum angular attachment of the jet decreases,
4) The area of the entrained flow region increases in relation to the attached flow region, and
5) Streaklines in the attached flow region become less apparent.

It is quite hard to draw definite conclusions from these observations since for a fixed slot area, decreasing slot aspect ratio with a constant wall radius causes ℓ/r to decrease and h/r to increase. However, if a metric for defining wall jet efficiency is based on the maximum angular attachment attained, then it is clear that long slots are more efficient than shorter ones. Bearing in mind that the effect of slot length is normally ignored when designing slot installations, this conclusion is less trivial than it might first appear. In particular, the full scale tests of slot blowing on an F/A-18[89], used a slot that was divided up into a number of small segments so that they could be individually controlled. This in effect meant that rather than producing a continuous jet sheet, similar to figure 4.9a, a number of smaller side by side jets were produced, similar to figure 4.9d. This may have seriously reduced the efficiency of the control device.

Point 5 mentioned above is probably an effect of the size of the non-uniformities at the jet exit compared to the slot height, i.e. δ/h, where δ is a suitable length scale of the non-uniformities. Increasing the slot aspect ratio for a fixed slot area reduces h and also makes it harder to achieve uniform flow at the slot exit, due to the increased impact of manufacturing tolerances and the increased difficulty of providing uniform plenum conditions. This means that δ/h is likely to increase as the slot aspect ratio increases. Subsequently the jet sheet from a high aspect ratio slot is more likely to suffer from spanwise instabilities and separate due to a cellular type breakup. Thus for a given slot area the optimum length slot will be arrived at by trade-off between spanwise instability effects and benefits of increased angular attachment.

4.2.2.3 Effect of Wall Radius

Figure 4.10 shows surface oil flow patterns for an aspect ratio 360 jet developing over walls of radius 35, 70, 140 and 280 mm. These tests show the effect of decreasing ℓ/r and decreasing h/r for a constant length slot. Note that the change in wall radius between tests means that the horizontal scale is different in each photograph. By measuring off the region of attached flow as a function of distance from the slot exit, s, the data may be 're-plotted' to the same angular scale, figure 4.11. Comparison of figures 4.10 and 4.11 show that although a jet of low ℓ/r may achieve an extended attachment in terms of s/ℓ, a high degree of angular attachment, which is more important for separation control applications, is achieved with a large ℓ/r.

The surface oil flow patterns for an aspect ratio 22.5 jet developing over walls of different curvature is shown in figure 4.12. Note that the wall in figure 4.12c is of infinite curvature, i.e. a flat plate, and that in figure 4.12d the wall has negative radius, i.e. concave curvature.

As the wall curvature decreases the distinction between the attached flow and entrained flow regions becomes less defined, and in the flat plate case the jet essentially becomes homogenous. It appears that for walls of high curvature the roll-up of the edges of the jet is rapid, giving rise to clearly defined separation lines

and intense edge vortices. As the wall curvature decreases, the tendency for roll-up of the edges of the jet decreases and the associated separation is weak. In the case of the flat plate, no roll-up of the jet edge occurs and the jet spreads in a manner similar to that of a free air jet.

The concave curvature result, figure 4.12d, shows some features not seen in the convex curvature results. The most obvious difference is the presence of wave crest structures at the downstream end of the jet. These crests arise as result of the action of gravity forces on the oil displaced by the jet. With convex curvature, gravity forces on the oil act in the same sense as the surface shear stress produced by the jet, and are not apparent in the flow visualisation results. However, for convex curvature, gravity forces oppose the jet shear stress and an equilibrium condition can arise in which there is no net force acting on a particle of oil, despite the local surface shear being finite. In this case, oil tends to build up to form the crests seen in figure 4.12d. In hindsight, this problem could have been avoided simply by turning the slot rig up side down to do the convex curvature experiments.

A further difference lies in the feathering of the edges of the main attached flow region of the convex jet. It is possible that this is the result of Taylor-Görtler vortices which form in flows with convex curvature, e.g. the underside of a highly cambered aerofoil. However it is more likely that it is due to the massive spanwise spreading of the jet. This increase in the spanwise spreading rate is caused by the increase in static pressure in the centre of the jet, compared to the static pressure in the surroundings, due to the convex curvature. Increasing convex curvature leads to increases in positive pressure within the jet and further increases in the spanwise spreading rate of the jet.

4.2.3 Summary of Slot Aspect Ratio and Wall Radius Effects

Figure 4.13 shows all the surface flow visualisation results from the variable geometry slot rig on a single page. The results are laid out in a matrix arrangement with changing aspect ratio in the horizontal direction and changing wall radius in the

vertical direction. The top left hand corner is a low aspect ratio jet on a surface of large positive curvature (small wall radius), whereas the bottom right hand corner is a high aspect ratio jet on a surface of zero curvature. The two pictures in the very bottom row are results for negative surface curvature. It is worth recalling that the area of the jet is the same in each case.

As a general observation it may be noted that the results are continuous, i.e. that the jet behaviour changes in a gradual way between quite different slot and wall geometries. In particular the change from positive to negative wall curvature does not radically alter the behaviour of the jet. As far as the author is aware, there have been no published numerical studies of the behaviour of quiescent, three-dimensional wall jets. Since the results are continuous, a single model for all the different configurations should suffice. However, it would be interesting to see what level of modelling is required to predict the behaviour of jets over a large range of slot/wall geometries and to capture the wealth of flow detail shown in figure 4.13.

4.2.3 Effect of Jet Reynolds Number

Figure 4.14 shows laser light sheet through the centre of an aspect ratio 360 jet developing over a wall of radius 70 mm for three different jet Reynolds number regimes.

In figure 4.14a the jet velocity is of the order of 1 m/s corresponding to a jet Reynolds number (Re_j) of 1×10^6. Under these conditions, the jet separates from the surface at approximately 80° from the jet exit, and is essentially laminar up to this point. Increasing Re_j by an order of magnitude, figure 4.14b, moves the turbulence transition point to with in a few tens of slot heights of the jet exit, and extends the attachment of the jet up to about 120°. An increase of the jet velocity to approximately 100 m/s, figure 4.14c, causes transition to occur almost immediately downstream of the slot and the region of attached jet flow is extended to approximately 180°.

Further increases in the jet Reynolds number beyond approximately 1×10^8 do not

appear to alter the profile of the jet or extend the amount of attached flow. The value of this critical Re_j for a two-dimensional jet is given in ref 16 is $4x10^4$. At present it is not clear whether the discrepancy arises from a weakness in the jet Reynolds number definition (equation 1.3) or the presence of three-dimensional effects.

In terms of practical blowing slot installations on aircraft forebodies, the jet Reynolds numbers associated with typical levels of blowing are of the order of $1x10^{10}$ and thus it is likely that jet Reynolds number effects will not be significant at full-scale. However during the sub-scale wind tunnel tests in the present investigation, high jet momentum coefficients were achieved at a relatively low jet velocity of 50 m/s and it is likely that jet Reynolds number effects are significant. Note however that control reversal at low blowing rates (Section 4.4.5), i.e. low jet Reynolds numbers, has been observed during full scale tests and thus is probably not a jet Reynolds number effect.

4.3 GENERIC COMBAT AIRCRAFT: UNBLOWN RESULTS

4.3.1 Longitudinal Forces and Moments

Attention will now be focused on the results from wind tunnel tests on the generic combat aircraft model.

The normal force acting on the wind tunnel model over an angle of attack range from 0 to 90° is shown in figure 4.15. Note that the bevelled leading edge of the wing gives an effective camber of approximately -0.5% and an expected zero lift incidence of approximately +0.25°. This is too small to show up in the normal force characteristic. From 0 to about 20° alpha the normal force increases approximately linearly with angle of attack giving an initial lift curve slope of 2.9. In this region, the LEX and wing leading edge vortices are highly stable and breakdown does not occur until some way downstream of the model. As the angle of attack increases beyond about 20° the normal force curve begins to flatten out, corresponding to breakdown of the leading edge or LEX vortices moving upstream of the wing trailing edge. From flow

visualisation studies it was observed that by about 25° angle of attack the burst point of the wing leading edge vortices had reached the wing crank, however the vortices emanating from the more highly swept LEXs remained coherent up to an alpha of approximately 45°. The angle of attack at which the LEX vortex burst reaches the apex of the LEX marks the stall point of the wing. Above this angle of attack the flow in the lee of the wing is generally unsteady and no coherent vortical structures are present. Referring to figure 4.13, it can be seen that there is a small increase in normal force between α = 45° and 90°. This is largely due to an increase in the lower surface pressure as a result of the wing being more nearly aligned perpendicular to the free-stream.

The solid lines in figure 4.15 show the normal force acting on the model resolved in the lift and drag senses. Note that for a more accurate measure of lift and drag, the normal and axial forces on the model must be resolved, however for angles of attack above about 5° the axial force is at least two orders of magnitude less than the normal force and may be ignored without affecting the overall form of the lift and drag curves.

The lift coefficient increases with angle of attack up to a maximum at alpha=35°. Beyond this angle of attack the lift coefficient steadily decreases, however the classic sharp drop-off in lift encountered when an unswept wing stalls is not experienced and useful lift coefficients are generated up to much higher angles of attack. Beyond 45° alpha the drag force becomes larger than the lift force and may be used to advantage in manoeuvres requiring a high degree of braking in the flight path direction.

The pitching moment curve for the wind tunnel model is shown in figure 4.16. Note that the pitching moment shown is that about the balance centre. The very small amount of wing camber means that the pitching moment at zero lift (α=0°) is very close to zero. As the angle of attack increases, the pitching moment becomes increasingly negative (i.e. nose-down). This is because the line of action of the normal force is aft of the balance centre. At, for example, 40° angle of attack, C_z=1.5 and C_M=-0.23. This gives

$$\frac{x_{CP}}{c} = \frac{C_M}{C_Z} = -0.15 \qquad (4.1)$$

i.e. the longitudinal centre of pressure lies approximately 0.05 m behind the balance centre.

4.3.2 Lateral Forces and Moments

Side force, yawing moment and rolling moment data for the model is shown in figure 4.17. The side force and yawing moment results can be correlated with the three types of forebody vortex configuration shown in figure 1.12. For angles of attack up to 25° the vortices are steady and symmetric resulting in zero lateral forces and moments. Between 25° and 65° a steady asymmetric vortex pattern appears leading to the generation of large out-of-plane forces. At an angle of attack of 48° the yawing moment reverses sign, consistent with the forebody vortex pair switching to a mirror image configuration. Beyond 65° angle of attack the flow is dominated by periodic vortex shedding and the time-averaged side force and yawing moment tend towards zero.

Flow visualisation of asymmetric forebody vortex arrangement on the wind tunnel model at 40° angle of attack is shown in figure 4.18. The image was captured on video from laser light sheet/smoke experiments and a photograph taken of a still on the video monitor. The image is shown as a negative such that the black background is white and the lighter coloured smoke is black. Although the image lacks detail, the asymmetric arrangement of the forebody vortex cores and asymmetry in the crossflow separation lines can be inferred. In particular, it may be noted that the port side forebody vortex is in a high position and the starboard vortex is in the low position. Also the starboard vortex is located further inboard compared to the port vortex. This vortex arrangement corresponds to forebody side force to starboard (positive) and hence a positive yawing moment.

Deflecting the rudder of the model $\pm 30^{\circ}$ produces a ΔC_N of ± 0.075 at zero angle of attack. This control power remains constant up to approximately 25° angle of attack, after which it begins to decrease. Beyond an angle of attack of about 40° the rudder power reduces to zero due to the shielding effect of the fuselage and wing. Note that above 35° angle of attack the destabilising yawing moments generated by the forebody flow asymmetry are larger than the restoring moment available from the rudder.

Tests with the fin on and off at zero rudder deflection over the whole angle of attack range showed that the fin made no steady state contribution to the zero sideslip side forces and moments. This implies that steady state asymmetries in the forebody flowfield do not produce steady state asymmetries in the flow at the rear of the model. However, the highly unsteady nature of the flow at the rear of the model meant that the fin experienced quite a high degree of buffeting which introduced significant unsteady yawing moments. For this reason all further tests were performed with the fin removed.

The rolling moment on the model is zero apart from between 20° and 35° alpha and for a very small region at 45°. Flow visualisation studies have shown that these regions mark the beginning and end of a larger region in which the forebody and LEX flowfields are coupled and that asymmetric forebody vortices lead to asymmetric bursting of the LEX vortices, figure 4.19. Resulting asymmetric pressure distributions on the wing upper surface lead to the observed rolling moments, which may be quite large compared to the rolling moment available from the ailerons. Note that asymmetries introduced into the forebody flowfield through the application of blowing will also produce asymmetries in the LEX vortex burst points. This can have an important effect on the aircraft response to blowing control inputs and will be discussed further in section 4.4.2.

4.3.3 Unblown Pressure Distributions

Figure 4.20 shows a pressure distribution round the forebody for the aft pressure tapping station at an angle of attack of 40°. Note that 40° angle of attack produces a maximum out-of-plane side force. Also shown on this graph is a theoretical potential flow pressure distribution for a cylinder skewed 40° to the free stream, given by equation 4.2 below[102].

$$C_p = \sin^2\alpha\,(1 - 4\cos^2\theta) \qquad (4.2)$$

Equation 4.2 does not strictly apply to conical noses. However the local forebody shape at the aft tapping station is closely approximated by a cylinder (figure 3.20) and the pressure distribution from equation 4.2 makes a useful comparison. Due to the rather coarse spacing of the pressure tappings it is quite hard to identify the angular location of the cross separation points. On the port side it appears that there is a small amount of pressure recovery after 90° followed by separation at around 110°. On the starboard side there is less evidence of any pressure recovery and the separation point would appear to be around 90°. After the pressure recovery peak on the port side there is a second peak at 135°. This is due to the suction induced under the port forebody vortex, which, at this angle of attack, is located close to the forebody. On the starboard side there is a very small peak at 255°. This presumably arises as a result of the much weaker starboard vortex, which is located in the high position, away from the forebody.

The pressure distribution given by equation 4.2 is based on inviscid, irrotational flow. In the real flow, viscous effects lead to boundary layer separation at around 90° from the windward generator, preventing full pressure recovery at the leeward generator. Note that, up to separation, especially on the port side, the agreement between the potential flow solution and the observed pressure distribution is quite good. The other feature, apart from the presence of separation, that distinguishes the real flow from the potential flow pressure distribution is asymmetry. The potential flow has exact

lateral symmetry. The real flow pressure distribution is clearly asymmetric with a large increase in suction on the port side relative to the starboard.

Figure 4.21 compares the experimental pressure distribution shown in figure 4.20 with a pressure distribution around a cone at 35° angle of attack, at a roll angle giving maximum side force and for fully laminar separation[54]. Ignoring the difference in magnitude at the windward attachment line, the similarity of the data is remarkably good, suggesting similar boundary layer conditions at separation and a similar degree of vortex asymmetry. Smoke flow visualisation on the present model suggest that the forebody crossflow boundary layers are indeed laminar at separation. This has important consequences for the side-force-with-incidence characteristic for the forebody and will be discussed further with relation to test Reynolds number in Section 4.7.2.

Pressure distributions at an angle of attack of 40° for all three tapping stations are shown in figure 4.22. For conical flow conditions these pressure distributions should be similar[103]. The flow is only approximately conical in the present tests because,

a) The forebody profile is an ogive, and not a straight-sided cone, and

b) The physical presence of slots part way along the forebody introduces a localised effect on the crossflow boundary layer.

Note that the forward tapping station cross section includes the blowing slots. The cross sections at the mid and aft stations are circular and continuous. This may explain why the pressure distribution at the forward station shows a marked difference to the distributions at the mid and aft stations.

Each of the three pressure distributions shows a greater suction on the port side relative to the starboard. This difference increases the further aft the tapping station, suggesting that the vortex asymmetry is increasing as the flowfield develops in a streamwise sense. This is a departure from what would be expected from a conical

flow analysis.

Pressure distributions around the perspex nose cone at a range of angles of attack are presented in figure 4.23. At 20°, the pressure distribution is laterally symmetric with very little evidence of crossflow separation. This corresponds to a very weak, symmetric forebody vortex pattern and zero side force. At 40° the pressure distribution shows evidence of separation and there is a large increase in suction on the port side. At 50° the suction peak moves to the starboard side and finally, at 80° the pressure distribution returns to being laterally symmetric, with the crossflow separation points located at approximately 75° from the windward generator. The absence of any peaks in the time averaged pressure distribution after separation at 80° angle of attack suggests that coherent vortical structures are no longer present and that there is unsteady vortex shedding in the lee of the forebody.

Smoke and laser light sheet flow visualisation shows that a suction peak on the port side of the forebody corresponds to a port side low, starboard side high vortex arrangement, and vice versa. At around 45° angle of attack the vortex asymmetry changes from port side low, starboard side high to port side high, starboard side low. This change over is, however, not instantaneous. Rather, as the angle of attack increases, the original asymmetric vortex arrangement becomes more and more unsteady, with the vortex pair occasionally jumping to its mirror image state, then back to its original state. As the angle of attack increases further the vortex pair tended to remain in the mirror image state for longer periods of time and eventually, at higher angles of attack, remained there permanently. The two or three degrees of angle range over which the handedness of the vortex asymmetry changed was marked by quite severe yaw oscillation of the model, presumably driven by the unsteadiness of the forebody flowfield.

Figure 4.24 shows the 40° and 50° pressure distributions plotted in polar form. At 40° the windward attachment line is rotated towards the starboard side, the peak suction is on the port side and side force is to port. At 50° the windward attachment line is rotated to port, the peak suction is on the starboard side and the side force is to

starboard. These results suggest that some form of forebody crossflow circulation may responsible for the generation of out-of-plane side forces at high angles of attack. This concept is currently speculative, and will be discussed further in Section 4.4.4.

4.4 GENERIC COMBAT AIRCRAFT MODEL: BLOWN RESULTS

4.4.1 Longitudinal Forces and Moments

At blowing levels consistent with forebody flow control (e.g. C_μ=0.08) changes in the model normal force are small compared to the changes in yawing moment and side force. However at higher blowing rates (e.g 0.015) some trends begin to emerge in the normal force characteristic, figure 4.25, and it is useful to correlate them with the behaviour of the model flowfield.

The first point to note is that changes in forebody normal force due to blowing are small (as evidenced by blown forebody pressure distributions, see figure 4.32) and not sufficient to account for the observed changes in normal force. This means that changes in normal force are due to changes in the wing/LEX flowfield introduced through coupling with the forebody flowfield (see sections 4.3.2 and 4.4.2). Comparing figure 4.25 with the rolling moment plot in figure 4.17, it can be seen that in the initial coupling region between α=20° and α=35°, the overall normal force is reduced. Thus the asymmetry produced in the LEX vortices by the forebody blowing leads to an average reduction in LEX vortex lift compared to the unblown case. Between an angle of attack of approximately 38° and 45° the normal force produced by the airframe is increased slightly due to blowing, i.e. the average LEX vortex lift is increased. However, the end of the forebody/LEX flowfield coupling region (α=45°) is marked by steep decrease in the blown normal force curve, due to the relatively abrupt decoupling of the flowfields at that angle of attack and an associated decrease in the LEX vortex lift. Above 60° angle of attack, blowing has little effect on the model normal force.

The blown pitching moment characteristic for the wind tunnel model is shown in

figure 4.26. Generally, there is little change from the unblown characteristic, apart from between $\alpha=30°$ and $\alpha=50°$. Blown pitching moments in this region can be attributed to changes in the wing normal force due to the flowfield coupling, recalling that changes in the forebody normal force due to blowing are small.

4.4.2 Lateral Forces and Moments

The effect of a fixed level of blowing on the lateral forces and moments acting on the wind tunnel model is shown in figure 4.27. Note that a relatively low blowing momentum coefficient of 0.008 produces a very large change in the yawing moment characteristic. This is fundamental to the success of tangential forebody blowing as a high angle of attack yaw control device.

An interesting feature of the data is the dip in the yawing moment response at 20° angle of attack. This reversal in the general trend of increasing yawing moment with angle of attack is initiated at the beginning of the region of forebody/LEX flowfield coupling and is accompanied by a rolling moment excursion. The side force characteristic in the coupling region does not show the same behaviour as the yawing moment. This suggests that the dip in the yawing moment response is associated with a large aft shift in the lateral centre of pressure caused by the interaction of the LEX vortices with the forebody flowfield.

Figure 4.28 shows flow visualisation of the starboard wing flowfield at an angle of attack of 30°. The smoke probe is located just below the wing at the apex of the LEX. This ensures smoke is convected directly in to the core of the LEX vortex. With no blowing, figure 4.28a, the starboard LEX vortex burst (evidenced by rapid spreading of the vortex core) occurs about half way along the length of the LEX. When blowing is applied to the port slot ($C_\mu=0.005$), figure 4.28b, the starboard LEX vortex burst point moves downstream, locating just aft of the wing crank. A further increase of blowing to $C_\mu=0.010$, figure 4.28c, moves the burst point even further aft and causes the track of the vortex to swing out towards the starboard wing tip. Flow visualisation of the port wing flowfield shows that as port side blowing is applied, the burst point

of the port LEX vortex moves forward, and at C_μ of 0.010, reaches the apex of the LEX. Blowing on the starboard side has the opposite effect on LEX vortex burst point movement.

Figure 4.29 shows flow visualisation of both port and starboard LEX vortices at 40° angle of attack and port side blowing. In this case the smoke probe is located on the fuselage centreline so that both LEX vortices are seeded. Unfortunately this means that it is not possible to get smoke into the core of the vortices, and it is quite hard to identify a clear burst position. Indeed, careful observation of the seeded vortices shows that the cores are completely clear, with the smoke remaining in the turns of the vortex just outside the core. Interpretation of figure 4.29 is also made difficult by the oblique view. However the asymmetry of the LEX vortices and their interaction with the burst wing leading edge vortices is apparent.

Figure 4.30 shows a sketch of the estimated lateral side force distribution along the model deduced from flow visualisation studies and forebody pressure distributions at around 25° angle of attack. Notice that the increase in suction on the blown side of the forebody is opposed by the increase in suction on the unblown side of the fuselage in the vicinity of the LEX. Thus the yawing moment due to blowing at angles of attack where forebody/wing flowfield coupling occurs may be of either sign, depending on the relative magnitudes of the lateral pressures on the forebody and fuselage. This provides a explanation for the yawing moment dip seen at around 25° angle of attack in figure 4.274. Note that the asymmetry in LEX suction due to asymmetric burst location also explains the observed blown rolling moments.

The relatively complex interaction between the forebody and LEX flowfields described above is likely to be very sensitive to aircraft geometry, in particular the location of the LEX relative to the fuselage and forebody. For example by placing the LEX higher up on the fuselage the side area available to generate forces from the differential pressure associated with a longitudinal asymmetry in the LEX vortex burst points will be reduced. In this way the non-linear yawing moment response to blowing shown in figure 4.274 may be alleviated. Similarly, it may be possible to arrange the

forebody/LEX geometry such that the blown roll coupling is removed, or enhanced in such a way that useful pro-turn rolling moments are produced.

Numerical/experimental studies on an F/A-18 configuration by Gee et al[104] have shown a blown response of the burst locations of the LEX vortices similar to that reported here, figure 4.31. However it appears that the F/A-18 configuration does not produce the yawing moment non-linearity associated with the longitudinal asymmetry of the LEX vortex burst positions. This is probably due to the higher relative position of the LEX/wing on the F-18 and the increased amount of wing/fuselage blending.

4.4.3 Blown Pressure Distributions

Forebody pressure distributions at 40° angle of attack for a range of blowing levels are presented in figure 4.32. Blowing is from the starboard slot, located 90° from the windward generator. The unblown case (open squares) is the same as that discussed in Section 4.2.3.

The pressure distributions at the aft station will be considered first. With no blowing, there is a large suction peak on the port (unblown) side. As blowing is applied, the suction on the port side diminishes while the suction on the starboard (blown) side increases. At a blowing momentum of 0.0035 (open circles) the pressure distribution is a mirror image of the unblown distribution, implying a complete reversal of the original unblown vortex asymmetry.

The blown pressure response at the mid station is very similar to that at the aft station. At the forward station, however, the jet has a large impact on the pressure distribution on the blown side of the forebody. For blowing rates up to 0.0020 (filled circles), increasing blowing produces an enhanced suction ahead of the jet exit followed by a decrease in the suction downstream of the jet exit. The latter observation is counter to what would be expected from consideration of pressure distribution beneath a two-dimensional curved wall jet under quiescent conditions, (see figure 1.9). The reason for this is not clear. It may be that the pressure tappings are

located downstream of a disturbance in the jet (indeed, the tappings themselves may be causing the disturbance) and the resulting split in the jet sheet causes a departure from the pressure distribution expected from two-dimensional conditions. Alternatively, the decrease in suction downstream of the jet exit may be due to intense streamline curvature (of opposite sign to the local surface curvature) in the entrained flow in this region.

The pressure distributions on the unblown side of the forebody at the forward tapping station show a well-behaved trend of decreasing peak suction with increasing blowing. Note, however, that the change in magnitude of the suction peak due to blowing at this station is much smaller than the change at the mid and aft stations.

Comparing the forward and aft station blown pressure distributions it is clear that the local side force due to blowing is greater at the aft station than it is at the forward station. Thus the largest side forces are not being produced at the point of application of the blowing, but some distance downstream of the slot. This has relevance to choice of slot location for optimum efficiency and will be discussed further in Section 4.6.2.

4.4.4 Model for Side Force Generation on Slender Bodies at Incidence

The generation of lift due to circulation around a wing is a well established concept, figure 4.33a. However the application of the circulation concept to the generation of side forces on slender bodies at incidence, figure 4.33b, is currently speculative. An argument sometimes used against the circulation concept for slender bodies is based on the application of Kelvin's theorem to a closed contour which is convected from upstream to surround the configuration[55]. In the free stream ahead of the body, the circulation round a closed contour is zero. When this contour is convected downstream to surround a given crossflow plane of the body, the circulation around the contour remains constant. This means that the overall crossflow circulation about the configuration must be zero. However this does not mean that the circulation about the body has to be zero.

A slender body at incidence may be compared to a swept forward wing that has been rotated through 90° such that it is vertical. Figure 4.34 shows the conventional bound and trailing vortex system associated with such a wing applied to a slender body. The circulation about any closed contour convected from upstream that surrounds the whole configuration, including the trailing vortex system, is zero. However, it is possible to choose a new contour around the body about which the circulation is non-zero. This is the basis of the concept of circulation about an aerofoil.

An aerofoil produces circulation through the restriction imposed on the flow by the Kutta condition at a sharp trailing edge. It is proposed that crossflow circulation about a slender body at incidence is produced by a steady asymmetric vortex arrangement.

The application of tangential slot blowing to a slender body also introduces circulation, but this time by direct momentum injection. By making a number of simplifications, it is possible to estimate the circulation induced by a given jet momentum. From this, the side force on the body can be calculated using the Kutta-Joukowski theory for lifting bodies. An example calculation of the estimated blown side force and yawing moment acting on the wind tunnel model is given in Appendix A. Calculation of circulation induced about the body cross section by the jet is greatly simplified by assuming that the jet velocity is equal to the slot exit velocity at all points, and that the jet separates 90° round from the slot. These assumptions allow the jet circulation to be calculated in terms of a spinning cylinder analogy. Assuming that the jet remains attached for one quarter of the circumferential distance round the forebody means that the equivalent spinning cylinder has a surface tangential velocity equal to one quarter of the jet exit velocity.

Through the principle of conservation of vorticity, any changes in circulation about a body must be accompanied by the shedding of a vortex of appropriate sign and magnitude into the surroundings. This gives rise to the familiar 'starting' and 'stopping' vortices in the wake behind a wing when the lift increases or decreases. Similarly, when the jet induced circulation about a cylinder changes due to a change in the jet blowing rate, an appropriate vortex must be shed into the wake. This is

illustrated in water tank flow visualisation of the jet from the vacuum formed slot rig, figure 4.35. Figure 4.35a shows the jet under steady conditions with a jet exit velocity of 1 m/s. Figure 4.35b shows the jet approximately 0.1 s after the jet exit velocity has been increased to 2 m/s. Since the jet velocity has increased and the separation location remained approximately steady at 90° from the slot exit, the circulation about the slot rig must have increased. This clockwise (as viewed in figure 4.35) circulation increase is accompanied by the shedding of volume of fluid with anticlockwise circulation, figure 4.35c, which breaks away from the jet and exists as a vortex in the surroundings. This is equivalent to the 'starting' vortex from a wing, shed, for example, after a step increase in angle of attack.

A plot of the estimated yawing moment acting on the wind tunnel model due to jet-induced crossflow circulation combined with the free stream crossflow for a C_μ of 0.01 is shown in figure 4.36. Also shown is the equivalent experimental result. Note that for the experimental case a slot angular position of 130° from the windward generator has been chosen. This slot position is most efficient in the respect that it gives the largest control gain (though not necessarily the best control response, see section 4.6.1). The continuous line through the experimental data between 20° and 50° angle of attack represents the expected yawing moment response for no coupling between forebody and wing/LEX flowfields.

Considering the simplistic way in which the yawing moment due to jet-induced circulation is calculated, the fit with the experimental data is reasonable. At zero angle of attack, the free stream crossflow component is zero so the calculated yawing moment due to the jet circulation is zero. The experimental yawing moment is, however, finite. This is due to the relatively small surface suction beneath the jet on the blown side of the forebody which is ignored in the jet circulation model.

A key aspect of the jet circulation model is that the yawing moment available from a given amount of blowing increases with increasing free stream crossflow component. i.e. the yawing moment depends on $\sin\alpha$. This $\sin\alpha$ dependence is reflected quite well in the experimental data at angles of attack above 20°.

4.4.5 Yawing Moment Response to Varying Blowing Levels

Figure 4.37 shows the response to varying blowing momentum at fixed angles of attack. Generally, port side blowing produces a nose-to-port (negative) yawing moment and starboard side blowing produces a nose-to-starboard (positive) yawing moment. However, at low blowing rates, a control reversal appears that increases in magnitude as the angle of attack increases up to 70°, then disappears. This type of control reversal has been reported by a number of researchers[105] for various different model geometries, slot locations and free stream Reynolds numbers, and would appear to be a fundamental characteristic of this type of control device. Figure 4.38 shows a typical control reversal experienced on an F/A-18 model the same size as the model used for the present work, but tested at twice the Reynolds number (cross-plotted from data from Ng et al[106]).

A conceptual model of the observed yaw control response is shown in figure 4.39. Figure 4.39a indicates the expected yawing moment due to the forebody crossflow circulation induced by the jet momentum. Figure 4.39b indicates the reversal which is superimposed on the jet circulation contribution. The control gain, i.e. the slope of the jet circulation yawing moment curve, increases with increasing angle of attack. This is consistent with the increasing forebody crossflow component with increasing angle of attack. The control reversal contribution also becomes larger with angle of attack, but does not occur in the periodic vortex shedding angle of attack range, suggesting that it is related to forebody vortex strength.

Figure 4.40 shows pressure distributions around the forebody during a blown control response with an initial reversal. With no blowing (open circles) there is a larger suction on the port side relative to the starboard side. When a small blowing rate of 0.0003 is applied to the starboard side (filled circles) the suction peak on the port side increases further and the port side suction actually decreases. This results in a net side force acting towards the unblown side. When the blowing momentum is increased to 0.0008 (open triangles) the pressure distribution finally changes in the desired sense and a net side force towards the blown side is generated. Further increases in blowing

momentum beyond 0.0008 continue to increase the suction on the blown side and decrease the suction on the unblown side. At a blowing momentum of 0.0025 (open squares) both the blown and unblown side cross flow separation lines are relocated approximately 15° round (in a pilot's view anticlockwise sense) from their unblown locations.

Wind tunnel tests alone do not suggest a fluid mechanism for the blown control reversal and at this point it is useful to refer to the wall jet fluid dynamics work.

4.5 WALL JET/FOREBODY FLOWFIELD INTERACTION

4.5.1 Flowfield Topology

In Section 4.2.1 the topology of a wall jet in quiescent conditions was discussed. In this Section a mechanism is proposed for the interaction between a wall jet and a forebody flowfield.

Wall jet and forebody crossflow boundary layer velocity profiles for two-dimensional flow are shown schematically in figure 4.41, ref 107. Note that the vorticity associated with the crossflow boundary layer is of opposite sign to the vorticity associated with the majority of the jet. Thus at low blowing rates, figure 4.41a, we should expect the vortex associated with the separation of the crossflow boundary layer to be weakened. At high blowing rates, figure 4.41b, we should expect a vortex of opposite sign to the original crossflow separation vortex. These predictions are based on a simple linear superposition of velocity profiles and do not take into account any movement of the separation point due to blowing, or three-dimensional effects.

At angles of attack less than 90° the forebody crossflow is not aligned with the direction of the jet and the jet flowfield becomes skewed in a downstream sense. This is shown by surface oil flows on the forebody of the model, figure 4.42. In this figure, the separation line associated with the vortex at the upwind edge of the jet is

clearly marked. Surface flow behaviour at the downwind end of the slot is unfortunately masked by the presence of the tape used to seel the nose cone to the fuselage. Surface flow visualisation by Celik et al[90], figure 4.43, shows the separation lines associated with the jet edge vortices at both the upwind and downwind ends of the slots. It is interesting to note that in this case the primary separation line on the forebody ahead of the slot is significantly curved. It appears that this is due to it being constrained to join up with the upwind end of the slot.

Three-dimensional behaviour of the jet is illustrated by water tank studies of slot blowing on an F/A-18 forebody by Ng[88], figure 4.44. These researchers make observations on possible flowfield interactions, but generally, the important three-dimensional nature of the wall jet flows are ignored.

A proposed schematic of the interaction between a wall jet and forebody flowfield based on work performed in the present research programme is shown in figure 4.45. A key feature of the flowfield interaction is that the jet edge vortex at the upwind end of the slot, hereafter called the upwind slot vortex, figure 4.45a, rotates in the same sense as the unblown side forebody vortex but in the opposite sense to the blown side forebody vortex, figure 4.45b. At a sufficiently high blowing rate, the blown side forebody vortex is suppressed and the upwind slot vortex combines with the unblown side forebody vortex, figure 4.45c.

The new vortex created by the combination of the upwind slot vortex and the unblown side forebody vortex has been observed during smoke flow visualisation experiments with the wind tunnel model. Figure 4.46 shows a video still of the view from the rear of the model with port side blowing. Smoke is introduced at the underside of the nose apex. Although the resolution of the image is relatively poor, the general form of the flowfield in the vicinity of the nose cone may be discerned. In particular, it is apparent that the vortex pair arrangement associated with the unblown case is replaced by single vortex. This vortex was observed to originate from the upwind end of the slot and contained vorticity of the opposite sign to the blown side forebody vortex. At 40° angle of attack the vortex lifted away form the body just downwind of the

downstream end of the slot, and remained unburst until reaching the diffuser of the working section.

Figure 4.47 shows smoke/laser light sheet photographs from blown and unblown tests by Celik[90] on the same model shown in figure 4.43. The upwind slot/unblown side forebody vortex may be discerned in the blown case.

4.5.2 Mechanism for Control Reversal

A possible mechanism for the yaw control reversal experienced by forebody slot blowing schemes is shown in figure 4.48. At low blowing rates, figure 4.48a, the interaction of the jet with forebody flowfield induces an asymmetric vortex arrangement in which the blown side vortex is in the high position and the unblown side vortex is in the low position. This leads to an increase in suction in the unblown side attached flow region, and thus a side force towards the unblown side. The displacement of the blown side forebody vortex away from the body at low blowing rates has been observed during smoke/laser light sheet experiments. However it is not clear exactly why this happens. It is believed that at low blowing rates, the crossflow velocity profile induced by the jet (see figure 4.41) is such that the blown side forebody vortex is weakened and displaced away from the body. To maintain equilibrium of the leeside forebody flowfield, the unblown side forebody vortex strengthens and moves closer to the body, producing the observed asymmetric vortex arrangement. Note that in the unblown case, it is generally recognised that in an asymmetric vortex arrangement, the vortex in the high position is usually strengthened compared to the vortex in the low position. This is the other way round to the situation proposed for the vortex asymmetry at the low blowing condition.

At high blowing rates, figure 4.48b, the situation is more straight forward. Here, the blown side forebody vortex is completely suppressed by the vorticity in the jet and the upwind slot vortex combines with the unblown side forebody vortex. This produces a large increase in suction in the blown side attached flow region, consistent with a

large increase in circulation round the forebody, and a side force towards the blown side.

Thus, as blowing is applied, the forebody side force first acts towards the unblown side. Then, as the blowing level exceeds a given threshold, the side force switches to acting towards the blown side.

The above explanation of control reversal is relatively basic and ignores the effects of slot angular and longitudinal location. The way in which the yaw control response is affected by these parameters will be explored in the next section.

4.6 EFFECTS OF SLOT GEOMETRY AND LOCATION

4.6.1 Slot angular Position

Figure 4.49 shows the effect of slot angular position on the blown yawing response at 30, 50 and 70° angle of attack. The starboard blowing data was produced using a vacuum formed nose cone with a single, full length slot (x=30 mm, ℓ=240 mm), on the starboard side. Similarly the port blowing data was produced using a nose cone with a single slot on the port side. Different slot angular positions were achieved by rotating each of the nose cone assemblies relative to the fuselage. The data shown in figure 4.49 is complex since there are three effects at work. These are the effects of:

1) the physical disturbance created by the slot lip on the baseline flow asymmetry,
2) baseline asymmetry on the interaction between the wall jet and forebody flowfield, and
3) The angular location of the slot exit.

At 30° angle of attack the forebody vortices are weak and the physical asymmetry presented by the slot does not give rise to asymmetric baseline yawing moments. At 50° the forebody vortices are strong and tend to form stable asymmetric arrangements.

With the starboard slot at 30 or 50° from the windward generator, the baseline yawing moment is -0.1, implying a high vortex on the slot side of the forebody and a low vortex on the smooth side. With the slot at 70, 90 or 110° the baseline yawing moment is +0.1, implying a reversal of the vortex arrangement. At a slot angle of 130° (not shown in the figure) the vortex asymmetry reverses once again, going back to the original arrangement. Note that the baseline asymmetric yawing moments for the port slot are a mirror image of the corresponding starboard slot values. At an angle of attack of 70° the baseline yawing moments for different slot angles are essentially zero, consistent with periodic vortex shedding.

The effect of baseline flow conditions on the blown control response is summarised in figure 4.50. Where there is no steady vortex asymmetry present in the baseline flow, figures 4.50a and 4.50c, the yawing moment response with increasing blowing is relatively linear. When the baseline flow forms stable asymmetric vortex arrangements, figure 4.50b, the control response at low blowing rates may be highly non-linear. The shaded area in this figure represents an envelope within which the control response is likely to lie. The exact path the control response follows in this area is highly dependent on both the initial flow asymmetry and the slot position. At high blowing rates the effects of initial flowfield asymmetry are dominated by the jet flowfield effects and the control yawing moment becomes simply related to blowing level.

Figure 4.51 shows a simplified representation of the control response data for various slot angles at 50° angle of attack. For the slot at 30° from the windward generator the control response is relatively linear but the overall control gain is quite low. With the slot at 50° the gain increases but a small reversal develops at low blowing rates. With the slot at an angle of 70°, or greater, the sign of the baseline asymmetry reverses making direct comparison with the previous slot angles difficult. It would appear, however, that as the slot is located further round the forebody in the crossflow sense that both the control gain and the magnitude of the reversal increase. Note that the port and starboard slot models show similar responses.

A simplified sketch of the control response data at 70° angle of attack is shown in figure 4.52. With the slot at 30° the control response is linear with low gain. Increasing the slot angle up to 90° increases the control gain, but unlike the 50° angle of attack data, no control reversal develops. At a slot angle of 110° the slot exit is located leeward of the crossflow separation line and a phenomenon referred to as slot stall occurs, figure 4.53. At low blowing rate, figure 4.53a, the jet has a small local influence on the separated unsteady flow in the lee of the forebody. This results in little change in the overall crossflow circulation and the net side force/yawing moment produced is small. At a higher blowing level, figure 4.43b, the increased jet entrainment leads to a small area of favourable pressure gradient in the vicinity of the slot. This, however, does not extend far enough upstream to influence the crossflow separation line and the resultant crossflow circulation increment remains small. At a sufficiently high blowing level, figure 4.43c, the favourable pressure region created by the jet extends far enough upstream to capture the blown side separation line. The blown side crossflow now experiences a favourable pressure gradient over a large extent of the leeside of the forebody and there is subsequently a large leeward shift in the separation line. This leads to a large step change in the crossflow circulation and corresponding step increase in the control yawing moment. With the blowing slot located at 130° from the windward generator, the increased distance of the crossflow separation line ahead of the slot exit requires a very high jet momentum before the blown side separation can be influenced. In the current tests a blowing momentum of 0.014 was insufficient to "un-stall" the slot at this location.

Figure 4.54 shows the yawing moment produced from a fixed blowing level over an angle attack range of 0 to 90°, for different slot angles. This figure clearly demonstrates the increasing control power available as the slot angular location is moved increasingly leeward. If the slot is located too far leewards, however, the slot stall phenomenon is encountered. In this case, the favourable pressure gradient created by the jet is constant, but the adverse pressure gradient in the lee of the forebody is increasing with angle of attack. At a given angle of attack the jet is unable to maintain its influence over the blown side cross flow separation and the separation line rapidly returns to its unblown location. This results in a very large step decrease in the

control yawing moment. As the slot angle is increased the angle of attack at which slot stall occurs decreases. Similarly, the lower the fixed level of blowing, the earlier slot stall is encountered.

The data in figure 4.54 suggests that slot stall does not occur for angles of attack less than 60°, whatever the slot angle. This means that the slot stall only occurs in the periodic vortex shedding angle of attack regime (60° to 90°). At angles of attack below 60° some form of steady vortex equilibrium is established in the lee of the forebody. Thus where ever the slot is located, the jet will always be able to disturb the equilibrium condition to some extent and the almost complete lack of control response associated with slot stall does not occur.

Slot stall is usually accompanied with some form of hysteresis with blowing level or angle of attack, depending on how the stall is initiated. Figure 4.55 shows a typical hysteresis loop for the angle of attack initiated slot stall. Here the hysteresis is spread over 20° angle of attack. This figure also illustrates the region of forebody/LEX flowfield coupling between 20 and 45° angle of attack. The continuous line in this region is the expected yawing moment characteristic for an increasing crossflow component with increasing angle of attack.

The phenomenon of slot stall and control hysteresis has previously been observed on tests with delta wing leading edge blowing at the University of Bath[26]. In this study it was shown that crossflow boundary layer trips ahead of the slot could increase the angle of attack at which slot stall occurred. This suggests, as might be expected, that a turbulent crossflow boundary layer is better able to remain attached than the equivalent laminar boundary layer.

For full-scale application of TFB the forebody crossflow boundary layer will either be laminar or turbulent depending on the local diameter of the forebody and the angle of attack. In this sense it is not clear by how much the problem of slot stall would be reduced at larger scale.

4.6.2 Effect of Slot Longitudinal Position

Figure 4.56 shows the effect of slot longitudinal position on the blown control response. For these tests the nose cone with a single starboard slot was used. The slot was 120 mm long and located at 90° from the windward generator. From this data a number of useful deductions can be made:

1) For efficiency at low angles of attack the slot must be located as far forward on the forebody as possible.
2) At high angles of attack slot longitudinal position does not effect the control efficiency.
3) At angles of attack exhibiting baseline asymmetry, control reversal at low blowing rates is minimised by moving the slot aftwards on the forebody.

Point 1 above has been noted by many previous researchers. For efficient control it is advantageous to perturb the vortices at the nose apex where they are least strong. Disturbances introduced here are then amplified as the flowfield develops down the length of the forebody.

At high angles of attack, moving the slot forward increases the moment arm of the control side force but at the same time decreases the effective area of action of any differential pressures produced. It would appear that these two effects cancel each other out, point 2.

4.6.3 Effect of Slot Length

Figure 4.57 illustrates the effect of slot length on the blown control response. Note that the slot height was constant in the tests so increasing the slot length also increased the slot area. This data indicates that:

1) At low angles of attack increasing slot length does not increase the slot

efficiency.

2) For efficient control at high angles of attack long slots are essential.

3) At angles of attack exhibiting baseline asymmetry, longer slots lead to a control reversal spread over a greater jet momentum range.

Point 1 suggests that at low angles of attack only the forward part of the slot is doing useful work. This is consistent with the observed effects of changing the slot longitudinal position at low angles of attack (section 4.6.2).

At angles of attack where periodic shedding occurs it is misleading to talk of vortex control; a more appropriate description is forebody flow control. At these angles of attack, long slots are essential for an efficient control. The reason for the increase in efficiency with slot length lies in the effect of slot length on the three-dimensional behaviour of curved wall jets (Section 4.2.2).

Point 3 above is probably an effect of changing the slot area, rather than changing the slot length. If C_Q is used to collapse the data instead of C_μ then correlation between the curves in the reversal region is much closer. This suggests that the control reversal mechanism is driven by the jet velocity ratio, rather than the square of the jet velocity ratio, though there is limited data to confirm this. Evaluation of scaling parameters for forebody slot blowing will be explored in more detail in Section 4.7.

4.7 SCALING PARAMETERS

4.7.1 Introduction

Aerodynamic scaling parameters are required such that the results from small scale, low speed wind tunnel tests can be used for the basis of the design of full scale aircraft. For a body inclined at a given angle to the free stream, the aerodynamic forces acting on the body linearly scale with the product of the free stream dynamic

pressure, q, and a suitable reference area related to the size of the body, S. An aerodynamic force coefficient is thus defined by non-dimensionalising the actual body force by qS. Similarly a moment coefficient is defined by non-dimensionalising the aerodynamic moment by qSl, where l is a suitable reference length on the body.

For a moving surface control such as a rudder, the control input is non-dimensionalised by simply defining an angular displacement. The control yawing moment coefficient, C_N, is then uniquely related to the control deflection.

With forebody blowing work the goal is to provide a non-dimensional jet parameter so that at any physical scale and free stream conditions, the change in yawing moment coefficient due to blowing is uniquely related to the jet parameter.

4.7.2 Free Stream Reynolds Number Effect, Unblown Data

Figure 4.58 shows yawing moment coefficient data measured at a range of free stream speeds corresponding to a Reynolds number range from 0.61×10^6 to 1.72×10^6 per metre. The correlation of this data is good indicating that the forebody flow is Reynolds number insensitive over the relatively limited range of free stream speeds tested. Smoke flow visualisation indicated that at angles of attack where forebody vortex asymmetry was present, the handedness of the asymmetry remained constant from a free stream speed of 30 m/s down to about 1 m/s. At lower speeds it appeared that the laminar crossflow boundary layer failed to transition after separation and existed as laminar free shear layer. The forebody vortex pair in this case was highly unsteady and continually shifted from one equilibrium position to another.

At full scale flight Reynolds numbers it is likely that crossflow separation will be laminar only for a small distance downstream from the nose apex. As the diameter of the body increases in the downstream sense the crossflow boundary layer will transition before separation and eventually become fully turbulent. The distance downstream of the nose at which transition takes place will be sensitive to both angle of sideslip and angle of attack. This adds additional degrees of freedom to the

forebody vortex equilibrium condition and significantly increases the complexity of the flowfield.

A very thorough experimental investigation of the effects of Reynolds number on a slender body at incidence has been performed by Lamont[108]. An important conclusion from this work is that maximum out of plane side forces occur either at low Reynolds numbers, when the flow is fully laminar (as in the case of the present investigation) or at high Reynolds numbers, when the flow is fully turbulent. At in between Reynolds numbers, corresponding to an equal mixture of laminar and turbulent flow, the out of plane side forces reach a relatively unstable minimum. The problems of testing at these intermediate Reynolds numbers is highlighted by a series of experiments performed with various scale Saab Gripen models[109]. In these tests force and moment data taken at a range of Reynolds numbers showed very poor correlation and was often unrepeatable.

4.7.3 Evaluation of C_μ and C_Q as Scaling Parameters

A comparison will now be made between the ability of either C_Q or C_μ to correlate blown yawing moment coefficient data taken under various conditions.

For fixed slot geometry (A_j/S = const) and incompressible flow ($\rho_j = \rho_\infty$) then the relationship between C_μ and $(C_Q)^2$ (and therefore C_Q) is independent of the free-stream speed. This means that under these conditions C_μ or C_Q will collapse C_N data taken at different speeds to exactly the same degree.

Figure 4.59 shows yawing moment coefficient data taken at various free-stream speeds for fixed slot area and fixed values of C_μ and C_Q. In physical terms, each of the test runs shown in this figure are, to a first approximation, kinematically similar, i.e. the ratio of the jet velocity to free stream velocity (the jet velocity ratio) is the same in each case. Below 50° alpha the similarity of the data is very good. Above 50° at low free-stream speeds C_N is generally lower than at high free stream speeds. Unblown C_N

data taken at different test speeds collapses equally well throughout the alpha regime, suggesting that the lack of correlation in the blown data is due to a jet Reynolds number effect, rather than a free-stream Reynolds number effect.

The assessment of the ability for C_Q or C_μ to collapse data taken at fixed speed but with varying slot area (A_j) requires some subtlety. Some researchers have changed the slot area by changing the slot length. From slot aspect ratio tests described in Section 4.7.2 it is clear that slot length has a fundamental effect on the attachment characteristic of the resulting wall jet and conclusions drawn from scaling investigations performed in this way are likely to be invalid. For the present set of tests the slot area was varied by changing the slot height, the slot length remaining fixed. This will not greatly effect the behaviour of the resulting wall jet as long as the slot aspect ratio remains high, e.g. greater than 50, and h/r remains small, e.g. less than 0.05.

There was some concern that changing the slot height would affect the baseline asymmetry of the forebody, and thus make interpretation of the results of the tests difficult. Placing a slot on a previously smooth forebody has a large effect on the baseline aerodynamics. However, changing the height of the slot once it is on the forebody, figure 4.60, has almost no effect on the baseline aerodynamics for the range of slot heights tested.

C_N data at a fixed speed, but with different slot heights (and therefore different slot areas) is presented for constant C_Q in figure 4.61. It is clear that C_Q is a very poor parameter for collapsing C_N taken with different slot areas.

The results of a similar set of tests at constant C_μ are shown in figure 4.62. The similarity of the data is fair below 40° alpha, becoming less reliable at higher alpha, but still significantly better than the similarity produced by using C_Q. The lack of similarity at high alpha may be due to an h/r effect or the effect of changing slot aspect ratio with slot height.

4.8 FULL SCALE APPLICATION OF TANGENTIAL FOREBODY BLOWING

Successful application of TFB to full scale flight vehicles depends on keeping the mass flow requirements within typical engine bleed flow capacity. To this end it is essential to maximise the efficiency of the blowing control implementation in terms of the augmentation ratio, k_a. It is also important to minimise the physical size of the slots for drag, weight and installation reasons. The drag penalty will probably require fully faired in slots that are opened up when required.

Since TFB becomes more efficient as alpha increases the most demanding flight regime is likely to be at lower alphas where the rudder power is diminished but the destabilising yawing moments from the natural forebody flow asymmetry are large. As an example, the mass flow and slot size requirement for a full scale aircraft of similar shape to the model used in the wind tunnel tests will be calculated.

Assume an aircraft with 40m^2 wing area powered by two RB199 engines of 75 kgs^{-1} mass flow each and that a yawing moment coefficient of 0.08 is required at $\alpha = 40°$ during a manoeuvre at 10 000 feet and 0.3M. From figure 4.27, the required C_{n_β} is approximately 0.005. Assuming the jet exit velocity is just sonic ($V_j/V_\infty = 3.33$, $\rho_j/\rho_\infty = 0.634$), the mass flow requirement is of the order of 3 kgs^{-1} and a 2m long slot would be approximately 7mm wide. The bleed mass flow requirement of 2% of engine mass flow is significant but not excessive. For example the Pegasus engine in the Harrier is often run up to bleed levels of 10% of compressor mass flow. The slot size is workable but ideally the slot height should be smaller to minimise disturbance to the external flow.

Note that the above calculation is only approximate and for optimised slot geometry and location for a limited alpha range, the appropriate yawing moment could be generated with blowing levels perhaps an order of magnitude less.

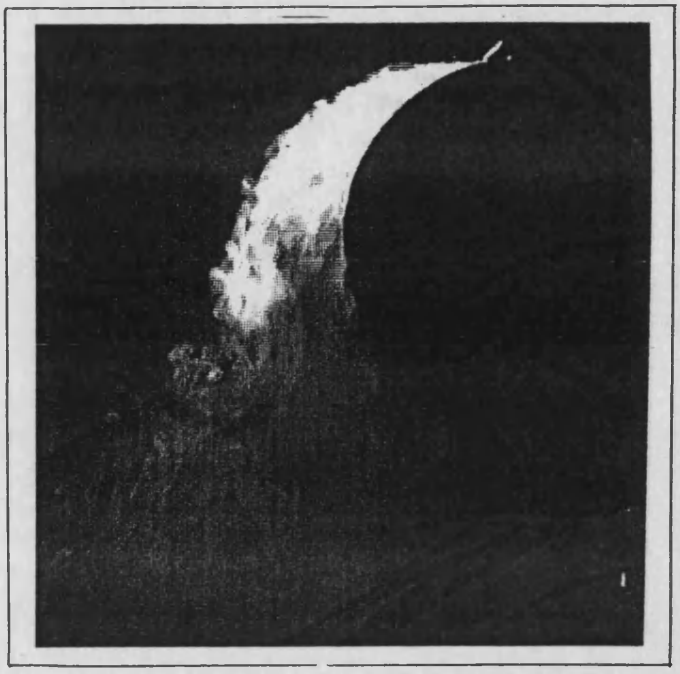

Figure 4.1 *Laser Light Sheet Section Through Centre of an Aspect Ratio 360 Jet Developing Over a Wall of 70 mm Radius*

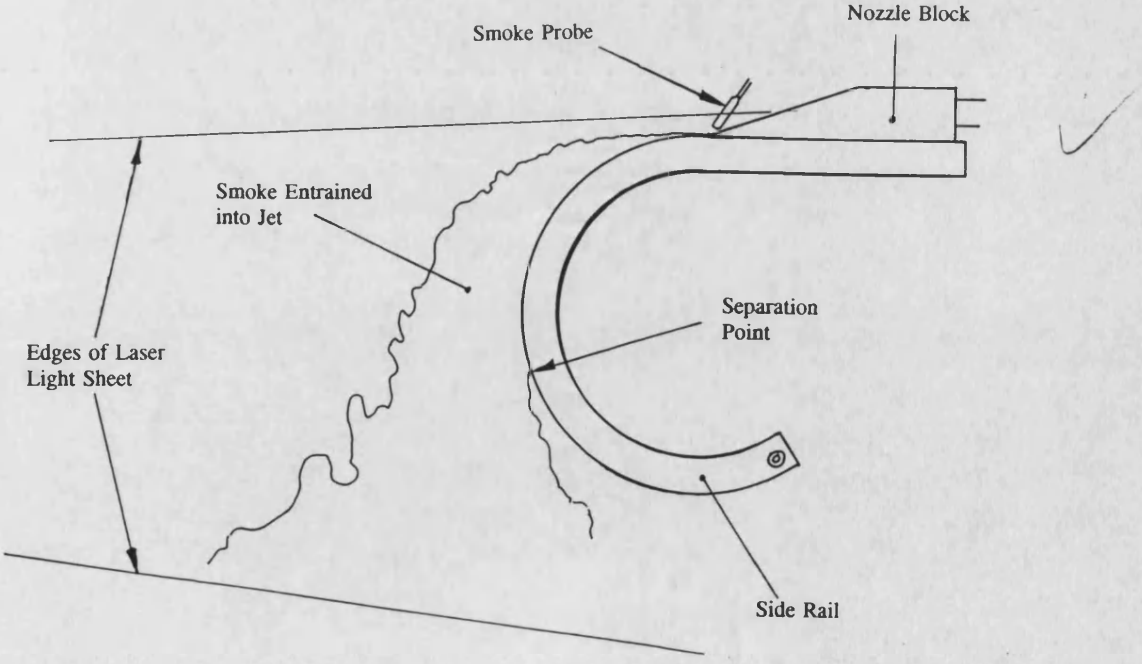

Figure 4.2 *Annotated Sketch of Figure 4.1*

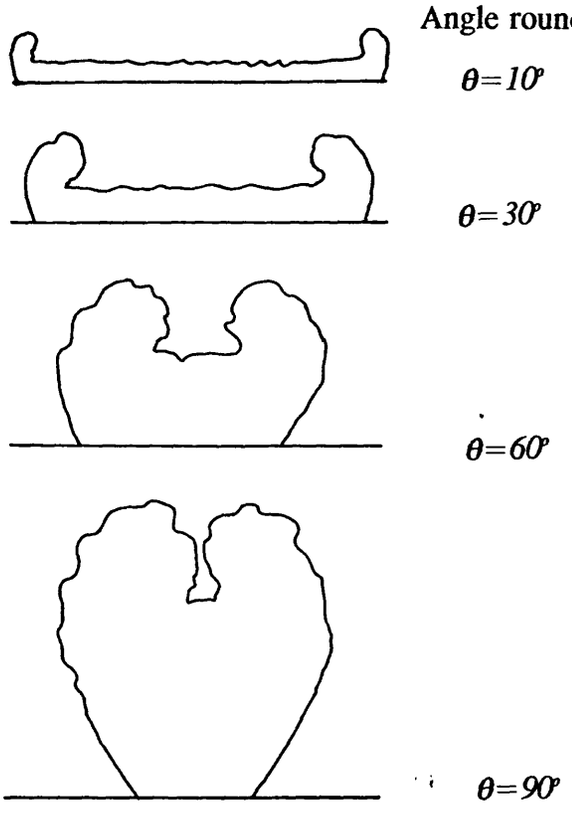

Figure 4.3 *Sketch of Transverse Laser Light Sheet Sections Through Wall Jet Shown In Figure 4.1*

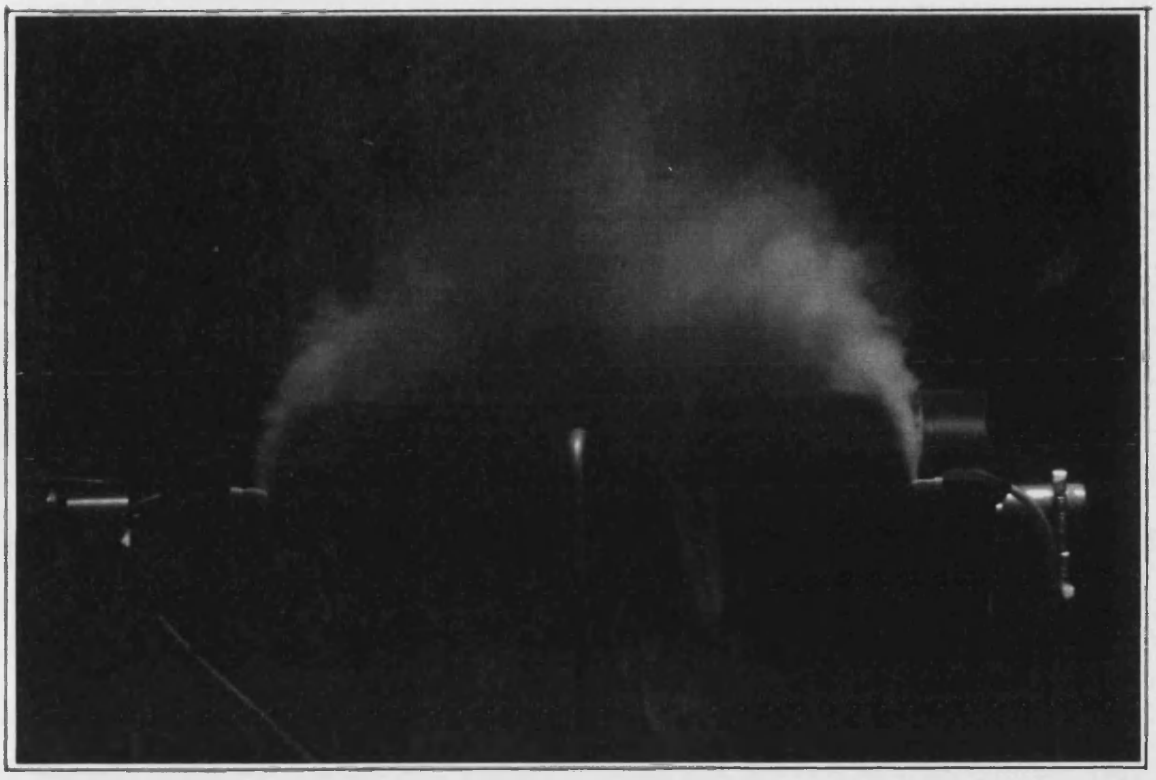

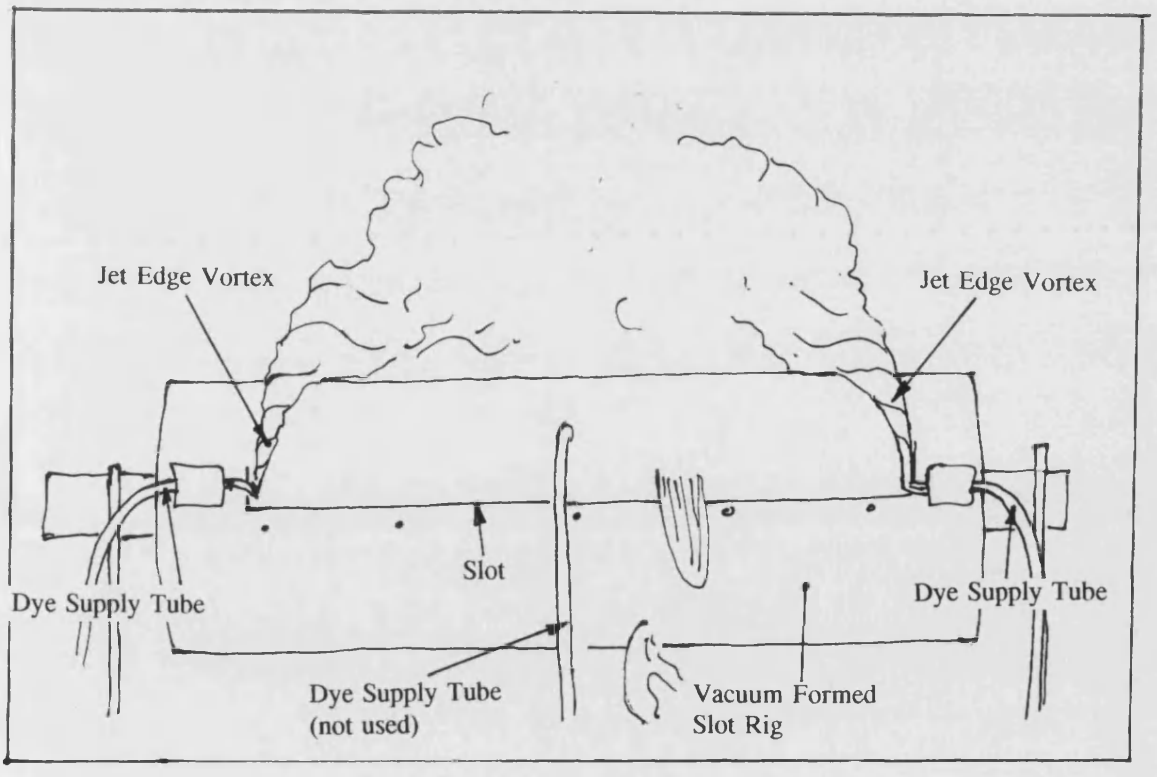

Figure 4.4 *Water Tank Flow Visualisation of Jet Edge Vortices*

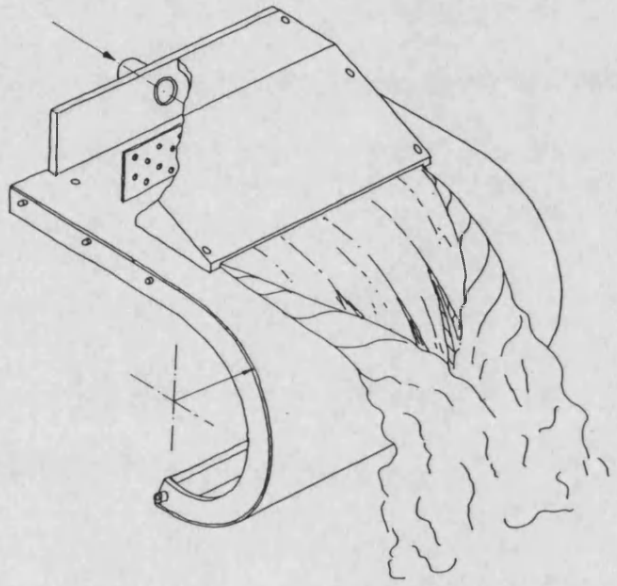

Figure 4.5 *Three-Dimensional Sketch of Wall Jet Flow from an Aspect Ratio 360 Jet Developing Over a Wall of 70 mm Radius*

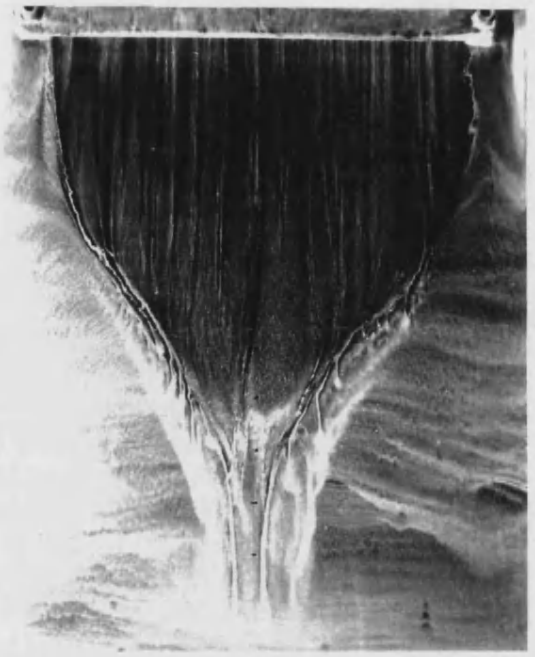

Figure 4.6 *Surface Oil Flow Pattern Made by Aspect Ratio 360 Jet Developing Over a Wall of 70 mm Radius*

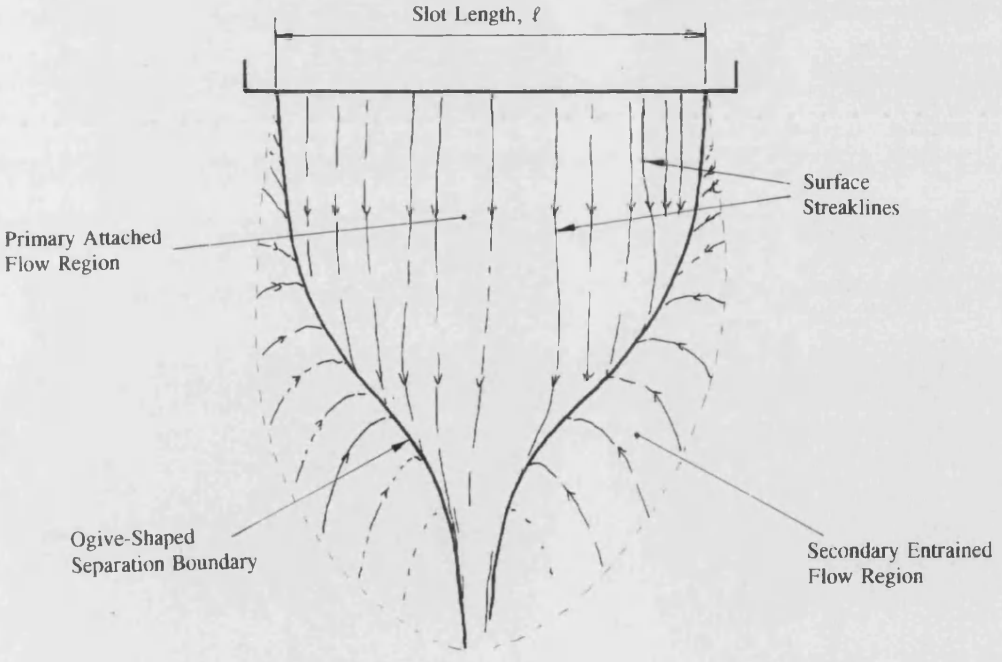

Figure 4.7 *Explanatory Sketch of Figure 4.6*

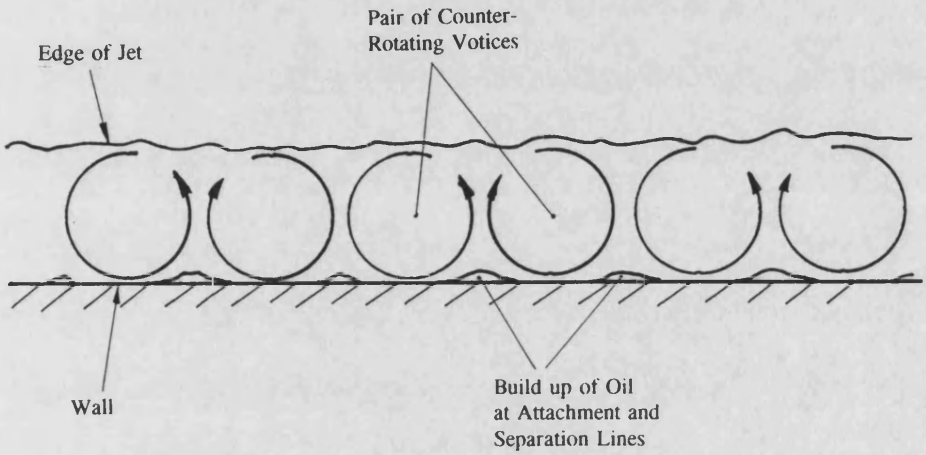

Figure 4.8 *Schematic of Vortices Embedded in Jet Sheet and Associated Separation/Attachment Lines*

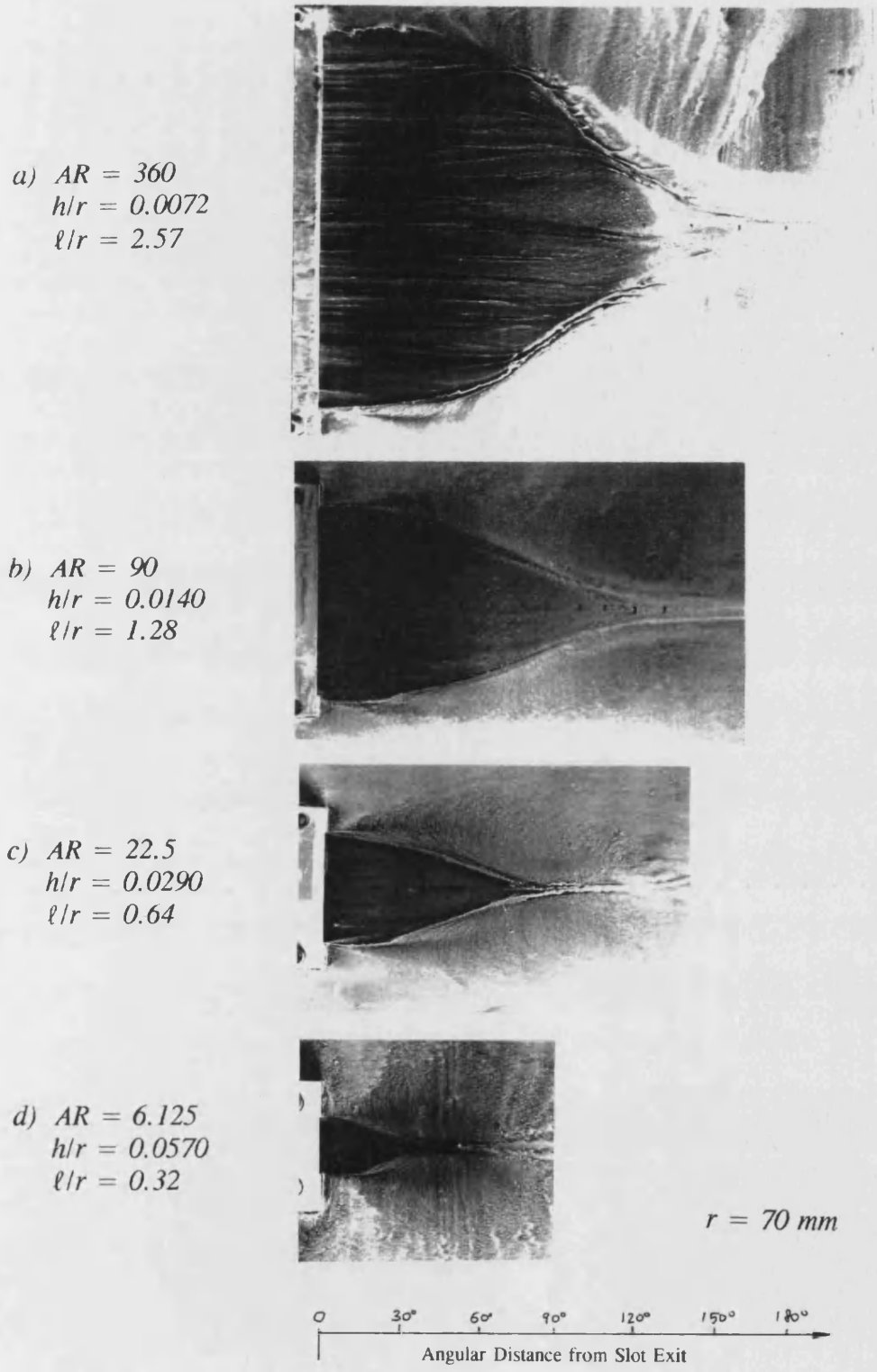

Figure 4.9 *Effect of Slot Aspect Ratio on Surface Oil Flow Pattern of a Jet Developing Over a Wall of Radius 70 mm*

a) $r = 35$ mm
$h/r = 0.01400$
$\ell/r = 5.14$

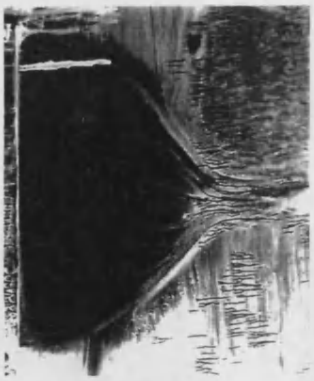

$h = 0.5$ mm, $\ell = 180$ mm

b) $r = 70$ mm
$h/r = 0.0071$
$\ell/r = 2.57$

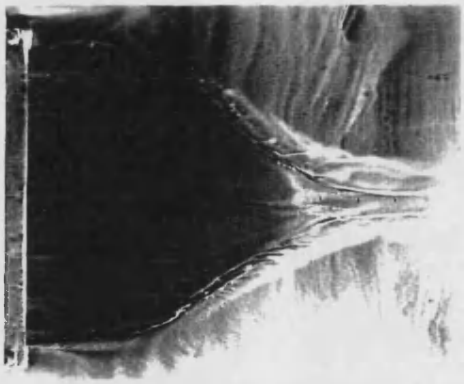

c) $r = 140$ mm
$h/r = 0.0036$
$\ell/r = 1.29$

d) $r = 280$ mm
$h/r = 0.0018$
$\ell/r = 0.64$

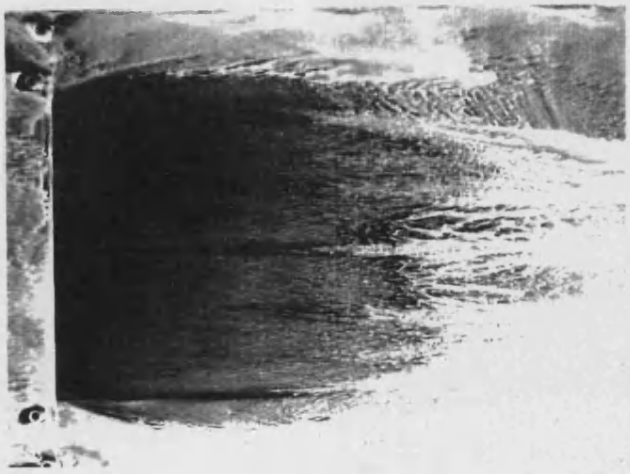

Figure 4.10 *Effect of Wall Radius on Surface Oil Flow Pattern of an Aspect Ratio 360 Jet*

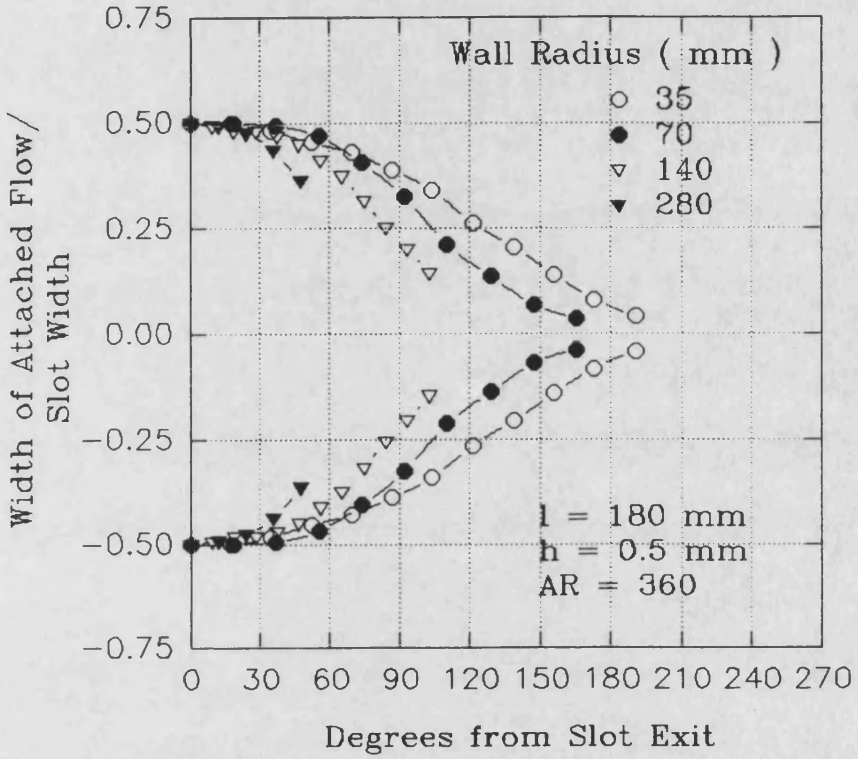

Figure 4.11 *Attached Flow Areas of Figure 4.9 'Replotted' to the Same Angular Scale*

a) $r = 140$ mm
$h/r = 0.0140$
$\ell/r = 0.32$

$h = 2$ mm, $\ell = 45$ mm

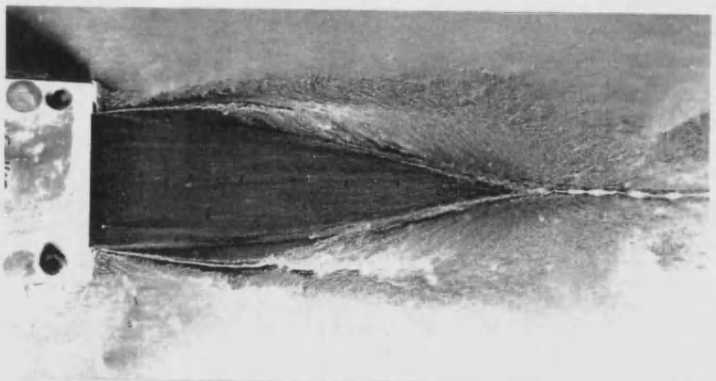

b) $r = 280$ mm
$h/r = 0.0071$
$\ell/r = 0.16$

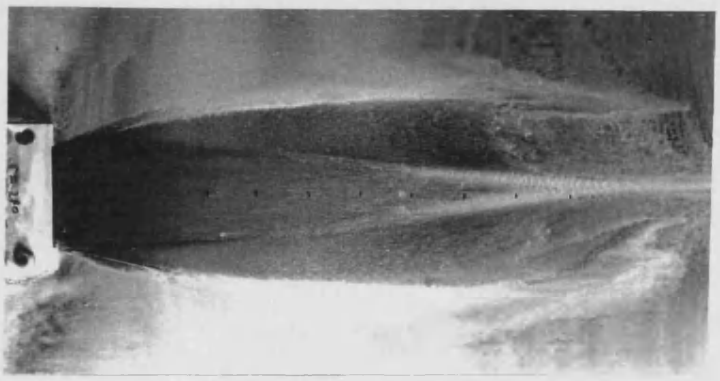

c) $r = \infty$
(flat Plate)
$h/r = 0000$
$\ell/r = 0.00$

d) $r = -280$ mm
(concave curvature)
$h/r = -0.0071$
$\ell/r = -0.016$

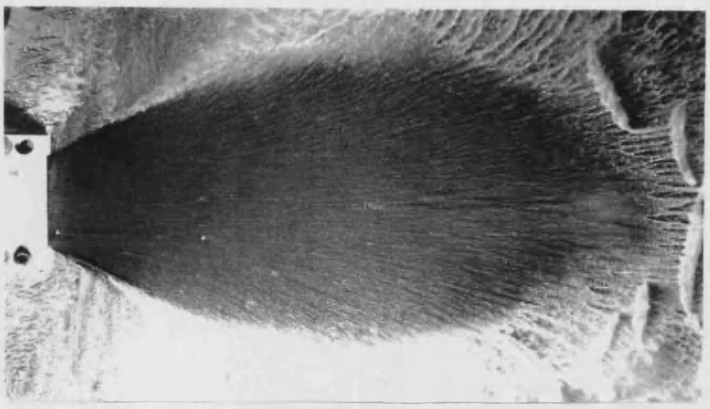

Figure 4.12 *Effect of Wall Radius on Surface Oil Flow Pattern of an Aspect Ratio 22.5 Jet*

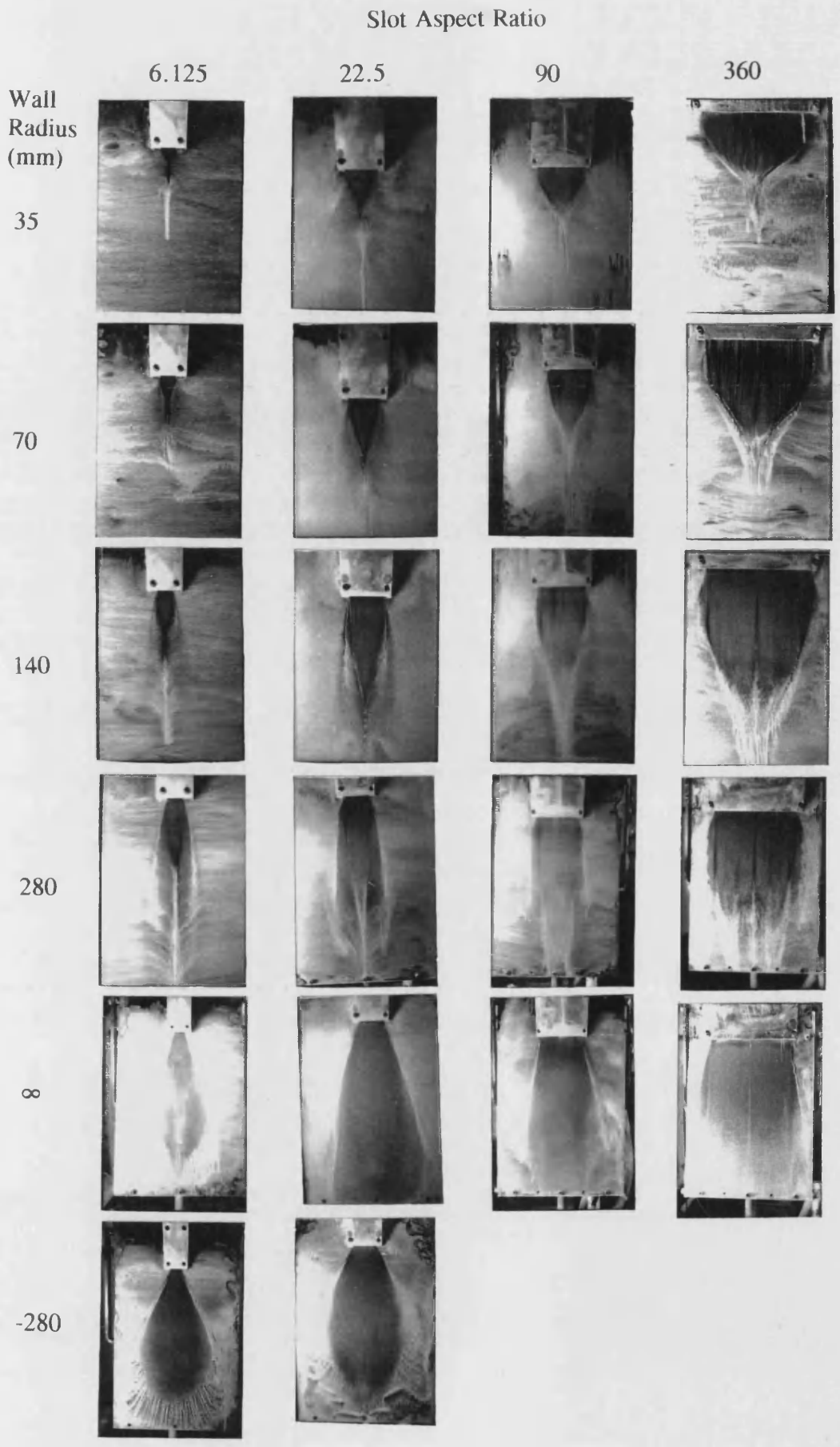

Figure 4.13 *Summary of the Effects of Slot Aspect Ratio and Wall Radius on the Surface Flow Characteristics of a Wall Jet*

a) $Re_j \approx 1 \times 10^6$
$(V_j \approx 1$ m/s)

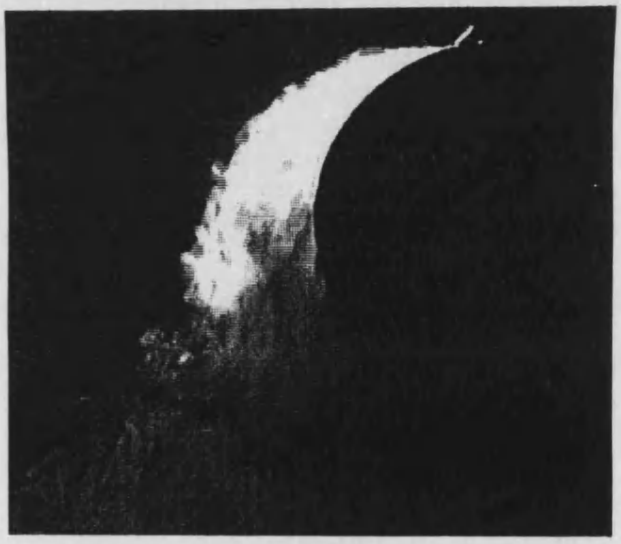

b) $Re_j \approx 1 \times 10^7$
$(V_j \approx 10$ m/s)

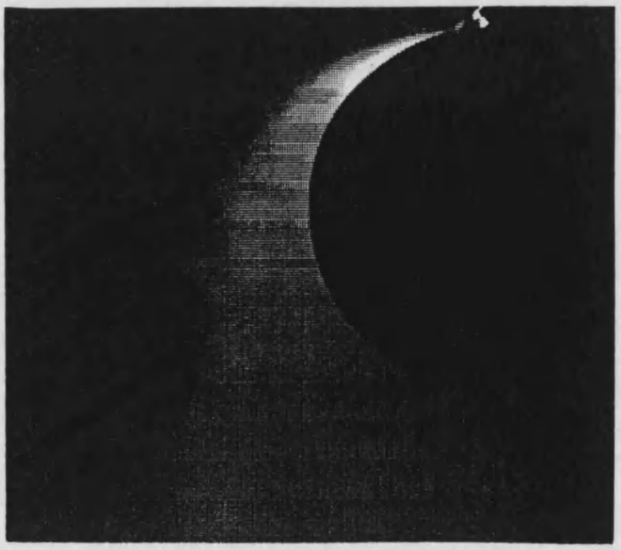

c) $Re_j \approx 1 \times 10^8$
$(V_j \approx 100$ m/s)

$AR = 360$, $r = 70$ mm

Figure 4.14 *Laser Light Sheet Sections Through a Curved Wall Jet for Increasing Jet Reynolds Numbers*

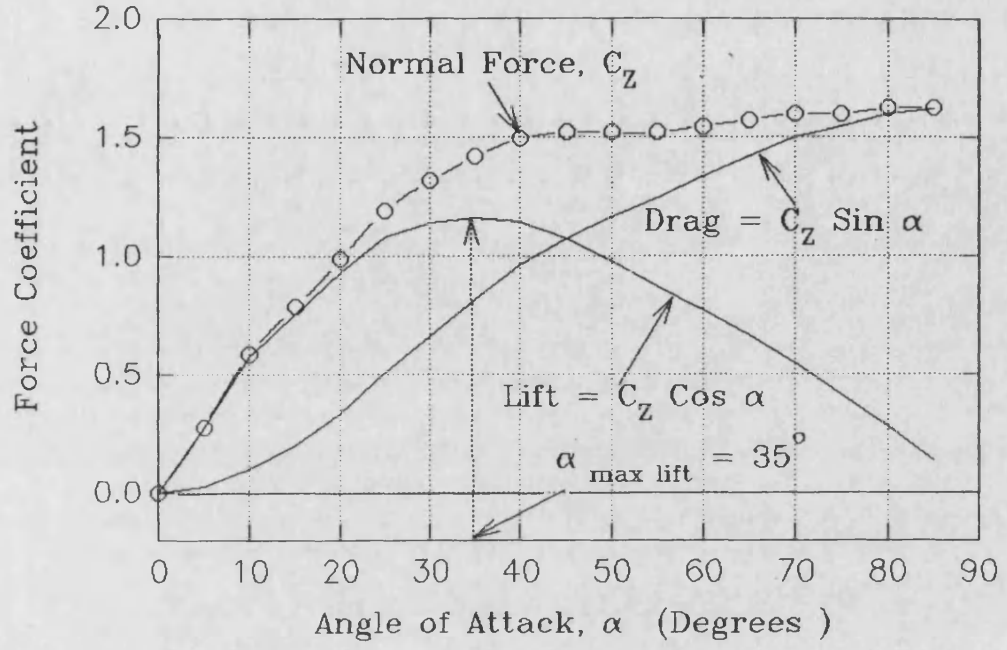

Figure 4.15 *Normal Force, and Normal Force Resolved in to Lift and Drag Components*

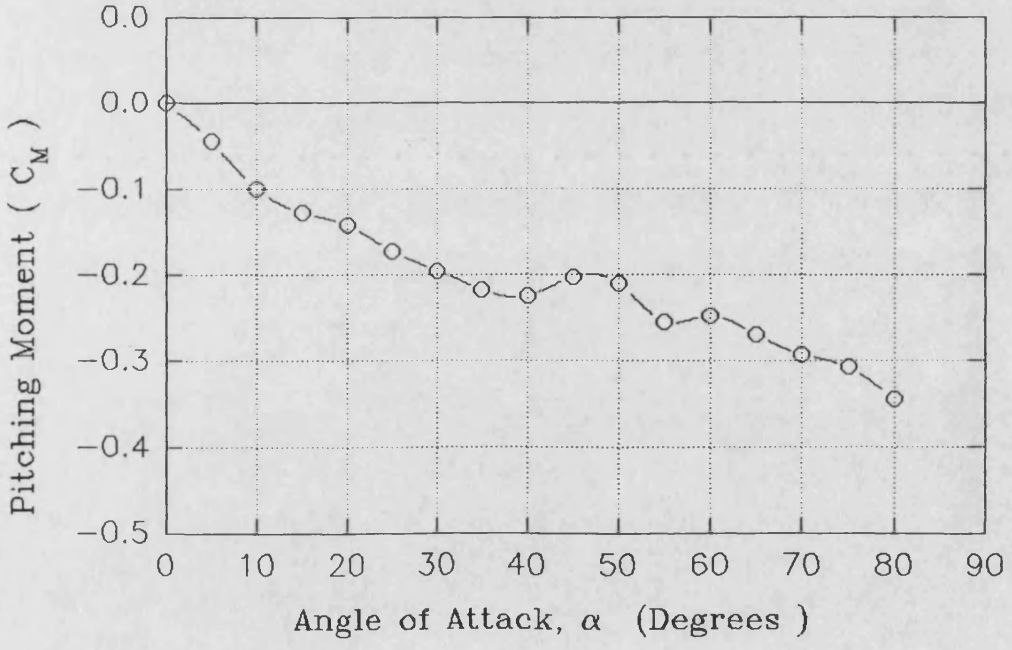

Figure 4.16 *Model Pitching Moment Characteristic*

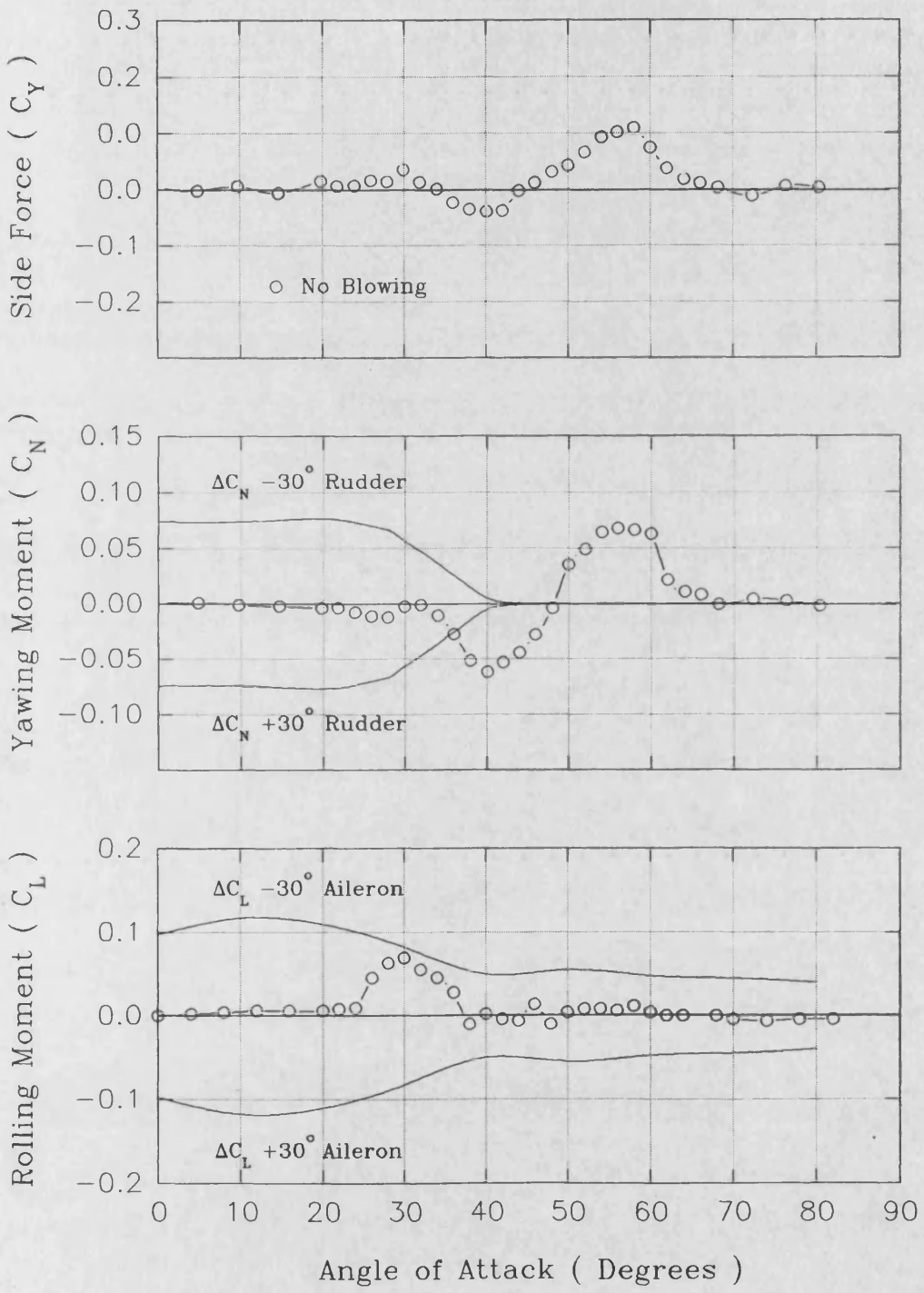

Figure 4.17 *Unblown Lateral Forces and Moments*

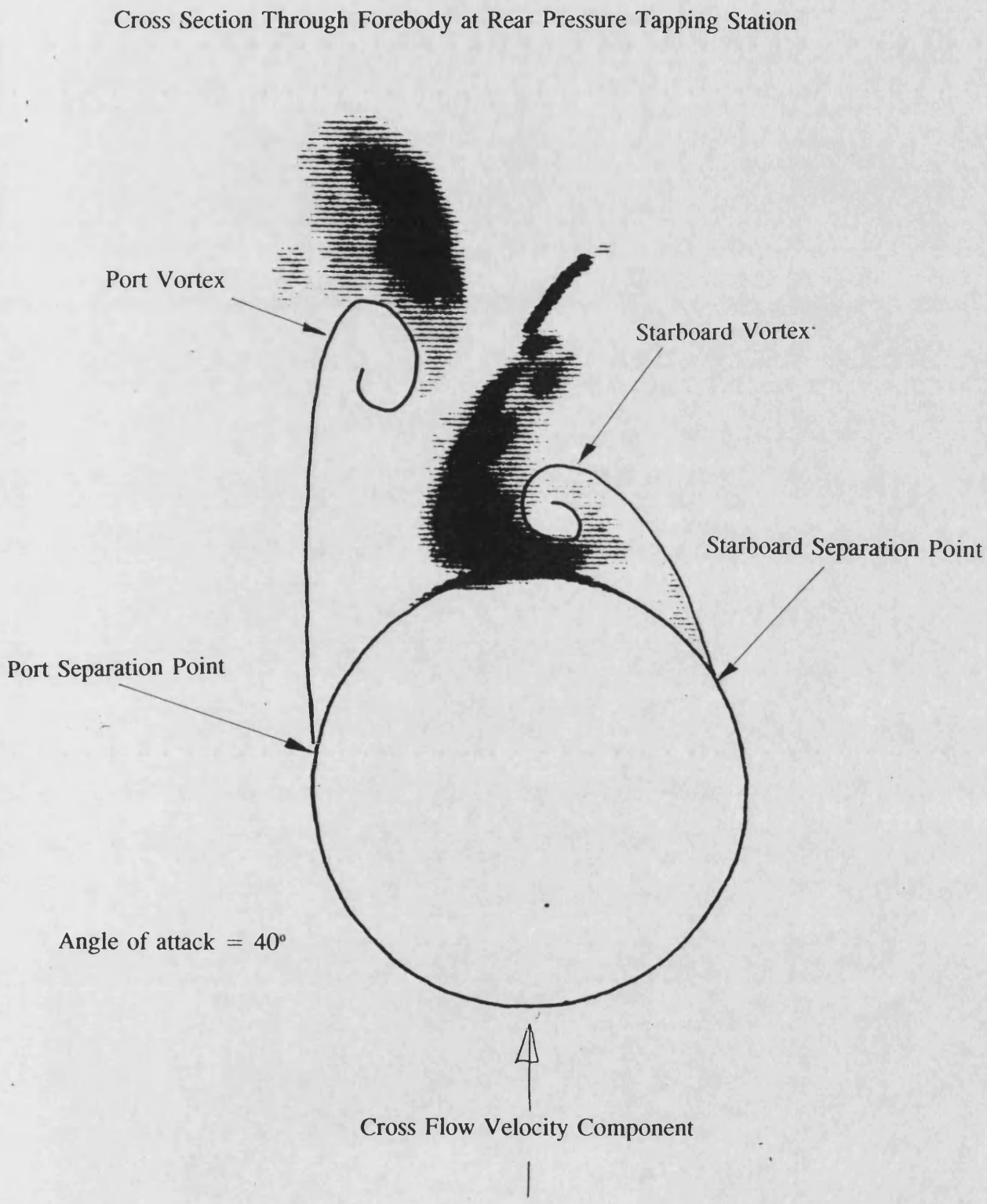

Figure 4.18 *Unblown Asymmetric Vortex Formation at 50° Angle of attack*

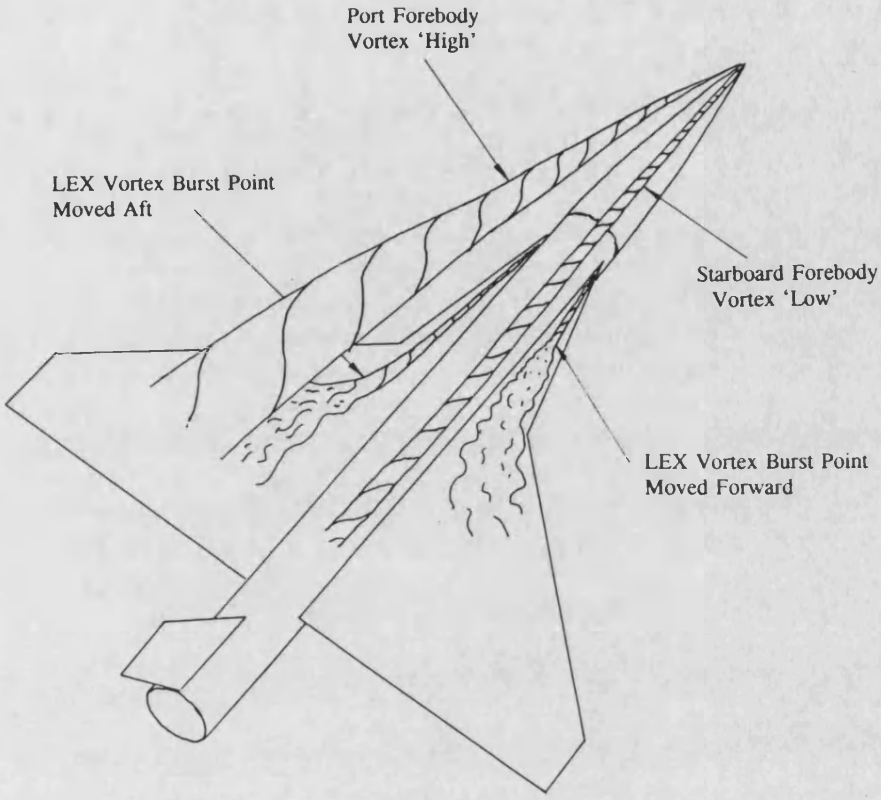

a) Sketch Showing Asymmetry of LEX Vortex Burst Positions

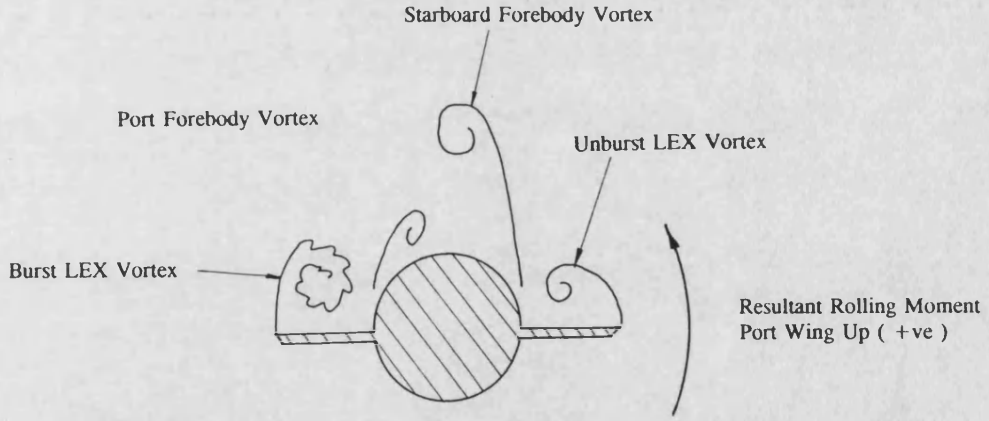

b) Cross-Section at Wing-LEX Junction
Looking Towards Tail of Aircraft

Figure 4.19 *Schematic of Unblown LEX/Forebody Flowfield Coupling Between 20 and 35° Angle of Attack*

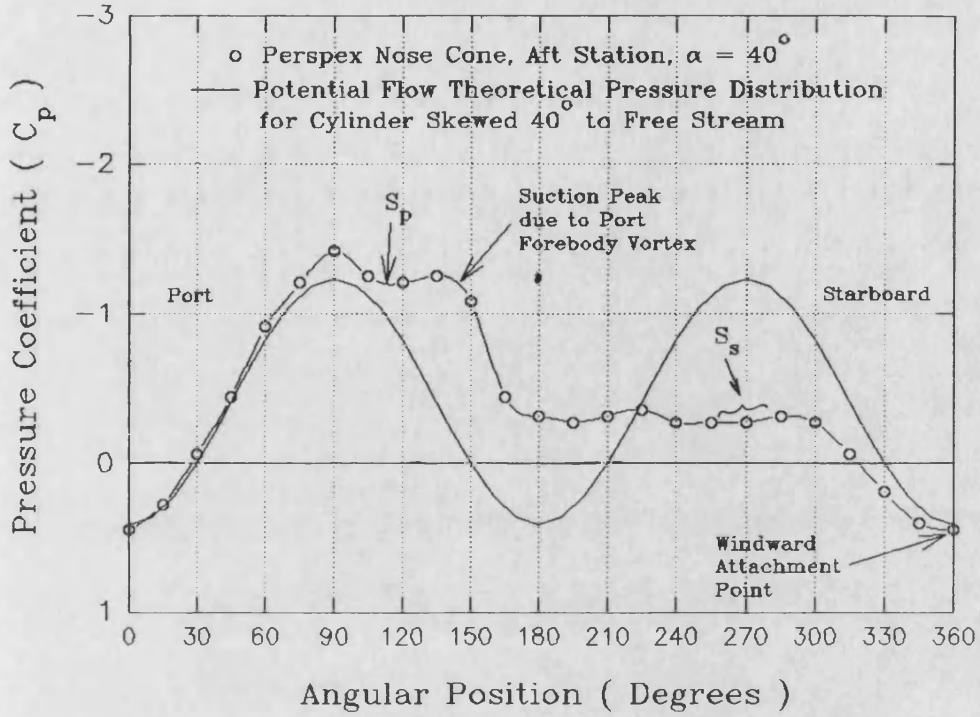

Figure 4.20 *Comparison of Aft Station Forebody Pressure Distribution with Potential Flow Distribution Given By Equation 4.2*

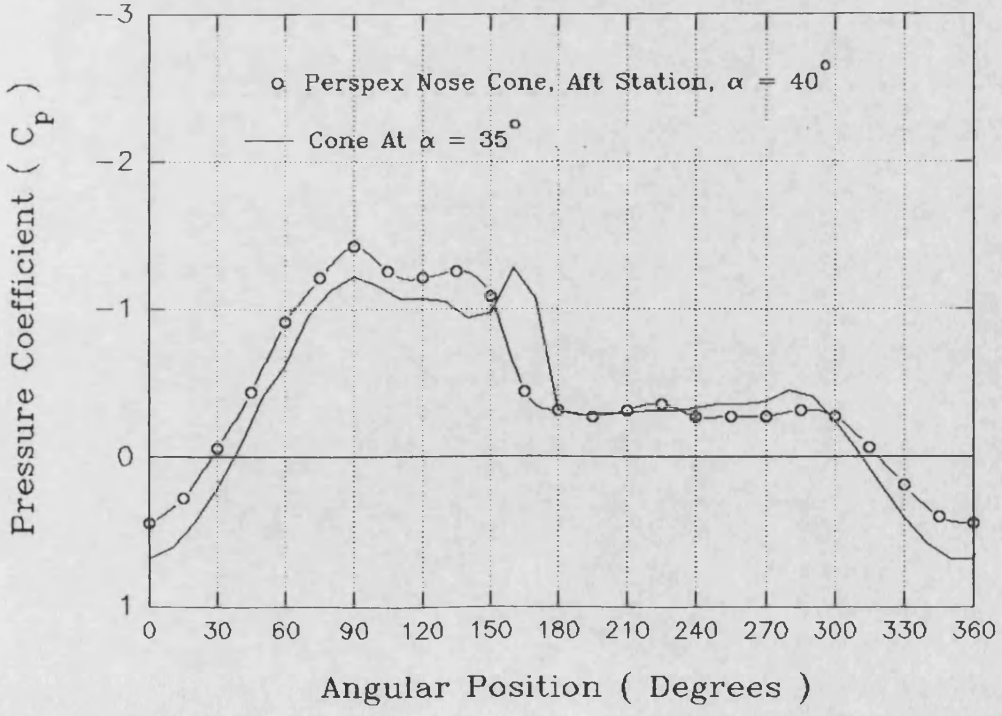

Figure 4.21 *Comparison of Aft Station Forebody Pressure Distribution with Pressure Distribution Round a Circular Cone after Fiddes, ref 89*

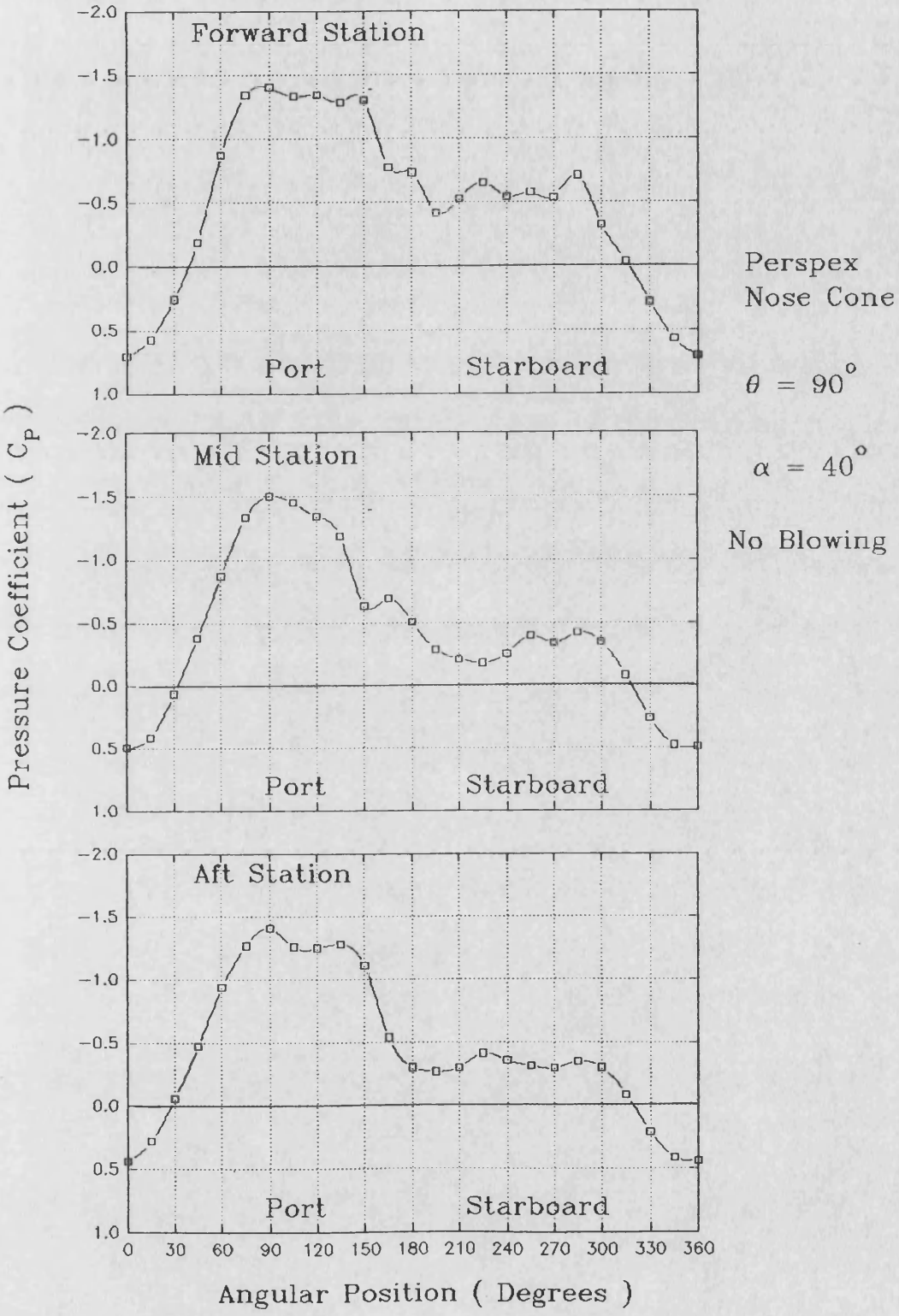

Figure 4.22 *Forebody Pressure Distributions at Different Longitudinal Locations, No Blowing, Fixed Angle of Attack*

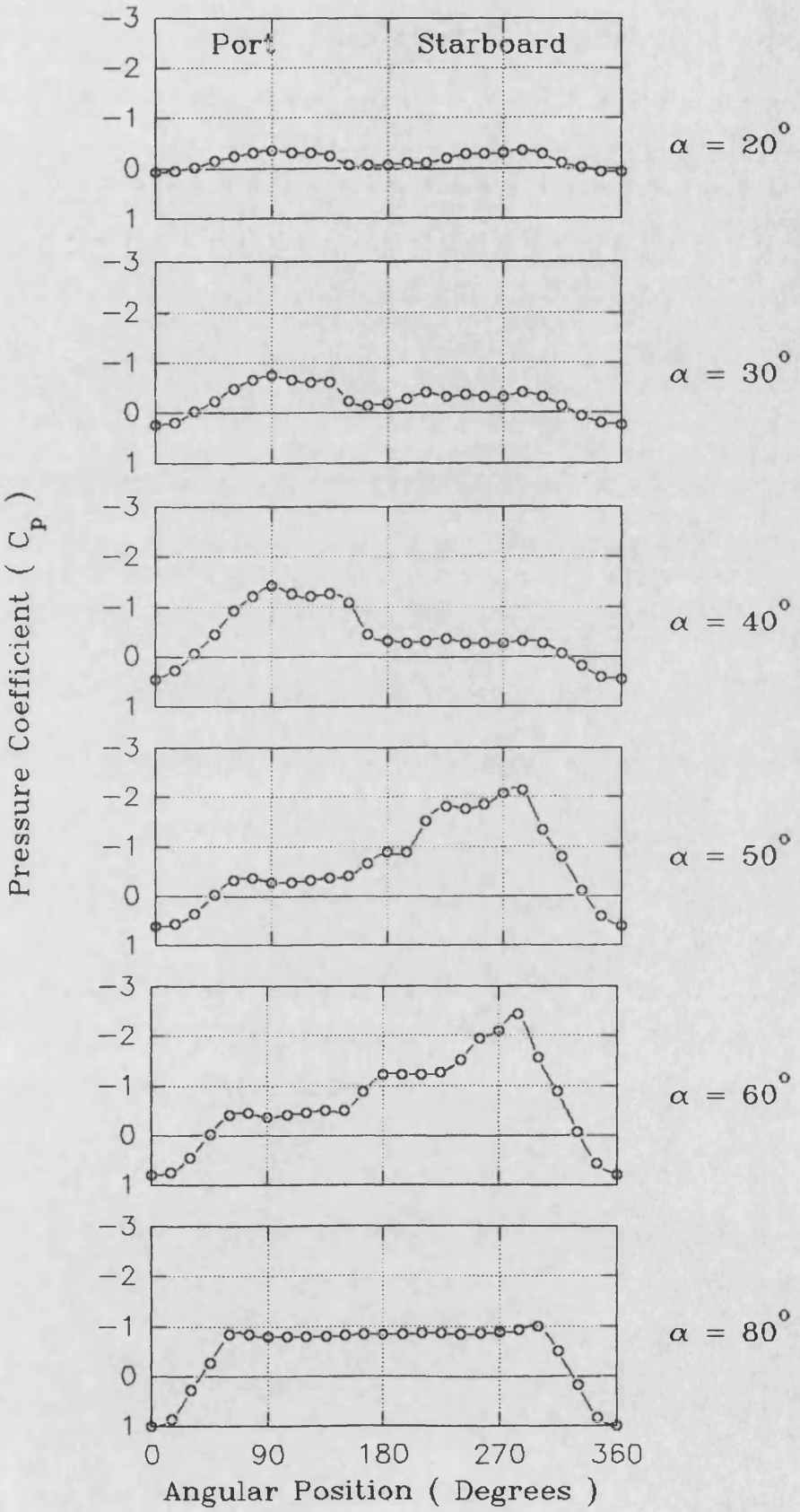

Figure 4.23 *Aft Station Pressure Distributions for a Range of Angles of Attack, No Blowing*

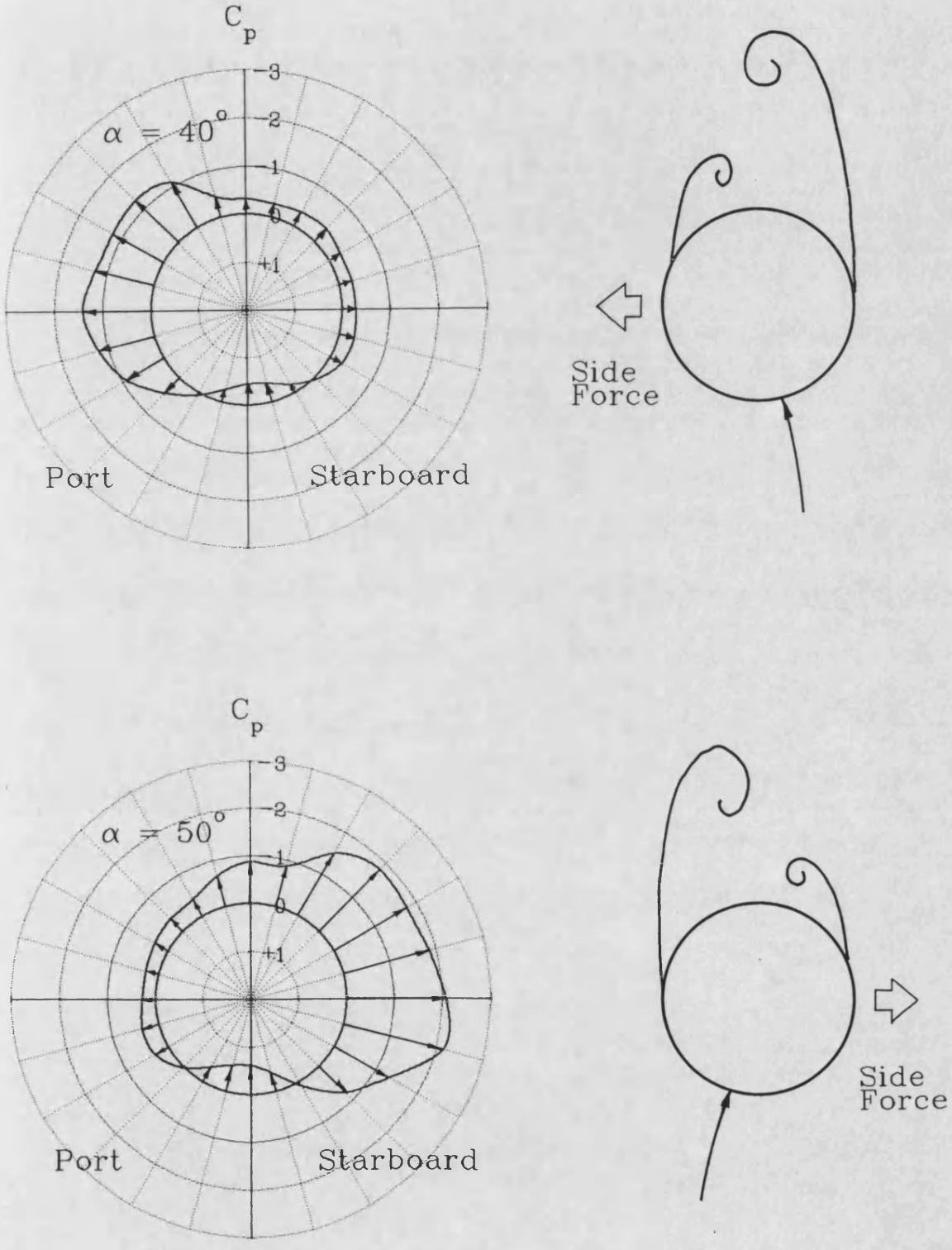

Figure 4.24 *Link Between Asymmetric Pressure Distribution, Vortex Arrangement and Forebody Side Force*

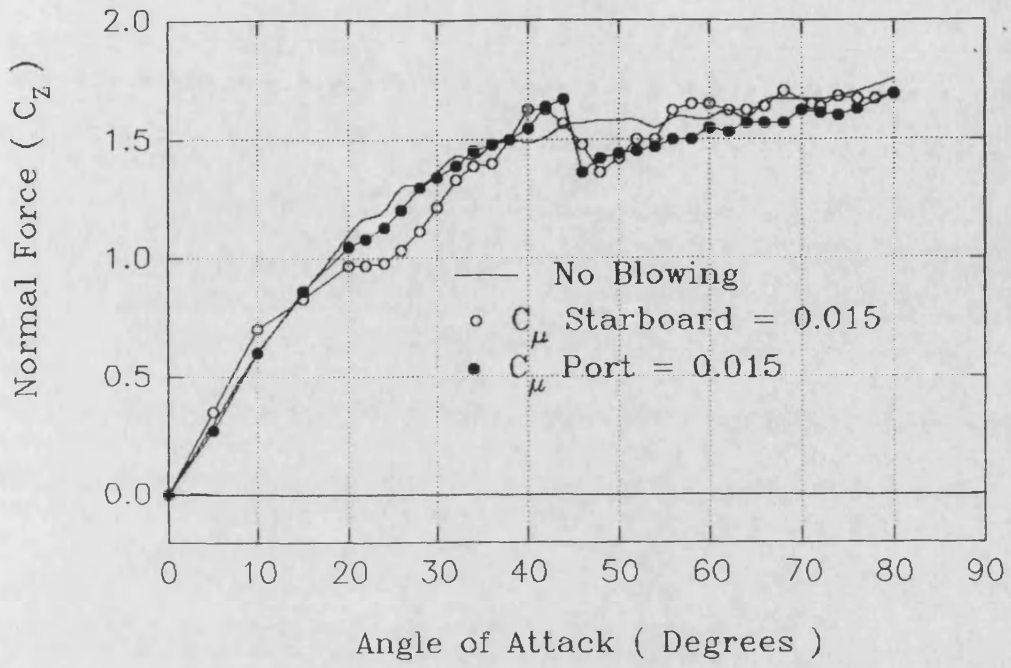

Figure 4.25 *Blown Normal Force Characteristic*

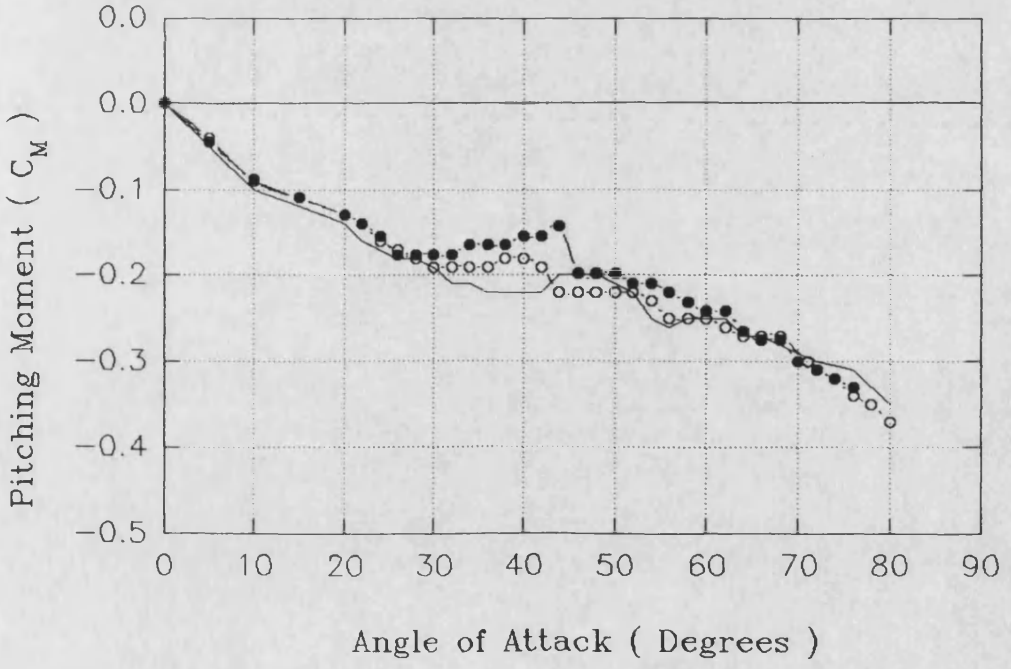

Figure 4.26 *Blown Pitching Moment Characteristic*

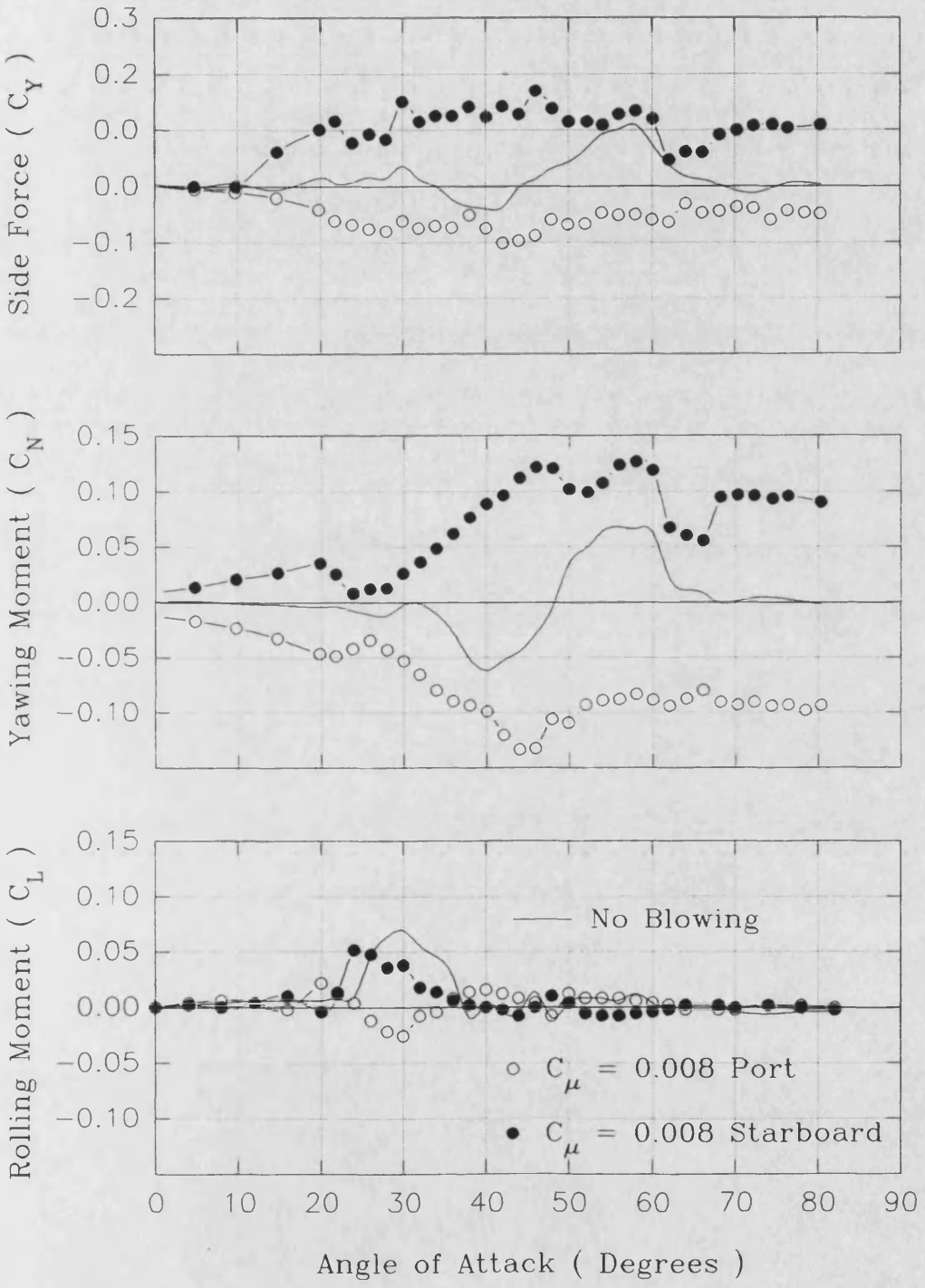

Figure 4.27 *Blown Lateral Forces/Moments*

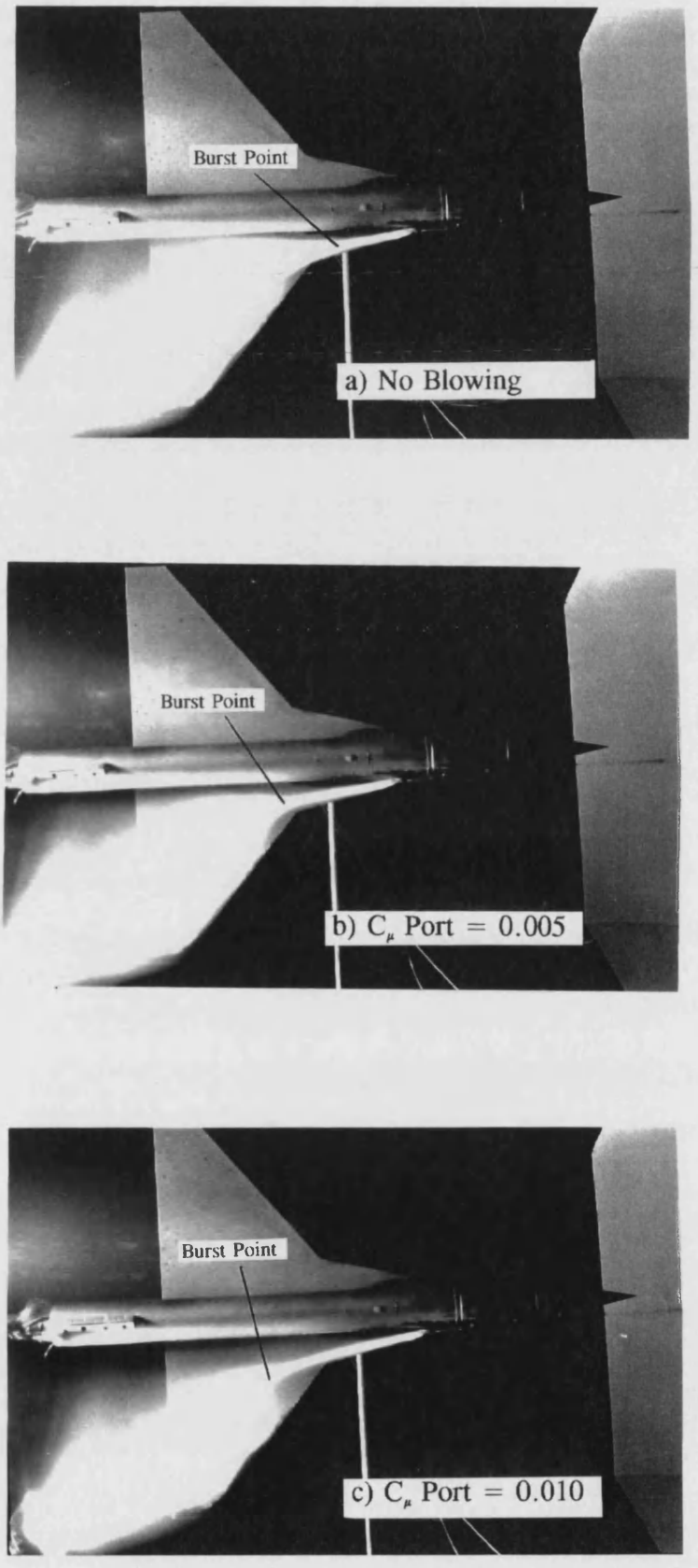

Figure 4.28 *Effect of Blowing on Unblown Side Lex Vortex Burst Position*

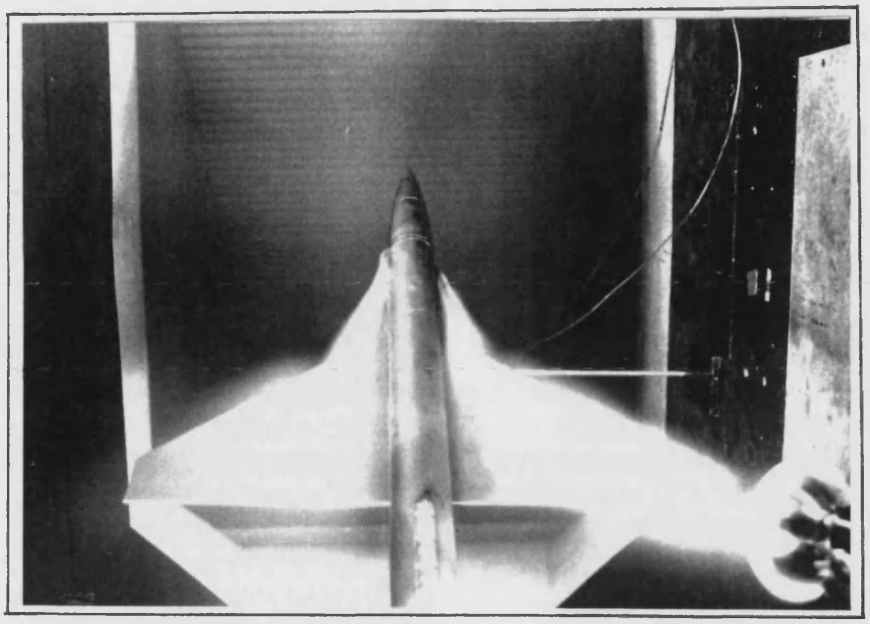

$\alpha = 40^{o}$ $V_{\infty} = 3$ m/s

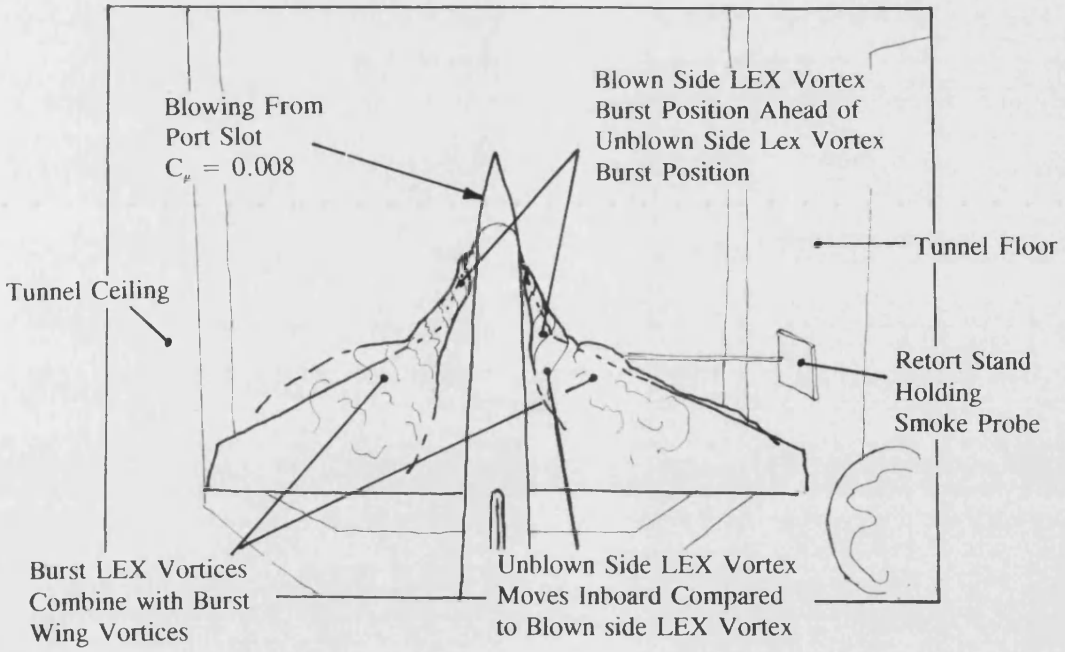

Figure 4.29 *Smoke Flow Visualisation of Port and Starboard LEX Vortices. Port Side Blowing, 40° angle of attack*

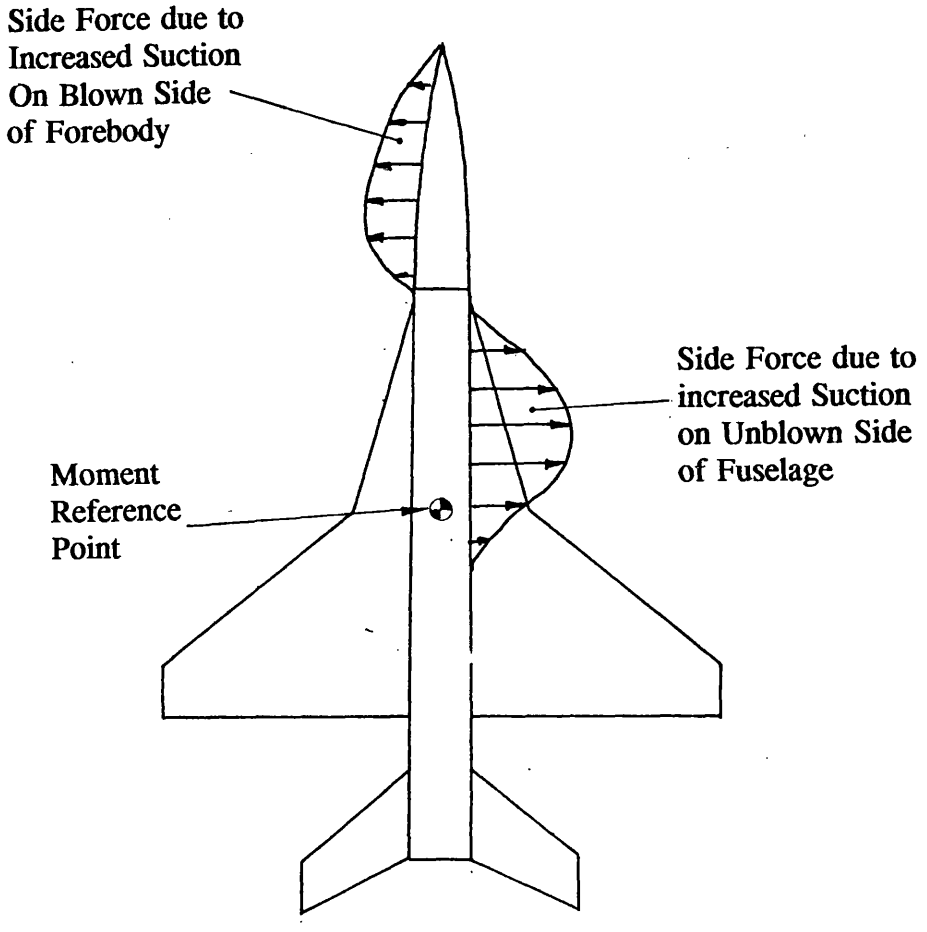

Figure 4.30 *Blown Side Force Distribution on Fuselage at Angles of Attack where the Forebody and Wing/LEX Flowfields are Coupled*

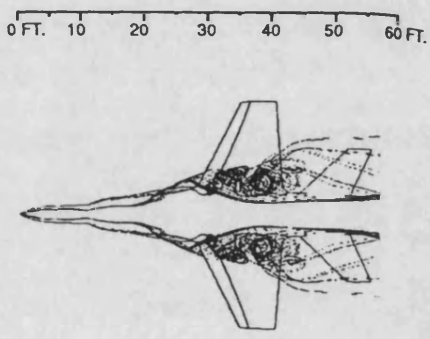

a) no blowing solution

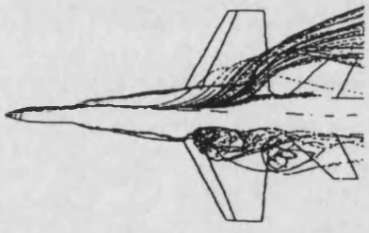

b) blowing solution (PORT SIDE)

$M_\infty = 0.243$, $\alpha = 30.3°$, $Re_z = 11.0 \times 10^6$.

Figure 4.31 *Computed Effect of Blowing on LEX Burst Locations for an F-18 Configuration, after Gee, ref 104*

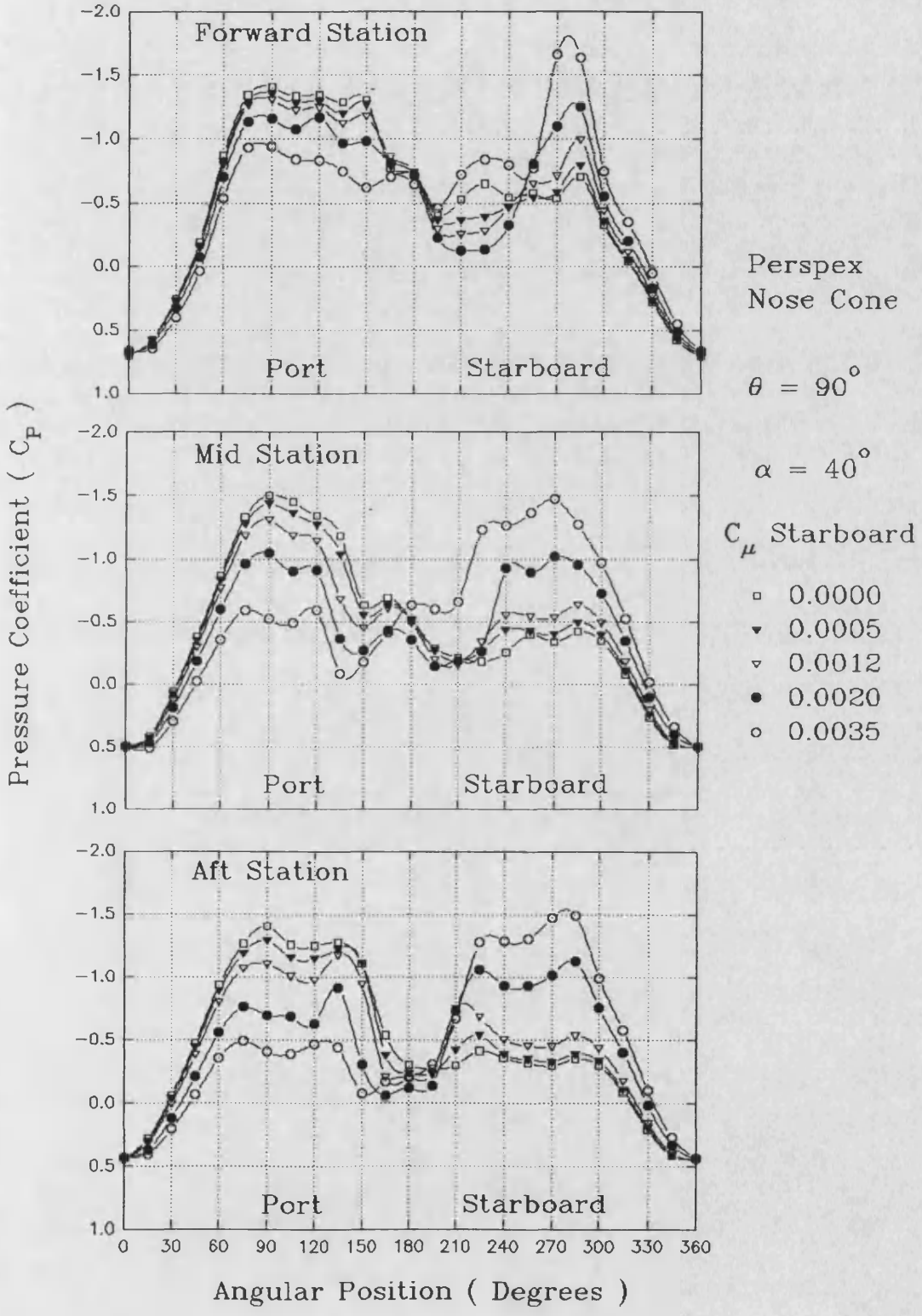

Figure 4.32 *Blown Forebody Pressure Distributions*

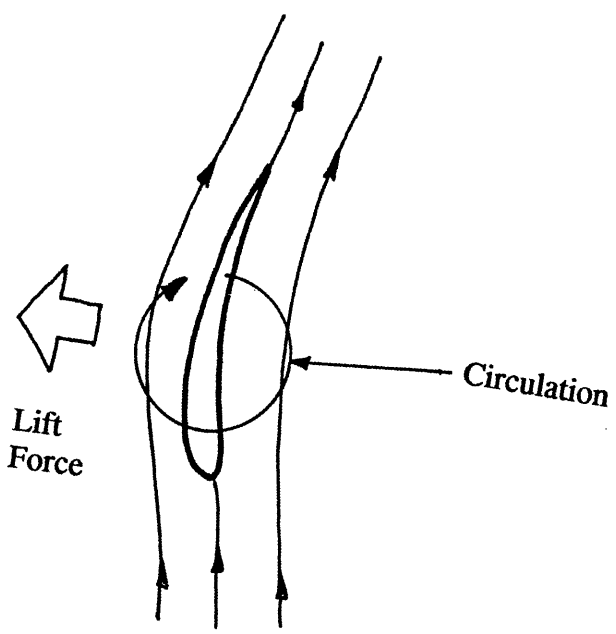

a) Wing

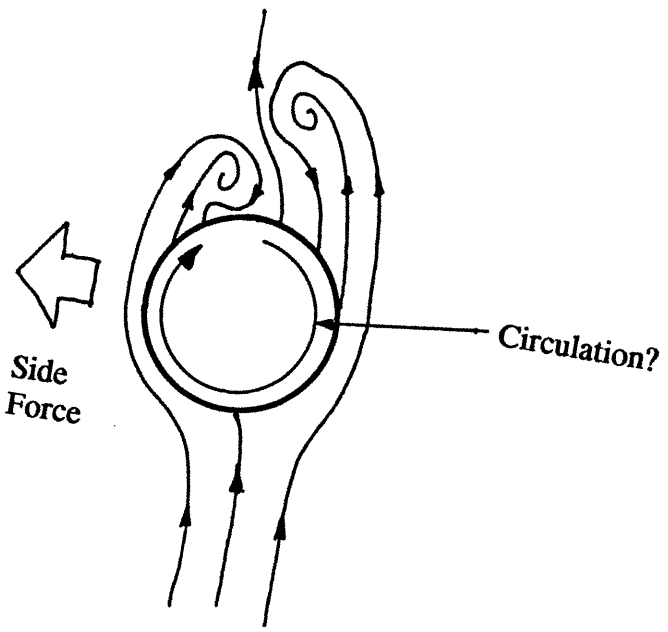

b) Slender Body at High Angles of Attack

Figure 4.33 *Comparison of Flow Around an Aerofoil Section and Crossflow about a Slender Body at Incidence*

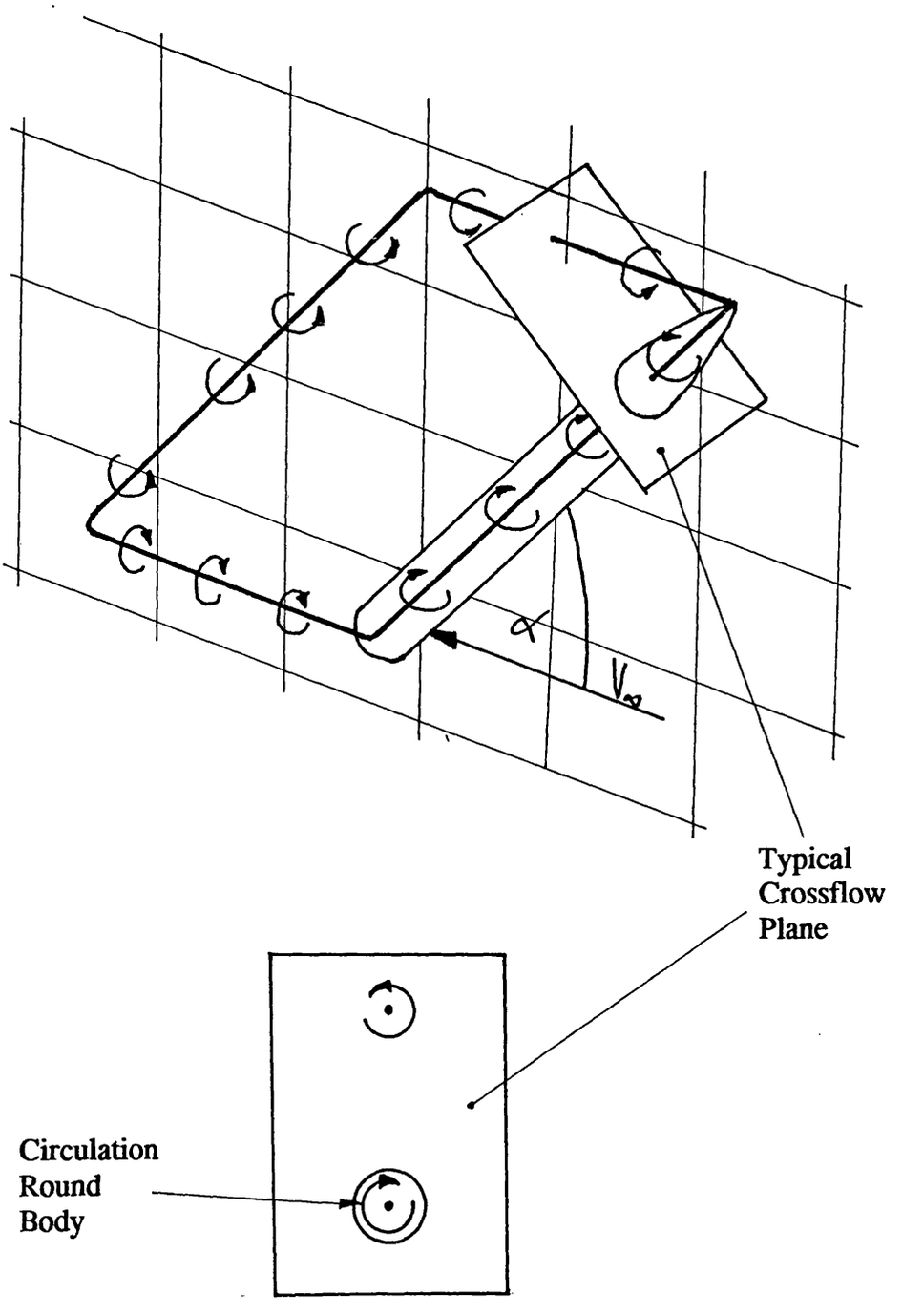

Figure 4.34 *Bound and Trailing Vortex System Applied to a Slender Body at Incidence*

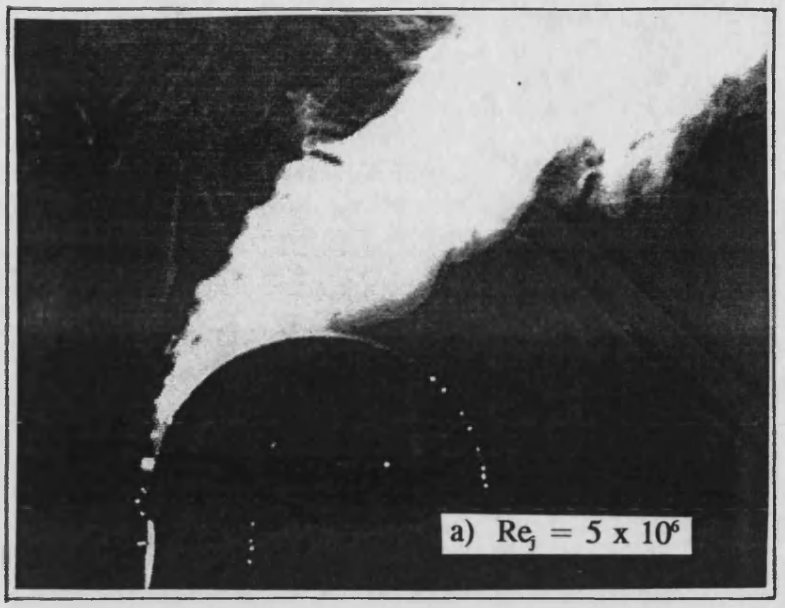

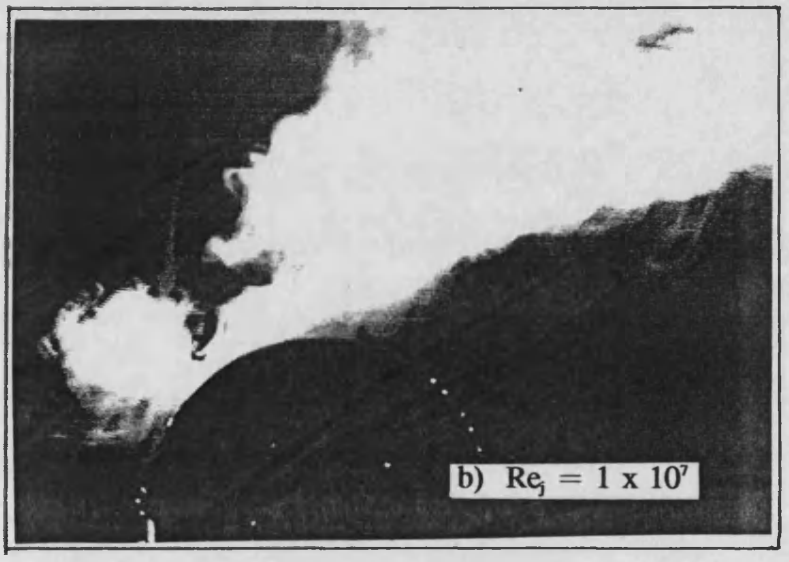

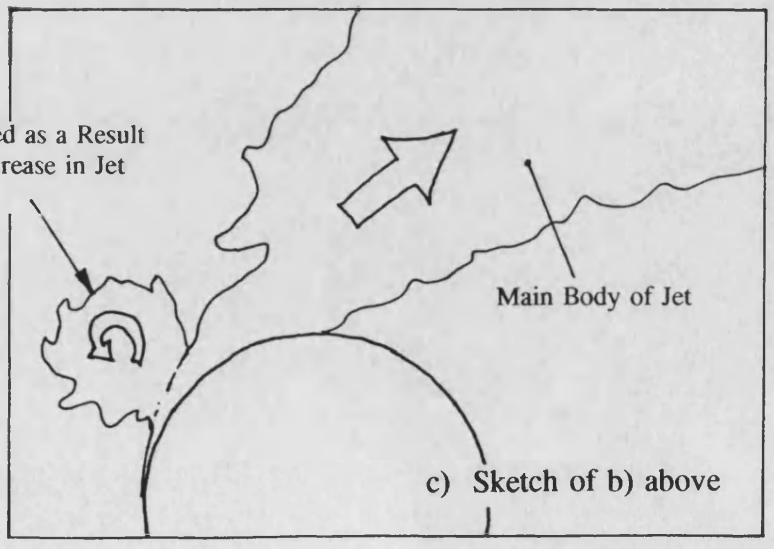

Figure 4.35 *Illustration of a Vortex Shed as a Result of a Change in Circulation About a Cylinder*

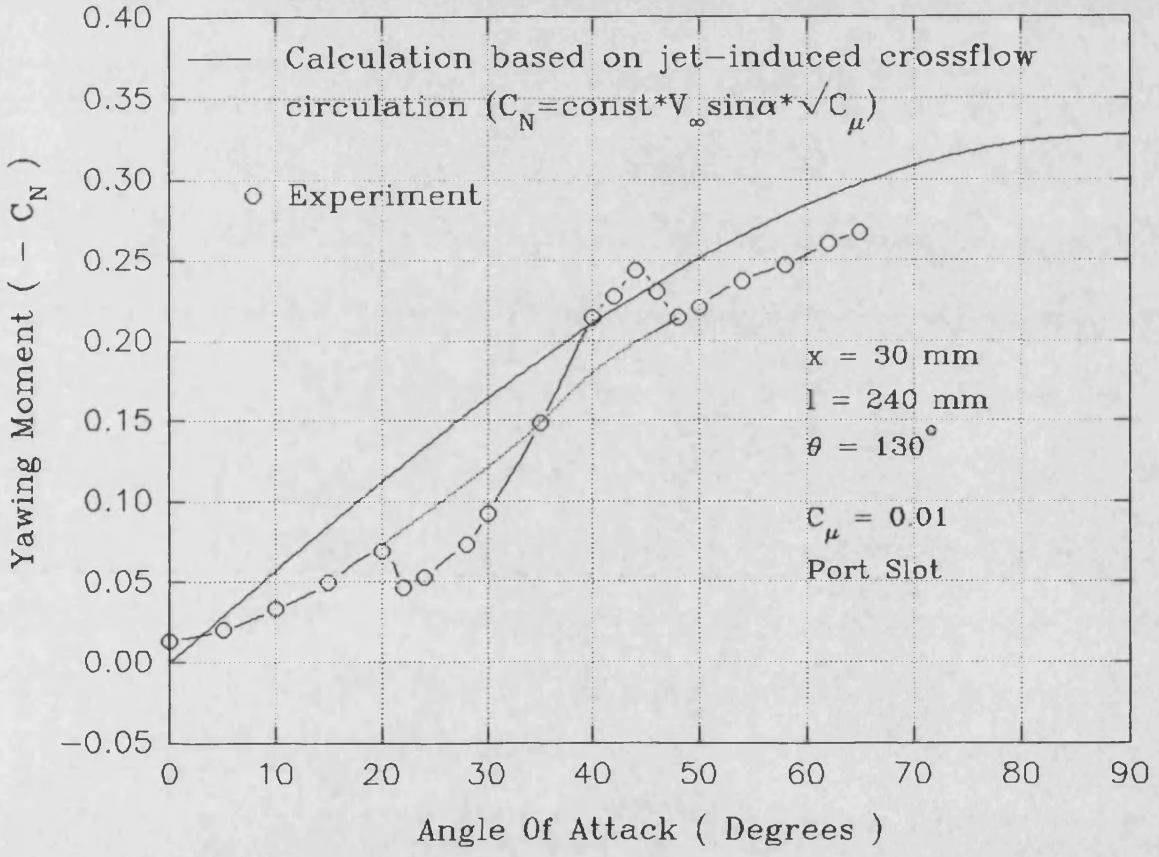

Figure 4.36 *Comparison of Experiment with the Yawing Moment Predicted by a Simple Crossflow Circulation Model*

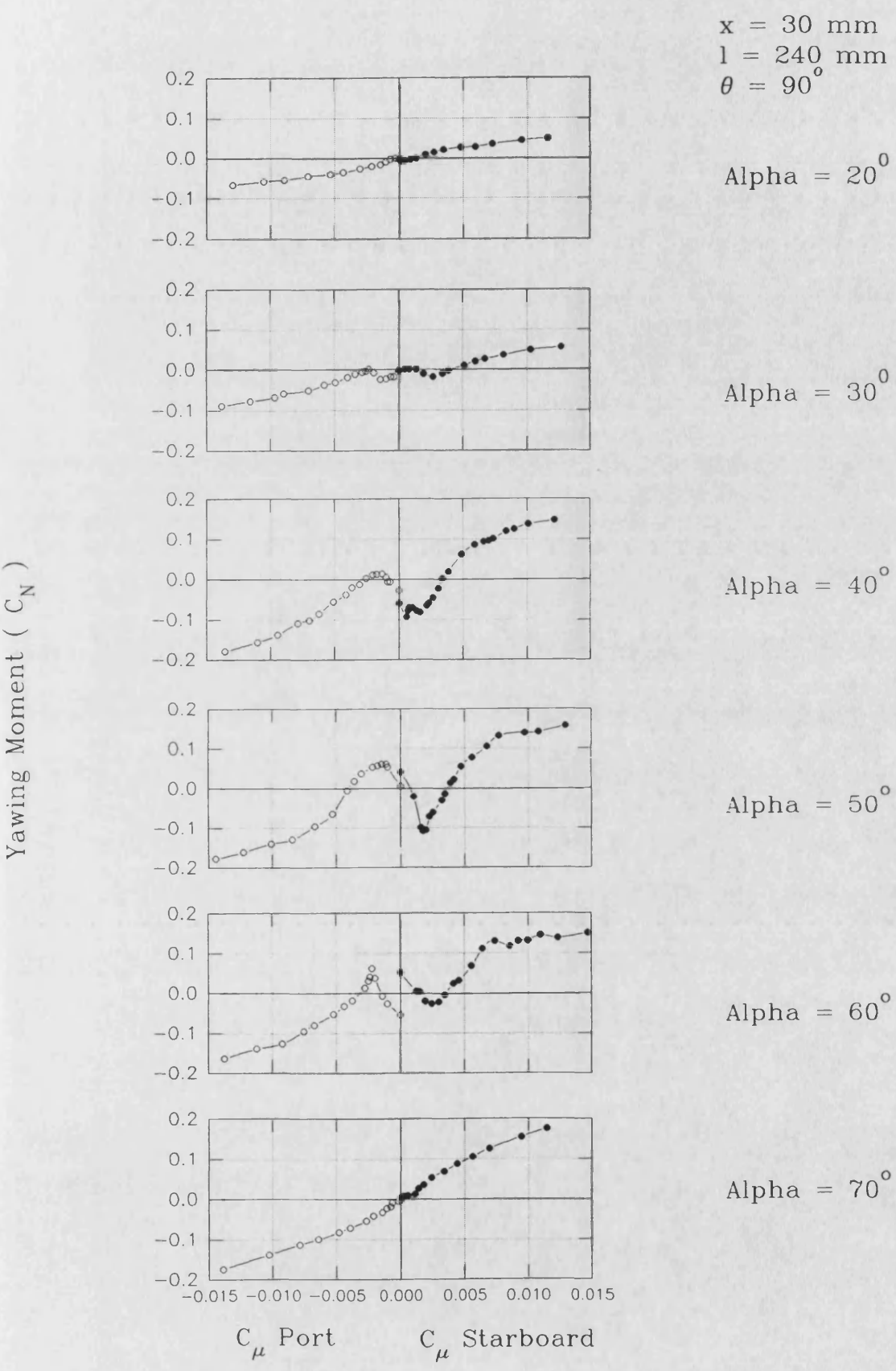

Figure 4.37 *Blown Control Response at Various Angles of Attack*

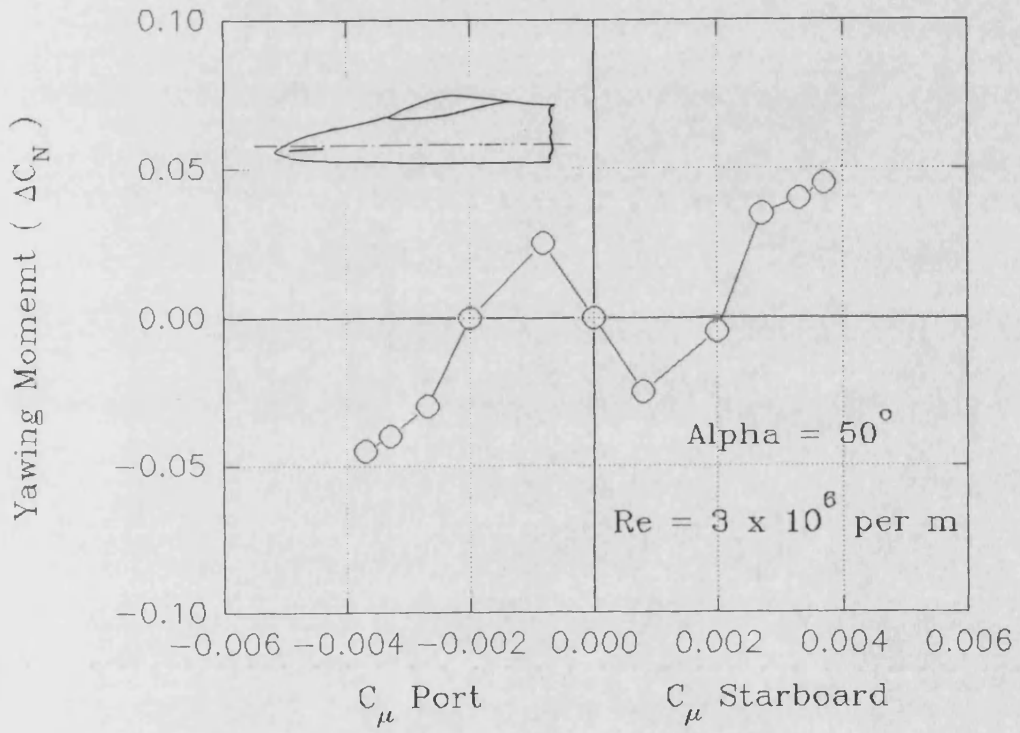

Figure 4.38 *Blown Control Response for Slot Blowing Test on 6% Scale F-18 Model, after Ng, ref 106*

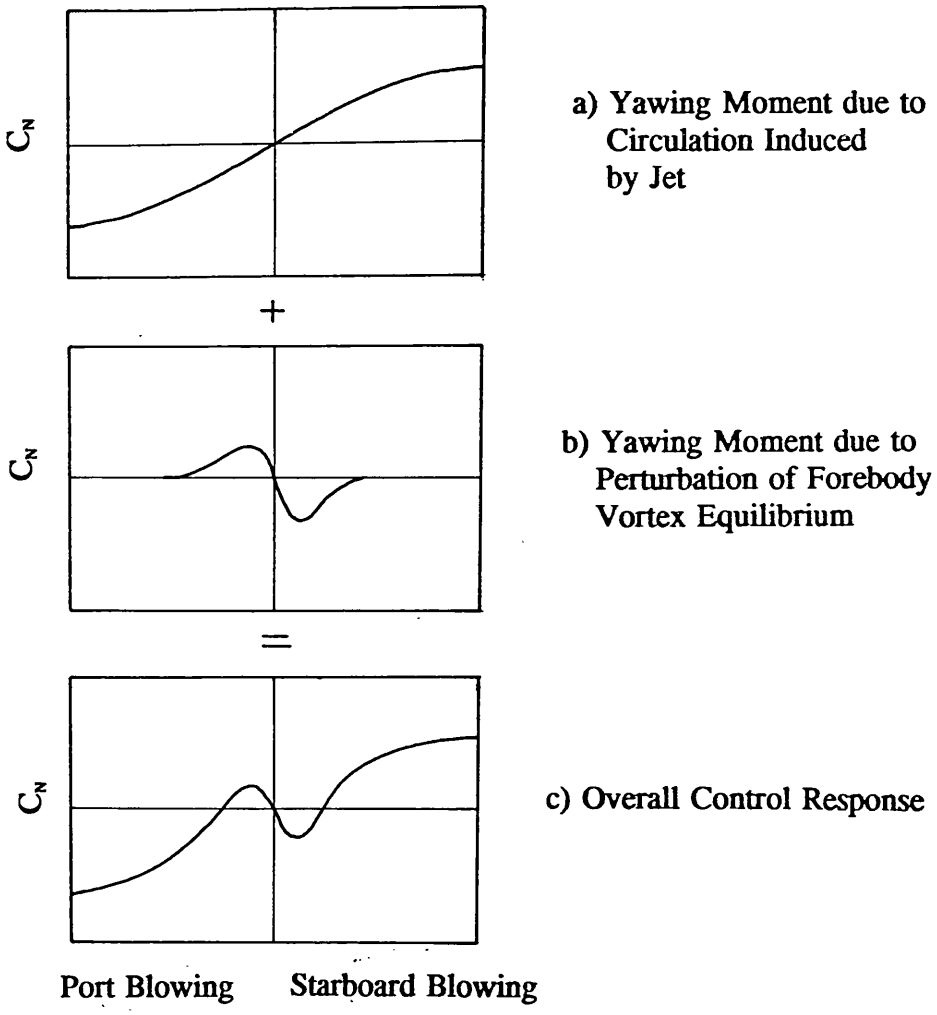

Figure 4.39 *Conceptual Model of Blown Control Response*

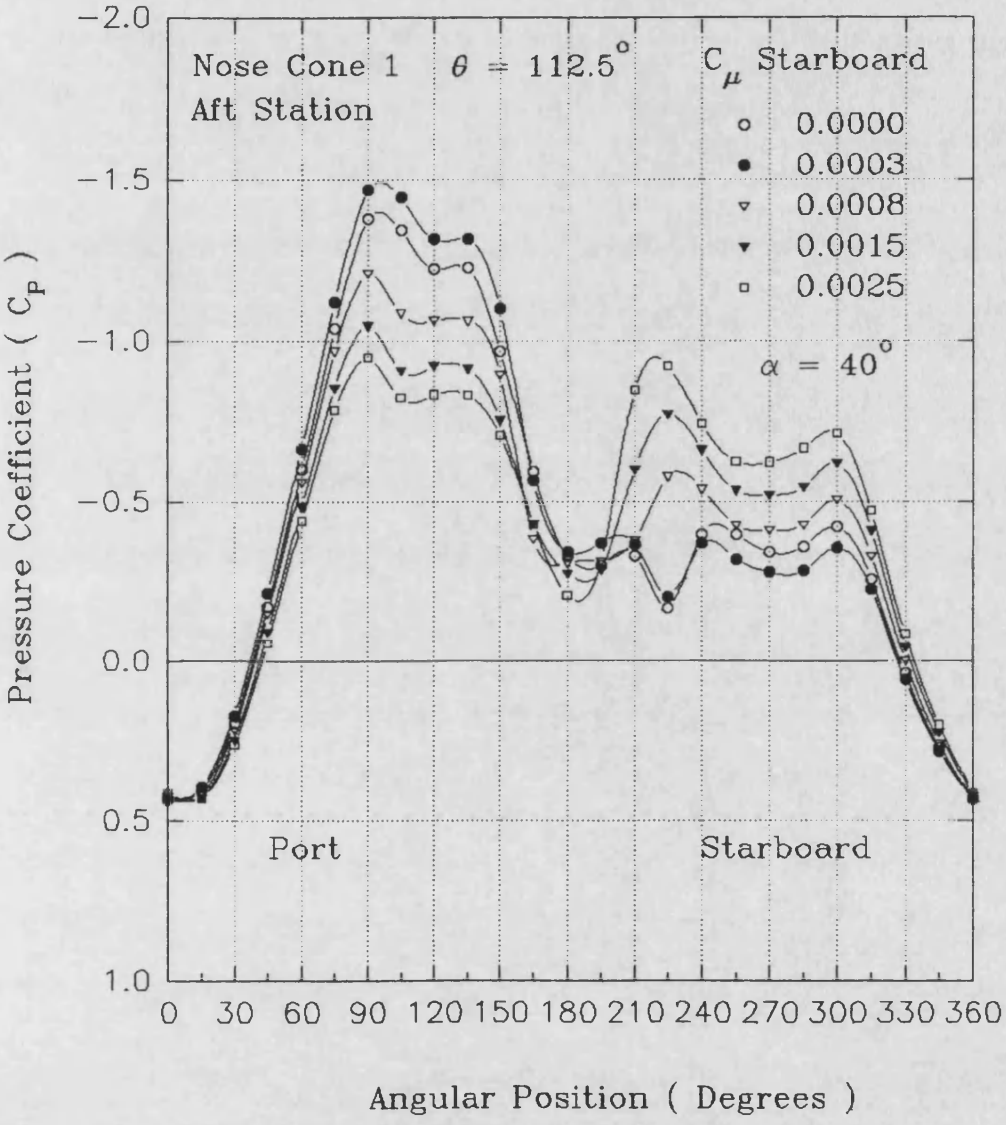

Figure 4.40 *Pressure Distributions at Aft Forebody Tapping Station During Blown Control Reversal*

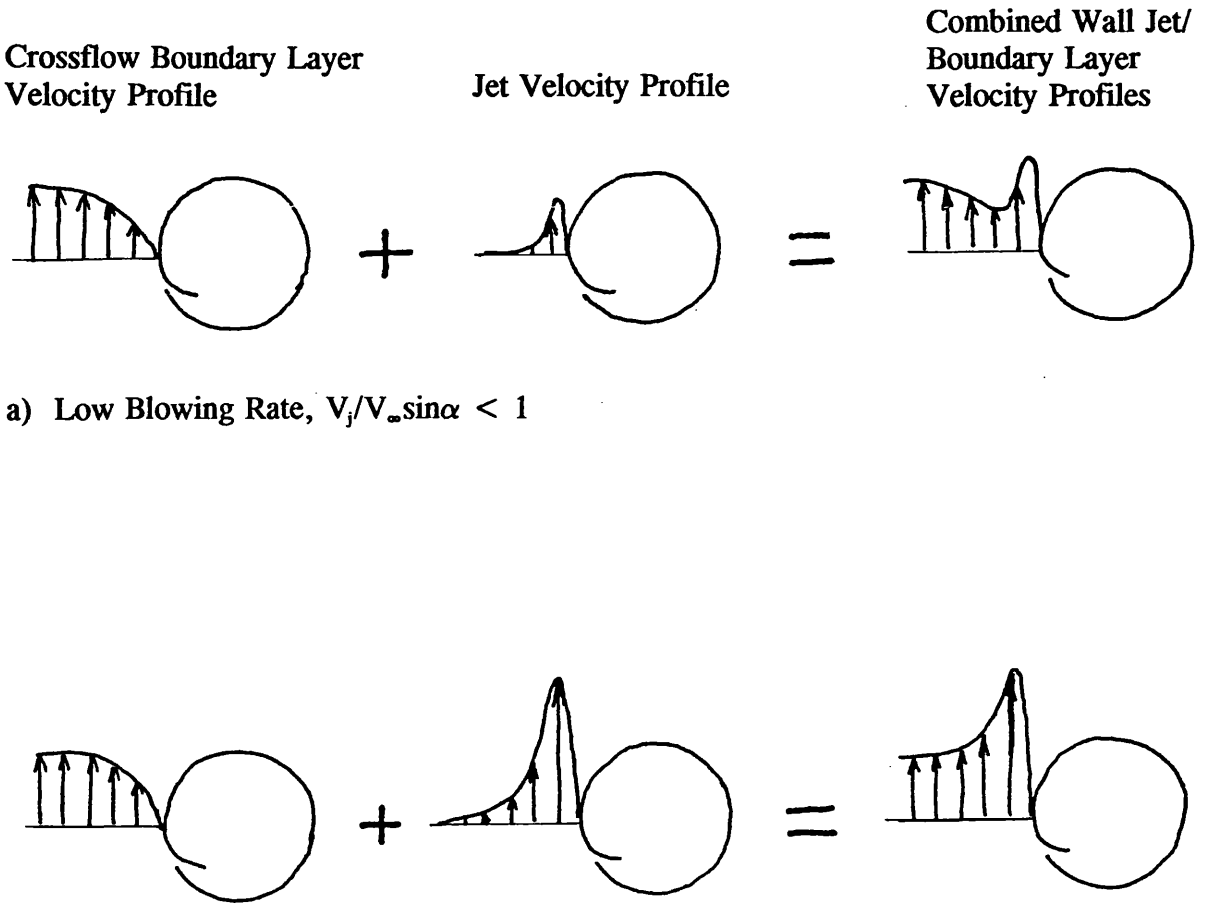

Figure 4.41 *Crossflow Velocity Profiles for Low and High Blowing Rates*

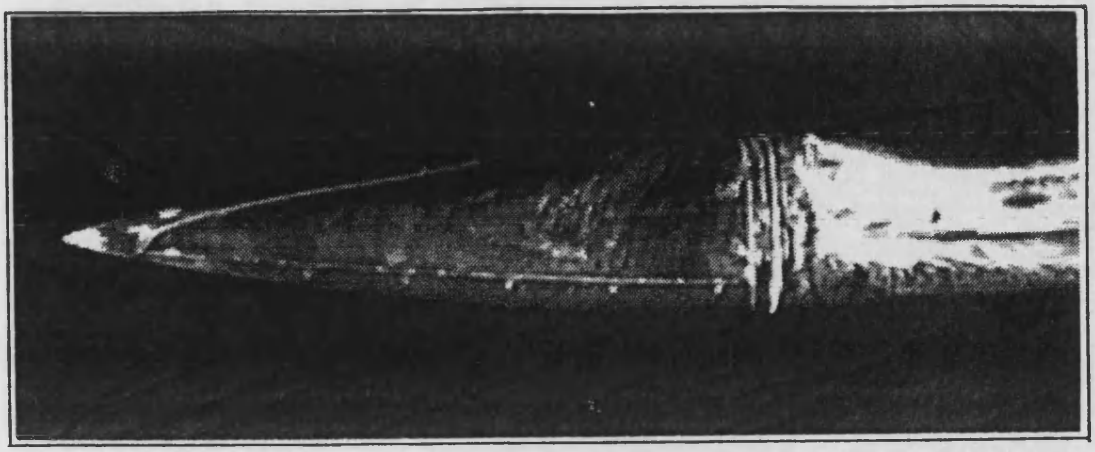

$\alpha = 40^{\circ}$ $C_{\mu} = 0.001$ $\theta = 50^{\circ}$ $\ell = 240\text{mm}$

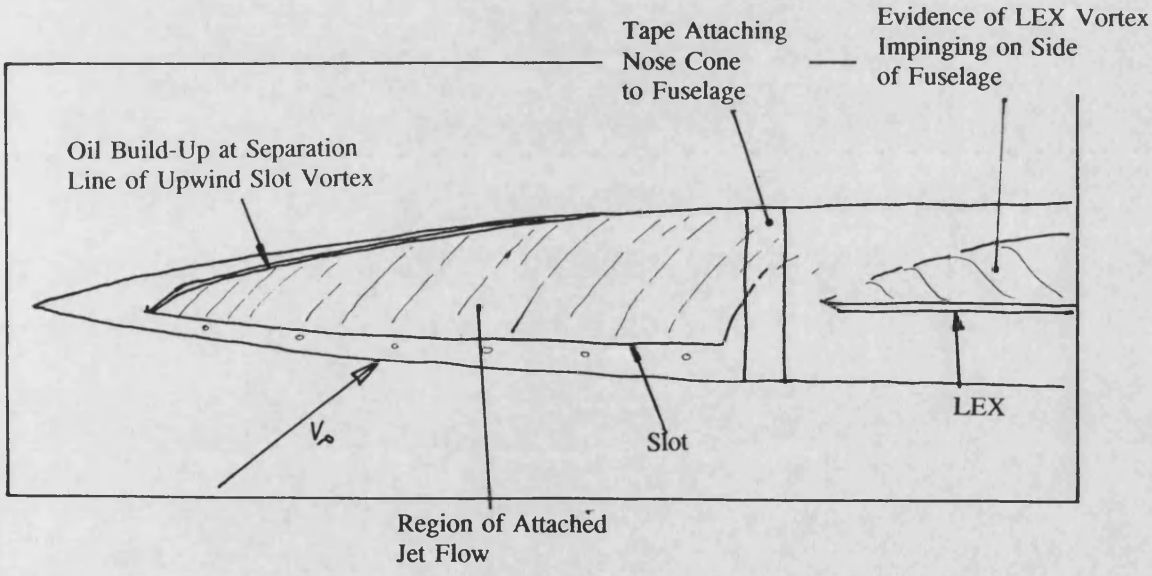

Figure 4.42 *Surface Flow Visualisation on Blown Side of Forebody at 40° angle of attack*

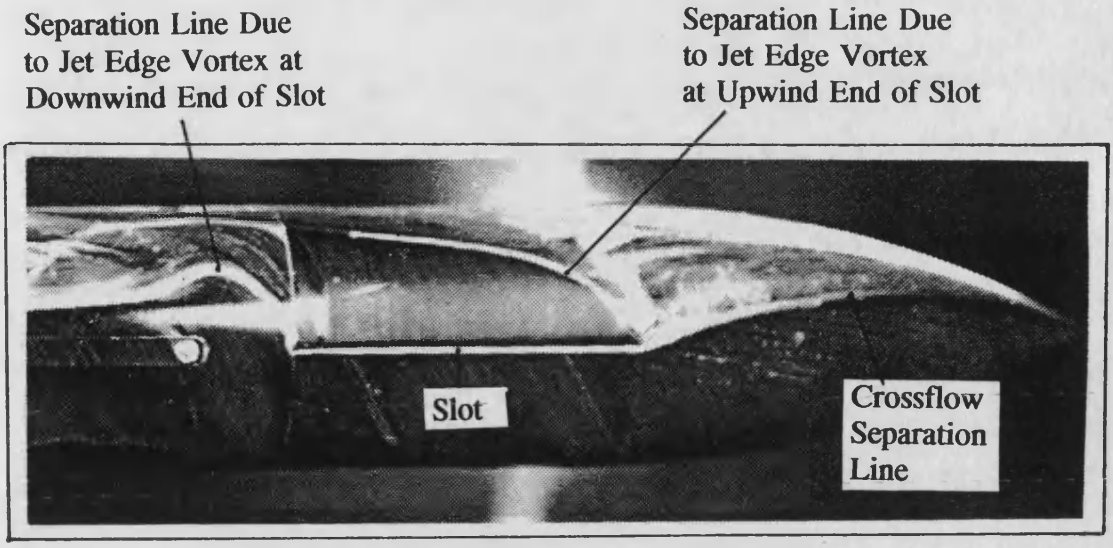

$\alpha=30°$ $C_{\mu}=0.2$ $Re_D=50000$

Figure 4.43 *Surface Flow Visualisation of Slot Blowing on a Slender Body at Incidence, after Celik, ref 90*

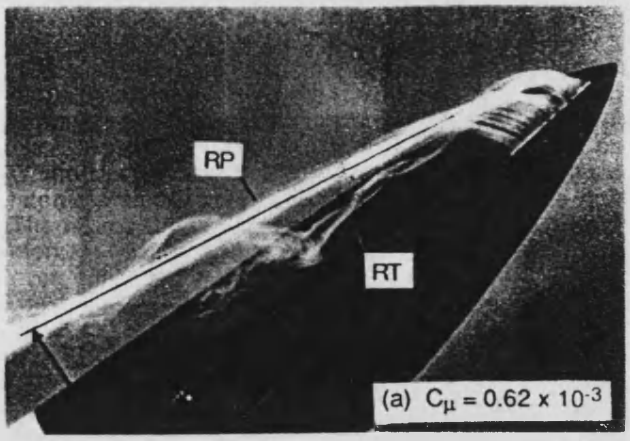

Figure 4.44 *Water Tank Flow Visualisation of Slot Blowing on an F-18 Forebody, after Ng, ref 88*

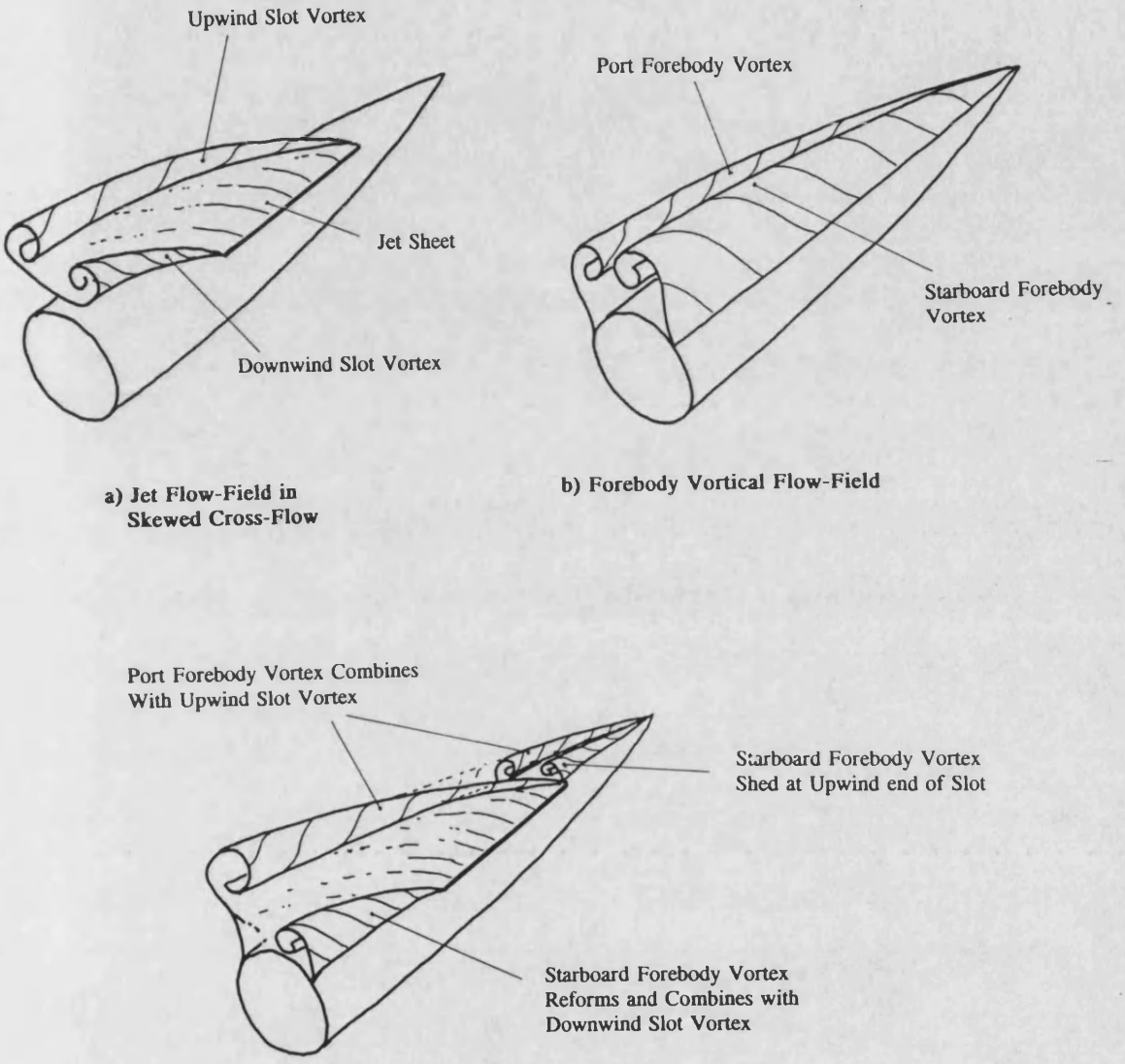

a) Jet Flow-Field in Skewed Cross-Flow

b) Forebody Vortical Flow-Field

c) Combination of Flow-Fields a) and b)

Figure 4.45 *Schematic of Interaction Between Wall Jet and Forebody Flows*

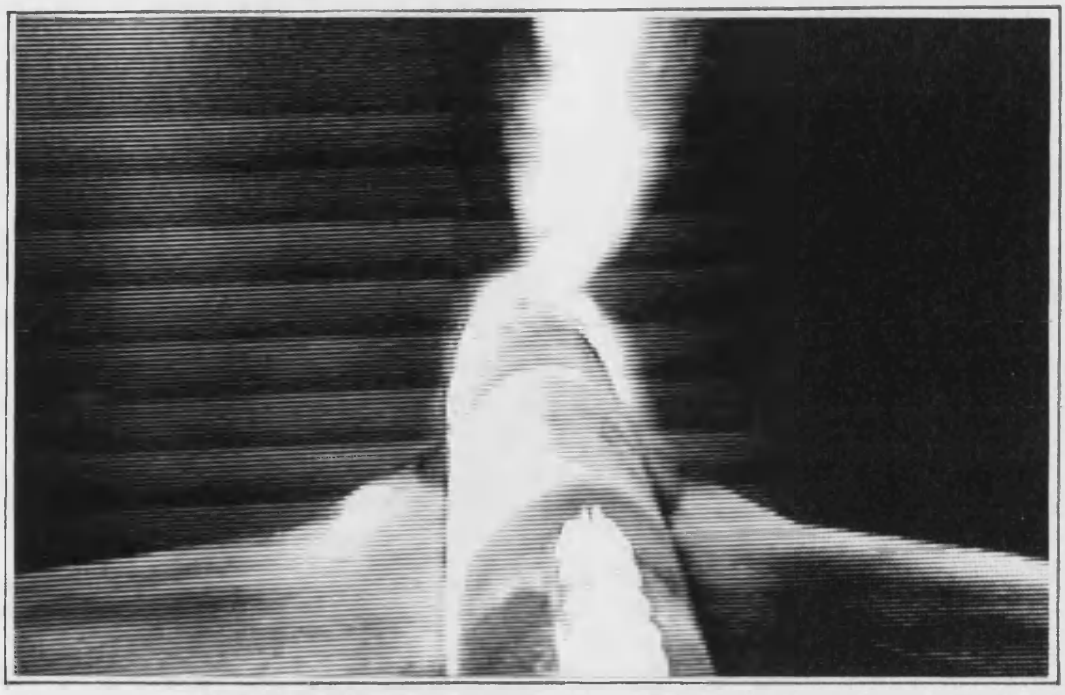

View From Rear of Model,
Looking Upstream
$\alpha = 40°$ C_μ Port = 0.004 Perspex Nose Cone

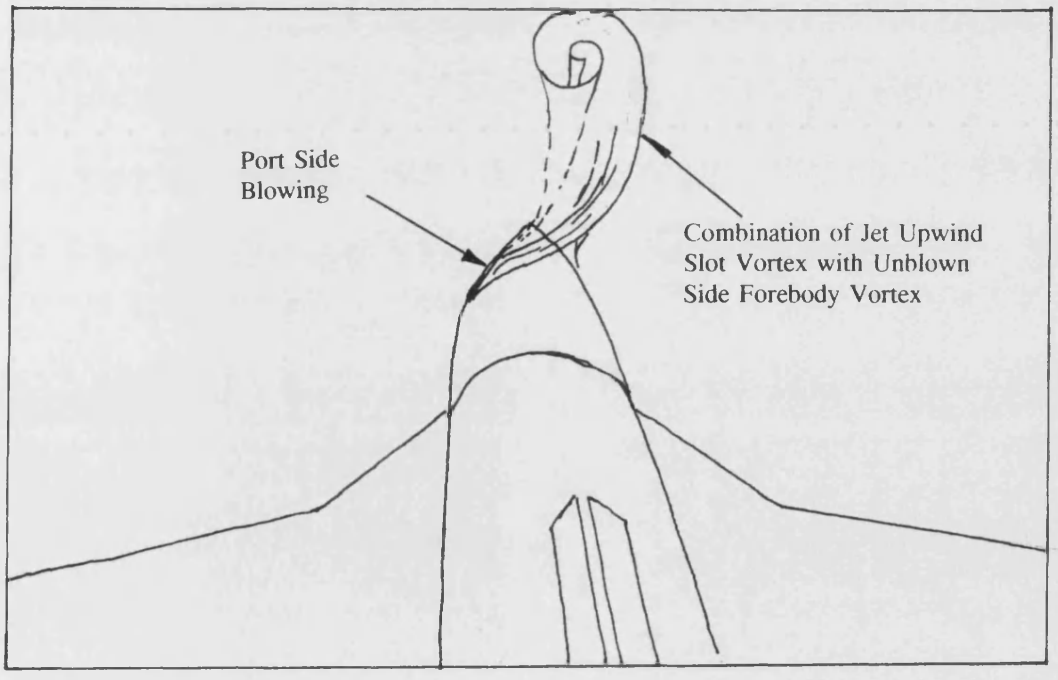

Figure 4.46 *Flow Visualisation of Upwind Slot Vortex Combining with Unblown Side Forebody Vortex*

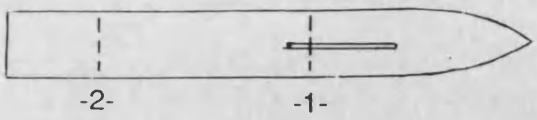

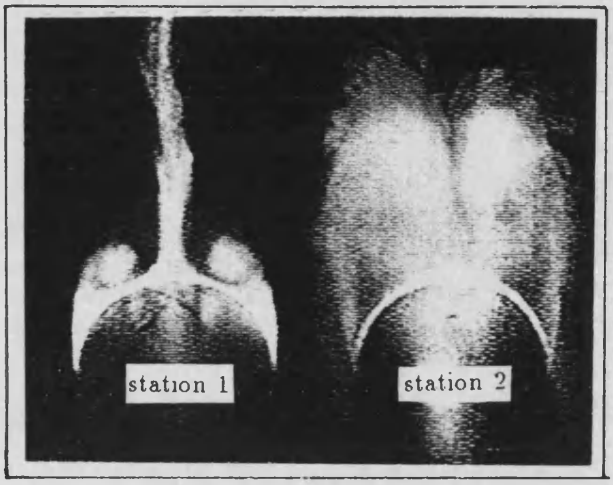

$Re_D = 20000$
$M_\infty = 0.02$
$C_\mu = 0.0$

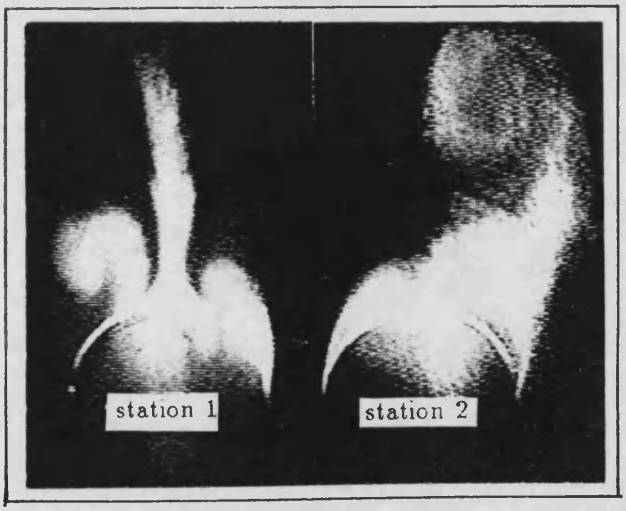

$Re_D = 20000$
$M_\infty = 0.02$
$C_\mu = 0.2$

Figure 4.47 *Smoke/Laser Light Sheet Flow Visualisation Showing Strengthened Unblown Side Forebody Vortex Due To Blowing, after Celik, ref 90*

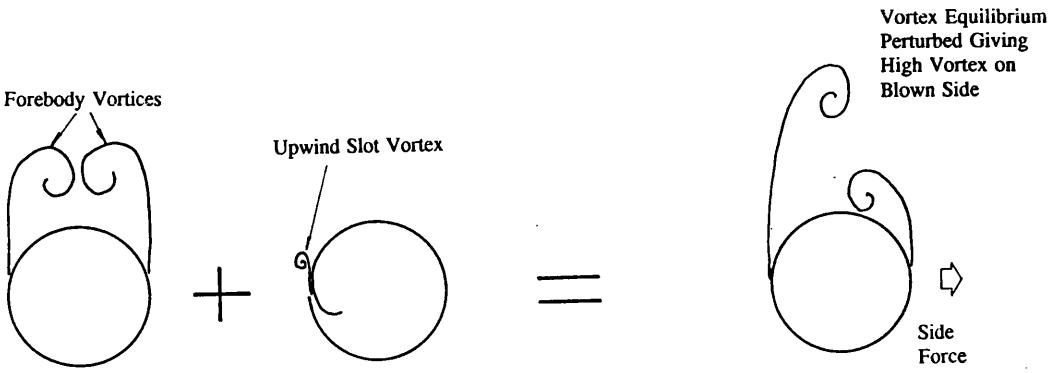

a) Low Blowing Rate $V_j < V_\infty \sin \alpha$

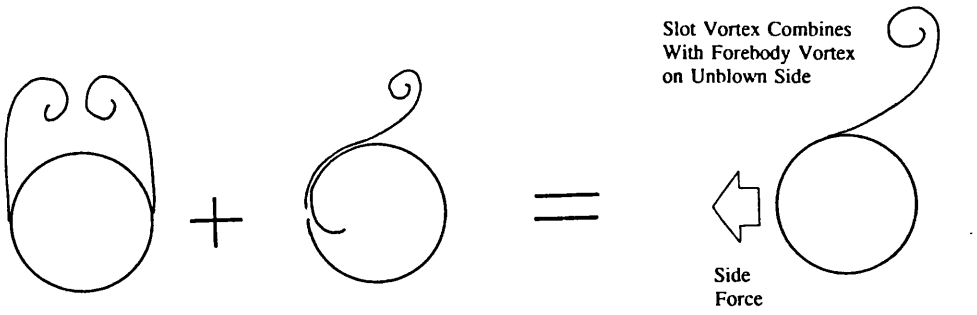

b) High Blowing Rate $V_j > V_\infty \sin \alpha$

Figure 4.48 *Mechanism for Control Reversal at Low Blowing Rates*

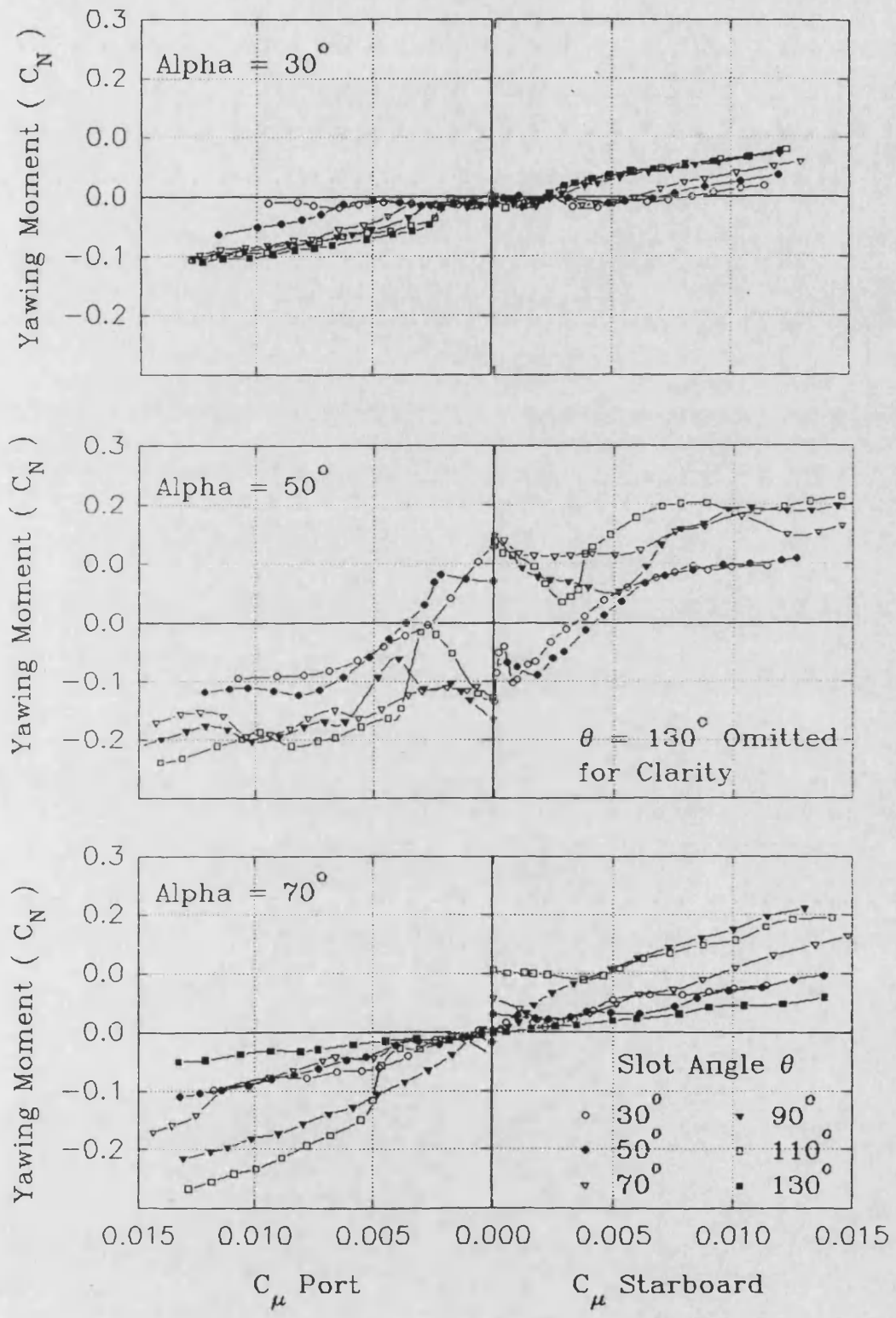

Figure 4.49 *Effect of Slot Angular Position on Blown Control Response*

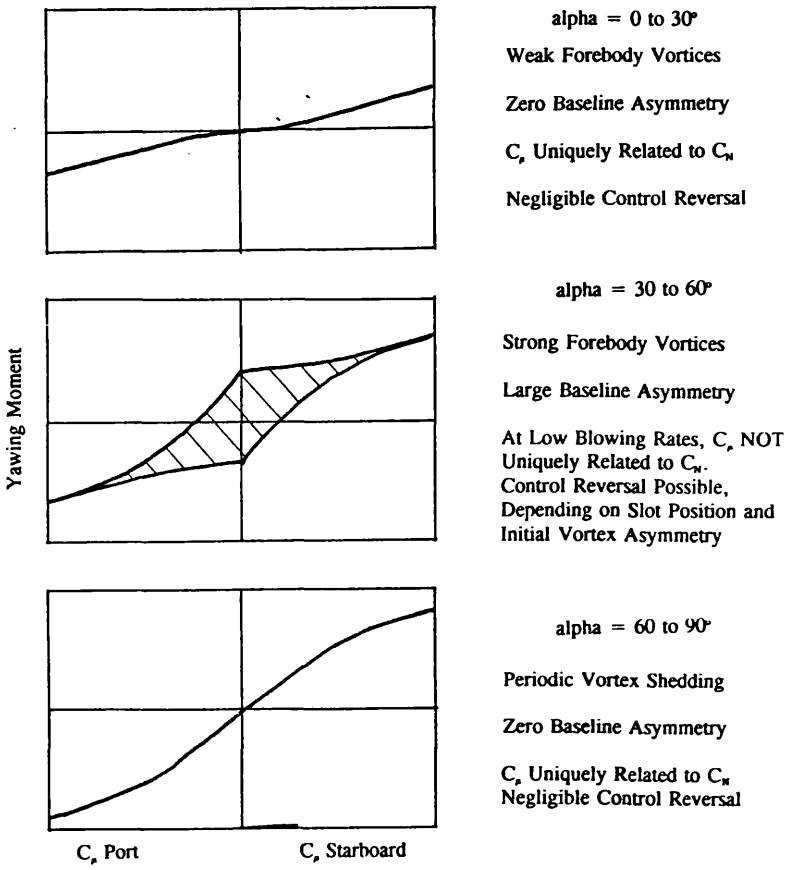

Figure 4.50 *Effect of Baseline Flow Conditions on Blown Control Response*

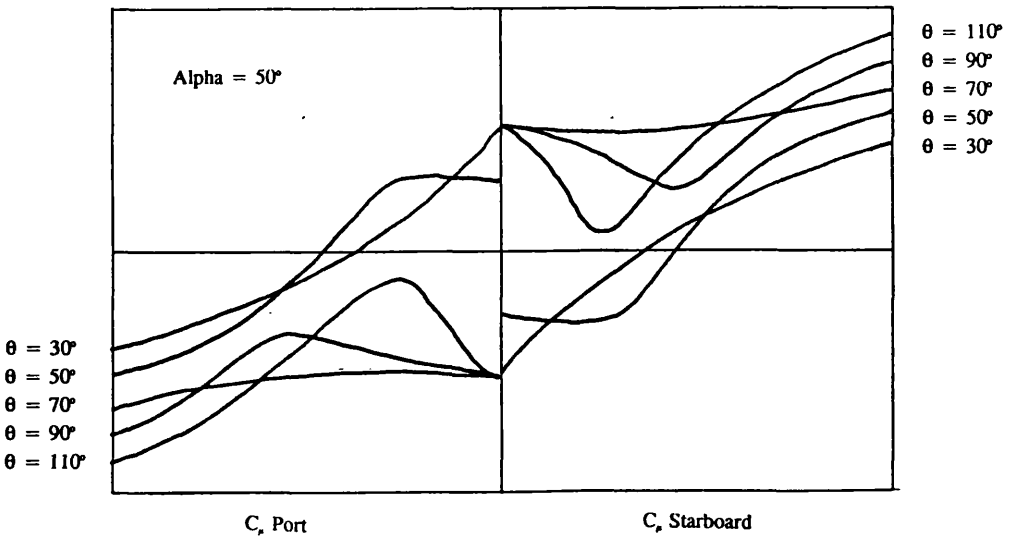

Figure 4.51 *Sketch of Blown Control Response for Different Slot Angles at 50° Angle of attack*

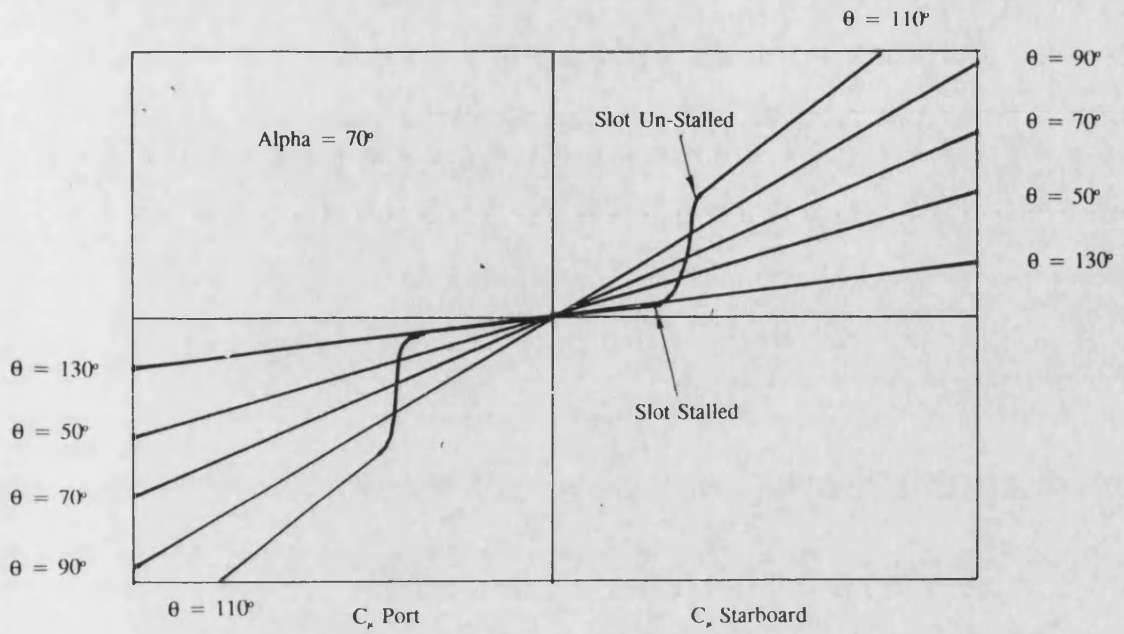

Figure 4.52 *Sketch of Blown Control Response for Different Slot Angles at 70° Angle of Attack*

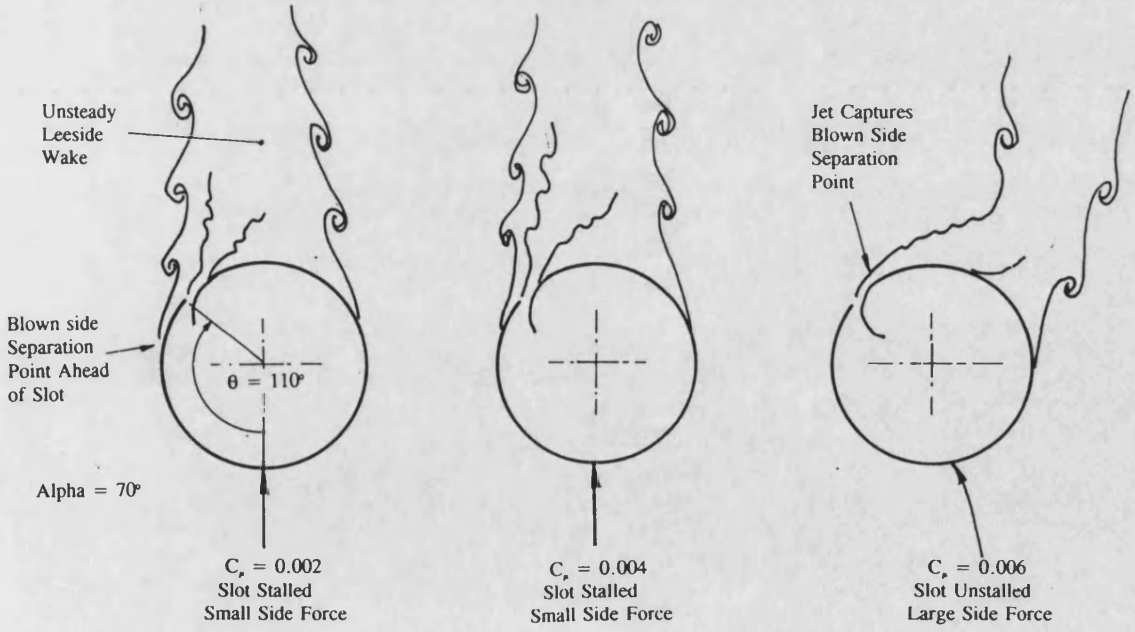

Figure 4.53 *Schematic of Slot Stall Phenomenon*

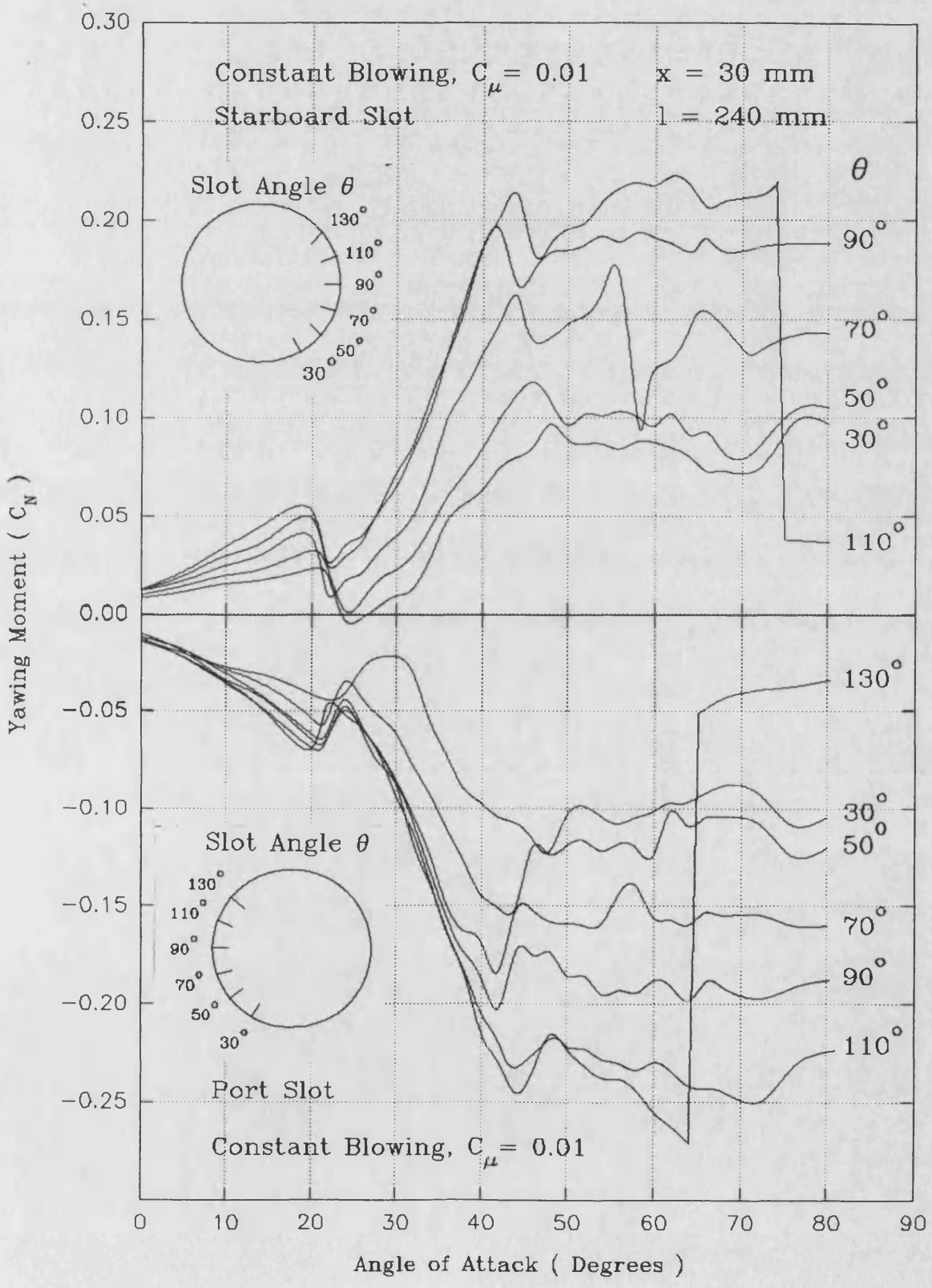

Figure 4.54 *Effect of Slot Angle on Magnitude of Yawing Moment Available From a Fixed Blowing Level*

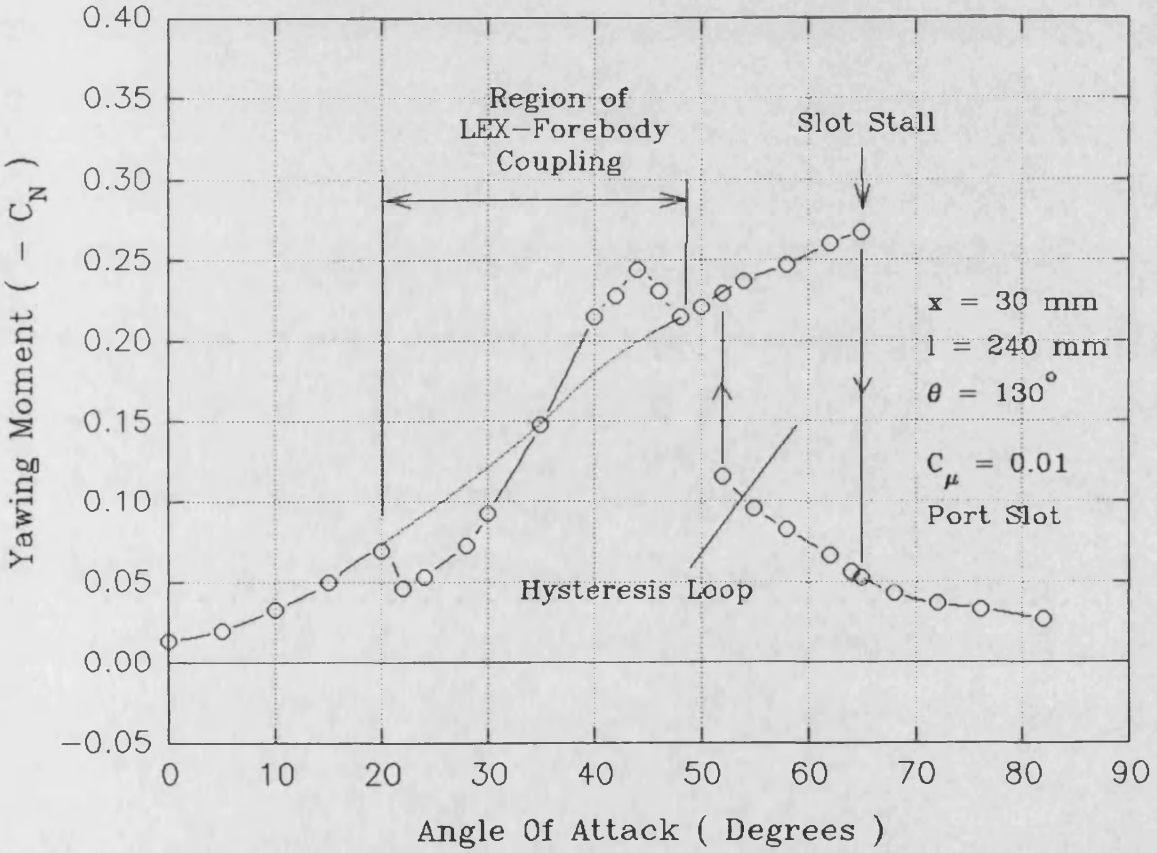

Figure 4.55 *Hysteresis Loop for Angle of Attack Initiated Slot Stall*

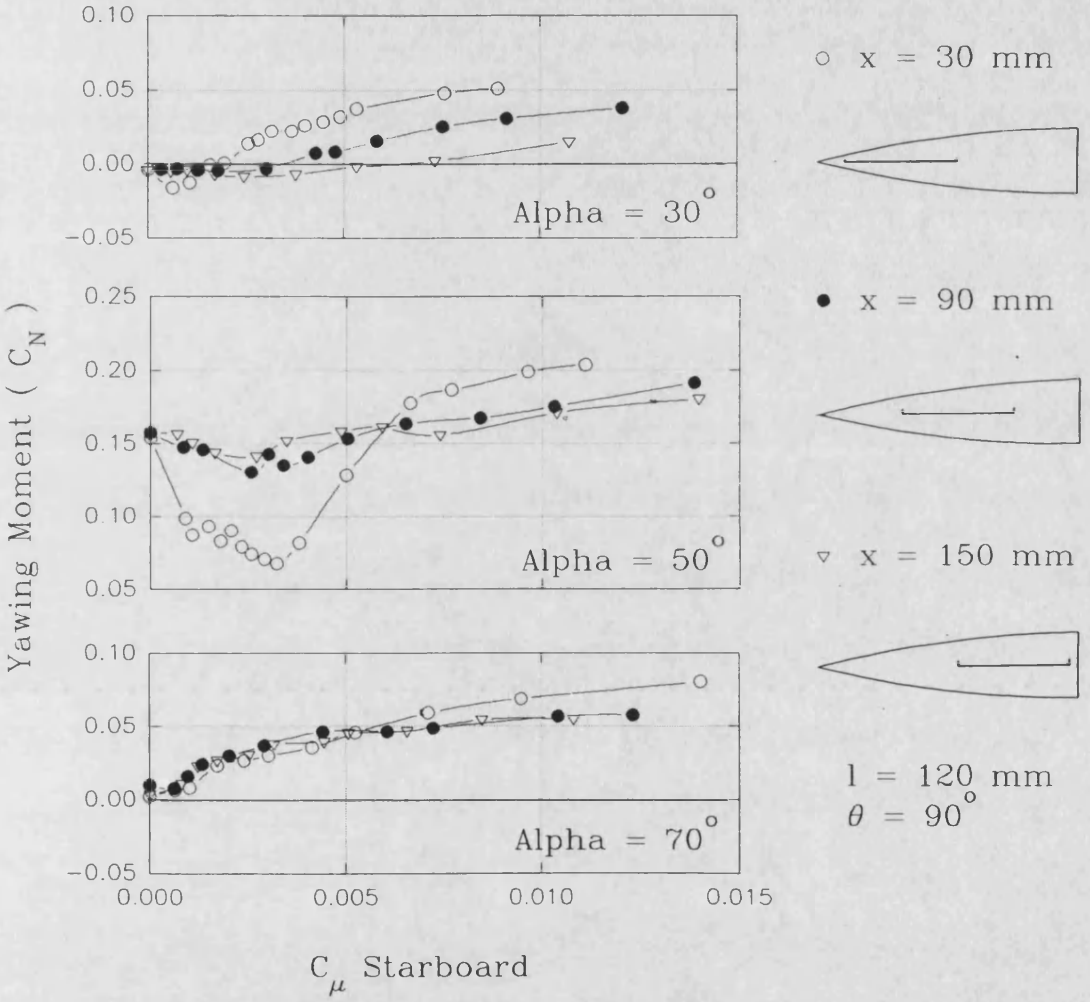

Figure 4.56 *Effect of Slot Longitudinal Position on the Blown Control Response*

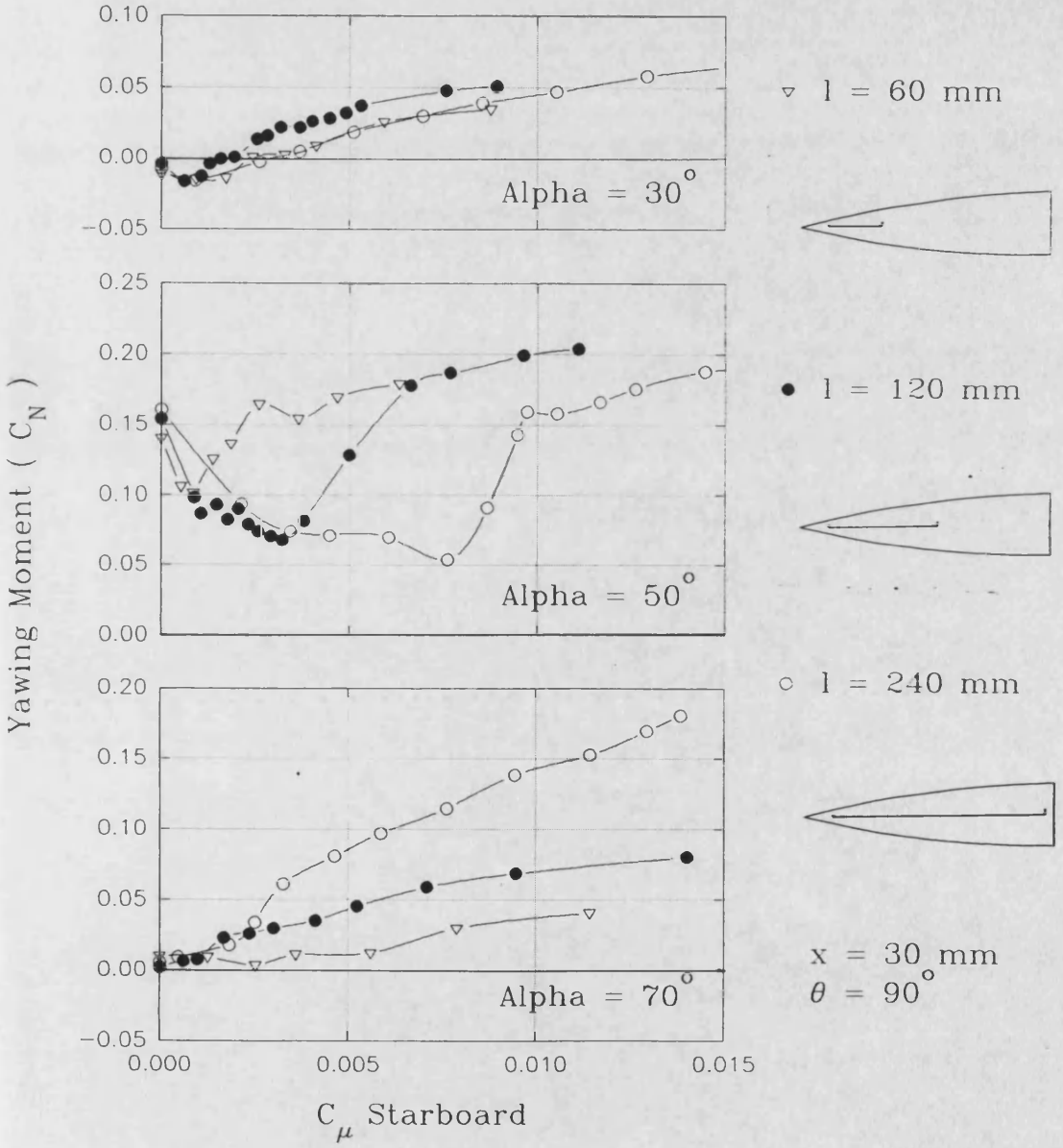

Figure 4.57 *Effect of Slot Length on the Blown Control Response*

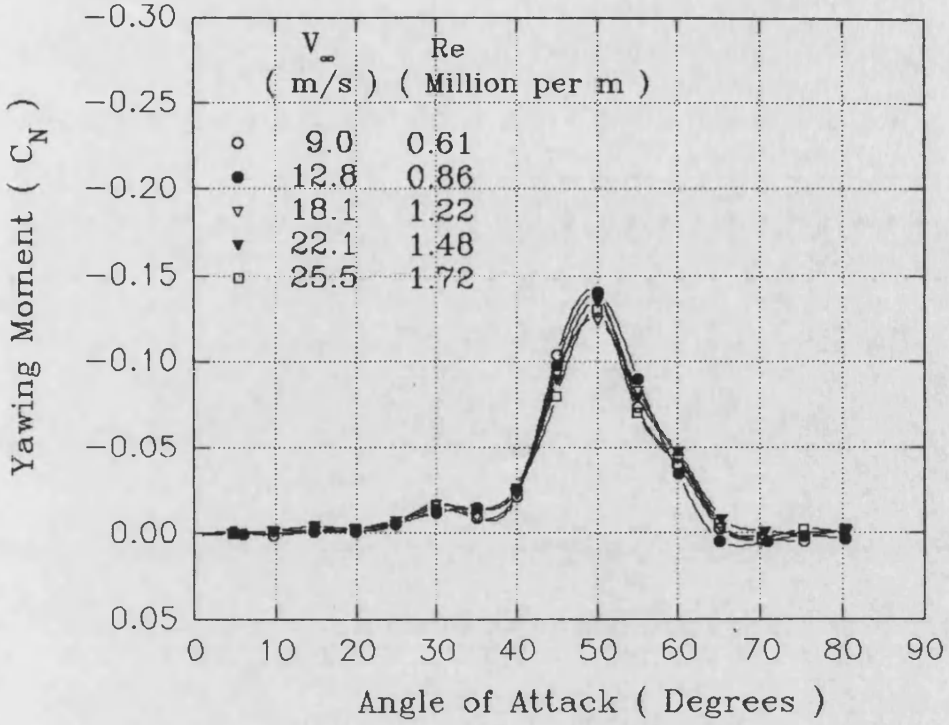

Figure 4.58 *Effect of Free Stream Reynolds Number on Unblown Yawing Moment Characteristic*

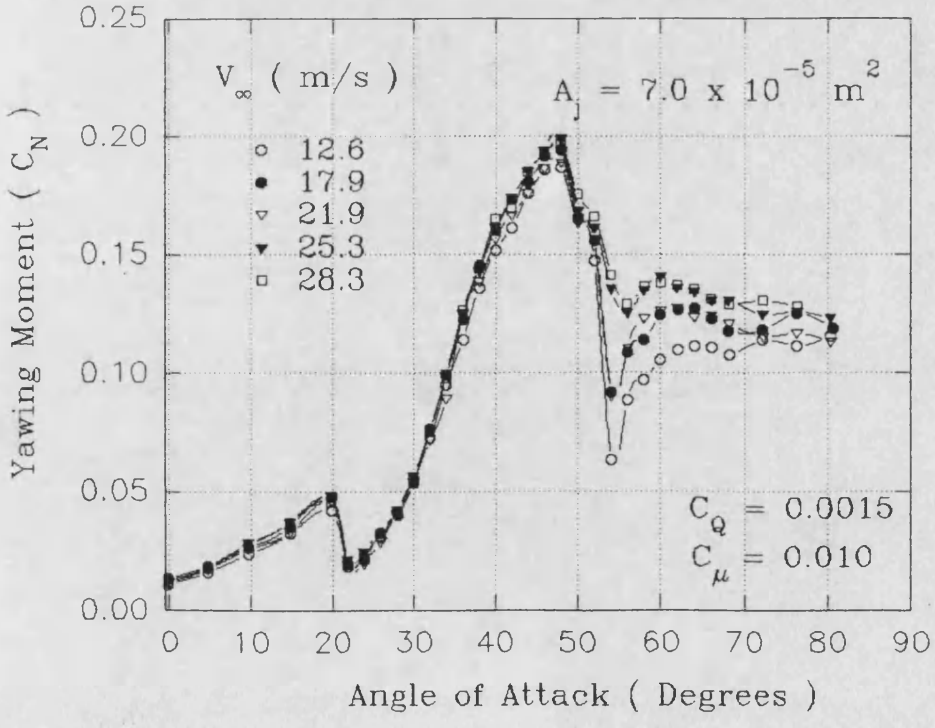

Figure 4.59 *Effect of Free Stream Speed on Ability of C_μ and C_Q to Collapse Yawing Moment Data, Slot Area Constant.*

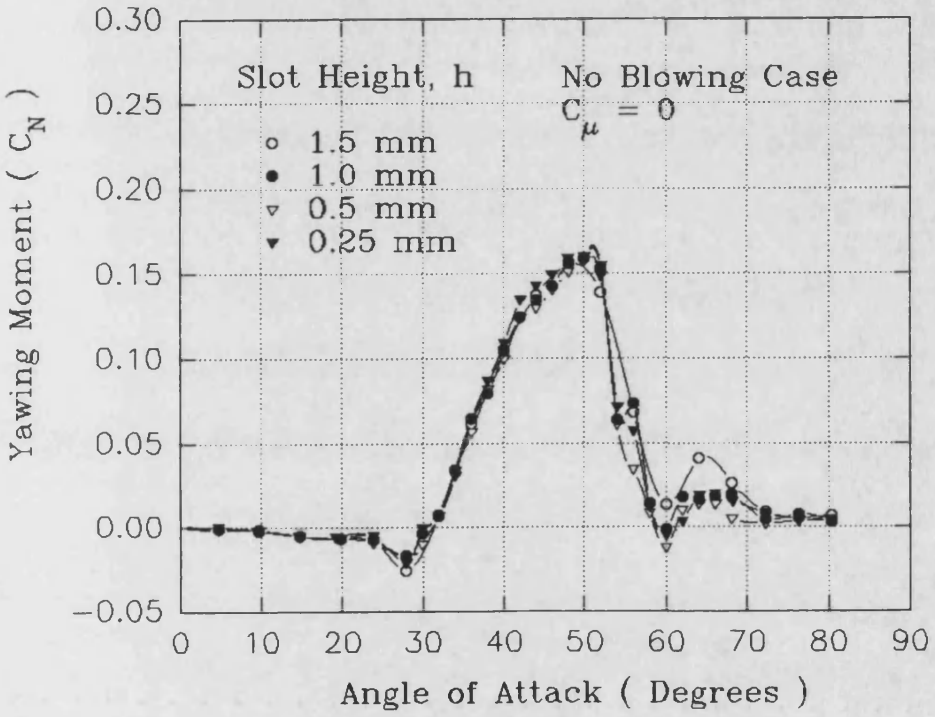

Figure 4.60 *Effect of Changing Slot Height on Unblown Yawing Moment Characteristic*

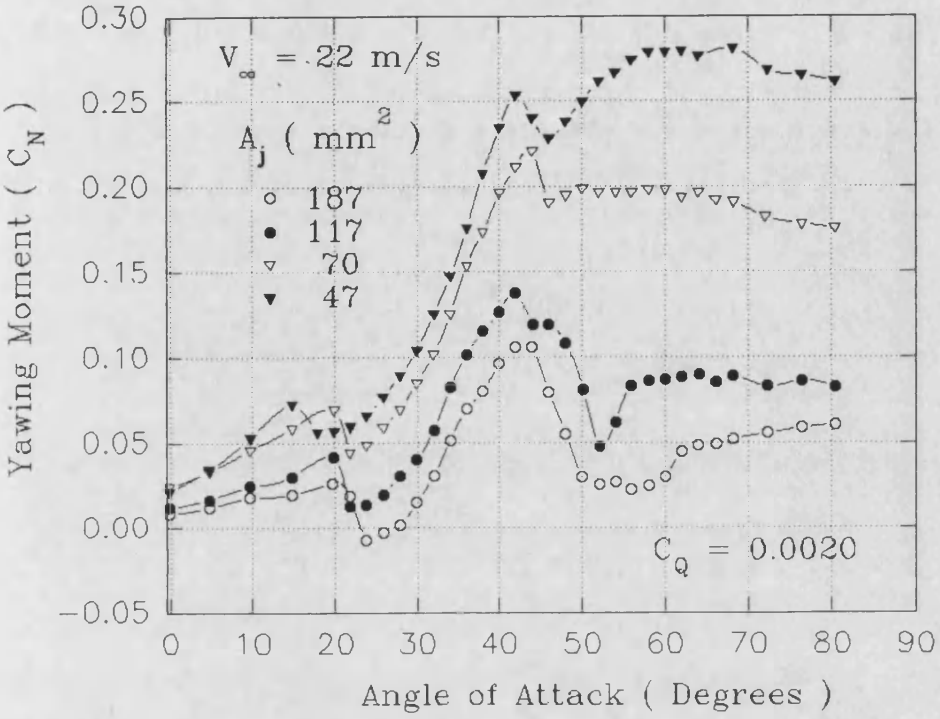

Figure 4.61 *Use of C_Q to Collapse Yawing Moment Data, Variable Slot Area*

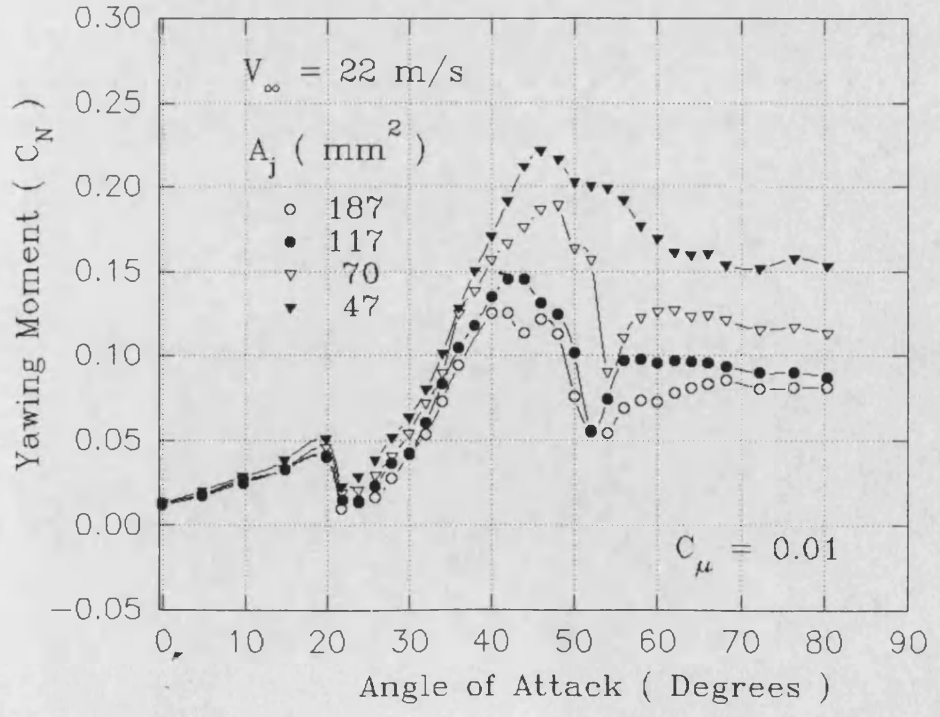

Figure 4.62 *Use of C_μ to Collapse Yawing Moment Data, Variable Slot Area*

CHAPTER 5

CONCLUDING REMARKS

5.1 SUMMARY OF RESULTS

5.1.1 Scope of Experiments

In the present study, the concept of aircraft yaw control by Tangential Forebody Blowing has been investigated experimentally. Three-dimensional behaviour of incompressible, curved wall jets under quiescent conditions was examined through flow visualisation experiments on a variable wall radius/slot aspect ratio test rig. Wind tunnel tests on a generic combat aircraft model fitted with blowing slots in the nose cone were performed statically at sub-scale Reynolds number and incompressible flow conditions. Angles of attack from 0° to 90° and a range of blowing levels were investigated. All tests were with the model at zero yaw angle.

5.1.2 Curved Wall Jet Fluid Dynamics

For finite length blowing slots, the edges of a curved wall jet roll up into a pair of intense vortices. As the jet develops, these vortices grow in size and converge towards the jet centreline. Convergence of the edge vortices effectively limits the angular attachment capability of three-dimensional curved wall jets. The most important parameter for describing slot/wall geometry is ℓ/r. This determines the degree of two-dimensionality for a particular slot installation. To achieve approximately two-dimensional flow values of ℓ/r in excess of 10 are required. For most practical slot installations on aircraft forebodies ℓ/r values are of the order of 3 and the resulting jet flow is expected to be highly three-dimensional.

5.1.3 Generic Combat Aicraft Model: Baseline Aerodynamics

Rudder yaw control is acceptable up to 35° angle of attack. Beyond this destabilising yawing moments from forebody flowfield asymmetry are greater than stabilising moments available from maximum control deflection.

Two angle of attack break points are identified: α_{asym} defines the angle of attack at which the forebody vortices become asymmetric and α_{pvs} marks the angle of attack at which the forebody vortical flow becomes unsteady.

For the fineness ratio 4 tangent ogive nose cone used on the wind tunnel model $\alpha_{asym} \approx 20°$ and $\alpha_{pvs} \approx 60°$.

Out-of-plane forces on the forebody between $\alpha_{asym} < \alpha < \alpha_{pvs}$ are due to steady asymmetric arrangement of the forebody vortices. It is speculated that this establishes circulation in the crossflow plane. The combination of circulation and the crossflow component of the free stream velocity generates a side force in accordance with the Kutta-Joukowski theory for lifting bodies. The majority of the side force comes from the attached flow on the windward side of the forebody. Asymmetric suction on the leeside of the forebody from the forebody vortices contributes little to the overall side force.

Over an angle of attack range dependent on aircraft geometry, the forebody and wing flowfields are coupled. Here, forebody flowfield asymmetry leads to asymmetric bursting of the LEX vortices and significant rolling moments may be generated.

5.1.4 Forebody Flow Control

Tangential forebody blowing utilises the unique attachment and entrainment properties of a curved wall jet to control the forebody flowfield. However, the vortices produced

at the edges of the jet reduce the efficiency of the control and can interact unfavourably with the forebody flowfield.

For a given blowing rate, the magnitude of yawing moment available increases with angle of attack. This contrasts with decreasing rudder yaw control power.

For efficient yaw control in the region $\alpha_{asym} < \alpha < \alpha_{pvs}$ it is most appropriate to perturb the forebody flowfield at the nose tip. This may be achieved by placing a short blowing slot as far forward as possible on the forebody. Control inputs are then amplified as the forebody vortices develop downstream.

When $\alpha > \alpha_{pvs}$ the term vortex control no longer applies. Here, longer slots are required. These slots may be placed further aft on the forebody without loss of efficiency.

Control schemes utilising nose tip perturbation devices such as actuated strakes can only work up to $\alpha = \alpha_{pvs}$. For flow control above this angle of attack, tangential forebody blowing appears to be the only viable approach.

The slot angle (Θ) is an important parameter. Increasing Θ increases the magnitude of yawing moment available from a given blowing rate. Increasing Θ too far, however, results in a high alpha slot stall which is characterised by a rapid step decrease in yawing moment and a hysteresis loop in the C_N - α history.

Tangential forebody blowing produces control yawing moments by modifying the forebody crossflow circulation. This is achieved in two ways, by:

1) modification of the forebody vortex equilibrium condition

2) direct angular momentum injection by the jet

Typically, at low blowing rates the side force is towards the unblown side. As the

blowing level increases the jet momentum mechanism becomes dominant and the side force changes sign. This causes an undesirable control reversal.

Control reversal is dependent on slot geometry and location, and angle of attack. It does not occur for $\alpha > \alpha_{pvs}$. For $\alpha < \alpha_{pvs}$ it may be minimised by careful slot positioning.

At high blowing rates, control forces scale with the jet momentum coefficient. At low blowing rates during the control reversal region forces may scale better with the jet mass flow coefficient.

Mass flow requirements based on C_μ scaling for full scale application are within reasonable engine bleed flow levels. However slot geometry and location optimisation is essential.

5.2 CONCLUSIONS

1) TFB can provide control yawing moments at up to, and beyond, 90° angle of attack. Other types of forebody flow control schemes, such as actuated strakes, can only provide yaw control up to around 60° angle of attack. This makes them less useful as a strategy for enhancing the manoeuvrability of combat aircraft.

2) Effective application of TFB requires careful choice of slot geometry and location. For efficient control between $\alpha_{asym} < \alpha < \alpha_{pvs}$ short slots should be placed near the nose tip. For control above α_{pvs} longer slots are required such that jet three-dimensional effects are reduced. These slots may be located aft of the radome without loss of efficiency.

3) Control response is strongly influenced by the slot angular position. Increasing the slot angle increases the control gain at the expense of lowering the angle of attack at which slot stall occurs. A slot angle of 90° offers a sensible compromise.

4) Control reversal at low blowing rates is experienced between $\alpha_{asym} < \alpha < \alpha_{pvs}$. This is linked to an unfavourable interaction between the upwind slot vortex and the blown side forebody vortex. Control reversal may be reduced by placing the slots further aft on the forebody or by reducing the slot angle. Both these approaches reduce the control gain.

CHAPTER 6

FUTURE WORK

6.1 SHORT TERM

6.1.1 Angle of Attack Extension

The current work tested a wind tunnel model up to 90° angle of attack. There may, however, be advantages in increasing the working angle of attack range of a combat aircraft to in excess of 120°. This would extend the aircraft's pointing cone into the rear hemisphere. Tangential Forebody Blowing, in principle, would be able to generate control moments up to the very high angles of attack required for this type of manoeuvre. Verification of this could be achieved with a relatively simple modification of the present high alpha rig.

6.1.2 Better Understanding of Control Reversal

The fluid mechanism underlying the control reversal at low blowing rates is currently not fully understood, in particular the interaction between the jet edge vortices and the blown side forebody vortex. Careful flow visualisation experiments using a smoke and laser light sheet technique should show what is happening under these flow conditions. This will probably require a specially designed nose cone made from a material that will not melt from the heat of the smoke (as the current plastic nose cones do) and has special provision for smoke outlets built in to the surface.

6.1.3 Multiple Slots

The sensitivity of the blowing performance to slot angular position could be possibly be reduced and the control reversal problem alleviated by using multiple slots at different slot angles, as used on the NOTAR tail boom. Ideally each slot should be

individually controlled. With the current nose cone design it would be relatively simple to add a second or third slot, although with a common plenum chamber individual control of the blowing from each slot could not be achieved.

6.1.4 Non-Circular Forebody Cross Section

One of the major simplifications of the current wind tunnel model is that the fuselage and forebody are of circular cross section. Real combat aircraft may have elliptical, triangular or chined cross sections. Low observable requirements also dictate cross sections which are far from circular.

Non circular cross sections introduce two changes. Firstly the cross flow separation characteristics of the body are altered. For chined type bodies this may effectively fix the separation line. Secondly, the wall profile for the Coanda jet is modified. For a profile with increasing curvature down stream of the jet this should enhance the jet attachment. Conversely, decreasing curvature will reduce the jet attachment. For chined bodies, very high local curvatures may make the application of wall jets inappropriate.

Figure 6.1 shows two possible forebody shapes that could be tested using the vacuum formed construction technique. Note that in both these cases the effective squashing of the body provides increased separation between the forebody vortex cores and an increase in α_{asym}. This has been demonstrated numerically by Fiddes[59] using a vortex sheet model. Non-circular forebody shapes might also show less tendency for control reversal at low blowing rate.

6.2 LONG TERM

6.2.1 Dynamic Experiments

The experiments in the current investigation were performed statically. A number of

researchers, particulary Ericsson[14], have shown the importance of dynamic effects on separated flows at incidence. For this reason some form of dynamic testing is desirable, with at least freedom in yaw and roll. Difficulties in building dynamic rigs and problems of inertia scaling make this a non-trivial problem.

6.2.2 Experiments at Larger Scale

The controversy over the appropriate scaling parameter to use for pneumatic forebody flow control devices has yet to be fully resolved. It is likely that either C_μ or C_Q may be required depending on the particular flow interaction at hand. In particular, the fluid mechanism for the control reversal part of the yawing moment response appears to be driven by C_Q whereas the 'circulation control' part of the response is C_μ driven.

A major limitation of the present work is the relatively low Reynolds number and free stream Mach number at which the tests were performed. This meant that the forebody crossflow separation was always laminar and jet Mach numbers for high blowing rates were well subsonic. At full scale, laminar separation is only to be expected towards the front of the forebody, followed by turbulent separation further aft. It is also likely that slots will be run at choked conditions to maximise the jet momentum for a given size of slot installation. These problems can only be addressed by testing a larger scale model at higher speeds.

6.2.3 Integration of Lateral Control Devices

It is anticipated that combat aircraft in the next century will achieve lateral control by a combination of techniques, including conventional moving surface controls, forebody/wing flow control and thrust vectoring. The use of thrust vectoring for yaw control at low angles of attack and forebody flow control for yaw control at high angles of attack means that the fin area can be substantially reduced[110]. This will provide significant reductions in drag and weight, and improve aircraft low-observability. A sketch of a possible future finless aircraft is shown in figure 6.2.

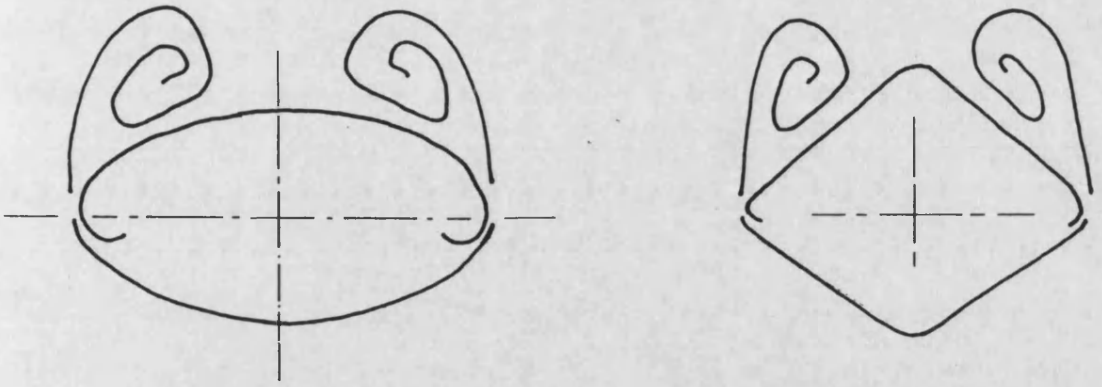

Figure 6.1 *Application of Tangential Forebody Blowing to Forebodies of Non-Circular Cross Section*

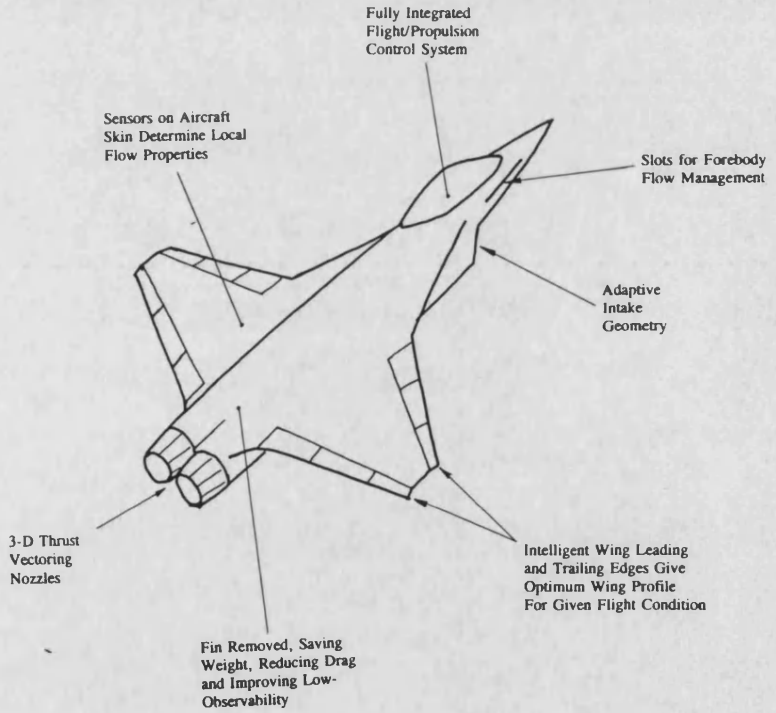

Figure 6.2 *Future Finless Combat Aircraft Concept Made Possible by the Integration of Novel Control Methods with Advanced Control Systems*

APPENDIX A

Crossflow Circulation Model for Calculation of Blown Yawing Moments

A1 Overview

This appendix describes a simple model for the generation of side forces on a cylindrical body in crossflow due to the circulation induced by a tangential jet. The model is used to predict blown yawing moment coefficients acting on the wind tunnel model.

A2 Jet Induced Circulation

The circulation about a cylinder may be defined as the integral of the surface tangential velocity (strictly at the edge of the boundary layer) around the body cross section, equation A1.

$$\Gamma = \oint V_T ds \tag{A1}$$

For the purposes of determining jet induced circulation, a tangential jet may be represented by a given surface velocity distribution. Assuming a very simple jet in which the velocity is at all points equal to the jet exit velocity and that the jet separates from the surface at a given angle θ_{sep} from the slot, figure A1, the circulation induced by the jet is given by

$$\Gamma_j = V_j r \theta_{sep} \tag{A2}$$

Note that there is a direct analogy between the circulation produced by the attachment of a jet on a cylinder to the circulation produced by spinning a cylinder. If a jet of constant velocity V_j remains attached to a cylinder for $\pi/2$ radians (i.e. one quarter of the way round the cylinder) the circulation produced is equivalent to spinning the cylinder at an angular velocity that gives a surface tangential velocity equal to one quarter of the jet velocity.

Using the definition of the jet momentum coefficient (equation 3.13 with $\rho_j = \rho_\infty$), the jet velocity in equation A2 may be replaced by

$$V_j = V_\infty \sqrt{\frac{C_\mu A_{ref}}{2 A_{jet}}} \tag{A3}$$

giving

$$\Gamma_j = V_\infty \sqrt{\frac{C_\mu A_{ref}}{2 A_{jet}}}\, r\,\theta_{sep} \tag{A4}$$

The side force (per unit length) due to this circulation coupled with a free stream crossflow component is given by the Kutta-Joukowski theorem for lifting bodies, equation A5

$$y = \rho\, V_\infty \sin\alpha\, \Gamma_j \tag{A5}$$

Substituting equation A4 into A5, leads to

$$y = \rho\, V_\infty^2 \sin\alpha \sqrt{\frac{C_\mu A_{ref}}{2 A_{jet}}}\, r\,\theta_{sep} \tag{A6}$$

Converting this to coefficient form, the side force per unit length of slot on a cylindrical body is

$$C_y = \sin\alpha \sqrt{\frac{2 C_\mu}{A_{ref} A_{jet}}}\, r\,\theta_{sep} \tag{A7}$$

Assuming an effective slot length of ℓ and a moment arm x of the slot about a moment reference point, figure A2, the yawing moment coefficient due to blowing is given by

$$C_N = \sin\alpha \sqrt{\frac{2 C_\mu}{A_{ref} A_{jet}}}\, r\,\theta_{sep}\, \ell\, \frac{x}{c} \tag{A8}$$

i.e.

$$C_N = const \sin\alpha \sqrt{C_\mu} \qquad \text{(A9)}$$

A3 Calculation of Blown Yawing Moment for Wind Tunnel Model

The yawing moment produced by for a given jet momentum coefficient will be calculated using the following data

$A_{ref} = 0.15\ m^2$

$A_{jet} = 6x10^{-5}\ m^2$

$x = 0.3$ m

$r = 0.025$ m (average radius of forebody)

$\theta_{sep} = \pi/2$ (90° round from slot exit)

$c = 0.3$ m

$\ell = 0.180$ m

Note that the effective slot length is appreciably less than the geometric slot length due to contraction of the edges of the jet, figure A3. If the attached area of the jet is assumed to be elliptic then the ratio of the attached area ($\pi \ell r \theta_{sep}/4$) to the ideal area ($\ell r \theta_{sep}$) is $\pi/4$. Thus as an approximation, the effective length of the slot may be estimated at 75% of the geometric length.

Substitution of the above numbers into equation A8 leads to

$$C_N = 3.3 \sin\alpha \sqrt{C_\mu} \qquad \text{(A10)}$$

This is shown graphically in figure 4.36.

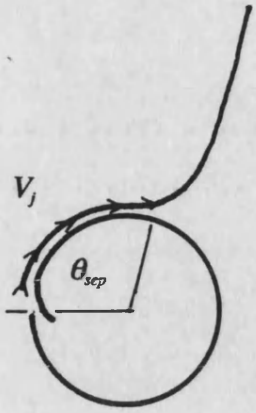

Figure A1 *Simplified Representation of Tangential Jet*

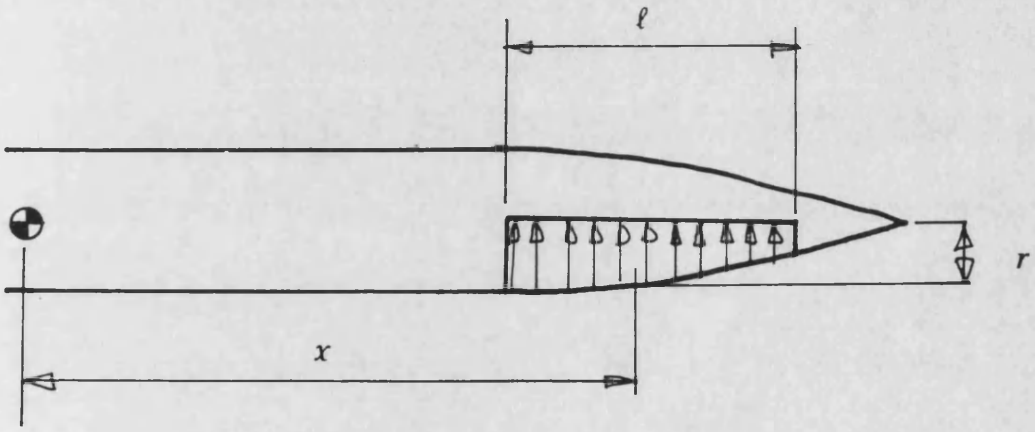

Figure A2 *Model Geometry for Calculating Blown Yawing Moment*

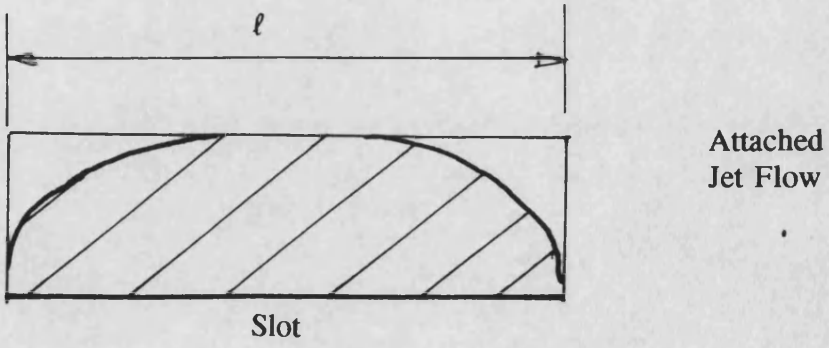

Figure A3 *Reduction in Attached Flow Area of Jet to Edge Contraction*

REFERENCES

1. Whitford, R., "Design for Air Combat", Janes Publishing , 1987.

2. Skow, A., "Agility as a Contributor to Design Balance", Journal of Aircraft, Vol 29, No 1, May 1990, pp 34-46.

3. Ashley, H. "On the Feasibility of Low-Speed Aircraft Manoeuvring Involving Extreme Angles of Attack", J of Fluids and Structures, 1:319-335, 1987.

4. Chody, J "Combat Aircraft Control Requirements for Agility", AGARD Symposium on Aerodynamics of Combat Aircraft Controls and of Ground Effects, Madrid, October, 1990.

5. Lang, J., Francis, M., "Unsteady Aerodynamics and Dynamic Aircraft Manoeuvrability", Paper 29, AGARD CP-386.

6. Herbst, W. "Future Fighter Technologies", J of Aircraft, Vol 17, No 8, pp 561-566. August 1980.

7. Herbst, W. "Dynamics of Air Combat", J of Aircraft, Vol 20, No 7. pages 594-599.

8. Ross, A. "High Incidence - The Challenge to Control Systems", Lecture presented to the Royal Aeronautical Society, January 1990.

9. Wood, N., "Developments in Lateral Control on Aircraft Operating at High Angles of Attack", ICAS 90-5.6.3, 1990.

10. Hopkins, H., "A Schematic Notation and Nomenclature for Aircraft Dynamics and Associated Aerodynamics", ARC R&M No 3562,1970.

11. Fratello, D., Croom, M. Nguyen, L., Domack, C., "Use of the Updated NASA Langley Radio-Controlled Drop Model Technique for High Alpha Studies of the X-29A Configuration", AIAA 87-2559 CP.

12. Ross, H., "X-31 enhancement of Aerodynamics for Manoeuvrability Beyond Stall", AGARD CP-497.

13. Bowers, A., Noffz, G, Peron, L., "An Aerodynamic and Jet Deflection Model for Thrust Vectoring on the NASA F/A-18 High-Alpha Research Vehicle", Proceedings of the NASA High Angle of Attack Technology Conference, NASA Langley Research Centre, October 1990.

14. Ericsson, L., "Cobra Manoeuvre Considerations", ICAS 92-4.6R, September 1992.

15. "New Su-35 Boasts Greater Agility", Aviation week & Space Technology pp 44-45, December 6, 1993.

16. Newman, B., "Boundary Layer & Flow Control - Its principles and Applications", Pergamon press, 1961.

17. Schlichting, H., "Boundary-Layer Theory", sixth edition, 1968, McGraw-Hill Book Company, p 696.

18. Glauert, M., "The Wall Jet", Journal of Fluid Mechanics, Vol 1, August 1956.

19. Coanda, H., "Procedé de propulsion dans un Fluide", Brevet Invent, Gr C12, No 762688, Rép Française.

20. Englar, R., "Further Developments of Pneumatic Thrust-Deflecting Powered Lift Systems", Journal of Aircraft, Vol 25 No 4, April 1988, pp 324-333.

21. Wood, N., Nielsen, J., "Circulation Control Aerofoils as Applied to Rotary Wing Aircraft", Journal of Aircraft, Vol 23 No 12, December 1986, pp 865-875.

22. Harris, M., Nichols, Jr., Englar, R., Huson, G., "Development of the Circulation Control Wing/Upper surface Blowing Powered-Lift System for Stol Aircraft", ICAS 82-6.5.1, 1982.

23. Wood, N., Ward, S., and Roberts, L., "Wind Tunnel Boundary Layer Control by Coanda Wall Jets", AIAA 89-0146, January 1989.

24. Freund, J., Mungal, M., "Drag Modification and Wake Control of An Axisymmetric Bluff Body Using the Coanda Effect", AIAA 92-2705, 1992.

25. Wood, N., Roberts, L., "Control of Vortical Lift on Delta Wings by Tangential Leading Edge Blowing", Journal of Aircraft, Vol 25 No 3, March 1988, pp 236-243

26. Greenwell, D., Wood, N., "Static Roll Moment Characteristics of Asymmetric Tangential Leading Edge Blowing on a Delta Wing at High Angles of Attack", to be published, 1992.

27. Lighthill, M., "Note on the Deflection of Jets by Insertion of Curved Surfaces and on the Design of Bends in Wind Tunnels", ARC R&M 2105, 1945.

28. Thomann, H., "Effect of Streamwise Curvature on Heat Transfer in a Turbulent Boundary Layer", Journal of Fluid Mechanics, Vol 33, p 283, 1968.

29. Bradshaw, P., "Effect of Streamline Curvature on Turbulent Flow", AGARD-AG-169, 1973.

30. Von Kaman, T., "Some Aspects of the Turbulence Problem", Proc of the 4th Int Congress of Applied Mechanics, Cambridge 1934, pp 54-91.

31. Roberts, L., "A Theory for Turbulent Curved Wall Jets", AIAA 87-0004, January 1987.

32. Kizilos, A., Rose, R., "Experimental Investigation of Flight Control Surfaces Using Modified Air Jets", Honeywell Document No. 12055-FR1, Nov 1969.

33. Gee, K., Rizk, Y. Schiff, L., "Analysis of Tangential Slot Blowing on an F/A-18 Isolated Forebody", AIAA 94 1831-CP, 1994.

34. Patankar, U., Sridhar, K., "Three-Dimensional Curved Wall Jets",

Transactions of the ASME, J. Basic Engineering, vol 94, 1972, pp 339-344.

35. Launder, B., Rodi, W., "The Turbulent Wall Jet", Progress in Aerospace Science, Vol 19, 1981, pp 81-128.

36. Rodman, L., "An Experimental Investigation of Straight and Curved Annular Wall Jets", PhD Dissertation, Stanford University, 1987.

37. Rodman, L., Wood, N., Roberts, L., "Experimental Investigation of Straight and Curved Annular Wall Jets", AIAA Journal, Vol 27, No 8, August 1989, pp 1059-1067.

38. "MD Explorer Blends New Technologies", Aviation Week & Space Technology, 22 February, 1993, pp 48-52.

39. Clark, W., Peoples, J. and Briggs, M., "Occurrence and Inhibition of Large Yawing Moments During High Incidence Flight of Slender Missile Configurations", AIAA 72-968, September 1972.

40. Clark, W., "Body Vortex Formation on Missiles in Incompressible Flows", AIAA 77-1154, 1977.

41. Nielson, J., "Non-Linearities in Missile Aerodynamics", AIAA 78-20, January 1978.

42. Lamont, P. and Hunt, B., "Pressure and Force Distributions on a Sharp-Nosed Circular Cylinder at Large Angles of Inclination to a Uniform Subsonic Stream", J. of Fluid Mechanics, Vol. 76, Pt. 3, Pages 519-559, August 1976.

43. Lamont, P. and Hunt, B., "Prediction of Aerodynamic Out of Plane Forces on Ogive-Nosed Cylinders", J. of Spacecraft and Rockets, Vol. 14, No 1, January 1977, pages 31-44.

44. Wardlaw, A., "High Angle of Attack Missile Aerodynamics", AGARD LS-98.

45. Yanta, W., Wardlaw, Jr. "Flowfield About and Forces on Slender Bodies at High Angles of Attack", AIAA Journal, Vol 19, No 3, pp 296-302, 1980.

46. Ericsson, L. and Reding, J., "Review of Vortex-Induced Asymmetric Loads - Part One", Z. Flugwiss. Weltraumforsch., Vol. 5, 1981, Heft.

47. Yuan, C., Howard, R., "Effects of Forebody Strakes on Asymmetric Vortices for a Vertically Launched Missile", AIAA 91-2864, 1991.

48. Modi, V., Stewart, A., "Approach to Side Force Alleviation Through Modification of the Pointed Forebody Geometry", J. of Aircraft, Vol 29, No 1, pp 123-129, Jan-Feb 1992.

49. Edwards, O. "Northrop F-5F Shark Nose Development", NASA CR-158936, October 1978.

50. Stahl, W., "Experimental Investigation of Asymmetric Vortex Flows Behind Elliptic Cones at Incidence", AIAA Journal, Vol 31, No 5; Technical Notes, 1992.

51. Bauer, S., Hemsch, M., "Alleviation of Side Force on Tangent Ogive Forebodies using Passive Porosity", AIAA 92-2711-CP, 1992.

52. Murri, D., Rao, D., "Exploratory Studies of Actuated Forebody Strakes for Yaw Control at High Angles of Attack", AIAA 87-2557-CP, 1987.

53. Zilliac, G., Degani, D., Tobak, M., "Asymmetric Vortices on a Slender Body of Revolution", AIAA 90-0388, 1990.

54. Fiddes, S., "Separated Flow About Cones at Incidence - Theory and Experiment", Royal Aircraft Establishment Technical Memorandum Aero 2055, December 1985.

55. Smith, J.H.B., "Theoretical Modelling of Three-Dimensional Vortex Flows in Aerodynamics", AGARD CP-342, No 17, 1983, Also Aeronautical Journal, April 1984.

56. Brown, C., Michael, W., "On Slender Wings with Leading Edge Separation", Journal of Aeronautical Sciences, Vol 21, 1954, also NACA TN-3430, 1955.

57. Bryson, A., "Symmetric Vortex Separation on Circular Cylinders and Cones", ASME Journal of Applied Mechanics (JASME) 26, pp 643-648, 1959.

58. Fiddes, S., "A Theory for the Separated Flow Past a Slender Elliptic Cone at Incidence", AGARD CP-291, No 30, 1980.

59. Fiddes, S., Williams, A., "Recent Developments in the Study of Separated Flows Past Slender Bodies at Incidence", Royal Aeronautical Society Conference on The Prediction and Exploitation of Separated Flow, pp 31.1-31.17, 1989.

60. Smith, J.H.B., "Inviscid Fluid Models Based on Rolled Up Vortex Sheets for Three-Dimensional Separation at High Reynolds Number", AGARD LS-94, No 9.

61. Mangler, K., Smith, J.H.B, "A Theory of the Flow Past a Slender Delta Wing with Leading Edge Separation", RAE Report Aero 2593, 1957.

62. Smith, JHB., "Behaviour of a Vortex Sheet Separating from a Smooth Surface", RAE Technical Report 65178, 1965.

63. Sacks, A., Lundberg, R., Hanson, C., "A Theoretical Investigation of the Aerodynamics of Slender Wing-Body Combinations Exhibiting Leading Edge Separation", NASA CR-719, 1967.

64. Tritton, D., "Physical Fluid Dynamics", Van Nostrand Reinhold, 1977, p 51.

65. Baldwin, B., Lomax, H., "Thin-Layer Approximation and Algebraic Turbulence Model for Separated Turbulent Flows", AIAA Journal, Vol 25, April 1987, pp 527-534.

66. Degani, D., Schiff, L., "Computation of Turbulent Supersonic Flows Around Pointed Bodies Having Crossflow Separation", J of Computational Physics, Vol 66, No 1, Sept 1986, pp 173-196.

67. Hartwich, P. and Hall, R., "Navier-Stokes Solutions for Vortical Flows over a Tangent Ogive Cylinder", AIAA Journal, Vol 28, No 7, July 1990.

68. Siclari, M. and Marconi, F., "Computation of Navier-Stokes Solutions Exhibiting Asymmetric Vortices", AIAA Journal Vol 29, No 1, 1990.

69. Degani, D., Levy, Y., "Asymmetric Turbulent Vortical Flows Over Slender Bodies", AIAA Journal, Vol 30, No 9, September 1992, pp 2267-2273.

70. Vanden, K., Belk, D., "Numerical Investigation of Subsonic and Supersonic Asymmetric Vortical Flow", AIAA 91-2871, 1991.

71. Wood, N., Private Communication.

72. "Vector Victor: Benefits of Thrust Vectoring and Reversing on the F-15", Flight International pp 23-27, 28 August-3 September, 1991.

73. "Alpha Beater: Three-Dimensional Thrust Vectoring on the F-16", Flight International pp 24-25, 5-11 January, 1994.

74. Murri, D. and Rao, D. "Exploratory Studies of Actuated Forebody Strakes for Yaw control at High Angles of Attack", AIAA 87-2557, August 1987.

75. Malcom, G., NG, T., Lewis, L. and Murri, D. "Development of Non-Conventional Control Methods for High Angle of Attack Flight Using Vortex Manipulation", AIAA 89-2192, July 1989.

76. Peak, D., Owen, F. and Johnson, D., "Control of Forebody Vortex Orientation To Alleviate Side Forces", AIAA 80-0183, January 1980.

77. "New High-AoA Tests for F-18 Proposed", Flight International, 23 Feb, 1994, p 21.

78. Murri, D., Gautam, S., DiCarlo, D., "Actuated Forebody Strake controls for the F-18 High Alpha Research Vehicle", AIAA 93-3675, 1993.

79. Moskovitz, C., Hall, R. and Dejarnette, F., "Experimental Investigation of a New Device to Control the Asymmetric Flow on Forebodies at Large Angles of Attack", AIAA 90-0068, January 1990.

80. Ross, A., Jeffries, E. and Edwards, G., "Control of Forebody Vortices by Suction on the Nose of the RAE High Incidence Research Model", AGARD CP-494, October 1990.

81. Ross, A., Jeffries, E. and Edwards, G., "Aerodynamic Data for the Effects of Nose Suction on a High Incidence Research Model with a Large Forebody", RAE Tech Memo, Aero 2204, January 1991.

82. Ross, A., Jefferies, E., Edwards, G., "Dynamic Wind Tunnel Tests on Control of Forebody Vortices with Suction", DRA Tech Memo Aero 2206, 1991.

83. Almosnino, D. and Rom, J. "Alleviation of the Side Force and the Yawing Moment Acting on a Slender Cone-Cylinder Body at High Angle of Attack, Using Small Jet Injection at Subsonic and Transonic Speeds", TAE No 380, Techion Israel Institute of Technology, Dept of Aeronautical Engineering, September 1979.

84. Mundell, A., "Low Speed Wind Tunnel Tests on the Use of Air Jets to Control Asymmetric Forces and Moments Occurring on Aircraft at High Incidences", RAE Aero Tech Memo, Jan 1984.

85. Skow, A., Moore, W. and Lorincz, D., "Forebody Vortex Blowing - A Novel Concept to Enhance the Departure/Spin Recovery Characteristics of Fighter Aircraft", AGARD CP-262, May 1979.

86. Gittner, N. and Chokani, N., "An Experimental Study of the Effects of Aft Blowing on a 3.0 Calibre Tangent Ogive Body at High Angles of Attack", AIAA 91-3252, September 1991.

87. "Vortex Flow Control Provides Aircraft Stability", Mechanical Engineering, Vol 115, No 4, p 30, April 1993.

88. Ng, T., Suavez, C. and Malcolm, G., "Forebody Vortex Control Using Slot Blowing", AIAA 91-3254, September 1991.

89. Meyn, L., Lanser W., James K., "Full-Scale High Angle-of-Attack Tests of

an F/A-18", AIAA 92-2676, June 1992.

90. Celik, Z., Roberts, L., "Vortical Flow Control on a Slender Body at High Angles of Attack", AIAA 91-2868, 1991.

91. Tavella, D., Schiff, L. and Cummings, R., "Pneumatic Vortical Flow Control at High Angles of Attack", AIAA 90-0098, January 1990.

92. Font, G., Celik, Z. and Roberts, L., "A Numerical and Experimental Study of Tangential Jet Blowing Applied to Bodies at High Angles of Attack", AIAA 91-3253, 1991.

93. Murman, M., Rizk, M., Cummings, R., Schiff, L., "Computational Investigation of Slot Blowing for Fuselage Forebody Flow Control", AIAA 92-0020, 1992.

94. Greenwell, D., Bean, D., Wood, N., "Calibration of the High Speed Working Section of the 7' x 5' Wind Tunnel", School of Mech Eng Report 49/1992, July 1992.

95. Greenwell, D., Bean, D., Wood, N., "A High Angle of Attack Model Support System for the 7' x 5' Wind Tunnel" School of Mech Eng Report 50/1992, July 1992.

96. Greenwell, D., Wood, N., "Some General Purpose Data Acquisition and Reduction Programs in Use in the Aerodynamics Group", School of Mech Eng Report 52/1992, July 1992.

97. Lanser, W., Meyn, L., "Forebody Flow Control on a Full-Scale F/A-18 Aircraft", AIAA 92-2674, June 1992

98. Rae, W., Pope, A., "Low Speed Wind Tunnel Testing", Wiley 1984.

99. Hummel, D., "On the Vortex Formation Over Slender Wings at Large Angles of Incidence", AGARD CP-247.

100. Weinberg, Z., "Effects of Tunnel Walls on Vortex Breakdown Location Over

Delta Wings", AIAA Journal, Vol 30 No 6, June 1992, pp 1584-1586.

101. Greenwell, D., "Control of Asymmetric Vortical Flow Over a Delta Wing at High Angles of Attack", Phd Thesis, University of Bath, 1993.

102. Massey, D. "Mechanics of Fluids", 4th edition, Van Nostrand Reinhold Company, New York.

103. Smith, J.H.B., "Remarks on the Structure of Conical Flow", Progress in Aeronautical Science, Vol 12, Pergamon Press, 1972.

104. Gee, K., Tavella, D., Schiff, L., "Computational Optimisation of a Pneumatic Forebody Flow Control Concept", AIAA 91-3249, 1991.

105. Malcolm, G., "Forebody Vortex Control", Agard Report No 776, April 1991.

106. Ng, T. and Malcolm, G. "Aerodynamic Control Using Forebody Blowing and Suction", AIAA 91-0619, January 1991.

107. Zhou, m., Wygnanski, I., "Parameters Governing the Turbulent Wall Jet in an External Stream", AIAA Journal, Vol 31, No5, pp 848-853, May 1993.

108. Lamont, P., "The Effect of Reynolds Number on Normal and Side Forces on Ogive-Cylinders at High Incidence", AIAA 85-1799, 1985.

109. Widing, K., "Experimental Study of Vortex Effects on a Fighter Aircraft Forebody at high Angle of Attack", ICAS 92-4.6.2, 1992.

110. "X-31A Vertical Tail to be Removed in Trials", Flight International p 18, 6-12 October, 1993.